Development of an active methodology for hybrid RANS-LES computations of turbulent flows.Développement d'une méthodologie active pour la simulation hybride RANS-LES des écoulements turbulents.

Mahitosh Mehta

THESIS

for the degree of

DOCTOR OF PHILOSOPHY

from Université de Pau et des Pays de l'Adour
École doctorale SEA
Sciences Exactes et leurs Applications

SPECIALITY : FLUID MECHANICS

Presented by :
MAHITOSH AJAYKUMAR MEHTA

Development of an active methodology for hybrid RANS/LES computations of turbulent flows

---

Director of the thesis :
RÉMI MANCEAU

Defended on 27 November 2023 in front of jury

Pr. Lars Davidson	Chalmers University of Technology	Evaluator
Dr. Christophe Friess	Université Aix-Marseille	Evaluator
Pr. Sylvain Laizet	Imperial College London	Examiner
Dr. Celine Baranger	CEA/CESTA, Le Barp	Examiner
Dr. Vladimir Duffal	EDF R&D, Chatou	Examiner
Dr. Rémi Manceau	CNRS, LMAP, Pau	Supervisor

To my family.

Acknowledgements

First of all, I would like to thank Dr Rémi MANCEAU, a research director at CNRS, leader of the Inria project - team CAGIRE, who gave me this precious opportunity to start the thesis in his laboratory. This dissertation would not have become a reality without the extensive support, guidance and assistance of many individuals. I would like to extend my sincere thanks to all of them. This thesis is the outcome of 3 years of research, which I started at the Laboratory of Mathematics (LMAP), team CAGIRE, University of Pau (UPPA).

My sincere gratitude goes towards Pr Lars DAVIDSON from Chalmers University of Technology and Dr Christophe FRIESS from IUT Aix-Marseille Université, for accepting to be the evaluator of my thesis.

My grateful thanks to Pr Sylvain Laizet from Imperial College London, Dr Celine BARANGER from CEA and Dr Vladimir DUFFAL from EDF R&D for accepting to be the part of the jury as examiners.

Foremost, I would like to express my sincere gratitude to my advisor Dr Rémi MANCEAU for the continuous support during my PhD study and related research and for his patience, motivation, and knowledge. Please be assured of my gratitude. Working with such an involved researcher is an honour.

I would like to thank Dr Marcello Meldi and Dr Jacque Borèe who introduced me to the intriguing world of turbulence during my Master at ISAE-ENSMA, Poitiers.

I would like to thank all the members of the team CAGIRE whom I was able to meet during this thesis:

To Dr Kevin SCHMIDMAYER, for always entertaining a discussion with me and for bearing several stupid questions. To Dr Pascal BRUEL, for always encouraging me to think outside the box and enriching my limited knowledge of turbulence.

I would like to thank Puneeth for always answering the question regarding the model and code. To Dr Martin David, for the discussions regarding the application of the hybrid approach in the self-adaptive study and other general discussions. To Dr Sofen kumar JENA, for helping me with the Ansys Fluent Workbench.

I thank my other fellow lab mates at LMAP: Dr Vincent, Dr Jonathan, Dr Sangeeth, Ibtissem and Anthony for the stimulating discussions and for all the fun we had in the last few years. To all the members of the lab for their warm welcome and good humor that have made it possible for us to live those three years as the most enjoyable years of thesis.

Thanks to Mr Bruno Demoisy and Madame Isabelle WENDLING for facilitating the administrative work.

I would like to extend my special thanks to Jean-Pierre BEDECARRATS for providing me with a wonderful opportunity to teach about turbulence and its modeling. I would also like to thank my students for listening to me very sincerely.

I am forever grateful to Lord SHIVA, my parents, my sister, my brother-in-law and friends for their encouragement which helped me in completion of this dissertation. I

would like to thank them for listening to me and for always asking about my research especially my father. I wouldn't have been at this stage in my life without their continuous support, guidance and love. I dedicate this work to all of them.

Résumé

La puissance et le coût de calcul restent hors de portée dans un avenir prévisible pour la plupart des cas qui nécessitent de résoudre une grande partie du spectre de la turbulence. Pour cette raison, la recherche sur les méthodes hybrides RANS/LES, qui sont basées sur une résolution multi-échelle, est en plein essor depuis les deux dernières décennies. Les approches hybrides sont principalement divisées en deux catégories basées sur l'interface entre RANS et LES : i) approches zonales : caractérisées par une pré-division entre les zones RANS et LES par une interface discontinue, et ii) approches continues : caractérisées par une interface diffuse entre RANS et LES. Ces approches hybrides souffrent d'une diminution des contraintes turbulentes lorsqu'elles passent d'une description statistique (RANS) à une description filtrée (LES), ce qui est connu sous le nom de "Modelled Stress Depletion (MSD)", ou problème de "zone grise". Le but de cette thèse est de proposer un modèle actif pour corriger ce problème.

Dans les approches zonales, à l'interface entre RANS et LES, il est nécessaire d'ensemencer l'entrée de la zone LES afin qu'elle génère rapidement des structures turbulentes et limite ainsi les effets de zone grise. Cependant, les approches zonales sont trop restrictives et peu flexibles pour les applications industrielles. Le travail effectué dans cette thèse s'inscrit dans le cadre des approches continues. Dans les méthodes hybrides continues, le passage de RANS à LES est activé par des critères basés sur la comparaison d'échelles, généralement l'échelle de longueur intégrale et la taille des mailles locales. Actuellement, les simulations hybrides continues RANS/LES sont assez simples à réaliser, mais Les fluctuations résolues doivent apparaître assez rapidement dans la zone grise et au début de la région LES pour éviter une sous-estimation de la contrainte turbulente lors du passage des zones entièrement modélisées aux zones partiellement résolues.

Une génération naturelle de ces fluctuations est observée mais leur croissance n'est pas assez rapide. Pour résoudre ce problème, l'objectif est de générer une turbulence synthétique qui ajoute artificiellement des fluctuations pendant la transition RANS-LES. La présente thèse propose une méthode de forçage volumique basée sur le forçage linéaire anisotrope (ALF) pour générer des fluctuations résolues dans l'équation de quantité de mouvement résolue afin d'éviter le problème de la réduction des contraintes modélisées ("Modelled Stress Depletion (MDS)"). La méthode de forçage proposée est très simple et générale. En effet, elle ne nécessite aucune information sur les directions relatives de l'écoulement et de l'interface diffuse et est indépendante de tout formalisme sous-jacent. L'intensité du forçage est dérivée analytiquement de telle sorte que, lorsque la résolution est raffinée, l'énergie perdue par le mouvement modélisé est injectée dans le mouvement résolu.

Cette nouvelle méthode de forçage est appelée "active HTLES", car elle est appliquée à l'approche Hybrid Temporal LES (HTLES). Dans cette thèse, la méthode de forçage est développée, mise en œuvre, calibrée et testée dans trois cas d'écoulement différents : écoulement en canal, écoulement en collines périodiques et écoulement le long d'une marche

descendante. L'introduction de ce forçage dans l'équation de quantité de mouvement résolue accélère la transition vers la LES et améliore les résultats. Bien qu'il faille la tester dans d'autres configurations, cette approche est très encourageante pour les applications industrielles.

Abstract

As the computational power and computing cost remain out of the reach for foreseeable future for most of the cases that require scale-resolving computations, research in the hybrid RANS/LES methods which are based on multi-scale resolution are thriving for the last couple of decades. Hybrid approaches are primarily divided into two categories based on the interface between RANS and LES: i) zonal approaches: which are characterized by a pre-division between RANS and LES zones by a discontinuous interface, and ii) continuous approaches: which are characterized by a diffuse interface between RANS and LES. These hybrid approaches suffer from stress decay when they transition from statistical description (RANS) to filtered description (LES), which is known as "Modeled Stress Depletion (MSD)", or "grey area" problem, and the purpose of this thesis is to propose an active model to correct this problem.

In zonal approaches, at the interface between RANS and LES, it is necessary to seed the LES zone inlet so that it rapidly generates vortex content and thus limits grey zone effects. The zonal approaches are too restrictive and inflexible for industrial applications. The work done in this thesis is under the framework of continuous approaches. In continuous hybrid methods, the switch from RANS to LES is activated by criteria based on scale comparison, generally the integral length scale and the local mesh size. With the current state of the art, continuous hybrid RANS/LES simulations are quite straightforward to perform. The question then arises as to whether the resolved fluctuations will appear quickly enough in the grey zone and the beginning of the LES region to avoid an underestimation of the turbulent stress when we move from completely modeled to partially resolved zones.

A natural generation of these fluctuations is observed but their growth is not fast enough. To avoid this problem the aim is to generate synthetic turbulence that artificially adds fluctuations during the RANS-to-LES transition. The present thesis proposes a volume forcing method based on Anisotropic Linear Forcing (ALF) to generate resolved fluctuations in the resolved momentum equation to avoid the problem of modeled stress depletion. The new forcing methodology is very simple, as it requires no information on the relative directions of the flow and the diffuse interface, and general, as it is independent of any underlying formalism. The intensity of the forcing is derived analytically in such a way that, when the resolution is refined, the energy lost by the modeled motion is injected into the resolved motion.

This new forcing method, called "active HTLES", as Hybrid Temporal LES (HTLES) is used as the preferred hybrid method, is developed, implemented, calibrated, and tested in three different flow cases: channel flow, periodic hill flow, and backward-facing step flow during the duration of this thesis. Introducing this forcing into the resolved momentum equation accelerates the transition to LES and improves the results. Although it requires testing in more configurations, it is very encouraging for industrial applications.

Contents

Nomenclature

Acronyms

ALF	Anisotropic Linear Forcing
CFD	Computational Fluid Dynamics
DDES	Delayed Detached Eddy Simulation
DES	Detached Eddy Simulation
DNS	Direct Numerical Simulation
ELES	Embedded Large Eddy Simulation
HTLES	Hybrid Temporal Large Eddy Simulation
ICC	Internal Consistency Constraint
IDDES	Improved Delayed Detached Eddy Simulation
LDS	Laraufie Deck Sagaut
LES	Large Eddy Simulation
LIC	Line Integral Convolution
MSD	Modeled Stress Depletion
PANS	Partially Averaged Navier-Stokes
PITM	Partially Integrated Transport Model
RANS	Reynolds-Averaged Navier-Stokes
SEM	Synthetic Eddy Method
SFS	Sub-Filter Scales
SKK	Spille-Kohoff Kaltenbach
SST	Shear Stress Transport
STG	Synthetic Turbulence Generator
TLES	Temporal Large Eddy Simulation
TPITM	Temporal Partially Integrated Transport Model

Latin symbols

$\mathcal{C}$	Coefficient of Active HTLES model
$\mathcal{C}_{ij}$	Cross-stress tensor
$\mathcal{D}$	Domain
$\mathcal{G}$	Filter kernel
$\mathcal{L}_{ij}$	Leonard's tensor
$\Phi_{ij\text{sfs}}$	Subfilter pressure strain correlation
Φ_{ij}	Pressure strain correlation
τ_r	Relaxation time for the resolved stress tensor
τ_v	Relaxation time for the mean velocity
$\varepsilon_{ij\text{sfs}}$	Subfilter dissipation term
ε_{ij}	Dissipation term
$\widetilde{f}_d$	Blending function of IDDES model
ξ_D	Shielding function based on grid step
ξ_K	Shielding function based on Kolmogorov length scale
a_{ij} or b_{ij}	Anisotropy tensor
C_f	Wall friction coefficient
C_K	Kolmogorov constant
c_r	Coefficient representing Internal Consistency Constraint
C_s	Smagorinsky constant
C_{DES}	Adjustable constant of DES model
C_{ij}	Convective term
d_w	Distance to the wall
$D_{ij\text{sfs}}$	Subfilter diffusion terms
D_{ij}	Diffusion terms
D_{ij}^{ν}	Diffusion by molecular agitation
D_{ij}^{P}	Diffusion by pressure
D_{ij}^{T}	Diffusion by turbulent agitation
$E(\kappa)$	Turbulent kinetic energy per unit wavenumber (Energy density in wavenumber space)
$E(\omega)$	Turbulent kinetic energy per unit frequency (Energy density in frequency space)

e^*	Instantaneous internal energy
F_1, F_2	Blending functions of $k-\omega$ SST model
f_ε	Ratio of modeled-to-total dissipation in PANS model
f_c	Cut-off frequency
f_d	Shielding function of DDES model
F_i	Mean external force
f_i	Fluctuating external force
F_i^*	Instantaneous external force
f_k	Ratio of modeled-to-total kinetic energy in PANS model
f_s	Shielding function of HTLES model
F_{DES}	Hybridization function of DES model
f_{dt}	Shielding function of IDDES model
k	Total turbulent kinetic energy
$k^\dagger$	Target turbulent kinetic energy
k_m	Modeled turbulent kinetic energy
k_r	Resolved turbulent kinetic energy
k_{sfs}	Subfilter turbulent kinetic energy
L	Unit length
l_κ	Size of eddies in wavenumber space
l_c	Size of the largest eddy
l_{DDES}	Length scale of DDES model
l_{DES}	Length scale of DES model
l_{IDDES}	Length scale of IDDES model
M	Unit mass
N	Number of cells
P	Mean pressure
p	Fluctuating pressure
P^*	Instantaneous pressure
P_m	Modeled production term
$P_{ij\mathrm{sfs}}$	Subfilter production tensor
P_{ij}	Production tensor

r	Energy ratio
r_K	Energy ratio under Kolmogorov assumptions
r_{eff} or r_{observed}	Observed energy ration
r_{mod}	Modified (Imposed) energy ratio
R_{ij}	Reynolds stress tensor
Re	Reynolds number
Re_τ	Frictional Reynolds number
Re_b	Bulk Reynolds number
Re_t	Turbulent Reynolds number
S_{ij}	Mean strain tensor
s^*_{ij}	Instantaneous strain tensor
T	Unit time
T^*	Instantaneous temperature
T^f	Energy production due to the force
$T_m\,(r)$	Time scale of HTLES model
u_τ	Frictional velocity
U_b	Bulk velocity
$U_i = \overline{U^*_i}$	Mean velocity
u_i	Fluctuating velocity
U^*_i	Instantaneous velocity
u'_i	Resolved fluctuating velocity
u^t_i	Total fluctuating velocity
u''_i	Residual velocity
U_s	Sweeping velocity
V_{ref}	Arbitrary velocity constant in space and time

Greek symbols

Δ	Mesh size (grid step)
Δ_x	mesh size in $x-$direction
Δ_y	mesh size in $y-$direction
Δ_z	mesh size in $z-$direction
δ_{ij}	Kronecker delta

η	Kolmogorov length scale
γ_i	Heat flux
κ	Wavenumber
κ_c	Cut-off wavenumber
κ_d	Wavenumber in the dissipative zone
λ	Volumic viscosity
ν	Kinematic viscosity
ν_t	Turbulent viscosity
ν_{sfs}	Subfilter viscosity
ω	Frequency
ω_c	Cut-off frequency
Ω_{ij}	Mean rotation tensor
$\psi(r)$	Hybridization function of $k-\varepsilon$ HTLES model
$\psi'(r)$	Hybridization unction of $k-\omega$ SST HTLES model
$\psi_{ij}(\kappa)$ or $\psi_{ij}(\omega)$	Tensor of velocity spectrum
ρ	Density
ρ^*	Instantaneous density
σ_{ij}^*	Instantaneous stress tensor
τ	Kolmogorov time scale
$\tau_{ij\text{sfs}}$	Subfilter stress tensor
τ_{ij}	Stress tensor
$\tau_{ij}^\dagger$	Target stress tensor
τ_{ij}^m	Reynolds average of the modeled subfilter stress tensor
ε	Total dissipation
$\varepsilon^\dagger$	Target dissipation
ε_{sfs}	Subfilter dissipation
v	Kolmogorov velocity scale

Mathematical operators

$\frac{\mathrm{d}f}{\mathrm{d}t}$	Total derivative of f with respect to time
$\frac{\mathrm{d}f}{\mathrm{d}x_i}$	Total derivative of f with respect to distance x_i

$\frac{\partial f}{\partial t}$	Partial derivative of f with respect to time
$\frac{\partial f}{\partial x_i}$	Partial derivative of f with respect to distance x_i
$\langle \, . \, \rangle$	Filtering operator
$\nabla \cdot f$	Divergence of f
∇f	Gradient of f
$\nabla^2 f$	Laplacian of f
$\overline{.}$	Spatial filtering operator
$\widetilde{.}$	Temporal filtering operator

Introduction (English)

Some people want it to happen, some wish it would happen, others make it happen.
— Michael Jordan

Context

Computational Fluid Dynamics (CFD) plays a major role in the design, validation and optimization of industrial devices, and its role is set to become increasingly important. In the vast majority of industrial applications, flows are turbulent, and it can be shown that the optimal number of mesh cells is proportional to the turbulent Reynolds number at the 9/4 power, which leads to astronomical computational cost. This is why statistical turbulence modeling (RANS, Reynolds Averaged Navier-Stokes) has been the norm in industrial applications for many years.

For many applications, statistical modeling is not satisfactory, either because turbulence is far from equilibrium conditions, so that standard RANS models lack accuracy, or because unsteady information is explicitly required by the application (thermal fatigue, fluid/structure interaction, etc.). An intermediate solution between DNS and RANS is Large-Eddy simulation (LES). However, as noted by Spalart (2000), the computation of a whole airplane, turbine, or car using LES will not be affordable before 2045, due to computational cost, if the near-wall region is represented by the oversimplified wall function, and before 2070 if the near-wall region is resolved. As a result, in the design cycle of new industrial products, LES is currently and will in the foreseeable future only be used **in a few niche applications**.

The next generation of industrial CFD tools will be most probably based on the only approach compatible with admissible CPU costs in a foreseeable future, hybrid RANS/LES. Hybrid RANS/LES methods are based on multi-scale resolution, either in zones separated by an interface (zonal method), or by a gradual change in the scale description (continuous method), which radically reduces the computational cost of unsteady simulations (LES), while retaining a finer description of the physics in regions where it is necessary.

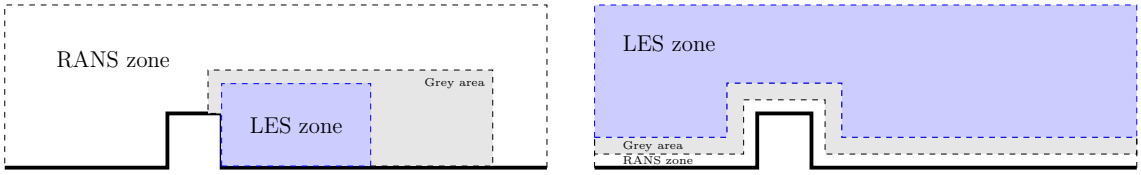

(a) Embedded LES (b) LES with a near-wall RANS layer

Figure 1 – Illustration of the two main application strategies for hybrid RANS/LES

A particularly attractive approach is the Embedded LES method, which involves reserving the LES for a small area included in a global RANS domain, which is a particular strategy for using the zonal hybrid RANS/LES. However, the zonal approach is characterized by a pre-division between the RANS zone and the LES zone, and by a discontinuous interface. This prohibits any evolution in the scale of the turbulence description, which would enable the model to be adapted according to physical criteria determined during the calculation. The work done in this thesis deals with the continuous approach, in which the interface between RANS and LES is a diffuse interface. In these approaches, the computational domain is not divided into predefined subdomains, instead there is a continuous evolving of the model towards a RANS or LES model. The diffuse interface, more commonly known as *grey zone* is the transition zone where the model moves from statistical description to filtered description or vice-versa.

Research on hybrid RANS/LES methods started more than two decades ago and has been very active in the last decade, especially concerning their validation in a wide range of configurations. For non-homogeneous turbulence, there exist only two approaches able to provide a fully consistent framework to derive an hybrid model from the equations of

motion. The first one, promoted by Germano (2004), Hamba (2011) and Nini (2016) is based on additive filtering and the second one, which was proposed by Fadai-Ghotbi et al. (2010) and Tran et al. (2012), is based on temporal filtering. The formalism used here in this work, called hybrid temporal LES (HTLES) (Manceau, 2016; Duffal et al., 2022), which hybridizes RANS and temporal LES (TLES) (Pruett, 2000), is particularly attractive in the context of a seamless hybrid RANS/LES framework since the compatibility between the statistical operator (RANS) and the temporal operator makes possible a continuous transition from RANS to LES by making the temporal filter width go to infinity.

Challenges

The continuous approaches are generally used to switch to statistical RANS modeling in the near-wall region. The idea of embedded LES, as described in Fig. 1, which consists of using LES only in a very limited region surrounded by a region in RANS mode has been developed by a few authors (Cokljat et al., 2009; Deck, 2012; Poletto et al., 2012; Davidson et al., 2013; Holgate et al., 2019). At the interface between RANS and LES it is then necessary to seed the LES zone inlet so that it rapidly generates vortex content and thus limits grey zone effects (modeled stress depletion). Since the zonal approaches are too restrictive and inflexible to be attractive for the majority of industrial applications, continuous approaches are attracting a great deal of interest, and can be expected to gradually become standard methods for industrial CFD by the end of the decade.

With the current state of the art, continuous hybrid RANS/LES simulations are quite straightforward to perform in practice. In continuous hybrid methods, the switch from RANS to LES is activated by criteria based on scale comparison, generally the integral scale of turbulence and the local mesh size. All that has to be done is either create a mesh that is coarse enough to remain in RANS mode in the domain where LES is not required, and refine it locally to switch to LES mode; or deactivate the switchover criterion to force RANS mode in the chosen zone. The question then arises as to whether the resolved fluctuations will appear quickly enough in the grey zone and the beginning of the LES region to avoid underestimation of turbulent stress (modeled-stress depletion).

A natural generation of these fluctuations is observed in cases where the flow is hydrodynamically unstable (notably with velocity profiles presenting an inflection point). But even in this case, the appearance of resolved vortices is too slow (Mockett et al., 2018). However, guaranteeing that the switch from RANS to LES will always take place in a hydrodynamically unstable region is far too restrictive, if not impossible for complex configurations. Hence, current continuous RANS/LES hybrid methods are not capable of achieving a physically representative transition from RANS-to-LES. To avoid this problem the aim is to generate synthetic turbulence that artificially adds fluctuations to the RANS solution. Numerous methods have been proposed for this purpose, the most widely used of which is Synthetic Eddy Method (SEM) (Jarrin et al., 2009). A relatively new enrichment method, Anisotropic Linear Forcing (ALF), developed by De Laage de Meux et al. (2015), is based on volume forcing, and not on the introduction of fluctuations in a plane, and requires an overlap zone between the RANS zone and the LES zone. Its operation is based on the introduction of a fluctuating force into the momentum equation, whose intensity in each direction is used to force the LES to satisfy the statistics given by the RANS, which are used as a target.

For the work presented in the thesis, a volume forcing method based on ALF is developed to avoid the problem of modeled stress depletion. The new forcing methodology aims to adapt the aforementioned ALF volume forcing, which was developed in the zonal hybrid RANS/LES framework, to the continuous hybrid RANS/LES framework. The con-

siderable advantage of this volumetric approach is that it is simply defined at each point by the local conditions: it requires no information on the relative directions of the flow and the diffuse interface, whereas plane forcing methods require the flow to be orthogonal to the interface when switching from RANS-to-LES.

In theory, therefore, it is sufficiently general to be applied to any type of diffuse interface: entrance to the LES zone, exit from LES zone, tangential or oblique interface, etc. This new forcing method called *active* HTLES is developed, implemented, tested, calibrated and validated on academic cases during the time of this thesis using Code_Saturne (Archambeau et al., 2004), an industrial open-source code developed by EDF.

Structure of the manuscript

Chapter 1 discusses the methods for modeling turbulence, before describing the main RANS models, and filtered approaches, focusing on LES models and classical hybrid RANS/LES approaches. Finally, the state of the art in temporal hybrid modeling is presented.

Chapter 2 is dedicated to the discussion of hybrid temporal LES (HTLES) model. The later part of the chapter introduces all the academic tests to be studied during the duration of the thesis and the performance of HTLES in these configurations.

Chapter 3 discusses a few pre-existing forcing methods before focusing on the development of a new *active* approach for continuous hybrid RANS/LES, volumetric in nature, based on pre-existing forcing method, Anisotropic Linear Forcing (ALF), originally developed for zonal hybrid RANS/LES.

Chapter 4 is devoted to testing and calibrating this newly developed *active* approach with the flow on periodic hills. The results are evaluated in order to evaluate the ability of this approach to create or dampen resolved fluctuation upon transitioning from RANS-to-LES and LES-to-RANS, respectively.

Chapter 5 is devoted to test the robustness of the model against standard test cases for turbulence model development: flow in a channel and flow in a backward-facing step. A particular attention is paid on the robustness of the model by varying the area of application of the forcing for the backward-facing step case.

Chapter 6 allows to come back to the main results of the thesis and to present an overview, before proposing perspectives to this work.

Finally, in Appendices A to D, the complete formulation of the $k-\omega$ SST HTLES model, a journal article and two conference articles are recalled, respectively.

Introduction (Français)

Contexte

La dynamique des fluides numérique (CFD) joue un rôle majeur dans la conception, la validation et l'optimisation des dispositifs industriels, et ce rôle est appelé à devenir de plus en plus important. Dans la grande majorité des applications industrielles, les écoulements sont turbulents et il peut être démontré que le nombre optimal de mailles est proportionnel au nombre de Reynolds turbulent à la puissance 9/4, ce qui entraîne des coûts de calcul astronomiques. C'est pourquoi la modélisation statistique de la turbulence (RANS, Reynolds Averaged Navier-Stokes) a été la norme dans les applications industrielles pendant de nombreuses années.

Pour de nombreuses applications, la modélisation statistique n'est pas satisfaisante, soit parce que la turbulence est loin des conditions d'équilibre, de sorte que les modèles RANS standard manquent de précision, soit parce que des informations instationnaires sont explicitement requises par l'application (fatigue thermique, interaction fluide/structure, etc.). Une solution intermédiaire entre la DNS (Direct Numerical Simulation) et les modéles RANS est la simulation des grandes échelles (LES). Toutefois, comme l'a fait remarquer Spalart (2000), en raison du coût de calcul, le calcul d'un avion, d'une turbine ou d'une voiture à l'aide des modéles LES ne sera pas abordable avant 2045, si la région proche de la paroi est représentée par une fonction de paroi simplifiée à l'extrême, et avant 2070 si la région proche de la paroi est résolue. Par conséquent, dans le cycle de conception des nouveaux produits industriels, la LES n'est actuellement et ne sera dans un avenir prévisible utilisée que dans quelques applications de niche.

La prochaine génération d'outils CFD industriels sera très probablement basée sur la seule approche compatible avec les coûts CPU admissibles dans un avenir proche, l'hybride RANS/LES. Les méthodes hybrides RANS/LES reposent sur une résolution multi-échelle, soit en zones séparées par une interface (méthode zonale), soit par un changement progressif de la description de l'échelle (méthode continue), ce qui réduit radicalement le coût de calcul des simulations instationnaires (LES), tout en conservant une description plus fine de la physique dans les régions où cela est nécessaire.

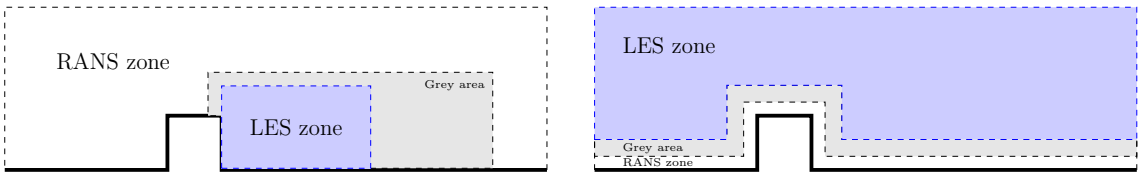

(a) Embedded LES (b) LES with a near-wall RANS layer

Figure 2 – Illustration des deux principales stratégies d'application des RANS/LES hybrides

Une approche particulièrement intéressante est la méthode Embedded LES, qui consiste à réserver la LES pour une petite zone incluse dans un domaine RANS global, ce qui est une stratégie particulière pour utiliser l'hybride zonal RANS/LES. Cependant, l'approche zonale se caractérise par une pré-division entre la zone RANS et la zone LES, et par une interface discontinue. Ceci empêche toute évolution de l'échelle de description de la turbulence, qui permettrait d'adapter le modèle en fonction de critères physiques déterminés lors du calcul. Les travaux effectués dans cette thèse portent sur l'approche continue, dans laquelle l'interface entre RANS et LES est une interface diffuse. Dans ces approches, le domaine de calcul n'est pas divisé en sous-domaines prédéfinis, mais il y a plutôt une évolution continue du modèle vers un modèle RANS ou LES. L'interface diffuse, plus communément appelée zone grise, est la zone de transition où le modèle passe de la description statistique à la description filtrée ou vice versa.

La recherche sur les méthodes hybrides RANS/LES a débuté il y a plus de deux décennies et a été très active au cours de la dernière décennie, notamment en ce qui concerne leur validation dans un large éventail de configurations. Pour la turbulence non homogène, il existe seulement deux approches capables de fournir un cadre totalement cohérent pour dériver un modèle hybride à partir des équations du mouvement. Le premier, promu par Germano (2004), Hamba (2011) et Nini (2016) est basé sur le filtrage additif et le second, proposé par Fadai-Ghotbi et al. (2010) et Tran et al. (2012), est basé sur un filtrage temporel. Le formalisme utilisé ici dans ce travail, appelé LES hybride temporelle (HTLES) (Manceau, 2016; Duffal et al., 2022), qui hybride RANS et LES temporelle (TLES) (Pruett, 2000), est particulièrement attractif dans le contexte de l'hybride RANS/LES continue puisque la compatibilité entre l'opérateur statistique (RANS) et l'opérateur temporel permet une transition continue de RANS vers LES en faisant tendre la largeur du filtre temporel vers l'infini.

Défis

Les approches continues sont généralement utilisées pour passer à la modélisation statistique RANS dans la région proche des parois. L'idée des LES embarquées, telle que décrite dans la Fig. 2, qui consiste à n'utiliser les LES que dans une région très limitée entourée d'une région en mode RANS a été développée par quelques auteurs (Cokljat et al., 2009; Deck, 2012; Poletto et al., 2012; Davidson et al., 2013; Holgate et al., 2019). À l'interface entre RANS et LES, il est alors nécessaire d'ensemencer l'entrée de la zone LES afin de favoriser rapidement la génération du contenu tourbillonnaire, limitant ainsi les effets de la zone grise (effondrement des contraintes modélisées). Les approches zonales étant trop restrictives et peu flexibles pour être attractives pour la majorité des applications industrielles, les approches continues suscitent beaucoup d'intérêt et devraient progressivement devenir des méthodes standards pour la CFD industrielle d'ici la fin de la décennie.

Dans l'état actuel de la technique, les simulations hybrides continues RANS/LES sont assez simples à réaliser en pratique. Dans les méthodes hybrides continues, le passage de RANS à LES est activé par des critères basés sur une comparaison d'échelle, généralement l'échelle intégrale de turbulence et la taille locale du maillage. Il suffit soit de créer un maillage suffisamment grossier pour rester en mode RANS dans le domaine où la LES n'est pas nécessaire, et de l'affiner localement pour passer en mode LES ; soit désactiver le critère de basculement pour forcer le mode RANS dans la zone choisie. La question se pose alors de savoir si les fluctuations résolues apparaîtront assez rapidement dans la zone grise et au début de la région LES pour éviter une sous-estimation des contraintes turbulentes (effondrement des contraintes modélisées).

Une génération naturelle de ces fluctuations est observée dans les cas où l'écoulement est hydrodynamiquement instable (notamment avec des profils de vitesse présentant un point d'inflexion). Mais même dans ce cas, l'apparition des tourbillons résolus est trop lente (Mockett et al., 2018). Cependant, garantir que le passage de RANS à LES se fera toujours dans une région hydrodynamiquement instable est beaucoup trop restrictif, voire impossible pour des configurations complexes. Par conséquent, les méthodes hybrides RANS/LES continues actuelles ne sont pas capables de réaliser une transition physiquement représentative de RANS à LES. Pour éviter ce problème, l'objectif est de générer une turbulence synthétique qui ajoute artificiellement des fluctuations à la solution RANS. De nombreuses méthodes ont été proposées à cet effet, la plus largement utilisée étant la méthode Synthetic Eddy (SEM) (Jarrin et al., 2009). Une méthode d'enrichissement relativement nouvelle, le Forçage Linéaire Anisotrope (ALF), développée par De Laage de Meux et al. (2015), est basée sur le forçage volumique, et non sur l'introduction de fluctu-

ations dans un plan, et nécessite une zone de recouvrement entre la zone RANS et la zone LES. Son fonctionnement est basé sur l'introduction d'une force fluctuante dans l'équation de la quantité de mouvement, dont l'intensité dans chaque direction est utilisée pour forcer la LES à satisfaire les statistiques données par le RANS, qui servent de cible.

Pour les travaux présentés dans la thèse, une méthode de forçage volumique basée sur le ALF est développée pour éviter le problème de l'effondrement des contraintes modélisées. La nouvelle méthodologie de forçage vise à adapter le forçage de volume ALF susmentionné, qui a été développé dans le cadre hybride zonal RANS/LES, au cadre hybride continu RANS/LES. L'avantage considérable de cette approche volumique est qu'elle est simplement définie en chaque point par les conditions locales : elle ne nécessite aucune information sur les directions relatives de l'écoulement et de l'interface diffuse, alors que les méthodes de forçage plan nécessitent que l'écoulement soit orthogonal à l'interface lors du passage de RANS à LES.

En théorie donc, elle est suffisamment générale pour s'appliquer à tout type d'interface diffuse : entrée de zone LES, sortie de zone LES, interface tangentielle ou oblique, etc. Cette nouvelle méthode de forçage appelée *active* HTLES est développée , implémentée, testée, calibrée et validée sur des cas académiques pendant la durée de cette thèse en utilisant Code_Saturne (Archambeau et al., 2004), un code industriel open source développé par EDF.

Structure du manuscrit

Le chapitre 1 discute des méthodes de modélisation de la turbulence, avant de décrire les principaux modèles RANS et les approches filtrées, en se concentrant sur les modèles LES et les approches hybrides RANS/LES classiques. Enfin, l'état de l'art en matière de modélisation hybride temporelle est présenté.

Le chapitre 2 est consacré à la discussion du modèle LES hybride temporel (HTLES). La dernière partie du chapitre présente tous les tests académiques à étudier pendant la durée de la thèse et la réalisation des HTLES dans ces configurations.

Le chapitre 3 discute de quelques méthodes de forçage préexistantes avant de se concentrer sur le développement d'une nouvelle approche active pour l'hybride RANS/LES continu, de nature volumique. Cette méthode est basée sur la méthode de forçage préexistante, le forçage linéaire anisotrope (ALF), développée à l'origine pour le forçage zonal hybride RANS/LES.

Le chapitre 4 est consacré au test et à la calibration de cette nouvelle approche *active* pour l'écoulement sur des collines périodiques. Les résultats sont analysés afin d'évaluer la capacité de cette approche à créer ou à atténuer les fluctuations résolues lors de la transition de RANS à LES et LES à RANS, respectivement.

Le chapitre 5 est consacré à tester la robustesse du modèle par rapport à des cas de tests standards pour le développement de modèles de turbulence : écoulement dans un canal et écoulement sur une marche descendante. Une attention particulière est portée à la robustesse du modèle en faisant varier la zone d'application du forçage pour le cas de la marche descendante.

Le chapitre 6 permet de revenir sur les principaux résultats de la thèse et d'en présenter une synthèse, avant de proposer des perspectives de ce travail.

Enfin, dans les annexes A à D, sont rappelés respectivement la formulation complète du modèle $k-\omega$ SST HTLES, un article de journal et deux articles de conférences.

CHAPTER 1

Modeling of turbulent flows

This chapter includes the main bibliographical reminders of the thesis. The first half of the chapter is dedicated to turbulence and modeling in general. That leads to an in-depth description of the equations of the statistical approach used in RANS models and the filtered approach used in LES models. Finally, the principles of the hybrid approaches are recalled, with a particular focus on the pre-existing hybrid approaches.

Contents

1.1 Turbulence & CFD

1.1.1 What is Turbulence?

The equations of motion for a viscous fluid have steady and well-behaved solutions as long as the Reynolds number is not too large. Such flows are termed as "laminar". At larger Reynolds numbers, velocity and pressure fluctuations appear in the flow which make the flow unsteady, and the viscous stresses are overpowered by the fluid's inertia. In general, this motion is described as "turbulent". Virtually all the flows we observe is turbulent in nature, for example, flow past vehicles, river currents, and cyclones to name a few. Turbulence has been called an unsolved mystery of classical physics as there are so many open questions regarding turbulence.

It is impossible to define what is turbulence by a simple definition. Over the last century many researchers have tried defining turbulence. One of the first definition of turbulence was given by von Kármán (1937):

> *"Turbulence is an irregular motion which, in general makes its appearance in fluids, gaseous or liquid, when they flow past solid surfaces or even when neighboring streams of the same fluid flow past or over one another."*

Over the time as the understanding of turbulence has progressed, the researchers have found the term "irregular motion" to be too ambiguous. The reason being there are flows that can be described as irregular but not turbulent in nature. A much sharper definition for turbulence was provided by Bradshaw (1972):

> *"Turbulence is a three-dimensional time-dependent motion in which vortex stretching causes velocity fluctuations to spread to all wavelengths between a minimum determined by viscous forces and a maximum determined by the boundary conditions of the flow. It is the usual state of fluid motion except at low Reynolds numbers."* To this he further added that the only short but satisfactory answer is that *"It is the general solution of the Navier Stokes equation."*

Turbulent flows exhibit random behaviour in the sense that the instantaneous measurements of velocity (any quantity of interest) of fluid particles taken at the same location and at the same time over a succession of repeated experiments will give a set of values instead of a single unique result. While the instantaneous properties of a turbulent flow are sensitive to initial conditions, the statistically averaged quantities are not. Based on this very explanation Hinze (1975) gave a revised definition for turbulence:

> *"Turbulent fluid motion is an irregular condition of flow in which the various quantities show a random variation with time and space coordinates, so that statistically distinct average values can be discerned."*

Many researchers refer to turbulent eddies while describing turbulence, as a wide range of eddies appear and give rise to strong mixing and turbulent stresses which can be enormous compared to the values from laminar flows. These eddies are characterized by different scales (length scale, time scale, velocity scale). Turbulence features a cascade process, where the energy transfer takes place from larger scales to smaller scales. The turbulent kinetic energy of the eddies can be studied with the help of the energy spectrum, which is divided into three zones depending on the length scale. Eddies in region I are the most energy-containing eddies, which extract energy from the mean flow and they are unstable in nature. They will break down into smaller eddies and a part of the energy extracted from the mean flow by the largest scales is transferred to the smaller eddies. This process,

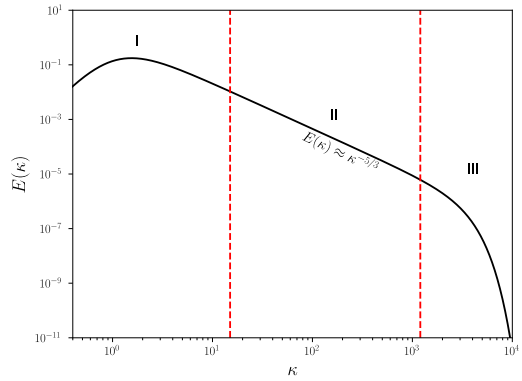

Figure 1.1 – Energy spectrum in wavenumber space: $E(\kappa)$ is the turbulent kinetic energy per unit wavenumber of eddies of size $l_\kappa = 2\pi/2\kappa$ and κ is the wavenumber.

continuous and repetitive, is referred to as cascade process. Eddies in region II display the decaying behaviour according to the Kolmogorov spectrum law. For eddies located in region III, described by Kolmogorov scales, the frictional forces (viscous stresses) become large and the turbulent kinetic energy is transferred into thermal energy through viscous dissipation.

The state of turbulence is fundamentally three-dimensional and unsteady due to the fact that vortex stretching is absent in two-dimensional flows, even when the mean field of a flow is statistically two-dimensional and stationary. Even though turbulence is deterministic and governed by the Navier-Stokes equations, it is chaotic, meaning modifications in the inlet and boundary conditions lead to a completely different evolution of the flow after a finite time, leading to unpredictability of the system.

1.1.2 Navier-Stokes equations

The three fundamental equations: conservation of mass, momentum and energy are Lagrangian in nature, meaning they apply to the same material systems. Thus, in order to apply it to the fluid flow it is fundamental to use the Eulerian description, which defines the motion of fluid at each instant depending on the spatial position x and time t. In this context, the material derivative is introduced to describe the variation with respect to time attached to an elementary particle that we follow in motion of any quantity $\phi(x,t)$.

$$\frac{\mathrm{d}\phi}{\mathrm{d}t} = \frac{\partial\phi}{\partial t} + U_i^* \frac{\partial\phi}{\partial x_i} \tag{1.1}$$

where U_i^* is the instantaneous velocity. In order to restrict the problem and carry out theoretical developments certain assumptions are made. The most important consideration is the fluid being studied is within the framework of **continuum mechanics**. The other important assumptions among many:

→ The fluid is **Newtonian** in nature, meaning the stress-strain relation is linear linked via viscosity coefficient.

→ The fluid considered is **single phase**.

→ The flow is **isothermal**, so there is no expansion and no variation in density of the fluid.

→ The flow is **incompressible** in nature, meaning the density is constant.

→ The flow under investigation is **fully turbulent**, without the consideration of phase transition or laminar flows.

Under the assumptions mentioned above, the system of equations can be written in the form of local balances, thus making it possible to write the Navier-Stokes equations.

The Navier-Stokes equations for an incompressible flow can be used to describe the evolution of the instantaneous velocity U_i^* and pressure P^*, as a function of density ρ^* and the kinematic viscosity ν^* of the fluid, which under the assumptions taken into consideration are constant.

Continuity equation (conservation of mass):

$$\frac{\partial U_i^*}{\partial x_i} = 0 \tag{1.2}$$

Momentum conservation:

$$\frac{\partial U_i^*}{\partial t} + \underbrace{U_j^* \frac{\partial U_i^*}{\partial x_j}}_{\text{Convection}} = \underbrace{-\frac{1}{\rho^*}\frac{\partial P^*}{\partial x_i}}_{\text{Pressure gradient}} + \underbrace{\nu \frac{\partial^2 U_i^*}{\partial x_j \partial x_j}}_{\text{Diffusion}} + \underbrace{F_i^*}_{\text{Body force}} \tag{1.3}$$

Energy conservation:

$$\frac{\partial e^*}{\partial t} + \underbrace{U_i^* \frac{\partial e^*}{\partial x_i}}_{\text{Convection}} = \frac{1}{\rho^*}\sigma_{ij}^* s_{ij}^* - \frac{\partial}{\partial x_i}\gamma_i \tag{1.4}$$

where the stress tensor σ_{ij}^* as a function of strain tensor s_{ij}^* due to the assumption of Newtonian fluid can be given as:

$$\sigma_{ij}^* = \left(-P^* + \lambda \frac{\partial U_k^*}{\partial x_k}\right)\delta_{ij} + 2\mu s_{ij}^* \quad \text{with} \quad s_{ij}^* = \frac{1}{2}\left(\frac{\partial U_i^*}{\partial x_j} + \frac{\partial U_j^*}{\partial x_i}\right) \tag{1.5}$$

and the heat flux γ_i as a function of the temperature gradient is given by Fourier's law:

$$\gamma_i = -k\frac{\partial T^*}{\partial x_i} \tag{1.6}$$

Here, F_i^* is the external force, k the conductivity, μ the dynamic viscosity, λ the volumic viscosity, and e^* the internal energy.

The two main types of transport highlighted here are the diffusive and convective transport.

→ The convective transport refers to the internal movements of the fluid particles as a function of velocity of the fluid particles in the non-linear convection term characterised by the time scale $T_c = L/U$.

→ The diffusive transport refers to the coherent transport on a macroscopic scale due to the agitation of molecules by kinematic viscosity. The characteristic time scale for that can be defined as $T_\nu = L^2/\nu$.

→ Upon comparing these two time scales a non-dimensional parameter (Reynolds number) appears, $Re = UL/\nu$, which characterises the flow regime (laminar or turbulent)

by determining the dominant transport mechanism out of the convective (inertial force) and diffusive effects (viscous force).

1.1.3 Computational Fluid Dynamics (CFD)

The computational Fluid Dynamics (CFD) is a "third approach" after experimental and theoretical approach in the study and development of fluid dynamics as a whole. Activities in the broad field of computational fluid dynamics range from the automation of well-established engineering design methods to the use of detailed Navier-Stokes equation solutions as substitutes for experimental research into the nature of complex flows.

The Navier-Stokes equations described in section 1.1.2 are very complex to solve analytically, as the number of unknowns are more than the number of equations, which requires introducing constitutive equations, which describe properties of the fluid, which is usually the case except if it is a special case. Using a discretization method, we can approximate the differential equations numerically by a system of algebraic equations that can then be solved on a computer. This numerical solution is generated at discrete spatial and temporal locations by applying approximations to small domains. The quality of discretization is as important to the accuracy of numerical solutions as the quality of experimental data.

CFD results are directly analogous to the results from experiments. Unlike the setup of experiments, which are generally heavy, difficult to move, a computer program is something you can carry around in your hands. CFD with a proper algorithm has revolutionized the way to solve a flow problem, turning it from a virtually unsolvable problem into a standard, everyday analysis.

1.2 Turbulence modeling

1.2.1 Generalities

Turbulence is considered to be a continuum phenomenon since its smallest scales are significantly larger than any molecular scale. This assertion can be corroborated by estimating the size of the smallest scales using dimensional analysis. Of course, the physics of turbulence at extremely small scales has to be investigated in order to determine the relevant dimensional values. All the turbulent flows involves a cascade process, meaning a transfer of kinetic energy per unit mass from larger scales to smaller scales. At the smallest scales the dissipation of this kinetic energy to heat occurs. It can be assumed that the small scale motions are independent of the relatively slow large scale motions and the mean flow due to the fact that the time scale associated with the small scale motions is short. Hence, the smaller eddies are in a state where the rate of receiving energy from the larger scales is almost equivalent to the rate of dissipation (Kolmogorov, 1991).

The Kolmogorov scales (smallest scales of turbulence) of length (η), time (τ) and velocity (v) are defined as:

$$\eta \equiv \left(\nu^3/\varepsilon\right)^{1/4}, \quad \tau \equiv \left(\nu/\varepsilon\right)^{1/2}, \quad v \equiv \left(\nu\varepsilon\right)^{1/4} \tag{1.7}$$

It is useful to consider the specific aspects of turbulent flows that make the development of an accurate model challenging. For instance, the velocity field $U(x,t)$ is a three-dimensional, time-dependent and random flow field. The largest scale of turbulence is as large as the characteristic width of the flow, and hence directly impacted by the boundary geometry and not universal unlike the smallest scales. As mentioned in the previous section, the difficulties in the modeling of the flow arises from the nonlinear convective term in the Navier-Stokes equations, also from the pressure gradient term as it is

both nonlinear and non-local. In the Navier-Stokes equations, the system of equations is solved for the time-dependent (instantaneous) fields. In contrast, in a turbulence model (RANS model), the system of equations is solved for the mean quantities. However, it is important to note that the solving for all the instantaneous quantities is computationally very expensive (depending on the algorithm, discretization, etc.). Hence, it is very important to develop turbulence models. It is critical to recognize that there is a wide variety of turbulent flows, and also a wide range of problems to be addressed. As a result, having a diverse set of models that differ in complexity, accuracy, and other characteristics is useful and beneficial.

The principle criteria that can be used to assess different turbulence models is mentioned below. Some of them can be considered more important than others, but it is impossible to rank them. These principles provide a mathematical framework for modeling. They give physical constraints that enable the modeler to make relevant choices. At the same time they are not sufficient for ensuring that the models will work properly.

→ **Level of description:** A higher degree of description can offer a more detailed characterisation of the turbulence, resulting in more accurate and broadly applicable models. For example, in RANS models the description of the flow is provided by the mean quantities, where in LES it is done by the filtered quantities which is a typical representation of the large scale turbulent motion. The limited description provided by these models are sufficient in many applications.

→ **Completeness:** The model is considered complete if none of its system of equations has flow dependent specifications. Most of the turbulence models' specifications are flow dependent, for example integral length scale, mixing length etc. However, completeness is certainly desired.

→ **Cost and ease of use:** The complexity of executing a turbulence model computation is determined by the flow under investigation as well as the turbulence model used for the execution. The computing difficulty rises with the flow's statistical dimensionality and decreases for the statistically stationary flow. In some approaches the computing cost is directly related to the Reynolds number and on some models it's effect is insignificant.

→ **Range of applicability:** Not all models are applicable to all flows. For example, a particular mixing-length model which makes the assumption about the flow geometry in the specification of the mixing length is applicable to that specific geometry only. It is important to note that the mixing-length model is not complete. Computational requirements impose yet another but an actual limitation on the application of some models. For example, in DNS the requirements for computing resources rises so quickly that it is restricted to the flow with low Reynolds number.

→ **Realizability:** Opinion on this parameter is divided in two groups: 1) This group believes that the realizability is a tool that helps guiding the modelers in creating a model which is mathematically more elegant. Realizability ensures that no non-physical solutions, like negative energies, can be observed. Realizability is a numerical robustness factor. 2) This group believes that realizability leads to non-linear and more complex models. Hence, the gain in terms of numerical robustness is compensated by the loss of linearity. Situations where non-realizable solutions are observed are extreme situations, which can be prevented by a posteriori corrections of the models.

→ **Accuracy:** It goes without saying that accuracy is an important feature of any turbulence model. The correctness of a model can be verified when applied to a specific flow and comparing the calculations with the experimental data. Numerical inaccuracy is unavoidable in a model. It might be due to a variety of factors, but more often than not it is caused by spatial truncation error.

The applicability of a given model for a particular turbulent flow issue is determined by a weighted combination of the criteria listed above. As a result, there is no "optimal" model, but a variety of models that may be advantageously applied to a wide range of turbulent flow issues. Based on these the turbulence models are primarily divided into four categories: 1) Direct Numerical simulation (DNS) 2) Statistical modeling of turbulence (Reynolds Averaged Navier-Stokes -RANS) 3) Large Eddy Simulation - LES 4) Hybrid RANS/LES.

1.2.2 Local resolution of scales

The LES models and the hybrid models depends on filtering, to separate the modeled and resolved turbulent scales, using the criteria related to the general shape of the energy spectrum. The turbulent energy spectrum represents the distribution of energy either as a function of wavenumber κ or frequency ω. Differences between the spatial (wavenumber space) and temporal (frequency space) spectrum can be described according to Pope et al. (2000), in spatial energy spectrum, and Tennekes et al. (1972) in temporal energy spectrum. Two point correlation tensor can be written as:

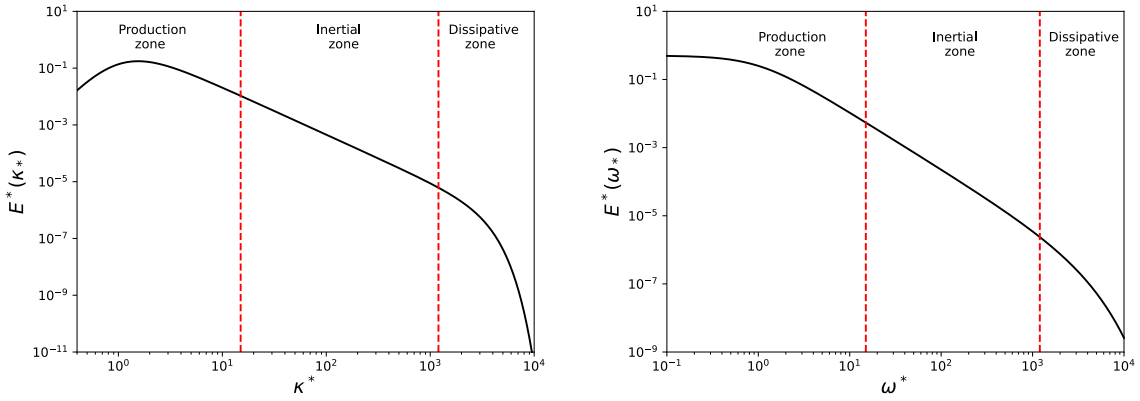

(a) (b)

Figure 1.2 – (a) Spatial energy spectrum, and (b) Eulerian temporal energy spectrum

$$R_{ij}(\mathbf{r}) = \overline{u_i\left(\boldsymbol{x},t\right)u_j\left(\boldsymbol{x}+\boldsymbol{r},t\right)}, \quad \text{and} \quad R_{ij}(\tau) = \overline{u_i\left(\boldsymbol{x},t\right)u_j\left(\boldsymbol{x},t+\tau\right)} \tag{1.8}$$

The tensor of velocity spectrum is:

$$\psi_{ij}(\kappa) = \frac{1}{(2\pi)^3}\iiint_{-\infty}^{\infty} R_{ij}(\mathbf{r})\exp\left(-i\kappa\cdot\mathbf{r}\right)\mathrm{d}\mathbf{r}, \quad \psi_{ij}(\omega) = \frac{1}{2\pi}\int_{-\infty}^{\infty} R_{ij}(\tau)\exp\left(-i\omega\tau\right)\mathrm{d}\tau \tag{1.9}$$

the energy density:

$$E(\kappa) = \oint \frac{1}{2}\psi_{ii}(\kappa)\mathrm{d}S(\kappa), \quad \text{and} \quad E_T(\omega) = \psi_{ii}(\omega) \tag{1.10}$$

and the total turbulent kinetic energy:

$$k = \int_0^\infty E(\kappa)\mathrm{d}\kappa, \quad \text{and} \quad k = \int_0^\infty E_T(\omega)\mathrm{d}\omega \tag{1.11}$$

The turbulent energy spectrum is divided into three zones in both the wavenumber and frequency space. Upon analyzing the Eulerian temporal energy spectrum, Tennekes (1975) proposed a dispersion relation concerning the frequency and wavenumber,

$$\omega = U_s\kappa \tag{1.12}$$

where U_s, the sweeping velocity represents the advection of the smallest vortices by the largest. It is defined as:

$$U_s = U + \gamma\sqrt{k} \tag{1.13}$$

where U is the mean velocity magnitude. The second term in the Eq. (1.13) defines the characteristic velocity of the most energetic eddies, with $\gamma = \sqrt{2/3}$ a constant. For homogeneous and isotropic turbulence this relation simplifies to $U_s = \gamma\sqrt{k}$.

→ **Production zone:** This zone contains the most energetic and large turbulent structures driven by the integral length scale L. The energy in this zone comes from the mean motion.

→ **Inertial zone:** This zone corresponds to the zone between the productive scales L and the dissipative scales η. Relations between these scales can be given by the Reynolds number of the flow $\eta = LRe_t^{-3/4}$, with $Re_t = UL/\nu$ and $U \sim \sqrt{k}$. Which means the scale separation between the largest and the smallest scales becomes more and more significant with the increase in Reynolds number. According to Kolmogorov, the statistics of turbulence is determined only by the dissipation rate ε in the inertial zone, i.e. the rate of energy transfer from large scales to small scales is conserved and it is equal to the dissipation rate (Kolmogorov, 1991). Based on this, the Kolmogorov energy spectrum in the inertial zone in spatial and temporal spectrum, respectively, is defined as:

$$E(\kappa) = C_K\varepsilon^{2/3}\kappa^{-5/3}, \quad \text{and} \quad E_T(\omega) = C_K\varepsilon^{2/3}U_s^{2/3}\omega^{-5/3} \tag{1.14}$$

where $E_T(\omega)$ is determined from $E(\kappa)$ using relation (1.12), and $C_K = 1.5$ is the Kolmogorov constant. These spectrum decay is referred to as the "minus five-third law".

→ **Dissipative zone:** This zone corresponds to the smallest scales of turbulence, where the energy is dissipated in the form of heat. In this zone the effect of molecular viscosity is no longer negligible. In this zone, there is no inhomogeneous and anisotropic aspect of the turbulence. The universal equilibrium assumption states that the statistics of turbulent motion for the smallest scales are driven by the kinematic viscosity ν and the dissipation rate ε. Based on this assumption the Kolmogorov scales are determined (refer to Eq. (1.7)).

1.3 Direct Numerical Simulation (DNS)

DNS, or direct numerical simulation, refers to a complete three-dimensional, time dependent solution of the Navier-Stokes equations. It seems that the simplest way to solve turbulent flow dynamics problem is by simulating these equations directly in a computer

code. They are, in theory, numerically precise due to the absence of additional modeling and empirical relations. This guarantees the accurate and reliable solution to the turbulence problem given that the appropriate numerical schemes are utilized. In practice, statistics derived from DNS can be utilized to validate suggested closure approximations in turbulence modeling. DNS can also be seen as an extra source of experimental data.

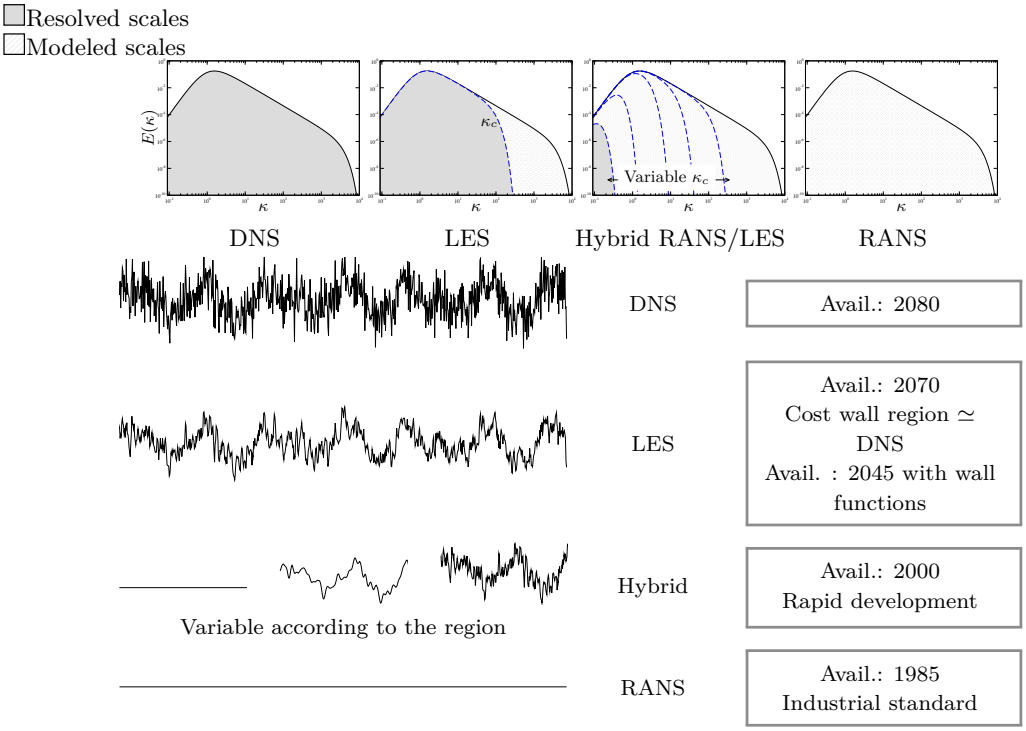

Figure 1.3 – Modeling approaches (from Manceau (2020)).

As mentioned earlier, turbulence is characterized by the eddies over a wide range of scales (refer to Fig. 1.1), which is separated by several orders of magnitude. As can be seen in Fig. 1.3, DNS consists in resolving all the scales of motion from large scales to the smallest dissipative scales, with appropriate initial and boundary conditions. Estimating the number of grid points and time steps in order to fully resolve the energy spectrum indicates the problem's computational complexity. In most of the cases the number of cells required to do DNS is prohibitive, making DNS inaccessible for majority of the turbulent flow problems due to the digital cost linked to the discretization and available computing power (true for practical applications, for many academic cases it is okay).

To appreciate how prohibitive these constraints are, consider channel-flow computation at $Re_\tau = 587.19$ studied by Moser et al. (1999), which required a mesh comprising nearly 38 million cells, to be compared to the flow computation at $Re_\tau = 178.13$, which required a mesh comprising only 2 million cells. To give a rough estimate the number of cells required for a DNS computation can be given as $N_{\text{DNS}} \approx Re_\tau^{9/4}$ (this estimation is true for an unstructured mesh, for a structured mesh $N_{\text{DNS}} \approx Re_\tau^{11/4}$). This clearly demonstrate that the DNS cannot be used for the industrial applications defined by far as complicated configurations due to the computing limitations. DNS results highlight one of the strange characteristics due to the chaotic nature of turbulence: upon introducing a small perturbation in the initial condition, the solution generated is very different from the solution which has no perturbation in the initial condition. However, statistically these two flows are identical (Sandham et al., 1992).

To conclude, the use of DNS is limited to a few simplified or low Reynolds number

configurations. DNS databases are accessible for a variety of flows of relevance to turbulence researchers, which makes it possible to analyze specific phenomena in order to give descriptions and develop models.

1.4 Statistical modeling of turbulence - Reynolds Averaged Navier-Stokes (RANS)

All the turbulent scales (refer to Fig. 1.3) are statistically modeled, from the smallest dissipative scales to large energetic scales in RANS models, based on a random distribution of turbulence (the chaotic character of the Navier-stokes equations makes this assumption possible, otherwise Navier-Stokes equations are deterministic in nature), with a sense that the same experiment will be repeated a large number of times. Thus, adopting this statistical approach makes it possible to describe the average movements of the flow. This modeling is achieved through the use of a statistical mean operator $\overline{(\cdot)}$.

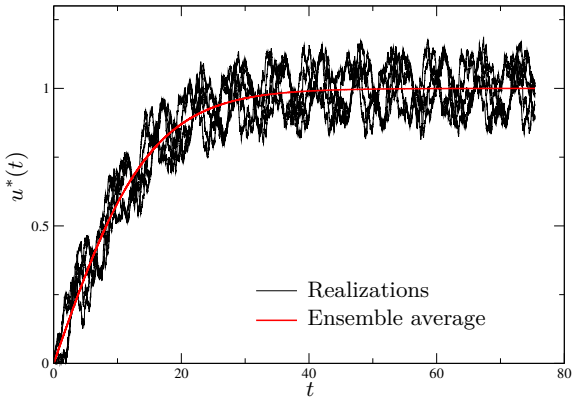

Figure 1.4 – Ensemble averaging (from Manceau (2020)).

Consider an instantaneous variable ϕ^*, its statistical mean can be calculated as the ensemble average over N realizations (law of large numbers), defined by:

$$\overline{\phi^*}(\boldsymbol{x},t) = \lim_{N\to\infty}\left(\frac{1}{N}\sum_{n=1}^{N}\phi_n^*(\boldsymbol{x},t)\right) \tag{1.15}$$

In a general context, the ensemble averaging is not easy to estimate due to the fact that the same experiment has to be repeated a large number of times with exactly the same control parameters. In many cases under certain assumptions, the ensemble average can be expressed in a different form:

→ **Statistical homogeneity**: If the statistical quantities are independent of the location (one or several directions, here x-direction is considered) $\overline{\phi^*}(x,y,z,t) = \overline{\phi^*}(y,z,t)$. Under this scenario, the ensemble average is equivalent to a spatial average.

$$\overline{\phi^*}(y,z,t) = \lim_{L\to\infty}\frac{1}{L}\int_0^L \phi^*(x,y,z,t)\,\mathrm{d}x \tag{1.16}$$

→ **Statistical stationarity**: If the statistical quantities are independent of time $\overline{\phi^*}(\boldsymbol{x},t) = \overline{\phi^*}(\boldsymbol{x})$, the ensemble average is equivalent to a temporal average.

$$\overline{\phi^*}(\boldsymbol{x}) = \lim_{T\to\infty}\frac{1}{T}\int_0^T \phi^*(\boldsymbol{x},t)\,\mathrm{d}t \tag{1.17}$$

→ **Statistical periodicity** : If the statistical quantities are periodic with a period τ $\overline{\phi^*}(\boldsymbol{x},t) = \overline{\phi^*}(\boldsymbol{x},\varphi)$, where $\varphi = 2\pi t/\tau \text{modulo} 2\pi$, the ensemble average is equivalent to a phase average:

$$\overline{\phi^*}(\boldsymbol{x},t) = \lim_{N\to\infty} \frac{1}{N+1} \sum_{n=0}^{N} \phi^*(\boldsymbol{x}, t+n\tau) \tag{1.18}$$

This statistical mean operator decomposes the instantaneous values into a mean and a fluctuating part using the Reynolds decomposition. Consider a characteristic quantity of the flow, here the velocity U_i^* as a function of time and space, it can be decomposed into its components such that:

$$\underbrace{U_i^*}_{\text{Instantaneous}} = \underbrace{\overline{U_i^*}}_{\text{Mean part}} + \underbrace{u_i}_{\text{Fluctuating part}} \tag{1.19}$$

here, the mean part can also be written as $\overline{U_i^*} = U_i$. This averaging operator has the properties of linearity, preservation of constants and commutativity with the spatial and temporal derivative operators. In addition to that

$$\overline{\overline{U_i^*}} = \overline{U_i^*} = U_i \quad \text{and} \quad \overline{u_i} = 0 \tag{1.20}$$

In the same way, the instantaneous pressure P^* and external forces F_i^* can be decomposed into their mean values P and F_i, and their fluctuating values p and f_i, respectively.

$$P^* = P + p \quad \text{and} \quad F_i^* = F_i + f_i \tag{1.21}$$

The statistical approach describes the mean flow behavior, but instantaneous turbulent structures are not captured and the energy spectrum is completely modeled. This makes it possible to drastically reduce the computational cost compared to DNS. For example, to study channel flow with RANS closure model, a suitable mesh requires only few hundreds of cells to describe the gradient of the averaged velocity compared to the million of cells required for DNS. Due to the low computational cost and relative ease in using these models, they have become standard industrial practice.

Reynolds Averaged Navier-Stokes equations

The introduction of the Reynolds decomposition leads to the averaged Navier-Stokes equations. The continuity equation of the mean motion:

$$\frac{\partial U_i}{\partial x_i} = 0 \tag{1.22}$$

The equation for the mean momentum:

$$\frac{\partial U_i}{\partial t} + U_j \frac{\partial U_i}{\partial x_i} = -\frac{1}{\rho}\frac{\partial P}{\partial x_i} + \nu \frac{\partial^2 U_i}{\partial x_j \partial x_j} - \frac{\partial \overline{u_i u_j}}{\partial x_j} + F_i \tag{1.23}$$

and the equation for the mean temperature:

$$\frac{\partial T}{\partial t} + U_j \frac{\partial T}{\partial x_i} = \alpha \frac{\partial^2 T}{\partial x_j \partial x_j} - \frac{\partial \overline{u_j \theta}}{\partial x_j} \tag{1.24}$$

Eq. (1.24) is a passive scalar, as the velocity field obtained from Eqs. (1.22) and (1.23) is used for solving the temperature equation. But throughout the thesis isothermal flow

assumption is implemented, Eq. (1.24) disappears. The remaining system is open with 4 equations for 10 unknowns: P, U, V, W, $\overline{u^2}$, $\overline{v^2}$, $\overline{w^2}$, $\overline{uv}$, $\overline{uw}$, $\overline{vw}$, which needs modeling to close the system. Upon transitioning instantaneous variables to statistically averaged variables, fluctuating parts are introduced into the system which require modeling.

The mean velocity meets the incompressibility constraint, according to the continuity equation for the mean flow (1.22). The general shape of the momentum equation for the instantaneous velocity and the mean velocity is similar except the term $\overline{u_i u_j}$, which introduces the second-order centered moments of velocity (refer to Eqs. (1.3) and (1.23)). This term in the statistically averaged equation appears due to the non-linearity of the convection term. This additional term is called "Reynolds-stress tensor", which is nothing but the correlation between the components of the velocity fluctuations. As mentioned earlier the system of equations (1.22) and (1.23) needs a closure. The system of equations is closed using a turbulence model for the Reynolds-stress tensor.

Transport equations for the Reynolds-stress tensor

The equation of the fluctuating motion can be obtained by subtracting the equation of mean motion from the instantaneous motion.

$$\frac{\partial u_i}{\partial t} + u_j \frac{\partial u_i}{\partial x_j} = -\frac{1}{\rho}\frac{\partial p}{\partial x_i} + \nu \frac{\partial^2 u_i}{\partial x_j \partial x_j} + \frac{\partial \overline{u_i u_j}}{\partial x_j} - u_j \frac{\partial U_i}{\partial x_j} - U_j \frac{\partial u_i}{\partial x_j} \tag{1.25}$$

The transport equations for the Reynolds-stress tensor are obtained by multiplying the fluctuating motion equation (1.25) with the velocity fluctuations u_j, and applying the averaging operator.

$$\begin{aligned} \frac{\partial \overline{u_i u_j}}{\partial t} + \underbrace{U_k \frac{\partial \overline{u_i u_j}}{\partial x_k}}_{C_{ij}} = {} & \overbrace{-\overline{u_i u_k}\frac{\partial U_j}{\partial x_k} - \overline{u_j u_k}\frac{\partial U_i}{\partial x_k}}^{P_{ij}} + \overbrace{\overline{\frac{1}{\rho} p \left(\frac{\partial u_i}{\partial x_j} + \frac{\partial u_j}{\partial x_i}\right)}}^{\Phi_{ij}} - \overbrace{2\nu \overline{\frac{\partial u_i}{\partial x_k}\frac{\partial u_j}{\partial x_j}}}^{\varepsilon_{ij}} \\ & + \underbrace{\nu \frac{\partial^2 \overline{u_i u_j}}{\partial x_k \partial x_k}}_{D^{\nu}_{ij}} - \underbrace{\frac{1}{\rho}\frac{\partial}{\partial x_k}\left(\overline{u_i p}\delta_{jk} + \overline{u_j p}\delta_{ik}\right)}_{D^{P}_{ij}} - \underbrace{\frac{\partial \overline{u_i u_j u_k}}{\partial x_k}}_{D^{T}_{ij}} \end{aligned} \tag{1.26}$$

This second-order transport equation leads to 6 new equations but unfortunately it reveals 34 new unknowns, including a triple correlation $\overline{u_i u_j u_k}$ due to the advective non-linearity, and the problem is still open. This triple correlation should be solved via a third-order transport equation, but the process always produces more unknowns than equations. Therefore, it is necessary to decide when to stop and propose models for these different high-order terms.

The terms on the LHS of Eq. (1.26), represents the material derivative of the Reynolds-stress tensor $R_{ij} = \overline{u_i u_j}$. The physical meaning of the terms on the RHS is as follows:

- → P_{ij}: This production term represents the transfer of energy from the mean flow to the large-scale eddies. Because this term is related to the anisotropic mean velocity gradient, it is responsible for the anisotropy of turbulence. In general, this term reflects the coupling with the mean flow, an input of turbulent energy. It acts as a source term in the equation.

- → Φ_{ij}: The pressure-strain correlation term tends to support a return of isotropy by redistributing the energy among the different components of the Reynolds stress.

→ ε_{ij}: This term represents the dissipation rate (loss of energy in the form of heat) due to viscous friction in the fluctuating motion. This term is independent of the mean flow and acts as a sink term in the transport equation.

→ D^{ν}_{ij}, D^{P}_{ij} and D^{T}_{ij}: These terms represent viscous diffusion by molecular agitation, diffusion by pressure due to the correlation between pressure and velocity which characterises the power of the pressure forces, and diffusion by turbulent agitation due to the triple correlation with velocity fluctuations which represents the convection of energy through fluctuating scales, respectively.

As mentioned earlier, RANS models solve statistically averaged Navier-Stokes equations, supplemented by a closure relation, which are themselves solved by algebraic models or a system of transport equations. It is necessary to establish an empirical relation between the variables that are not resolved as functions of the variables that are resolved. Based on this, RANS closures are divided into two categories:

→ **First moment closure**: These models provide a relation to the second moments $\overline{u_i u_j}$ as a functions of the first moments. These models are widely known as *eddy-viscosity model*. A linear eddy-viscosity model is equivalent to the model of Newton for the "turbulent flow".

→ **Second moment closure**: These models are based on the exact Reynolds stress tensor transport equation, and involve modeling for the terms in the equation that are not solved as functions of terms that are already solved.

To establish these closure relations and construct models for the unresolved terms, a major modeling effort is required because all the turbulent scales and their interactions must be included. The main limitation of RANS modeling comes from its fundamental itself, as they are not capable of reproducing instantaneous coherent structures, which amounts to a loss of information.

1.4.1 First-Moment closures (eddy-viscosity models)

In the first-moment closure, the Reynolds-stress tensor is expressed by means of a constitutive law which connects moments of second order to moments of first order. This is comparable to a material constitutive relation: for example, in a Newtonian, incompressible fluid, the stress tensor is connected to the strain tensor via molecular viscosity (Newton's model). Similarly, Boussinesq proposed a hypothesis that links the Reynolds-stress tensor to the mean strain by turbulent viscosity ν_t, on the basis that the enhancement of mixing by turbulence can be modeled as a mean diffusion effect:

$$R_{ij} = \overline{u_i u_j} = -2\nu_t S_{ij} + \frac{2}{3} k \delta_{ij} \quad \text{where} \quad S_{ij} = \frac{1}{2}\left(\frac{\partial U_i}{\partial x_j} + \frac{\partial U_j}{\partial x_i}\right) \tag{1.27}$$

and the resistance to the flow can be modelled as a mean dissipation effect which implies the mean transfer of energy from the mean flow to turbulence as a production $P = 2\nu_t S_{ij} S_{ij}$. Note that the half-trace of the Reynolds-stress tensor gives the turbulent kinetic energy.

$$\frac{1}{2}\overline{u_i u_i} = -\nu_t S_{ii} + \frac{1}{3} k \delta_{ii} = k \quad \text{since} \quad S_{ii} = 0 \tag{1.28}$$

This approximation makes it possible to reduce the number of unknowns in Eq. (1.26) by substituting the scalar quantities k and ν_t for the six components of the Reynolds stress tensor $\overline{u_i u_j}$. The eddy-viscosity and the turbulent kinetic energy play roles equivalent

to those of the molecular viscosity and the pressure, respectively. The introduction of the turbulent viscosity leads to a strong diffusion in the mean momentum equation, and also a strong production of turbulence. However, the Boussinesq approximation does not provide a relation to evaluate ν_t and k, which vary strongly in the flow and from one flow to another. To describe the evolution of turbulent kinetic energy, the system of equation described in Eq. (1.30), with the additional modeling for the open terms.

Transport equation for turbulent kinetic energy

The half-trace of the Reynolds stress tensor corresponds to the turbulent kinetic energy:

$$k = \frac{1}{2} R_{ii} \tag{1.29}$$

The transport equation for the turbulent energy can be derived from the Reynolds-stress tensor equation:

$$\frac{\partial k}{\partial t} + U_j \frac{\partial k}{\partial x_j} = \underbrace{-\overline{u_i u_j} \frac{\partial U_i}{\partial x_j}}_{P} \underbrace{- \frac{1}{\rho} \frac{\partial \left(\overline{p u_j}\right)}{\partial x_j}}_{D^P} \underbrace{- \frac{\partial}{\partial x_j} \left(\frac{1}{2} \overline{u_i u_i u_j} \right)}_{D^T} + \underbrace{\nu \frac{\partial^2 k}{\partial x_j \partial x_j}}_{D^\nu} \underbrace{- \nu \overline{\frac{\partial u_i}{\partial x_j} \frac{\partial u_i}{\partial x_j}}}_{\varepsilon} \tag{1.30}$$

Compared to the transport equation for Reynolds-stress tensor (refer to Eq.(1.26)), the transport equation for the kinetic energy has all the term but one, the redistribution term Φ_{ij}, because under the assumption of incompressibility, it redistributes the energy among the components without modifying the quantity of total energy. The terms in the transport equation are:

- P - Turbulent kinetic energy production $P = P_{ii}/2$
- D^P - Diffusion due to pressure fluctuations $D^P = D^P_{ii}/2$
- D^T - Diffusion due to turbulent agitation $D^T = D^T_{ii}/2$
- D^ν - Viscous diffusion due to molecular agitation $D^\nu = D^\nu_{ii}/2$
- ε - Turbulent kinetic energy dissipation rate $\varepsilon = \varepsilon_{ii}/2$

Upon constructing the transport equation for the energy of the mean motion $E = U_i U_i/2$, it can be seen that the production term P appears with a negative sign in Eq. (1.30), which confirms the fact that the energy transfer takes place from the mean motion to the fluctuating motion.

The Boussinesq approximation supposes a linear relation between the Reynolds-stress tensor R_{ij} and the strain tensor S_{ij}, whereas the principle axes of these tensors are not always aligned (Chassaing, 2000). Also, this approximation does not account for temporal or spatial memory effects. Due to the fact that the Reynolds stress is modeled quite empirically, first moment closures are poorly suited for very complex flows. However, due to their simplicity, numerical robustness and correct predictions of the shear stress which drives the boundary layer, the model is widely used. First moment closures also include simpler algebraic or zero-equation models or one-equation models, but they are less generic and not in common practice due to the lack of numerical robustness.

1.4.1.1 $k-\varepsilon$ model

The $k-\varepsilon$ model is one of the first two-equation transport models, in which the transport equations for turbulent energy k and dissipation rate ε are solved. These two quantities lead to formation of a length scale L and a time scale τ, making it independent of flow -dependent specifications, hence, making the model complete. The model was proposed by Jones and Launder (Jones et al., 1972).

If it is supposed that turbulent viscosity ν_t depends only on the turbulence defining quantities k and ε, then the length scale and the time scale can be given as:

$$L = C_\mu^{3/4}\frac{k^{3/2}}{\varepsilon} \quad \text{and} \quad \tau = C_\mu^{1/2}\frac{k}{\varepsilon} \tag{1.31}$$

Since turbulent viscosity is homogeneous at length squared over time,

$$\nu_t = \frac{L^2}{\tau} = C_\mu\frac{k^2}{\varepsilon} \tag{1.32}$$

The logarithmic zone where production over dissipation is close to unity helps calibrating the coefficient C_μ. It comes from the ratio of the mean shear stress to the turbulent kinetic energy.

$$\sqrt{C_\mu} = \frac{|\overline{uv}|}{k} \approx 0.3 \tag{1.33}$$

The turbulent energy is solved directly by the exact equation (refer to Eq. (1.30)), modeling the terms that cannot be resolved directly. The model for the production term is simply obtained by introducing the Boussinesq approximation such that:

$$P = -\overline{u_i u_j}\frac{\partial U_i}{\partial x_j} = 2\nu_t S_{ij}\frac{\partial U_i}{\partial x_j} - \frac{2}{3}k\delta_{ij}\frac{\partial U_i}{\partial x_j} = 2\nu_t S_{ij}S_{ij} = \nu_t S^2 \tag{1.34}$$

where $S = \sqrt{2S_{ij}S_{ij}}$. For the pressure diffusion term, there is no straightforward relation. Hence, it is necessary to model this term. Thus, to relate the diffusion flux to the gradient of transported quantity subject to diffusion a coefficient σ_k (Prandtl number) is introduced. This model is called the Simple Gradient Diffusion Hypothesis (SGDH). It works on the assumption that the turbulent agitation is at very small scale compared to the mean flow scale.

$$-\frac{1}{\rho}\left(\overline{pu_j}\right) - \frac{1}{2}\left(\overline{u_i u_i u_j}\right) = \frac{\nu_t}{\sigma_k}\frac{\partial k}{\partial x_j} \tag{1.35}$$

Based on these models the transport equation for k can be written as:

$$\frac{\partial k}{\partial t} + U_j\frac{\partial k}{\partial x_j} = \nu_t S^2 + \frac{\partial}{\partial x_j}\left[\left(\nu + \frac{\nu_t}{\sigma_k}\right)\frac{\partial k}{\partial x_j}\right] - \varepsilon \tag{1.36}$$

The dissipation rate ε is evaluated using the exact transport equation for ε, which is very complex (Wilcox et al., 1998). Individual modeling of the different terms of this transport equation has never been successful. Hence, to model dissipation, a phenomenological approach is obtained, meaning that the ε-equation must involve the same terms as the k-equation. The ε-equation involves the time scale k/ε to maintain the dimensional homogeneity.

System of equations for the $k-\varepsilon$ closure model

$$\nu_t = C_\mu\frac{k^2}{\varepsilon} \tag{1.37}$$

$$\begin{cases} \dfrac{\partial k}{\partial t} + U_j \dfrac{\partial k}{\partial x_j} &= \nu_t S^2 + \dfrac{\partial}{\partial x_j}\left[\left(\nu + \dfrac{\nu_t}{\sigma_k}\right)\dfrac{\partial k}{\partial x_j}\right] - \varepsilon \\ \dfrac{\partial \varepsilon}{\partial t} + U_j \dfrac{\partial \varepsilon}{\partial x_j} &= C_{\varepsilon 1}\dfrac{\varepsilon}{k}\nu_t S^2 + \dfrac{\partial}{\partial x_j}\left[\left(\nu + \dfrac{\nu_t}{\sigma_\varepsilon}\right)\dfrac{\partial \varepsilon}{\partial x_j}\right] - C_{\varepsilon 2}\dfrac{\varepsilon^2}{k} \end{cases} \tag{1.38}$$

and calibrated coefficients of the model:

C_μ	σ_k	σ_ε	$C_{\varepsilon 1}$	$C_{\varepsilon 2}$
0.09	1	1.3	1.44	1.92

Calibrating the closure constants is of the highest importance. It is done by studying particular flow configurations, in which the constants can be isolated from each other and then calibrated according to the experimental references (Launder et al., 1983). The $k-\varepsilon$ model is widely used due to its simplicity, numerical robustness, predictable behaviour and broad range of applicability. However, its accuracy is something that has to be discussed, because the linearity of the model makes it unsuitable for complex flow configurations. The quality of prediction decreases notably in near wall region due to the fact that the molecular viscosity is not negligible in this region, and the definition of the turbulent viscosity does not account for that. Hence, it is necessary to introduce some wall functions to take care of this situation. Due to the proportionality between anisotropy and strain, the predicted production is always positive. It also fails to correctly predict the diagonal components of the Reynolds stress tensor in boundary layers due to the improper representation of the anisotropy.

1.4.1.2 $k-\omega$ model

Kolmogorov proposed the first two-equation model of turbulence (Kolmogorov, 1941). One of the parameters chosen by him was the kinetic energy of turbulence k and another was the rate of dissipation of energy in unit volume and time ω, which has a dimension of a frequency. Purely on the grounds of dimensional analysis, he proposed $\omega = c\sqrt{k}/L$, where c is a constant and L the turbulent length scale, and the turbulent viscosity $\nu_t \sim k/\omega$. The inverse of this quantity ω^{-1} gives the time scale on which the dissipation occurs, indirectly associating ω with dissipative process. Equation for ω:

$$\frac{\partial \omega}{\partial t} + U_j \frac{\partial \omega}{\partial x_j} = -\beta\omega^2 + \frac{\partial}{\partial x_j}\left[\sigma\nu_t \frac{\partial \omega}{\partial x_j}\right] \tag{1.39}$$

where β and σ are two closure coefficients. There are some fundamental flaws to this model. The model is rather empirical, based on reasoning. The model is applicable to high Reynolds number flows only due to the absence of accounting of the influence of viscosity ν on the modeled terms (ν_t, P, ε, etc.). The absence of production term in the model suggest no direct interaction with the mean flow (ω is associated with the smallest scales), which is flawed due to the fact that the large scale eddies are responsible for determining the turbulence time scale and the dissipation rate.

The ω-equation has changed over the time as the development of $k-\omega$ model has progressed. A production term in the ω-equation has been added. Wilcox (1988) presented one of the first improved $k-\omega$ model. This model proposed the transport equation for the specific dissipation rate ω in the same form as the transport equation for the dissipation rate ε in $k-\varepsilon$ models.

$k-\omega$ formulation:

$$\nu_t = \frac{k}{\omega} \tag{1.40}$$

$$\begin{cases} \dfrac{\partial k}{\partial t} + U_j \dfrac{\partial k}{\partial x_j} & = \nu_t S^2 - \beta' k\omega + \dfrac{\partial}{\partial x_j}\left[\left(\nu + \dfrac{\nu_t}{\sigma_k}\right)\dfrac{\partial k}{\partial x_j}\right] \\ \dfrac{\partial \omega}{\partial t} + U_j \dfrac{\partial \omega}{\partial x_j} & = \alpha \dfrac{\omega}{k}\nu_t S^2 - \beta\omega^2 + \dfrac{\partial}{\partial x_j}\left[\left(\nu + \dfrac{\nu_t}{\sigma_\omega}\right)\dfrac{\partial \omega}{\partial x_j}\right] \end{cases} \tag{1.41}$$

Coefficients of the model:

β'	β	α	σ_k	σ_ω
0.09	3/40	5/9	2	2

This model presents some advantages compared to the standard $k-\varepsilon$ model. The specific dissipation rate is actually independent of the turbulent kinetic energy as the production term in the ω-equation reduces to αS^2. This decoupling of the ω-equation from the k-equation makes the system more robust numerically. Unlike the $k-\varepsilon$ model, this model is integrable down to the wall, and gives better prediction of the flow separation due to adverse pressure gradients. However, at the wall, ω tends to infinity, which implies that the correct near-wall behaviour cannot be reproduced. It also overpredicts the expansion rate of jets. Hence, introducing correction terms in the model is necessary to make it more robust and accurate.

1.4.1.3 $k-\omega$ SST model

As mentioned in the previous section, the $k-\omega$ model is integrable up to the wall, but suffers from a high degree of sensitivity to turbulence in the external region. To overcome this, and in order to take the advantage of both $k-\epsilon$ and $k-\omega$ in the areas where their behaviour is satisfactory, Menter developed $k-\omega$ SST model by coupling both the approaches. $k-\omega$ SST model handles transition between models using weighting functions.

It is desirable that in free flow the $k-\omega$ SST model behaves like $k-\varepsilon$ model, while retaining the specific dissipation rate as the second transport equation apart from turbulent kinetic energy. Therefore it makes sense to use the same turbulent variables in both branches of the model. Upon performing a change of variable in Eq. (1.38) according to $\varepsilon = C_\mu k\omega$, it introduces a cross diffusion term between k and ω. It is necessary to introduce a blending function F_1 in front of this cross diffusion term, to drive the transition between the $k-\omega$ and the $k-\varepsilon$ model. This blending function assumes the value of unity in the near wall region and tends towards zero far from wall, and is defined as a hyperbolic tangent, so that it can continuously transition between 0 and 1.

One of the main difference between eddy-viscosity models and Reynolds-stress models is that the eddy-viscosity models do not include the transport equation for the shear stress $\tau = -\rho\overline{uv}$. If included it leads to significantly improved adverse pressure gradient flow prediction. Following the development of the $k-\omega$ model by Wilcox (Wilcox, 1988), Menter proposed an improved model to include a constraint on the shear stress (Menter, 1994). The characteristic frequency of the large eddies (specific dissipation rate) can be defined as:

$$\omega = \frac{\varepsilon}{C_\mu k} \tag{1.42}$$

In eddy-viscosity models, the shear stress is modeled using the Boussinesq approximation (2.11), which has certain limitations. To avoid this Menter proposed to use Bradshaw's assumption that the shear stress in a boundary layer is proportional to the turbulent kinetic energy k.

$$\tau = a_1 k \tag{1.43}$$

where a_1 is a constant. On the other hand, in two-equation models, the shear stress is

defined as:

$$\tau = \nu_t S \tag{1.44}$$

Hence, the turbulent viscosity can be defined from the ratio of Eqs. (1.43) and (1.44). However, this definition of turbulent viscosity is not desirable, due to the fact that when the shear-strain rate S goes towards zero, the turbulent viscosity becomes infinitely high. However, in the flows with adverse pressure gradient the production is larger than the dissipation ($S > a_1\omega$) for most of the wake region of the boundary layer. By introducing this phenomena in addition to a blending function F_2, the turbulent viscosity is now defined as:

$$\nu_t = \frac{a_1 k}{\max\left[a_1\omega; SF_2\right]} \tag{1.45}$$

The blending (weighting) function F_2, provides the modification to the $k-\omega$ SST model, allowing for Bradshaw's assumption to be taken into account. $F_2 = 1$ at the wall and goes to zero far from the wall, thus activating the SST limiter in Eq. (1.45) in near-wall region only. Away from the wall the standard formulation for the turbulent viscosity $\nu_t = k/\omega$ is obtained. Hence, introducing a bound avoids an overestimation of the shear stress in adverse pressure gradient boundary layer. The stagnation-point anomaly, i.e., the strong overestimation of turbulent energy due to the linear eddy-viscosity formulation is observed. A simple way to avoid this is to introduce an production limiter into the transport equation of the turbulent energy, such that:

$$P_k = \min\left[\nu_t S^2; 10 C_\mu k\omega\right] \tag{1.46}$$

The upper limit for the production is based on the dissipation rate.

$k-\omega$ SST formulation:

$$\nu_t = \frac{a_1 k}{\max\left[a_1\omega; SF_2\right]} \tag{1.47}$$

$$\begin{cases} \dfrac{\partial k}{\partial t} + U_j \dfrac{\partial k}{\partial x_j} & = P_k + \dfrac{\partial}{\partial x_j}\left[\left(\nu + \dfrac{\nu_t}{\sigma_k}\right)\dfrac{\partial k}{\partial x_j}\right] - C_\mu k\omega \\ \dfrac{\partial \omega}{\partial t} + U_j \dfrac{\partial \omega}{\partial x_j} & = \gamma_\omega S^2 + \dfrac{\partial}{\partial x_j}\left[\left(\nu + \dfrac{\nu_t}{\sigma_\omega}\right)\dfrac{\partial \omega}{\partial x_j}\right] - \beta_\omega \omega^2 \\ & \quad +2(1-F_1)\dfrac{\nu_t}{\sigma_{\omega 2}}\dfrac{1}{k}\dfrac{\partial \omega}{\partial x_j}\dfrac{\partial k}{\partial x_j} \end{cases} \tag{1.48}$$

Production limiter:

$$P_k = \min\left[\nu_t S^2; 10 C_\mu k\omega\right] \tag{1.49}$$

Closure coefficients for the model are defined as:

$$C = F_1 C_1 + (1-F_1)C_2 \tag{1.50}$$

$$\gamma_{\omega 1} = \frac{\beta_{\omega 1}}{C_\mu} - \frac{C_\kappa^2}{\sigma_{\omega 1}\sqrt{C_\mu}} \quad \text{and} \quad \gamma_{\omega 2} = \frac{\beta_{\omega 2}}{C_\mu} - \frac{C_\kappa^2}{\sigma_{\omega 2}\sqrt{C_\mu}} \tag{1.51}$$

C_μ	C_κ	a_1	σ_{k1}	σ_{k2}	$\sigma_{\omega 1}$	$\sigma_{\omega 2}$	$\beta_{\omega 1}$	$\beta_{\omega 2}$	$\gamma_{\omega 1}$	$\gamma_{\omega 2}$
0.09	0.41	0.31	1/0.85	1	2	1/0.856	0.075	0.0828	0.55	0.44

The weighting (blending) functions are defined as:

$$F_1 = \tanh\left[arg_1^4\right], \qquad F_2 = \tanh\left[arg_2^2\right],$$
$$arg_1 = \min\left[\max\left[\frac{k^{1/2}}{C_\mu \omega d_w}; \frac{500\nu}{\omega d_w^2}\right]; \frac{4\rho k}{\sigma_{\omega 2} CD_{k\omega} d_\omega^2}\right], \quad arg_2 = \max\left[\frac{2k^{1/2}}{C_\mu \omega d_w}; \frac{500\nu}{\omega d_w^2}\right],$$
$$CD_{k\omega} = \max\left[2\rho \frac{1}{\sigma_{w2}\omega}\frac{\partial k}{\partial x_j}\frac{\partial \omega}{\partial x_j}; 10^{-20}\right]. \tag{1.52}$$

Since the $k-\omega$ SST is a linear eddy viscosity model, it suffers from the limitations of these models. However, it benefits from the good qualities of both the $k-\omega$ and the $k-\varepsilon$ models. The model has been successfully applied to many configurations, due to its numerical robustness and better prediction capabilities than the original $k-\omega$ model. It is a low Reynolds number model, i.e., it does not require wall functions.

1.4.2 Second-Moment closures (Reynolds-stress models)

A stress-transport model or second moment closure can benefit from universality, despite being more challenging to construct in terms of closure. The second-moment closure or Reynolds-stress model relies on resolving the transport equation of Reynolds-stress tensor (refer to Eq. (1.26)) instead of assuming that they have a given behaviour. These closure models naturally include complex effects, such as streamline curvature, secondary motion, etc.

Since the transport equation for the Reynolds-stress tensor is resolved, it takes into account the flow history, because of the fact that the dissipation and turbulent transport term have the same time scales but one can observe a response delay. Moreover, the anisotropy of the Reynolds-stress tensor is very well described via the resolution of its exact transport equation, without requiring an algebraic relation. These equations contain the main physical mechanisms that drive turbulence (production, dissipation, viscous diffusion, redistribution, turbulent transport). In particular, production is solved directly, without a model.

To close the transport equation, modeling of the dissipation tensor ε_{ij}, the turbulent transport tensor $D_{ij}^P + D_{ij}^T$, and pressure-strain redistribution tensor Φ_{ij} is necessary. The pressure-strain redistribution term has received the greatest amount of attention from turbulence modelers, due to the fact that it is of the same order as production, and plays a vital role in most flows of engineering interest. The second-moment closures give more realistic and satisfactory results than the first moment closure models in many configurations.

As the transport equation for the Reynolds-stress tensor has to be solved, it introduces six additional equations and many unknowns to be modeled and requiring boundary conditions (unlike the first-moment closures where transport equation for k and ε or ω have to be resolved), making models numerically less stable. Even if the terms to be modeled is less decisive in providing the description of turbulence then also a number of models and empirical coefficients have to be introduced, whose calibration is very difficult to do. Also, the most common models require to introduce wall functions to correctly predict the flow in the near-wall region (Manceau et al., 2001). Due to their apparent complexity in utilization, despite having lower degree of empiricism compared to the first-moment closures, these models are not widely used.

Since the production term does not need modeling, it is the redistribution term that essentially characterizes the models.

1.4.2.1 Launder-Reece-Rodi Model

Based on ε-equation, Lander, Reece and Rodi proposed a stress-transport model, which is one of the most utilized and thoroughly tested second moment closure model (Launder et al., 1975). The model is as follows:

Dissipation approximation: Since dissipation occurs at the smallest scales, Kolmogorov hypothesis of local isotropy is implied (Kolmogorov, 1991):

$$\varepsilon_{ij} = \frac{2}{3}\varepsilon\delta_{ij} \quad \text{where} \quad \varepsilon = \nu\overline{\frac{\partial u_i}{\partial x_j}\frac{\partial u_i}{\partial x_j}} \tag{1.53}$$

Transport equation for dissipation rate:

$$\frac{\partial \varepsilon}{\partial t} + U_j\frac{\partial \varepsilon}{\partial x_j} = C_{\varepsilon 1}\frac{\varepsilon}{k}\overline{u_i u_j}\frac{\partial U_i}{\partial x_j} - C_{\varepsilon 2}\frac{\varepsilon^2}{k} - C_\varepsilon\frac{\partial}{\partial x_k}\left[\frac{k}{\varepsilon}\overline{u_i u_m}\frac{\partial \varepsilon}{\partial x_m}\right] \tag{1.54}$$

Turbulent transport: Triple products of velocity fluctuations and pressure fluctuations appear in the tensor of turbulent transport:

$$C_{ij} = D_{ij}^T + D_{ij}^P = -\frac{\partial}{\partial x_k}\left[C_s\frac{k}{\varepsilon}\overline{u_k u_l}\frac{\partial \overline{u_i u_j}}{\partial x_l}\right] \tag{1.55}$$

where D_{ij}^T results from the mean effect of the convection of energy by the fluctuating velocity, its approximation was given by Daly et al. (1970), and D_{ij}^P results from the mean effect of the fluctuating pressure forces.

Reynolds-stress tensor:

$$\frac{\partial \overline{u_i u_j}}{\partial t} + U_k\frac{\partial \overline{u_i u_j}}{\partial x_k} = P_{ij} + \frac{2}{3}\varepsilon\delta_{ij} - \Phi_{ij} - C_{ij} \tag{1.56}$$

Pressure-strain correlation:

$$\Phi_{ij} = C_1\frac{\varepsilon}{k}\left(\overline{u_i u_j} - \frac{2}{3}k\delta_{ij}\right) - g_1\left(P_{ij} - \frac{2}{3}P\delta_{ij}\right) \tag{1.57}$$

Auxiliary closure relations:

$$P_{ij} = -\overline{u_i u_m}\frac{\partial U_j}{\partial x_m} - \overline{u_j u_m}\frac{\partial U_i}{\partial x_m}, \quad P = \frac{1}{2}P_{kk} \tag{1.58a}$$

$$g_1 = \frac{8 + C_2}{11} \tag{1.58b}$$

Coefficients of the model:

C_1	C_2	C_s	C_ε	$C_{\varepsilon 1}$	$C_{\varepsilon 2}$
1.5	0.4	0.22	0.15	1.44	1.90

It is also interesting to point out that the transport equation for the dissipation rate only differs from the standard $k - \varepsilon$ model in the form of the diffusion term.

1.4.2.2 Speziale-Sarkar-Gatski Model

Speziale, Sarkar and Gatski proposed a nonlinear expansion in terms of the anisotropy tensor b_{ij} (refer to Eq. (1.61)) (Speziale et al., 1991). The model differs from LRR model (Launder et al., 1975) in terms of defining the pressure strain correlation. This model is generally referred to as SSG model. Based on the analysis of homogeneous turbulent flow subjected to plane strains, based on study of the solution for short times (rapid

distortion theory) and equilibrium solutions for long times ($t \to \infty$), Speziale et al. (1991) have shown that the following quasi-linear formulation can be used.

$$\begin{aligned}\Phi_{ij} = &-\left(c_1\varepsilon + C_1^* P_{ij}\right) b_{ij} + C_2\varepsilon\left(b_{ik}b_{kj} - \frac{1}{3}b_{mn}b_{nm}\delta_{ij}\right) \\ &+ \left(C_3 - C_3^*\sqrt{b_{ij}b_{ij}}\right) kS_{ij} + C_4 k\left(b_{ik}S_{jk} + b_{jk}S_{ik} - \frac{2}{3}b_{mn}S_{mn}\delta_{ij}\right) \\ &+ C_5 k\left(b_{ik}\Omega_{jk} + b_{jk}\Omega_{ik}\right)\end{aligned} \tag{1.59}$$

where Ω_{ij} is the mean rotation tensor defined as:

$$\Omega_{ij} = \frac{1}{2}\left(\frac{\partial U_i}{\partial x_j} - \frac{\partial U_j}{\partial x_i}\right) \tag{1.60}$$

The anisotropy tensor b_{ij} is defined as:

$$b_{ij} = \frac{\overline{u_i u_j} - \frac{2}{3}k\delta_{ij}}{2k} \tag{1.61}$$

Coefficients of the model:

C_1	C_1^*	C_2	C_3	C_3^*	C_4	C_5
3.4	1.8	4.2	0.8	1.3	1.25	0.4

The non-linearity of the *slow term* can be removed by taking $C_2 = 0$. This model has been applied to many cases with some success. It is one of the most widely used second closure moment model along with LRR model.

Apart from the models discussed above, there are many other models in the literature (Wilcox et al., 1998; Hanjalić et al., 2011). The two-equation eddy-viscosity models discussed here serves as a reference for further development of a hybrid model used in the thesis. The second-moment closures discussed here requires wall functions. Based on the success of $k-\omega$ model in predicting flow characteristics, Wilcox proposed a Reynolds-stress model resembling $k-\omega$ model (Wilcox et al., 1998), which overcame the shortcomings of the LRR model. Hanjalić et al. (1998) proposed a second-moment closure which accounts separately for wall blockage and pressure reflection effects allowing the model to integrate up to the wall. Elliptic Blending Reynolds-Stress Model (EB-RSM) introduces a weighting function to provide a more realistic treatment of near-wall flows (Manceau et al., 2002), also the elliptical weighting approach improves numerical stability. As during the thesis the second-moment closures are not used, these models are not described in detail here.

1.5 Large Eddy Simulations (LES)

LES, short for Large Eddy Simulation resolves the large scale eddies, and models the smallest scales. LES falls in between RANS and DNS in terms of computing cost and necessary resources, and it is driven by the limits of each of these techniques. Because large-scale unsteady movements are explicitly resolved, LES can describe the flow characteristics more accurately, which makes it more dependable than RANS models where the unsteady characteristics of the flow are required to be captured. The dynamics of the large-scale motions impacted by the flow geometry and not universal in nature are computed explicitly in LES, while the smallest dissipative scales which have some universality are represented by models. As a result, the computing expense of explicitly describing the small-scale motions is avoided.

Conceptually, LES involves four steps.

→ Instantaneous velocity is decomposed into a filtered part and a residual part using a filtering operator. The filtered velocity fields (three-dimensional and time-dependent in nature) represents the large scale motion.

→ Transport equations of the filtered velocity field are derived from the Navier-Stokes equations. The filtered momentum equation contains the residual stress tensor arising from the sub-filter motions.

→ Modeling of the sub-filter scale stress tensor is required to close the model. The most simple way to do so is an eddy-viscosity model.

→ The filtered equation for the velocity is solved numerically, which provides a description of large-scale motions in one realization of the turbulent flow.

Contrary to RANS models, for which the models must describe all the scales of turbulence, the contribution of models in LES is restricted to the small scales, making it possible to considerably reduce the modeling efforts. A major difficulty with Large Eddy simulation is the near wall resolution. Because near a wall all the eddies are small to the extent that it overlaps with the eddies in dissipative range. If LES is required to resolve most of the stress-bearing range, the grid spacing, the time step required by LES tends towards a DNS as the wall is approached (Choi et al., 2012). With LES models, it is important to ensure that a substantial part of the energy remains resolved. In addition to that, it must be ensured that a significant part of the dissipation is modeled. Thus, the dissipation induced by numerical methods must be reduced as much as possible, in particular when the mesh is irregular.

1.5.1 Filtering operators

The LES models depend on filtering to separate the modeled and resolved scales. In filtered approaches, a low-pass convolution filter is used to decompose the instantaneous velocity U_i^* into a resolved part $\widetilde{U}_i$ and a residual part u_i''.

$$U_i^* = \widetilde{U}_i + u_i'' \tag{1.62}$$

The filtering operator can be expressed as $\langle\cdot\rangle$. This filtered part can be demonstrated as a particular case of general spatio-temporal filtering operator.

$$\widetilde{U}_i\left(\boldsymbol{x},t\right) = \langle U_i^*\left(\boldsymbol{x},t\right)\rangle = \int_{\mathscr{D}}\int_{-\infty}^{t} \mathscr{G}(\boldsymbol{x},\boldsymbol{x}',t,t')U_i^*(\boldsymbol{x},\boldsymbol{x}')\mathrm{d}\boldsymbol{x}'\mathrm{d}t' \tag{1.63}$$

where $\mathscr{D}$ is the spatial domain and $\mathscr{G}$ is the normalized filter kernel. This filter satisfies the assumptions of constant preservation and linearity, but does not necessarily commute with the differential operators, as will be demonstrated in chapter 3. The filtering operators can be simplified as:

$$\widetilde{U}_i(\boldsymbol{x},t) = \int_{\mathscr{D}} \mathscr{G}_\Delta\left(\boldsymbol{x},\boldsymbol{x}'\right) U_i^*\left(\boldsymbol{x}',t\right)\mathrm{d}\boldsymbol{x}' \qquad \text{(spatial filtering)} \tag{1.64}$$

The spatial filter must respect the following condition of normalization:

$$\int_{\mathscr{D}} \mathscr{G}_\Delta\left(\boldsymbol{x},\boldsymbol{x}'\right)\mathrm{d}\boldsymbol{x}' = 1 \tag{1.65}$$

And Eulerian temporal filtering:

$$\widetilde{U}_i(\boldsymbol{x},t) = \int_{-\infty}^{t} \mathscr{G}_{\Delta_T}\left(t,t'\right) U_i^*\left(\boldsymbol{x}',t\right)\mathrm{d}t' \tag{1.66}$$

The temporal filter kernel must satisfy the following condition:

$$\mathscr{G}_{\Delta_T}(\tau) = \frac{1}{\Delta_T} g\left(\frac{\tau}{\Delta_T}\right), \quad \text{with} \quad g(t) \geq 0, \quad g(0) = 1, \quad \int_{-\infty}^{0} g(t)\mathrm{d}t = 1 \tag{1.67}$$

where Δ_T is the filter width, and $\tau = t - t'$.

Equations for filtered velocity:

Applying the filter operator to the Navier-stokes equations leads to:

$$\frac{\partial \widetilde{U}_i}{\partial x_i} = 0 \tag{1.68}$$

$$\frac{\partial \widetilde{U}_i}{\partial t} + \widetilde{U_j}\frac{\partial \widetilde{U}_i}{\partial x_j} = -\frac{1}{\rho}\frac{\partial \widetilde{P}}{\partial x_i} + \nu\frac{\partial^2 \widetilde{U}_i}{\partial x_j \partial x_j} - \frac{\partial \tau_{ij\text{sfs}}}{\partial x_j} + \widetilde{F}_i \tag{1.69}$$

where $\tau_{ij\text{sfs}}$ is the sub-filter stress tensor, defined as:

$$\tau_{ij\text{sfs}} = \langle U_i^* U_j^* \rangle - \langle U_i^* \rangle \langle U_j^* \rangle \tag{1.70}$$

It is important to note that assumptions of commutation between the filter operator and the differential operators have been made, as if the filter width were constant in space and time. In practice, any commutation errors that occur are generally neglected. The sub-filter scale stress tensor can be explicitly expressed with Leonard's decomposition (Leonard, 1975).

$$\tau_{ij\text{sfs}} = \underbrace{\langle \widetilde{U}_i \widetilde{U_j} \rangle - \widetilde{U}_i \widetilde{U_j}}_{\mathcal{L}_{ij}} + \underbrace{\langle \widetilde{U}_i u_j'' \rangle + \langle \widetilde{U_j} u_i'' \rangle}_{\mathcal{C}_{ij}} + \underbrace{\langle u_i'' u_j'' \rangle}_{\mathcal{R}_{ij}} \tag{1.71}$$

where Leonard's tensor $\mathcal{L}_{ij}$ depends on the resolved variables only, representing the large-scale interactions. The cross-stress tensor term $\mathcal{C}_{ij}$ represents the interactions between large (resolved) and small (residual) scales. The sub-filter Reynolds-stress tensor $\mathcal{R}_{ij}$ represents the interaction between the smallest scales. It is important to note that in the case of an idempotent filter, sub-filter stress tensor is exactly equal to the sub-filter Reynolds stress tensor, as $\mathcal{L}_{ij}$ and $\mathcal{C}_{ij}$ are equal to zero. In general, the sub-filter Reynolds-stress tensor is the dominant term with or without an idempotent filter. These three terms are sometimes modeled separately. However, most of the time, the sub-filter stress tensor $\tau_{ij\text{sfs}}$ is modeled globally, without considering the terms separately.

The transport equation for sub-filter stress tensor reads:

$$\begin{aligned}\frac{\partial \tau_{ij\text{sfs}}}{\partial t} + \widetilde{U_k}\frac{\partial \tau_{ij\text{sfs}}}{\partial x_k} = &\underbrace{-\tau_{ik\text{sfs}}\frac{\partial \widetilde{U_j}}{\partial x_k} - \tau_{ij\text{sfs}}\frac{\partial \widetilde{U}_i}{\partial x_k}}_{P_{ij\text{sfs}}} - \underbrace{\frac{\partial \tau\left(U_i^*, U_j^*, U_k^*\right)}{\partial x_k}}_{D^T_{ij\text{sfs}}} + \underbrace{\nu\frac{\partial^2 \tau_{ij\text{sfs}}}{\partial x_k \partial x_k}}_{D^\nu_{ij\text{sfs}}} \\ &\underbrace{-\frac{1}{\rho}\left[\tau\left(U_i^*, \frac{\partial P^*}{\partial x_j}\right) + \tau\left(U_j^*, \frac{\partial P^*}{\partial x_i}\right)\right]}_{\Phi_{ij\text{sfs}}} \underbrace{- 2\nu\tau\left(\frac{\partial U_i^*}{\partial x_k}, \frac{\partial U_j^*}{\partial x_k}\right)}_{\varepsilon_{ij\text{sfs}}}\end{aligned} \tag{1.72}$$

Any averaging operator that respects the assumptions of linearity, preservation of constants and commutativity with the differential operators, leads to the same system of equations (Germano, 1992). According to the general filtering approach (Germano, 1992),

the generalized central moments can be defined as:

$$\begin{cases} \tau\left(U_i^*, U_j^*\right) & = \langle U_i^* U_j^* \rangle - \langle U_i^* \rangle \langle U_j^* \rangle = \tau_{ij\text{sfs}} \\ \tau\left(U_i^*, U_j^*, U_k^*\right) & = \langle U_i^* U_j^* U_k^* \rangle - \langle U_i^* \rangle \langle U_j^* \rangle \langle U_k^* \rangle \\ & \quad - \langle U_i^* \rangle \tau\left(U_j^*, U_k^*\right) - \langle U_j^* \rangle \tau\left(U_k^*, U_i^*\right) - \langle U_k^* \rangle \tau\left(U_i^*, U_j^*\right) \end{cases} \tag{1.73}$$

It is important to note that the transport equation for the sub-filter stress tensor $\tau_{ij\text{sfs}}$ is formally identical to the transport equation of the Reynolds-stress tensor R_{ij} (refer to Eq. (1.26). The different terms are defined in a similar way as in the statistical approach. The terms $P_{ij\text{sfs}}$, $D^T_{ij\text{sfs}}$, $D^\nu_{ij\text{sfs}}$, $\Phi_{ij\text{sfs}}$, and $\varepsilon_{ij\text{sfs}}$ represent, respectively: energy transfer from the resolved to modeled scales, transport by sub-filter scales, viscous diffusion, redistribution and diffusion due to pressure, and sub-filter viscous dissipation.

The transport equation for sub-filter turbulent kinetic energy is:

The sub-filter turbulent kinetic energy can be defined as:

$$k_{\text{sfs}} = \frac{1}{2}\tau_{ii\text{sfs}} \tag{1.74}$$

whose transport equation can be written as:

$$\begin{aligned} \frac{\partial k_{\text{sfs}}}{\partial t} + \widetilde{U_k}\frac{\partial k_{\text{sfs}}}{\partial x_k} = & \underbrace{-\tau_{ik\text{sfs}}\frac{\partial \widetilde{U_i}}{\partial x_k}}_{P_{\text{sfs}}} - \underbrace{\frac{1}{2}\frac{\partial \tau\left(U_i^*, U_j^*, U_k^*\right)}{\partial x_k}}_{D^T_{\text{sfs}}} + \underbrace{\nu\frac{\partial^2 k_{\text{sfs}}}{\partial x_k \partial x_k}}_{D^\nu_{\text{sfs}}} \\ & \underbrace{-\frac{1}{\rho}\tau\left(U_i^*, \frac{\partial P^*}{\partial x_j}\right)}_{D^P_{\text{sfs}}} - \underbrace{\nu\tau\left(\frac{\partial U_i^*}{\partial x_j}, \frac{\partial U_i^*}{\partial x_j}\right)}_{\varepsilon_{\text{sfs}}} \end{aligned} \tag{1.75}$$

The sub-filter production term P_{sfs} plays the most important role in the energy transfer from the resolved velocity field $\widetilde{U_i}$ towards the sub-filter velocity field u_i''. It is important to note that, due to the backscatter the energy transfer can be negative locally ($P_{\text{sfs}} < 0$), even though in general there is a cascade of energy from the resolved scales to the sub-filter scales ($P_{\text{sfs}} > 0$). In LES the smallest scales are not resolved, the resolved dissipation can be considered negligible. Hence, unless the grid is very fine, the physical dissipation mechanism ε is entirely contained within the sub-filter scales. It is therefore necessary to ensure a spectral balance between statistically averaged sub-filter production term and the physical dissipation.

$$P_m \overset{\text{hypo}}{=} \overline{P_{\text{sfs}}} \simeq \varepsilon \overset{\text{hypo}}{=} \overline{\varepsilon_{\text{sfs}}} \tag{1.76}$$

Note that the sub-filter model must compensate for the absence of resolved molecular dissipation by adjusting the modeled dissipation rate.

1.5.2 Sub-filter viscosity

LES models are developed assuming the cutoff of the filtering operator is located in the inertial zone, sufficiently close to the dissipative scales, so that only the smallest scales of turbulence require modeling. The transport equation of the filtered velocity reveals an additional term, the sub-filter stress tensor $\tau_{ij\text{sfs}}$, which requires modeling. As mentioned earlier, sub-filter scales does not require a major modeling effort. However, neglecting them can lead to an energy accumulation at small scales due to the lack of sub-filter dissipation.

In some approaches called implicit LES, the dissipation induced by certain numerical schemes can play the role of physical dissipation. But in most cases, an additional viscosity $\nu_{\text{sfs}}(x,t)$ is introduced in the system of equations to model the sub-filter scales. The sub-filter stress tensor is evaluated using a Boussinesq-type relation, similar to the first moment RANS closure:

$$\tau_{ij\text{sfs}} = -2\nu_{\text{sfs}}\widetilde{S_{ij}} + \frac{2}{3}k_{\text{sfs}}\delta_{ij} \tag{1.77}$$

which defines the sub-filter viscosity as a function of the filtered strain tensor. Similar to eddy-viscosity RANS modeling, the sub-filter scale energy does not require modeling due to the fact that it can be absorbed in the pressure and does not affect the velocity.

1.5.3 Smagorinsky Model

To model the sub-filter viscosity, Smagorinsky proposed a spatial model based on an analogy of mixing length model (Smagorinsky, 1963). As molecular diffusion is introduced in the Navier-Stokes equations in order to mimic the effects of molecular agitation, this model proposed to replace the mixing due to convection at the sub-filter scale by diffusion with

$$\nu_{\text{sfs}} \propto l_c u = \frac{l_c^2}{\tau}. \tag{1.78}$$

l_c is the size of the largest sub-filter eddies, which is proportional to the filter width, which is proportional to grid size ($l_c = C_S\Delta$). u is the characteristic velocity, and τ the characteristic time-scale. It is assumed that the time scale of the largest sub-filter eddies is the same as the time scale of the smallest resolved eddies.

$$\tau = \frac{1}{\widetilde{S}}, \quad \text{with} \quad \widetilde{S} = \sqrt{2\widetilde{S_{ij}}\widetilde{S_{ij}}}, \quad \text{and} \quad \widetilde{S_{ij}} = \frac{1}{2}\left(\frac{\partial\widetilde{U_i}}{\partial x_j} + \frac{\partial\widetilde{U_j}}{\partial x_i}\right) \tag{1.79}$$

where $\widetilde{S}$ is the large scale strain tensor, and $\widetilde{U_i}$ the large scale velocity. Considering that the cutoff wavenumber $\kappa_c = \pi/\Delta$ is in the inertial zone of a Kolmogorov spectrum, with Δ being the filter width,

$$\overline{\widetilde{S^2}} = 2\int_0^{\kappa_c} \kappa^2 E(\kappa)\mathrm{d}\kappa = 2\int_0^{\kappa_c} C_K\varepsilon^{2/3}\kappa^{1/3}\mathrm{d}\kappa = \frac{3}{2}C_K\varepsilon^{2/3}\left(\frac{\pi}{\Delta}\right)^{4/3} \tag{1.80}$$

which leads to the formulation of dissipation linked to the resolved field.

$$\varepsilon = C_S^2\Delta^2\overline{\widetilde{S^2}}^{3/2}, \quad \text{with} \quad C_S = \frac{1}{\pi}\left(\frac{2}{3C_K}\right)^{3/4} \simeq 0.173 \tag{1.81}$$

where C_S is the Smagorinsky constant. For a sub-filter viscosity model, since the sub-filter production is given as $P_{\text{sfs}} = \nu_{\text{sfs}}\widetilde{S}^2$ (same formulation as first moment RANS closure models), and according to the relation given in Eq. (1.76), we have:

$$\overline{P_{\text{sfs}}} = \overline{\nu_{\text{sfs}}\widetilde{S}^2} = C_S^2\Delta^2\overline{\widetilde{S}^3} = \varepsilon \tag{1.82}$$

It is important to note that the averaged modeled dissipation $\overline{\widetilde{\varepsilon_{\text{sfs}}}}$ is indeed equal to the physical dissipation ε, under the assumption:

$$\overline{\widetilde{S^2}}^3 \approx \overline{\widetilde{S^3}}^2 \tag{1.83}$$

The filter size is often estimated as function of the grid step Δ, defined as a cubic root of cell volume, such that $\Delta = (\Delta_x\Delta_y\Delta_z)^{1/3}$. This formula is robust and easily applicable for both structured and unstructured meshes.

Note that the value for C_S mentioned above is adequate to compute an isotropic homogeneous turbulence, but must be adapted for other flows: this is the motivation for the dynamic model presented in the next section.

1.5.4 Dynamic Smagorinsky Model

To evaluate the Smagorinsky constant from the knowledge of resolved motion without requiring a calibration, the dynamic procedure introduces a second filter, called the *test* filter, of the same type as the first one but with a larger width (Germano et al., 1991; Germano, 1992). A double-filtered variable is denoted by $\widetilde{\widetilde{f}}$. The sub-filter scale tensor that appears in the double filtered velocity equation can be written as:

$$\mathcal{T}_{ij\text{sfs}} = \widetilde{\widetilde{U_i U_j}} - \widetilde{\widetilde{U}}_i \widetilde{\widetilde{U}}_j \tag{1.84}$$

The principle behind the dynamic procedure consist in assuming that the two tensors $\mathcal{T}_{ij\text{sfs}}$ and $\tau_{ij\text{sfs}}$ can be represented by the same model, using the same constant. Consider the resolved stress $\mathscr{L}_{ij\text{sfs}}$ defined as:

$$\mathscr{L}_{ij\text{sfs}} = \widetilde{\widetilde{U_i U_j}} - \widetilde{\widetilde{U}}_i \widetilde{\widetilde{U}}_j \tag{1.85}$$

The resolved turbulent stresses are due to the contribution by the scales in between the grid filter width and the test filter width. The resolved turbulent stresses, which is calculated explicitly, can be related to the sub-filter stresses at the test and the grid level by the following relation:

$$\mathscr{L}_{ij\text{sfs}} = \mathcal{T}_{ij\text{sfs}} - \widetilde{\tau_{ij\text{sfs}}} \tag{1.86}$$

This relation is called *Germano's identity*. This identity is used to derive more accurate sub-filter models by determining the most appropriate value of the Smagorinsky constant according to the instantaneous state of the flow. As mentioned earlier, the same functional form can be used to parametrize the stress tensor.

$$m_{ij\text{sfs}} = \tau_{ij\text{sfs}} - \frac{1}{3}\tau_{kk\text{sfs}}\delta_{ij} = -2\left(C_S\Delta\right)^2 \sqrt{2\widetilde{S_{kl}}\widetilde{S_{kl}}}\widetilde{S_{ij}} = -2C\beta_{ij} \tag{1.87}$$

$$\mathcal{M}_{ij\text{sfs}} = \mathcal{T}_{ij\text{sfs}} - \frac{1}{3}\mathcal{T}_{kk\text{sfs}}\delta_{ij} = -2\left(C_S\widetilde{\Delta}\right)^2 \sqrt{2\widetilde{\widetilde{S}_{kl}}\widetilde{\widetilde{S}_{kl}}}\widetilde{\widetilde{S}_{ij}} = -2C\alpha_{ij} \tag{1.88}$$

where $m_{ij\text{sfs}}$ and $\mathcal{M}_{ij\text{sfs}}$ are the models for the anisotropic parts of $\tau_{ij\text{sfs}}$ and $\mathcal{T}_{ij\text{sfs}}$. Germano's identity in Eq. (1.86) yields

$$\mathscr{L}_{ij\text{sfs}} - \frac{1}{3}\mathscr{L}_{kk\text{sfs}}\delta_{ij} = -2C\alpha_{ij} + 2\widetilde{C\beta_{ij}} \tag{1.89}$$

where C is a coefficient, which is a function of space and time. The problem in estimating the coefficient C lies in the integral nature of Eq. (1.89) because of the application of the test filter upon $C\beta_{ij}$. To avoid this, it is common to approximate $\widetilde{C\beta_{ij}}$ as $C\widetilde{\beta_{ij}}$ and C satisfies the following equation:

$$E_{ij} = \mathscr{L}_{ij\text{sfs}} - \frac{1}{3}\mathscr{L}_{kk\text{sfs}}\delta_{ij} + 2C\alpha_{ij} - 2C\widetilde{\beta_{ij}} = 0 \tag{1.90}$$

which leads to six independent relations that has to be satisfied by C. The best way to obtain the solution is to seek the minimum as:

$$\frac{\partial E_{ij}E_{ij}}{\partial C} = 0 \tag{1.91}$$

The new dynamic eddy viscosity sub-filter scale stress model is then defined as:

$$m_{ij} = \alpha_{ij} - \widetilde{\beta_{ij}}, \quad \text{with} \quad C = -\frac{1}{2}\frac{m_{ij}\left(\mathscr{L}_{ij\text{sfs}} - \frac{1}{3}\mathscr{L}_{kk\text{sfs}}\delta_{ij}\right)}{m_{kl}m_{kl}} \tag{1.92}$$

The dynamic model is self-contained, meaning it does not need the parameters to be specified. Hence, it can be seen as an automatic calibration of the model. It is important to notice that most of the time, the field $C(x,t)$ is too irregular, leading to numerical instabilities.

The dynamic procedure can give negative values for C, suggesting transfer of energy from the small scales to the large scales (backscatter). In addition to that choice of the test filter width $\widetilde{\Delta}$ has a strong influence on C.

There are many LES approaches based on spatial filtering beside the approaches presented above. As the thesis does not deal with LES modeling, relatively simple LES models have been discussed to present as a reference.

LES models with temporal filtering is more complex than the approaches with spatial filtering due to the difficulty with the definition of the filter width. Variation in characteristic time scale with the position in a flow renders the choice of time step irrelevant, as in practice the time step is fixed. In addition to that filtering due to the spatial discretization has to be taken into account.

1.6 Hybrid RANS/LES models

Both RANS and LES have their advantages and disadvantages. RANS models are the industrial standard due to their lower computational cost, but they cannot always provide accurate enough results and time-dependent information for the quantities of interest. On the other hand LES models have the capability of providing such information but at a higher cost. This leads to the desire to propose an intermediate form of modeling which is capable of providing the information regarding the unsteady behaviour of large-scale energetic structures but at a reduced numerical cost. It has been an active area of research over the last two decades.

The general idea behind these hybrid RANS/LES models, is to capture the large scale unsteady structures in LES mode in the regions of interest or far from the wall, where the mesh resolution is not fine enough for the LES to operate and to activate RANS mode in regions where LES is not required or too CPU demanding. Hence, hybrid RANS/LES modeling offers the best potential to balance between the reduced computational cost and increased numerical accuracy. Primarily, these hybrid RANS/LES models are divided into two categories: 1) zonal approaches and 2) continuous approaches.

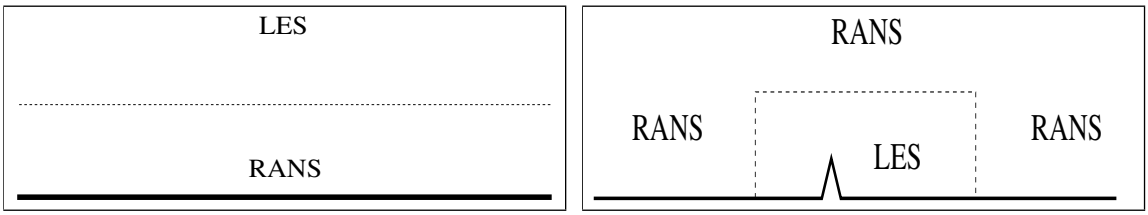

(a) (b)

Figure 1.5 – Illustration for the zonal methods (from Manceau (2020)).

Zonal Approaches

As shown in Fig. 1.5, this approach is conceptually very simple. It corresponds to a multi-domain problem for which the regions to be treated in RANS or LES modes are predefined and treated separately with a discontinuous transition of the variables at the interface. This method is ideal when the area of interest to be studied in LES is predefined. It

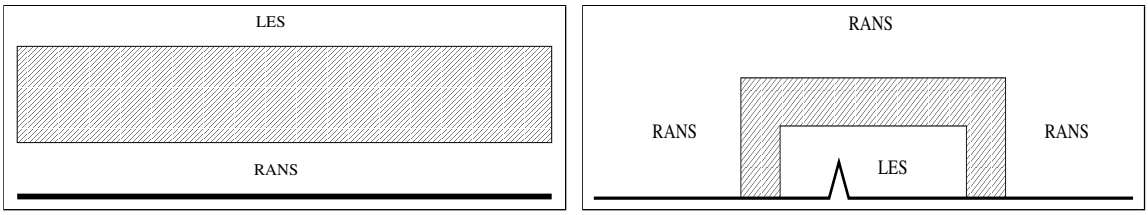

(a) (b)

Figure 1.6 – Illustration for the continuous methods (from Manceau (2020)).

helps to reduce the numerical cost by embedding this LES zone in a global RANS domain, as presented in Fig. 1.5(b). Zonal approaches make it possible to clearly distinguish the sub-domains and select the ideal RANS or LES models in each of them.

The main difficulty for these approaches lies in the coupling of different models at the interface between regions. As the descriptions provided by statistical averaging for RANS and filtering operators for LES are very different. The RANS model needs boundary conditions for the mean variables, whereas the LES needs filtered variables depending on time. Hence, in practice, it is necessary to introduce enrichment operators at the RANS/LES interface, which is not simple. In other words, the LES needs unsteady boundary condition, which the RANS computation cannot provide directly. In addition to this, zonal approaches are highly user-dependent and require in-depth knowledge of the configuration studied in order to predefine the regions treated in RANS or LES mode.

Continuous/Global Approaches

The continuous approaches aim to apply a single model in the entire field of study, which continuously transition from a RANS statistical description to a LES filtered description. The majority of continuous hybrid RANS/LES methods do not mention a generalized scale separation operator that explicitly defines resolved and unresolved scales. Practical simulations must identify the way unresolved scales are filtered out to gain a meaningful understanding of the hybrid RANS/LES approach (Sagaut et al., 2013). These hybrid

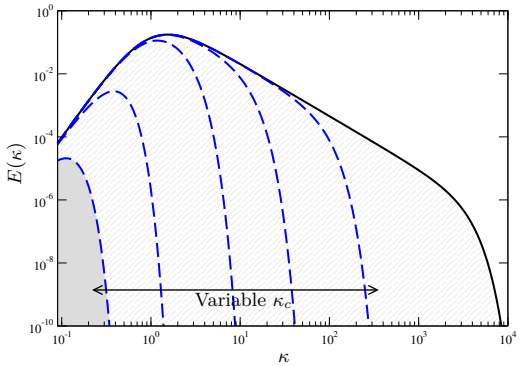

Figure 1.7 – Spectral energy partition corresponding to the variation of resolution (from Manceau (2020)).

models can be interpreted as filtered approaches, but unlike LES, the position of the cutoff wavenumber in the turbulent energy spectrum can vary widely as shown in Fig. 1.7. When the filter size tends towards zero ($\kappa_c \to 0$), the model must go to a RANS model, and when the filter size tends towards infinity ($\kappa_c \to \infty$), the model must go to DNS. Due to the fact that the modeling of unresolved scales is more demanding in LES, the closure model used

for continuous approaches are often the modified RANS models.

The main purpose of any hybrid RANS/LES method is to reduce the turbulent viscosity ν_t in the LES region either by modifying the ν_t formulation, or by directly manipulating the terms in the equation.

Continuous approaches are more "self-supporting" than the zonal approaches because a single model is used throughout the domain. On the other hand it is more difficult to distinguish the zones to be treated in RANS mode or in LES mode. The embedded coupling of LES mode in overall RANS computation leads to the "grey area" problem, which delays the development of the LES resolved turbulence.

Irrespective of the approach used, a major difficulty in any hybrid RANS/LES method resides at the RANS/LES transition regions, which can be seen as diffuse interfaces: both in controlling their position in the flow under consideration and the transition of the variables across the interface. The way in which the energy between modeled and resolved scales is distributed is also a fundamental issue. Here, in the framework of this thesis we will focus on the continuous approaches.

1.6.1 Principles of continuous/global hybrid approaches

Continuous hybrid models are generally built on empirical bases, by modifying the characteristic scales to move continuously from a RANS formulation to a LES formulation. To give a meaning to the variables and construct the model equations, these approaches can be expressed via a filtering formalism (Schiestel et al., 2005; Manceau, 2016).

Consistency of the filtering operator within RANS and DNS limits

→ If the cutoff wavenumber or frequency tend towards zero ($\kappa_c \to 0$ or $\omega_c \to 0$), the model must tend towards a RANS closure, which is not the case with standard LES models. The filtered quantities must tend towards the statistical average:

$$\overline{U_i^*} = U_i = \lim_{\substack{\kappa_c \to 0 \\ \text{or} \\ \omega_c \to 0}} \widetilde{U_i^*} \tag{1.93}$$

This underlines the fact that a significant modeling effort is necessary to represent the turbulent scales when the model is in RANS mode.

→ If ($\kappa_c \to \infty$ or $\omega_c \to \infty$), the model must recover the DNS resolution (which is the case with LES models). What this means is when the filter width tends towards zero, the filtered quantities tend towards their instantaneous values. So, the filtering operator must respect:

$$U_i^* = \lim_{\substack{\kappa_c \to \infty \\ \text{or} \\ \omega_c \to \infty}} \widetilde{U_i^*} \tag{1.94}$$

In LES, scales larger than the filter width contain the majority of the energy, which is not the case everywhere with the hybrid approach. And since only one set of equations is used which is generally a RANS closure, it is important to justify that the model is valid in the LES zone as well. Germano showed that the filtered equations are formally identical to the RANS statistical quantities (Germano, 1992).

1.6.2 Detached Eddy Simulation (DES)

Detached Eddy Simulation (DES) was originally developed by Spalart (1997) based on a first moment RANS closure, the Spalart-Allmaras (model with a transport equation for the

turbulent viscosity) (Spalart et al., 1992). It was developed with a view to solve massively separated flows in the field of aeronautics. The model is designed such a way that, in the boundary layer it offers a RANS solution and after massive separation a LES solution, within a single formulation. In other words, the attached eddies (eddies internal to the boundary layer) are modeled and detached eddies are resolved. The main idea behind the DES based on S-A was to adapt the driving length scale of turbulence. The driving length scale of the RANS S-A model is the distance to the wall d_w, whereas for the Smagorinsky model (standard LES model) it is the grid size Δ, hence the formulation:

$$l_{\text{DES}} = \min\left(d_w, C_{\text{DES}}\Delta\right), \quad \text{with} \quad \Delta = \max\left(\Delta_x, \Delta_y, \Delta_z\right). \tag{1.95}$$

where C_{DES} is an adjustable constant. In the boundary layer, typically $\Delta_y \ll d_w$, but due to the highly anisotropic grids, $d_w \ll \Delta$, giving the RANS behaviour. Far from the wall grid cells are more isotropic and where $\Delta \ll d_w$, the length scale becomes grid-dependent giving the LES behaviour.

This formulation was later generalized by extending its application to two-equation RANS models by Travin et al. (2000) and Strelets (2001). The general definition in Eq. (1.95) makes it possible for DES to adapt to any RANS closure model whose length scale can be modified implicitly or explicitly. For two-equation models, the RANS/LES transition is driven via a comparison of the turbulent length scale and the grid size, which explicitly intervenes in the model. Therefore, for a $k-\omega$ model, the hybridization function for DES can be defined as:

$$F_{\text{DES}} = \max\left[\frac{\sqrt{k_{\text{sfs}}}}{\beta^*\omega_{\text{sfs}}C_{\text{DES}}\Delta}, 1\right] \tag{1.96}$$

With this hybridization, the objective is to control the level of energy that has to be modeled by modifying the dissipative term such that:

$$\omega^*_{\text{sfs}} = F_{\text{DES}}\omega_{\text{sfs}} = \begin{cases} \omega_{\text{sfs}} & \text{if } \dfrac{\sqrt{k_{\text{sfs}}}}{\beta^*\omega_{\text{sfs}}} \leq C_{\text{DES}}\Delta, \quad \text{(RANS)}, \\ \dfrac{\sqrt{k_{\text{sfs}}}}{\beta^*\omega_{\text{sfs}}C_{\text{DES}}\Delta} & \text{if } \dfrac{\sqrt{k_{\text{sfs}}}}{\beta^*\omega_{\text{sfs}}} > C_{\text{DES}}\Delta, \quad \text{(LES)}. \end{cases} \tag{1.97}$$

Hence, when associated with the $k-\omega$ SST model, the following DES formulation is obtained:

$k-\omega$ SST DES formulation:

$$\nu_{\text{sfs}} = \frac{a_1 k_{\text{sfs}}}{\max\left(a_1\omega, F_2\widetilde{S}\right)} \tag{1.98}$$

$$\begin{cases} \dfrac{\partial k_{\text{sfs}}}{\partial t} + \widetilde{U_j}\dfrac{\partial k_{\text{sfs}}}{\partial x_j} &= P_k + \dfrac{\partial}{\partial x_j}\left[\left(\nu + \dfrac{\nu_{\text{sfs}}}{\sigma_k}\right)\dfrac{\partial k_{\text{sfs}}}{\partial x_j}\right] - \omega^*_{\text{sfs}} \\ \dfrac{\partial \omega_{\text{sfs}}}{\partial t} + \widetilde{U_j}\dfrac{\partial \omega_{\text{sfs}}}{\partial x_j} &= \gamma_\omega\widetilde{S}^2 + \dfrac{\partial}{\partial x_j}\left[\left(\nu + \dfrac{\nu_{\text{sfs}}}{\sigma_\omega}\right)\dfrac{\partial \omega_{\text{sfs}}}{\partial x_j}\right] - \beta\omega^2_{\text{sfs}} \\ & \quad +2\left(1-F_1\right)\dfrac{1}{\sigma_{\omega 2}}\dfrac{1}{\omega_{\text{sfs}}}\dfrac{\partial \omega_{\text{sfs}}}{\partial x_j}\dfrac{\partial k_{\text{sfs}}}{\partial x_j} \end{cases} \tag{1.99}$$

with the hybridization function:

$$F_{\text{DES}} = \max\left[\frac{\sqrt{k_{\text{sfs}}}}{\beta^*\omega_{\text{sfs}}C_{\text{DES}}\Delta}, 1\right] \quad \text{with} \quad \Delta = \max\left(\Delta_x, \Delta_y, \Delta_z\right) \tag{1.100}$$

Relation of constants: $\phi = F_1\phi_1 + (1 - F_1)\phi_2$
Constants of the model:

$C_{\text{DES}}^{k-\varepsilon}$	$C_{\text{DES}}^{k-\omega}$	σ_{k1}	σ_{k1}	$\sigma_{\omega 1}$	$\sigma_{\omega 2}$
0.61	0.78	1/0.85	1	2	1/0.856

→ Therefore, In two-equation RANS closure model, when in LES mode, the dissipation term in the transport equation of the turbulent energy is increased, which leads to the reduced level of modeled energy and in turn the turbulent viscosity. This decrease in the turbulent viscosity allow for the appearance of the resolved structures, and in turn for the increase in the resolved energy.

→ The mesh size is estimated using the widest cell dimension, which avoids the transition to the LES mode when the cells are too anisotropic.

→ The exact formulation of the $k - \omega$ SST model is found in the RANS branch of the model.

This formulation can be adapted to the $k - \varepsilon$ closure model with a hybridization function:

$$F_{\text{DES}} = \max\left[\frac{k_{\text{sfs}}^{3/2}/\varepsilon_{\text{sfs}}}{C_{\text{DES}}\Delta}\right] \tag{1.101}$$

A well identified problem with this model is the *grey* area issue, linked to the modeled-stress depletion, i.e. the fact that the decrease of modeled energy is not compensated by the resolved stresses in the transition region. Secondly, if the grid is suddenly refined in a boundary layer, the computed flow can separate artificially, which is known as grid-induced separation. This problem has motivated researchers to develop improved versions of DES.

1.6.3 Delayed DES (DDES)

To avoid the grid-induced separation Spalart et al. (2006) proposed to impose the RANS mode when the mesh is ambiguous in the boundary layer by implementing a shielding function. When the mesh is not fine enough to support the resolved fluctuations internal to the boundary layer, but the switch to the LES mode happens anyway due to the DES hybridization function, the eddy viscosity is reduced but without any sizeable increase in resolved stresses to restore the balance of reduced modeled stresses.

The application of DDES to the S-A based DES can be done by simply redefining the DES length scale l_{DES} such that

$$l_{\text{DDES}} = d_w - f_d \max\left(0, d_w - C_{\text{DES}}\Delta\right) \tag{1.102}$$

where f_d is the shielding function, which is defined in a manner that its value is zero in the boundary layer and unity elsewhere. The shielding function is defined as

$$f_d = 1 - \tanh\left([C_d r_d]^{p_d}\right) \tag{1.103}$$

Here, $C_d = 8$ and $p_d = 3$ are the constants chosen based on the shape requirements for the shielding function. These constants ensure that the solution is essentially identical to the RANS solution in the boundary layer, with r_d being

$$r_d = \frac{\nu_t + \nu}{C_\kappa^2 d_w^2 \sqrt{\frac{1}{2}\left(\widetilde{S}^2 + \widetilde{\Omega}^2\right)}} \tag{1.104}$$

where ν_t is the kinematic eddy viscosity, ν the molecular viscosity, C_κ the von-Karman constant and d_w the distance to the wall. The parameter r_d equals to unity in the log-layer, and gradually goes to zero towards the edge of the boundary layer. ν in Eq. (1.104) helps correcting the near wall behaviour by ensuring that r_d is not zero.

The role of the shielding function can be understood by looking at the limiting case:

$$f_d = \begin{cases} 0 \implies l_{\text{DDES}} = d_w & (\text{RANS})\,, \\ 1 \implies l_{\text{DDES}} = \min\left(d_w, C_{\text{DES}}\Delta\right) & (\text{DES})\,. \end{cases} \tag{1.105}$$

Due to the shielding function and its dependence on r_d, the model with the DDES length scale can refuse the LES mode to be active in the boundary layer unlike the DES model.

1.6.4 Improved DDES (IDDES)

The improved DDES proposed by Shur et al. (2008) merges a DDES-like branch and a WMLES (Wall-Modeled LES)-like branch by introducing a blending function, and modifies the expression of Δ in order to improve the *grey* area behaviour of the model. The blending function operates in such a way that when the inflow conditions do not have any turbulent content the DDES-like branch becomes active, and when the inflow conditions contain unsteady information and impose turbulent content, the WMLES-like branch becomes active. The blending function $\widetilde{f}_d$ is defined by

$$\widetilde{f}_d = \max\{(1 - f_{dt})\,, f_B\} \tag{1.106}$$

where f_{dt} is the shielding function defined in the DDES approach by Eq. (1.103), f_B is an empirical blending function depending on the distance to the wall d_w and maximum grid size $\Delta_{\max} = \max(\Delta_x, \Delta_y, \Delta_z)$. This empirical function f_B provides the rapid switching of the model from the RANS mode ($f_B = 1$) to the LES mode ($f_B = 0$) within the range of wall distance $0.5\Delta_{\max} < d_w < \Delta_{\max}$. With this criteria the length scale for the model is given by

$$l_{\text{IDDES}} = \widetilde{f}_d\,(1 + f_e)\,l_{\text{RANS}} + \left(1 - \widetilde{f}_d\right) l_{\text{LES}} \tag{1.107}$$

Here, f_e is a function which prevents excessive reduction of the Reynolds stresses in the RANS zone in order to reduce the log-layer mismatch. The LES length scale in Eq. (1.107) is modified by replacing Δ by Δ_m.

$$\Delta_m = \min\{\max\left[C_w d_w, C_w\Delta_{\max}, \Delta_y\right], \Delta_{\max}\} \tag{1.108}$$

where $C_w = 0.15$ is an empirical constant which does not depend on any specific model, and Δ_y is the grid step in the wall normal direction. The main purpose of modifying Δ is to obtain the correct behaviour in the log-layer in WMLES without having to change the value of the constant C_{DES}.

1.6.5 Partially Averaged Navier-Stokes (PANS)

With the purpose of bridging the gap between completely and partially modeled scales, Girimaji et al. (2005) proposed a Partially Averaged Navier-Stokes (PANS) model. In PANS, the transition from RANS to LES is controlled through two parameters: the modeled-to-total kinetic energy ratio f_k and modeled-to-total dissipation ratio f_ε.

$$f_k = \frac{k_{\text{sfs}}}{k}, \quad f_\varepsilon = \frac{\varepsilon_{\text{sfs}}}{\varepsilon}. \tag{1.109}$$

The PANS closure model was originally developed based on the underlying k-ε RANS model. Note that the large scales contain most of the energy and the dissipation occurs at smaller scales, meaning $0 \leq f_k \leq f_\varepsilon \leq 1$. Equations for k_{sfs} and ε_{sfs} are obtained from those of k and ε using Eq. (1.109).

PANS closure model:

$$\nu_t = C_\mu \frac{k_{\text{sfs}}^2}{\varepsilon_{\text{sfs}}} \tag{1.110}$$

$$\begin{cases} \dfrac{\mathrm{d}k_{\text{sfs}}}{\mathrm{d}t} &= \dfrac{\partial}{\partial x_j}\left[\left(\nu + \dfrac{\nu_t}{\sigma_{k_{\text{sfs}}}}\right)\dfrac{\partial k_{\text{sfs}}}{\partial x_j}\right] + P_{k_{\text{sfs}}} - \varepsilon_{\text{sfs}} \\ \dfrac{\mathrm{d}\varepsilon_{\text{sfs}}}{\mathrm{d}t} &= \dfrac{\partial}{\partial x_j}\left[\left(\nu + \dfrac{\nu_t}{\sigma_{\varepsilon_{\text{sfs}}}}\right)\dfrac{\partial \varepsilon_{\text{sfs}}}{\partial x_j}\right] + C_{\varepsilon 1} P_{k_{\text{sfs}}} \dfrac{\varepsilon_{\text{sfs}}}{k_{\text{sfs}}} + C_{\varepsilon 2}^* \dfrac{\varepsilon_{\text{sfs}}^2}{k_{\text{sfs}}} \end{cases} \tag{1.111}$$

Modified model coefficients:

$$C_{\varepsilon 2}^* = C_{\varepsilon 1} + \frac{f_k}{f_\varepsilon}\left(C_{\varepsilon 2} - C_{\varepsilon 1}\right); \quad \sigma_{k_{\text{sfs}},\varepsilon_{\text{sfs}}} \equiv \sigma_{k,\varepsilon}\frac{f_k^2}{f_\varepsilon} \tag{1.112}$$

The coefficients $C_{\varepsilon 1} = 1.44$, $C_{\varepsilon 2} = 1.92$, $C_\mu = 0.09$, $\sigma_k = 1.0$ and $\sigma_\varepsilon = 1.3$ are same as those of the standard k-ε RANS model.

By introducing $f_k < 1$ into the transport equation of dissipation, leads to a modification of the solution of the system (1.111), with a reduction of the value of k_{sfs}, which in turn reduces the modeled viscosity ν_t. The definition of f_k and f_ε depends on the desired physical resolution. Unless one want to resolve the dissipative scale, f_ε can be set to unity; Hence, f_k is the only relevant parameter associated to the resolution of the turbulence structure.

1.6.6 Partially Integrated Transport Model (PITM)

The Partially Integrated Transport Model (PITM) is based on spatial filtering and was proposed by Chaouat et al. (2005) and Schiestel et al. (2005). Within this approach, a spectral analysis of turbulent processes in the subgrid scale is fundamental to modeling the filtered transport equation of stress tensor. In this framework, the energy spectrum of homogeneous turbulence is partitioned into three different zones.

- → Resolved zone $[0, \kappa_c]$, where the turbulent scales are explicitly resolved.
- → Modeled energetic zone $[\kappa_c, \kappa_d]$,where the turbulent scales are modeled.
- → Modeled dissipative zone $[\kappa_d, \infty]$, where the turbulent scales are modeled but their energy level is negligible.

Here, the wavenumber κ_c, corresponding to the filter width, is introduced in the medium range of eddies, whereas the wavenumber κ_d is located at the end of inertial zone such that the distribution of the energy from dissipative zone to the total energy is negligible. The relation between them is defined as

$$\kappa_d - \kappa_c = \zeta_{\text{sfs}} \frac{\varepsilon_{\text{sfs}}}{k_{\text{sfs}}^{3/2}} \tag{1.113}$$

where ζ_{sfs} is a sufficiently large coefficient, which helps adjusting the cut-off wavenumber in the evolving spectrum. In the framework of homogeneous turbulence, the equation of

the energy spectrum balance is given as

$$\frac{\partial E}{\partial t} = -\lambda_{ij} A_{ij} + T - 2\nu\kappa^2 E \tag{1.114}$$

where λ_{ij} is the mean velocity gradient, A_{ij} the tensor corresponding to the velocity correlations in the wave vector space, the second term in the RHS of Eq. (1.114) represents the spectral transfer of energy and the third term viscous dissipation. The partial equations of turbulent kinetic energy and dissipation rate in the range $[\kappa_c, \infty]$ is given by

$$\begin{aligned} \frac{\mathrm{d}k_{\mathrm{sfs}}}{\mathrm{d}t} &= F_c - \varepsilon_{\mathrm{sfs}} \\ \frac{\mathrm{d}\varepsilon_{\mathrm{sfs}}}{\mathrm{d}t} &= C_{\varepsilon 1}\frac{\varepsilon_{\mathrm{sfs}}}{k_{\mathrm{sfs}}} F_c - C^*_{\varepsilon 2}\frac{\varepsilon^2_{\mathrm{sfs}}}{k_{\mathrm{sfs}}} \end{aligned} \tag{1.115}$$

where F_c is the total energy flux entering the subgrid zone from the resolved zone, which corresponds to the production in subgrid zone P_{sfs}. Similarly, the energy flow from the subgrid zone to dissipative zone corresponds to the dissipation rate. Placing this into Eq. (1.115), the system of equations look similar to that of a $k-\varepsilon$ RANS model. However, in contrast with the $k-\varepsilon$ RANS model, the coefficient $C^*_{\varepsilon 2}$ is variable and writes

$$C^*_{\varepsilon 2} = C_{\varepsilon 1} + \frac{k_{\mathrm{sfs}}}{k}\left(C_{\varepsilon 2} - C_{\varepsilon 1}\right) \tag{1.116}$$

In the inertial zone, according to Kolmogorov theory, the energy spectrum in the wavenumber space can be defined by

$$E(\kappa) = C_K \varepsilon^{2/3} \kappa^{-5/3} \tag{1.117}$$

and

$$k_{\mathrm{sfs}} = \int_{\kappa_c}^{\infty} E(\kappa)\,\mathrm{d}\kappa = \frac{3}{2} C_K \varepsilon^{2/3} \kappa_c^{-2/3} \tag{1.118}$$

According to the Heisenberg's hypothesis, the subgrid turbulent viscosity can be demonstrated as

$$\nu_{\mathrm{sfs}} = C_\nu \int_{\kappa_c}^{\infty} \kappa^{-3/2} E(\kappa)^{1/2}\,\mathrm{d}\kappa = \frac{3}{4} C_\nu C_K^{1/2} \varepsilon^{1/3} \kappa^{-4/3} = C_\mu \frac{k^2_{\mathrm{sfs}}}{\varepsilon} \tag{1.119}$$

where $C_\mu = 1/3 C_\nu C_K^{-3/2} = 0.09$. Here, k_{sfs}/k is nothing but the ratio of the modeled to total energy,

$$r = \frac{k_{\mathrm{sfs}}}{k} = \frac{3}{2} C_K \left(\kappa_c \frac{k^{3/2}}{\varepsilon}\right)^{-2/3} \tag{1.120}$$

The cutoff wavenumber κ_c is defined as

$$\kappa_c = \frac{\pi}{\Delta} \tag{1.121}$$

It is important to take note of the fact that since the cutoff wavenumber is defined in the inertial region of the turbulent spectrum, the resolved dissipation rate ε_r can be neglected in comparison with the subgrid dissipation rate $\varepsilon_{\mathrm{sfs}}$. Hence, $\varepsilon = \varepsilon_{\mathrm{sfs}}$.

$k-\varepsilon$ PITM model:

$$\nu_{\mathrm{sfs}} = C_\mu \frac{k^2_{\mathrm{sfs}}}{\varepsilon_{\mathrm{sfs}}} \tag{1.122}$$

$$\begin{cases} \dfrac{\mathrm{d}k_{\mathrm{sfs}}}{\mathrm{d}t} &= P_{\mathrm{sfs}} + \dfrac{\partial}{\partial x_j}\left[\left(\nu + \dfrac{\nu_{\mathrm{sfs}}}{\sigma_k}\right)\dfrac{\partial k_{\mathrm{sfs}}}{\partial x_j}\right] - \varepsilon_{\mathrm{sfs}} \\ \dfrac{\mathrm{d}\varepsilon_{\mathrm{sfs}}}{\mathrm{d}t} &= C_{\varepsilon 1}\dfrac{\varepsilon_{\mathrm{sfs}}}{k_{\mathrm{sfs}}}P_{\mathrm{sfs}} + \dfrac{\partial}{\partial x_j}\left[\left(\nu + \dfrac{\nu_{\mathrm{sfs}}}{\sigma_\varepsilon}\right)\dfrac{\partial \varepsilon_{\mathrm{sfs}}}{\partial x_j}\right] - C^*_{\varepsilon 2}\dfrac{\varepsilon^2_{\mathrm{sfs}}}{k_{\mathrm{sfs}}} \end{cases} \tag{1.123}$$

with the modified coefficient which acts as a mean to hybridize the model,

$$C^*_{\varepsilon 2} = C_{\varepsilon 1} + r\left(C_{\varepsilon 2} - C_{\varepsilon 1}\right) \quad \text{and} \quad r = \min\left(1; \frac{3}{2}C_K\left(\frac{\pi}{\Delta}\frac{k^{3/2}}{\varepsilon}\right)^{-2/3}\right) \tag{1.124}$$

The coefficients of the model:

C_μ	C_K	$C_{\varepsilon 1}$	$C_{\varepsilon 2}$	σ_k	σ_ε
0.09	1.50	1.44	1.92	1.0	1.3

It is interesting to discuss the limiting cases of the PITM model to understand how the different branches operate within the model.

→ When the grid step Δ is sufficiently large compared to the integral scale $k^{3/2}/\varepsilon$, the energy ratio r is unity, the hybridization function $C^*_{\varepsilon 2}$ is equal to the coefficient $C_{\varepsilon 2}$, and the exact k-ε RANS closure model is recovered: the RANS mode is activated.

→ When the grid is sufficiently fine, the energy ratio r is less than unity, $C^*_{\varepsilon 2} < C_{\varepsilon 2}$ leads to the reduction in the destruction term of the dissipation rate's transport equation. Consequently the dissipation $\varepsilon_{\mathrm{sfs}}$ increases and ultimately the turbulent viscosity decreases, which gradually activates the LES mode.

Although the spatial formulation of the PITM is developed in homogeneous turbulence, the model was successfully applied to inhomogeneous configurations (Chaouat et al., 2013a; Chaouat et al., 2021; Heinz, 2022).

1.6.7 Temporal PITM (TPITM)

In order to extend the validity of the PITM formalism to inhomogeneous turbulence, Fadai-Ghotbi et al. (2010) proposed an extension of the PITM model in the context of temporal filtering, the Temporal Partially Integrated Transport Model (TPITM). TPITM is developed in an analogous framework based on an analysis in the frequency domain for a statistically stationary inhomogeneous turbulence, unlike its spatial counterpart PITM which is developed under the assumption of homogeneous turbulence in wavenumber space.

Similar to the PITM model, the Eulerian temporal energy spectrum is subdivided into three zones: resolved $[0, \omega_c]$, modeled energetic $[\omega_c, \omega_d]$ and modeled dissipative $[\omega_d, \infty]$, where ω_c is the cutoff frequency and ω_d is a frequency large enough to neglect the energy in the dissipative zone compared to inertial zone. Since the cutoff frequency is outside the dissipative zone, the total dissipation rate can be assumed equal to the modeled dissipation rate, $\varepsilon = \varepsilon_{\mathrm{sfs}}$, because the resolved part is negligible. The turbulent viscosity is modeled with the same formulation as PITM. The energy ratio is computed under the similar assumption as PITM: cutoff frequency ω_c lies in the inertial zone of a Kolmogorov spectrum. The relation between cutoff frequency and cutoff wavenumber can be described as $\omega_c = U_s\kappa_c$ with $U_s = U + \gamma\sqrt{k}$ (Tennekes, 1975). The energy ratio from Eq. (1.120) can then be redefined as:

$$r = \frac{k_{\mathrm{sfs}}}{k} = \frac{3C_K}{2}\left(\omega_c\frac{k}{\varepsilon}\right)^{-2/3} \tag{1.125}$$

Integrating the Eulerian temporal energy spectrum in the inertial zone gives the system of equations for the model.

$k-\varepsilon$ TPITM model:

$$\nu_{\text{sfs}} = C_\mu \frac{k_{\text{sfs}}^2}{\varepsilon_{\text{sfs}}} \tag{1.126}$$

$$\begin{cases} \dfrac{\mathrm{d}k_{\text{sfs}}}{\mathrm{d}t} &= P_{\text{sfs}} + D_{k\text{sfs}} - \varepsilon_{\text{sfs}} \\ \dfrac{\mathrm{d}\varepsilon_{\text{sfs}}}{\mathrm{d}t} &= C_{\varepsilon 1}\dfrac{\varepsilon_{\text{sfs}}}{k_{\text{sfs}}} P_{\text{sfs}} + D_{\varepsilon\text{sfs}} - C_{\varepsilon 2}^{*}\dfrac{\varepsilon_{\text{sfs}}^2}{k_{\text{sfs}}} \end{cases} \tag{1.127}$$

The model is sensitized to the size of the filter via the hybridization function $C_{\varepsilon 2}^{*}$ in the destruction term of the transport equation of the dissipation rate.

$$C_{\varepsilon 2}^{*} = C_{\varepsilon 1} + r\left(C_{\varepsilon 2} - C_{\varepsilon 1}\right) \quad \text{and} \quad r = \min\left(1; \frac{3}{2} C_K \left(\omega_c \frac{k}{\varepsilon}\right)^{-2/3}\right) \tag{1.128}$$

Similar to the analysis done for the PITM model, the TPITM model in the RANS mode ($r = 1$), recovers the $k-\varepsilon$ closure, and, when $r < 1$ the reduction of the destruction term in the transport equation of the dissipation rate leads to the decrease in the sub-filter energy, as well as the subgrid viscosity, forcing the model to switch to LES mode.

1.7 Conclusion

This bibliographical chapter has allowed us to convey the prerequisite of the thesis, in particular the different approaches (DNS, RANS, LES, hybrid RANS/LES) by concentrating on the resolved portion of the turbulent energy spectrum. The statistical approach of modeling turbulence has been presented with the formulation of the exact transport equations of the statistically averaged variables with a view to make it easier to compare with the modified model (hybrid models), which are investigated in the next chapters.

Within the framework of scale resolving modeling, the filtering approach has been discussed, which recalls the main characteristics of the spatial and Eulerian temporal turbulent energy spectrum. Germano's generalized filtering approach is discussed and used in defining the filtered transport equations. In the same framework, different LES models have been discussed under the assumption that the spectral cutoff filter is in the inertial zone of a Kolmogorov spectrum. From the comparison of the transport equations of statistical modeling and scale resolving modeling, it can be established that they are are formally identical.

The consistency of the filtering operator with the statistical mean operator and the similarity in the form of the transport equations between RANS models and LES models provide a solid base for developing a hybrid RANS/LES approach. Various hybrid models have been discussed: DES, DDES, IDDES - based on a modification of the transport equation for the eddy viscosity or the turbulent energy. PANS, PITM, TPITM - based on the introduction of hybridization function in the transport equation of dissipation to control the transition between RANS and LES mode, which depends on the ratio of modeled (sub-filter) energy to the total energy. The introduction of the TPITM model acts as a guide for temporal hybrid approaches used in the following chapters.

CHAPTER 2

Hybrid Temporal LES (HTLES)

This chapter is dedicated to the theoretical framework of the HTLES (Hybrid Temporal Large Eddy Simulation) model. First, the chapter illustrates the interest of temporal filtering for hybrid approaches, then the HTLES model is developed. This chapter highlights the extension of the HTLES model to the $k-\omega$ SST closure, which was originally developed in association with $k-\varepsilon$ closure. At the end, by the use of various test cases the effectiveness and the limitations of the model is illustrated.

Contents

2.1 Introduction

It is highly desirable to define a rigorous formalism in order to facilitate the modelling of the subgrid stresses in continuous hybrid RANS/LES methods, comparing the solutions with experimental or DNS databases, and eventually understanding the phenomenology observed in the resolved motion (Spalart, 2009). It is well known that the usual methods to bridge RANS and LES suffers from the inconsistency between the statistical averaging of RANS and spatial filtering of LES (Gatski et al., 2007). The Hybrid Temporal Large Eddy Simulations (HTLES) tries to reconcile the two methodologies by defining consistent hybridization operators, based on the temporal filtering. It is important to note that the use of the denomination temporal in the name of the approach (HTLES, Hybrid Temporal LES) is merely an indication that the analytical developments are based on a temporal filtering formalism, which tends to the RANS equations in the case of inhomogeneous flows.

2.2 Temporal filtering

Any flow variable f can be decomposed into two parts: a filtered part, $\widetilde{f}$, and a sub-filtered (residual) part, f'', such as

$$f = \widetilde{f} + f'' \tag{2.1}$$

The resolved part can be defined based on a general spatio-temporal filtering operator (Kampé, 1951)

$$\widetilde{f}\,(\boldsymbol{x},t) = \int_{\mathscr{D}}\int_{-\infty}^{t} \mathscr{G}(\boldsymbol{x},\boldsymbol{x}',t,t')f(\boldsymbol{x}',t')\mathrm{d}\boldsymbol{x}'\mathrm{d}t' \tag{2.2}$$

where $\mathscr{D}$ is the domain and $\mathscr{G}$ is the filter kernel. This definition encompasses the standard LES based on spatial filtering, with a filter kernel of the form $\mathscr{G}(\boldsymbol{x},\boldsymbol{x}',t,t') = \mathscr{G}_\Delta(\boldsymbol{x},\boldsymbol{x}')\delta(t'-t)$, where δ denotes the Dirac delta function, parametrized by a spatial filter width Δ. Temporal LES (Pruett et al., 2003) is based on a filter kernel of the form $\mathscr{G}(\boldsymbol{x},\boldsymbol{x}',t,t') = \mathscr{G}_{\Delta_T}(t,t')\delta(\boldsymbol{x}-\boldsymbol{x}')$, where δ denotes the Dirac delta function parametrized by a temporal filter width Δ_T.

In order to favour a rigorous hybrid RANS-LES formulation, a consistent transition from the RANS statistical description to the LES filtered description is required. This can be obtained if the filter kernel go to a low-pass filter when the filter width is small and to the statistical average when the filter width goes to infinity (RANS limit). In the particular case of homogeneous turbulence the statistical average of the instantaneous velocity can be expressed as:

$$\begin{aligned}\overline{\mathbf{u}_i}\,(t) = \lim_{\Delta\to\infty}\widetilde{\mathbf{u}_i}\,(\boldsymbol{x},t) &= \lim_{\Delta\to\infty}\int_{\mathscr{D}}\int_{-\infty}^{t}\mathscr{G}_\Delta(\boldsymbol{x},\boldsymbol{x}')\delta(t-t')\mathbf{U}_i(\boldsymbol{x}',t')\mathrm{d}\boldsymbol{x}'\mathrm{d}t' \\ &= \lim_{\Delta\to\infty}\int_{\mathscr{D}}\mathscr{G}_\Delta(\boldsymbol{x},\boldsymbol{x}')\mathbf{U}_i(\boldsymbol{x}',t)\mathrm{d}\boldsymbol{x}',\end{aligned} \tag{2.3}$$

which means that spatially filtered quantities ($\widetilde{\mathbf{u}_i}$) go to the statistical quantities ($\overline{\mathbf{u}_i}$) in the limit of infinite filter width. Therefore, the consistency is ensured. But in industrial applications the condition of homogeneous turbulence is never satisfied.

In contrast, temporal filtering provides a consistent bridging between RANS and temporal LES for the wide range of statistically stationary inhomogeneous flows (Fadai-Ghotbi et al., 2010; Manceau, 2016).

In order to avoid confusion, it is worth mentioning that the HTLES model does not imply any explicit filtering but simply involves terms that vary as a function of the ratio

between the time scale of turbulence and the cutoff frequency, and only refers to the fact that the analytical developments are based on temporal filtering. Hence, they do not fundamentally differ in practice from the spatial approaches. The interest of the temporal framework lies in developing an analytical relation between the model parameters and the cut-off frequency such that the hybridization between LES and RANS is extended to inhomogeneous flows.

2.2.1 Galilean invariance

It was shown by Speziale (1987) that, the temporal filter does not satisfy Galilean invariance. To obtain Galilean invariance, Fadai-Ghotbi et al. (2010) defined the uniform temporal filter.

$$\mathscr{G}(\boldsymbol{x}, \boldsymbol{x}', t, t') = \delta\left(\xi(\boldsymbol{x}, t, t') - \boldsymbol{x}'\right) \mathscr{G}_{\Delta_T}\left(t, t'\right), \tag{2.4}$$

with,

$$\xi\left(\boldsymbol{x}, t, t'\right) = \boldsymbol{x} + \left(t' - t\right) \mathbf{V}_{\text{ref}} \tag{2.5}$$

which corresponds to a filtering operator with a moving application point. $\mathbf{V}_{\text{ref}}$ is an arbitrary velocity, constant in space and time. $\mathbf{V}_{\text{ref}} = 0$ must be chosen in the reference frame in which the assumption of statistical stationarity is verified.

2.2.2 Consistency with long-time averaging

Temporal filtering satisfies linearity and preservation of constants. In addition to that, assuming commutativity with the differential operators yields the similarity between the filtered equations and the RANS equations (Germano, 1992; Fadai-Ghotbi et al., 2010). Hence, within the limit of an infinite filter width Δ_T, the consistency between the statistical averaging operator $\overline{\cdot}$ and the filtering operator $\widetilde{\cdot}$ can be demonstrated as;

$$\overline{\mathbf{u}_i}\left(\boldsymbol{x}\right) = \lim_{\Delta_T \to +\infty} \widetilde{\mathbf{u}}_i\left(\boldsymbol{x}, t\right) = \lim_{\Delta_T \to +\infty} \int_{-\infty}^{t} \mathscr{G}_{\Delta_T}(t, t') \mathbf{U}_i(\boldsymbol{x}, t') \mathrm{d}t' \tag{2.6}$$

where $\overline{u_i}$ denotes the statistical average of the instantaneous velocity. The total and resolved fluctuations are defined by u_i^t and u_i' , respectively.

$$U_i = \overline{u_i} + u_i^t = \widetilde{u}_i + u_i'' \quad and \quad u_i^t = u_i' + u_i''. \tag{2.7}$$

These properties in association with the consistency of the filtering operator ensures the continuous bridging between RANS and LES models and make sure that the hybrid model tends to the exact RANS closure in RANS mode, as shown below in section 2.3. The issue of the lack of commutativity with the differential operators will be addressed in the next chapters.

2.3 HTLES formulation

The equation of the filtered momentum using the filtering approach writes:

$$\frac{\partial \widetilde{u}_i}{\partial t} + \widetilde{u}_j \frac{\partial \widetilde{u}_i}{\partial x_j} = -\frac{1}{\rho} \frac{\partial \widetilde{p}}{\partial x_i} + \nu \frac{\partial^2 \widetilde{u}_i}{\partial x_j \partial x_j} - \frac{\partial \tau_{ij\text{sfs}}}{\partial x_j} \tag{2.8}$$

where $\widetilde{p}$ is the filtered pressure, ν is the kinematic viscosity and the subfilter stress (SFS) is defined as the generalized second order moment $\tau_{ij\text{sfs}} = \widetilde{u_i u_j} - \widetilde{u}_i \widetilde{u}_j$. A subfilter stress tensor ($\tau_{ij\text{sfs}}$) transport equation is equivalent to Reynolds-stress tensor $\overline{u_i u_j}$ equation in

RANS. Within the limit of an infinite filter width, it tends exactly towards this equation (RANS equation), which can be used to develop hybrid RANS/LES approaches (Fadai-Ghotbi et al., 2010). Because of filtered-out scales, the equations contain subfilter stresses (SFS) that require closure similar to the case of standard LES.

Here, in the filtering framework, the total turbulent energy k is decomposed exactly into the modeled turbulent energy k_m and the resolved turbulent energy k_r, such that;

$$\begin{gathered} k = k_m + k_r, \quad \text{where} \quad k = \tfrac{1}{2}\overline{u_i^t u_i^t}; \\ k_r = \tfrac{1}{2}\left(\overline{\widetilde{u_i}\widetilde{u_i}} - \overline{\widetilde{u_i}}\,\overline{\widetilde{u_i}}\right) = \tfrac{1}{2}\overline{u_i' u_i'}, \quad \text{and} \quad k_m = \overline{k_{\text{sfs}}} = \tfrac{1}{2}\overline{\widetilde{u_i'' u_i''}}. \end{gathered} \tag{2.9}$$

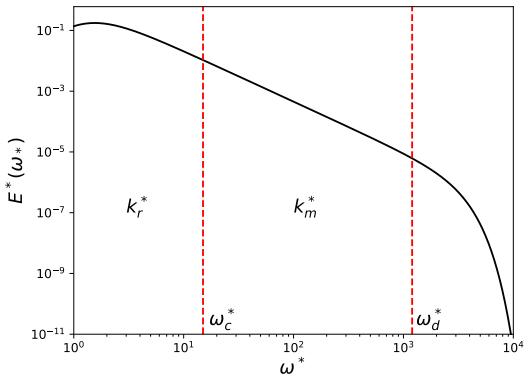

Figure 2.1 – Partition of the Eulerian energy spectrum in a filtered approach.

Here, Fig. 2.1 illustrates the division of the Eulerian energy spectrum into the filtered and residual scales by simplifying the analysis by considering the temporal filter width as a cutoff filter. In the frequency domain, the energy partition is defined as:

$$k = \int_0^\infty E_T(\omega)d\omega, \quad k_r = \int_0^{\omega_c} E_T(\omega)d\omega, \quad k_m = \int_{\omega_c}^\infty E_T(\omega)d\omega \tag{2.10}$$

Since the cutoff frequency is located far inside the inertial range in standard LES, generally the modeled energy is neglected (Pope et al., 2000). But in hybrid approaches, the cutoff frequency may vary in the spectrum from 0 at the RANS limit to the inertial range, such that providing an accurate modeling of the subfilter scales becomes necessary.

2.3.1 Modeling of the subfilter scales

Based on the usual LES assumptions, the error due to the non-commutativity of the filter and the differential operators is considered negligible when the filter width varies in time or space (Sagaut, 2006). Due to the reduced computational cost and numerical robustness compared to other modeling approaches, an eddy-viscosity model is used to solve the closure problem. Taking into account the Boussinesq approximation, the subfilter stress tensor is defined as:

$$\tau_{ij\text{sfs}} = -2\nu_{\text{sfs}}\widetilde{S_{ij}} + \frac{2}{3}k_{\text{sfs}}\delta_{ij} \tag{2.11}$$

Fadai-Ghotbi et al. (2010) showed that the exact transport equation for the subfilter energy can be obtained from the transport equation for the subfilter stress tensor, which gives

$$\frac{\mathrm{d}k_{\text{sfs}}}{\mathrm{d}t} = P_{\text{sfs}} + D_{\text{sfs}} - \varepsilon_{\text{sfs}} \tag{2.12}$$

where P_{sfs}, D_{sfs} and ε_{sfs} denotes the production term of the subfilter energy k_{sfs}, diffusion term and the dissipation rate, respectively.

2.3.2 Hybridization method

Fadai-Ghotbi et al. (2010) using uniform temporal filtering, proposed the Temporal Partially Integrated Method (TPITM), derived from the PITM originally developed in the spatial framework by Chaouat et al. (2005) which was derived from the multi-scale approach by Schiestel (1987). The development of the TPITM is based on the frequency domain analysis for inhomogeneous, stationary turbulence. Partitioning the domain into three regions based on characteristic frequencies ω_c and ω_d: resolved scales $[0, \omega_c]$, unresolved energetic scales $[\omega_c, \omega_d]$ and unresolved dissipative scales $[\omega_d, \infty]$, and integrating the equation over the range $[\omega_c, \omega_d]$ for the Eulerian temporal energy spectrum $E_T(\mathbf{x}, \omega)$, it can be shown that the modeled quantities satisfy the following relations (Fadai-Ghotbi et al., 2010):

$$\begin{aligned} \nu_m &= C_\mu \frac{k_m^2}{\varepsilon_m}, \\ \frac{\mathrm{d}k_m}{\mathrm{d}t} &= P_m + D_{k_m} - \varepsilon_m, \\ \frac{\mathrm{d}\varepsilon_m}{\mathrm{d}t} &= C_{\varepsilon 1} \frac{\varepsilon_m}{k_m} P_m + D_{\varepsilon_m} - C_{\varepsilon 2}^*(r) \frac{\varepsilon_m^2}{k_m} \end{aligned} \tag{2.13}$$

where P_m and D_{k_m} are the subfilter parts of the production and the diffusion of k_m and D_{ε_m} is the diffusion of ε_m (It is important to note that the theory is written for statistically averaged quantities such as $k_m = \overline{k_{\mathrm{sfs}}}$ and $\varepsilon_m = \overline{\varepsilon_{\mathrm{sfs}}}$. But the equations resolved in practice are those of k_{sfs} and $\varepsilon_{\mathrm{sfs}}$, assuming that applying the same $C_{\varepsilon 2}^*$ coefficient obtained for k_m and ε_m, it will work.). Not solving the dissipative scales is one of the goals of hybrid RANS/LES approaches; hence, ω_c must lie outside of the dissipative range, such that $\varepsilon_m = \varepsilon$. Making the equations of the model dependent on the filter width will help controlling how much energy is resolved, which is done by the modified dissipation rate equation (2.13). The transition between RANS and LES is controlled by the hybridization function $C_{\varepsilon 2}^*(r)$. Where,

$$C_{\varepsilon 2}^*(r) = C_{\varepsilon 1} + r\left(C_{\varepsilon 2} - C_{\varepsilon 1}\right) \tag{2.14}$$

which is a function of the energy ratio r, which is nothing but the modeled-to-total energy ratio $r = \overline{k_{\mathrm{sfs}}}/k = k_m/k$. When the RANS limit is applied, $r = 1$, the classical dissipation rate equation is recovered and the model tends towards the classical $k - \varepsilon$ RANS model (Jones et al., 1972). The hybridization function in the dissipation equation indirectly controls the level of modeled energy rather than directly through the energy equation, therefore the resolved turbulence is not always sustained, which can lead to pseudo-relaminarization of the flow.

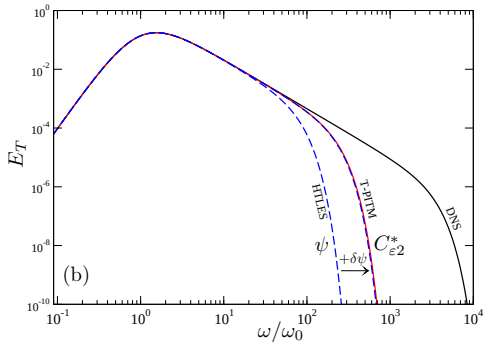

Figure 2.2 – Illustration of H-equivalence (from Manceau (2016)). Here, the HTLES is made H-equivalent to TPITM by introducing a variation $\delta\psi$ of the coefficient ψ.

Hence, it is suggested to develop an equivalent technique in the spirit of DES in order to handle this issue, in which this control is accomplished through a direct adjustment of the dissipation term in the turbulent energy or stresses. This approach is favorable in terms of robustness. By defining the H-equivalence (Friess et al., 2015) criterion such an approach can be determined, where H stands for Hybrid. If two methods provide the same energy partition for a specific circumstance and tend toward the same RANS model for large filter widths, they are said to be H-equivalent. I.e., despite different methods of controlling the energy partition, they yield the same level of subfilter energy. Such methods are developed by Friess et al., which is the equivalent DES (Friess et al., 2015) and by Manceau, which is Hybrid Temporal LES (HTLES) (Manceau, 2016).

These models are H-equivalent to the TPITM model, using the same closure but involves the hybridization function in the destruction term of the k_m equation. The developed model in the general form can be written as follows:

$$\begin{aligned} \nu_m &= C_\mu \frac{k_m^2}{\psi(r)\,\varepsilon_m^*}, \\ \frac{\mathrm{d}k_m}{\mathrm{d}t} &= P_m + D_{k_m} - \psi(r)\,\varepsilon_m^*, \\ \frac{\mathrm{d}\varepsilon_m^*}{\mathrm{d}t} &= C_{\varepsilon 1}\frac{\varepsilon_m^*}{k_m}P_m + D_{\varepsilon_m}^* - C_{\varepsilon 2}\frac{{\varepsilon_m^*}^2}{k_m} \end{aligned} \tag{2.15}$$

where $D_{\varepsilon_m}^*$ denotes the diffusion of ε_m^*, and the dissipation rate of k_m is given by $\psi(r)\,\varepsilon_m^* = \varepsilon_m$. H-equivalence, applied to HTLES and TPITM is represented in Fig. 2.2, a computation using this HTLES model reproduces a filtered spectrum, with a cutoff frequency depending on the coefficient ψ. If this coefficient is arbitrary, there is no reason for HTLES to exhibit the same partition of energy, as TPITM. A modification $\delta\psi$ of the coefficient ψ can be introduced in order to make HTLES H-equivalent to TPITM. The hybridization function, to ensure H-equivalence, is represented as follows:

$$\psi(r) = \frac{C_{\varepsilon 2}}{C_{\varepsilon 2}^*(r)} = \frac{C_{\varepsilon_2}}{C_{\varepsilon 1} + r\,(C_{\varepsilon 2} - C_{\varepsilon 1})} \tag{2.16}$$

It is worth noting that when $r = 1$, i.e. in the RANS mode $\psi(1) = 1$: this is the RANS limit, In contrast to that $\psi(r)$ increases with the decrease in r i.e., this is the LES mode, and its maximum value is reached when r goes to 0, $\psi(0) = C_{\varepsilon 2}/C_{\varepsilon 1}$: this is the DNS limit.

2.3.3 Mathematical framework

In the HTLES model (Manceau, 2016), the underlying RANS model is sensitize to the filter width via the time scale $T_m(r) = k_m/\varepsilon_m$, dependent on the resolution parameter r, which is the modeled-to-total energy ratio, such that $\psi(r)\,\varepsilon_m^* = k_m/T_m$, which gives

$$T_m(r) = \frac{r}{\psi(r)}\frac{k}{\varepsilon_m^*} \tag{2.17}$$

In the new formulation of HTLES, the subfilter viscosity and the transport equations can be written as follows because Chaouat et al. (2005) and Fadai-Ghotbi et al. (2010) showed that the control of the level of modeled energy by varying the coefficients works the same way in the time dependent equations as the averaged equations.

$$\nu_{\mathrm{sfs}} = C_\mu \frac{k_{\mathrm{sfs}}^2}{\psi(r)\,\varepsilon_{\mathrm{sfs}}^*}, \qquad \begin{cases} \dfrac{\mathrm{d}k_{\mathrm{sfs}}}{\mathrm{d}t} = P_{\mathrm{sfs}} + D_{k\mathrm{sfs}} - \dfrac{k_{\mathrm{sfs}}}{T_m}, \\ \dfrac{\mathrm{d}\varepsilon_{\mathrm{sfs}}^*}{\mathrm{d}t} = C_{\varepsilon 1}\dfrac{\varepsilon_{\mathrm{sfs}}^*}{k_{\mathrm{sfs}}}P_{\mathrm{sfs}} + D_{\varepsilon\mathrm{sfs}}^* - C_{\varepsilon 2}\dfrac{{\varepsilon_{\mathrm{sfs}}^*}^2}{k_{\mathrm{sfs}}} \end{cases} \tag{2.18}$$

To check for the limiting case, consider the scenario where the cutoff frequency goes to zero, the consistency of the filtering implies that the filtered quantity tend toward the statistically averaged quantities as discussed before, such that $r = 1$, which leads to the standard equations of the $k-\varepsilon$ RANS model. In contrast to that, in the LES zone, r is less than 1. It is very easy to show that when r decreases, the modeled time scale T_m decreases, which leads to the increase in the destruction term of the k_{sfs} equation, which implies a decreased level of subfilter energy. In turn, the subfilter viscosity is reduced.

$$\nu_m = C_\mu \frac{k^2}{\varepsilon}, \qquad \begin{cases} \dfrac{Dk}{Dt} = P + D_k - \varepsilon, \\ \dfrac{D\varepsilon}{Dt} = C_{\varepsilon 1}\dfrac{\varepsilon}{k}P + D_\varepsilon - C_{\varepsilon 2}\dfrac{\varepsilon^2}{k} \end{cases} \tag{2.19}$$

Because of the simplicity and wide use, the HTLES method is first applied to the $k-\varepsilon$ model, but the standard $k-\varepsilon$ model does not work well in the near wall region and need some modification to be extended to the wall. This is done by locally switching to the $k-\omega$ model, developed by Menter (1994) in the $k-\omega$ SST model. The $k-\omega$ SST based HTLES model can be written as follow:

$$\nu_{\text{sfs}} = \frac{a_1 k_{\text{sfs}}}{\max\left[a_1 \psi'(r)\,\omega^*_{\text{sfs}}, F_2 \widetilde{S}\right]} \tag{2.20}$$

$$\begin{aligned} \frac{\partial k_{\text{sfs}}}{\partial t} + \widetilde{u_j}\frac{\partial k_{\text{sfs}}}{\partial x_j} &= P_k + \frac{\partial}{\partial x_j}\left[\left(\nu + \frac{\nu_{\text{sfs}}}{\sigma_k}\right)\frac{\partial k_{\text{sfs}}}{\partial x_j}\right] - \frac{k_{\text{sfs}}}{T_m}, \\ \frac{\partial \omega^*_{\text{sfs}}}{\partial t} + \widetilde{u_j}\frac{\partial \omega^*_{\text{sfs}}}{\partial x_j} &= \gamma_\omega \frac{1}{\psi'(r)}\widetilde{S}^2 + \frac{\partial}{\partial x_j}\left[\left(\nu + \frac{\nu_{\text{sfs}}}{\sigma_\omega}\right)\frac{\partial \omega^*_{\text{sfs}}}{\partial x_j}\right] - \beta_\omega {\omega^*_{\text{sfs}}}^2 \\ &\quad + (1-F_1)2\frac{1}{\sigma_{\omega 2}}\frac{1}{\psi'(r)\,\omega^*_{\text{sfs}}}\frac{\partial \omega^*_{\text{sfs}}}{\partial x_j}\frac{\partial k_{\text{sfs}}}{\partial x_j} \end{aligned} \tag{2.21}$$

with F_1 and F_2 being the blending functions and γ_ω, β_ω, a_1, a_2, σ_k, σ_ω are the usual coefficients of the $k-\omega$ SST RANS model. (refer to the complete model in Appendices A.)

2.3.4 Switchover criterion

As mentioned earlier in section 2.2, HTLES does not imply any explicit filter width. Manceau (2016) showed the possibility of explicitly relating the model to the filter width, by analytically evaluating the energy ratio r based on the cutoff frequency ω_c. To do so, it appears ideal to connect the cutoff frequency to the time step related Nyquist frequency.

$$\omega_c = \frac{2\pi}{2\tau} \tag{2.22}$$

with the filter width $\Delta_T = 2\tau$, where τ is the time step. However, the grid also filters out eddies, making it impossible to resolve the highest frequency π/τ where the mesh is coarse. This leads to the dependence of the cutoff frequency on the grid step Δ. The largest eddies that can be observed are characterized by the spatial cut-off wavenumber $\kappa_c = 2\pi/2\Delta$. This can be related to the cut-off frequency by $\omega_c = U_s\kappa_c$, where U_s is the sweeping velocity. The sweeping mechanism (sweeping of the small scales by large scales) drives the maximum frequency observed at a fixed point rather than the eddy turnover time (Tennekes, 1975).

Fig. 2.3 shows the link between the cutoff frequency and the grid step. It shows the velocity signal measured at a fixed point due to the sweeping of the resolved (blue) and unresolved (red) eddies by the large-scale eddy. The right part of Fig. 2.3 shows the eddies

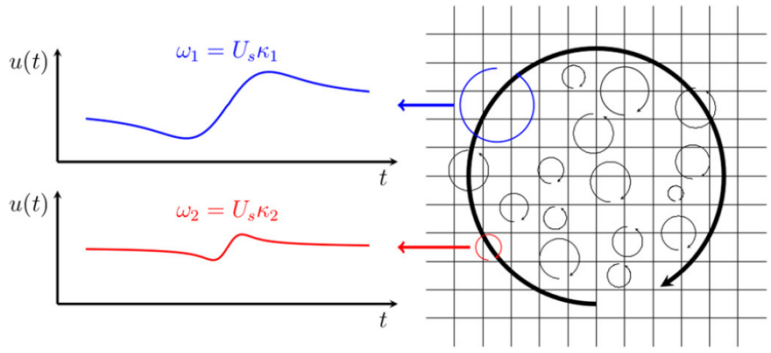

Figure 2.3 – Illustration of the sweeping mechanism (Duffal et al., 2022).

of various size and the mesh used to resolve them. According to the Nyquist-Shannon sampling theorem, the grid should be at lest 2 times smaller than the smallest eddy that you want to resolve (Shannon, 1949). If the small eddy at the bottom were resolved, it would provide a signal that would contribute to higher frequencies, but because the grid is too coarse, the corresponding frequencies are absent. Therefore, the highest resolvable frequency is,

$$\omega_c = \min\left(\frac{\pi}{\tau}, \frac{U_s \pi}{\Delta}\right) \tag{2.23}$$

with $U_s = U + \gamma\sqrt{k}$, where U is the mean velocity magnitude introduce to account for the sweeping due to the mean flow. To correlate the energy ratio r with the cut-off frequency ω_c, the assumption of an equilibrium Eulerian spectrum is used (Tennekes, 1975). Introducing the dispersion relation $\omega = U_s\kappa$ in a Kolmogorov wavenumber spectrum $E(\kappa) = C_K \varepsilon^{2/3} \kappa^{-5/3}$ leads to,

$$E_T(\omega) = C_K \varepsilon^{2/3} U_s^{2/3} \omega^{-5/3} \tag{2.24}$$

where C_K is the Kolmogorov coefficient. Based on this temporal energy spectrum the modeled energy is given as:

$$k_m = \int_{\omega_c}^{\infty} E_T(\omega)\, d\omega \tag{2.25}$$

The energy ratio r_K defined as k_m/k can be defined as (K stands for Kolmogorov)

$$r_K = \frac{k_m}{k} = \frac{1}{k}\int_{\omega_c}^{\infty} E_T(\omega)\, d\omega = \frac{1}{\beta_0}\left(\frac{U_s}{\sqrt{k}}\right)^{2/3}\left(\omega_c \frac{k}{\varepsilon}\right)^{-2/3} \tag{2.26}$$

with $\beta_0 = 2/3C_K$. Eq. (2.23) and Eq. (C.3) define the switchover criterion. If the time step τ is smaller than Δ/U_s everywhere in the domain , the cut-off frequency ω_c is imposed everywhere by the grid step Δ. It further reduces r_K to the relation used in PITM.

$$r_K = \frac{1}{\beta_0}\left(\frac{\pi}{\Delta}\frac{k^{3/2}}{2}\right)^{-2/3} \tag{2.27}$$

2.3.5 Internal Consistency Constraint (ICC)

It was observed by Duffal et al. (2022), that the resolved energy k_r is not zero in the RANS region because of the penetration of resolved structures from the LES region, which leads

to an inconsistency, since the model is based on the assumption of having no resolved energy in the RANS region. This leads to an overestimation of the total energy compared to the estimated total energy in the RANS solution. This overestimation lead to an overestimated time scale T_m and a modification of the destruction term compared to the RANS formulation. To address this issue a coefficient c_r is added in the definition of the turbulent time scale, which is defined as internal consistency constraint (ICC).

$$T_m = \frac{r}{\psi'(r)} \frac{k_m + c_r k_r}{C_\mu k_m \omega_m^*}, \qquad where \quad c_r = \begin{cases} 0 \text{ if } r = 1, \\ 1 \text{ if } r < 1. \end{cases} \tag{2.28}$$

This helps in better recovery of the solution of the RANS model. But it does not improve the conflicting results at the transition and LES region. These issues are addressed by further controlling the RANS to LES transition in the near-wall region.

2.3.6 Shielding of the near-wall region

The behaviour of hybrid RANS/LES approaches in the near-wall region is a major problem. The near-wall region must be treated in RANS mode to avoid the very high cost of LES. The concept of shielding was first proposed for the DDES approach by Spalart et al. (2006) to avoid the model to switch to LES in the near-wall region. This idea was further developed by Duffal et al. (2022) in the framework of HTLES model.

In wall-bounded flows, the estimation of the energy ratio based on Kolmogorov assumption can be unrealistic because of non relevance of Kolmogorov assumption in the viscous wall region. To counter this issue, an upper bound was introduced by (Tran et al., 2012) to the definition of the energy ratio (2.29).

$$r = \min\left[1, r_K\right] \tag{2.29}$$

The objective of imposing RANS to LES transition is to significantly reduce the number of cells in the near-wall region. In the log layer Pope et al. (2000) showed that $C_\mu^{3/4} k^{3/2} \varepsilon = C_\kappa d_w$ is satisfied, where C_κ is the Von-Karman constant and d_w is the wall distance. Along with that if assumed that the time step τ is smaller than Δ / U_s everywhere in the computational domain, the cutoff frequency is fixed by mesh size Δ only. Hence, the energy ratio can be evaluated as:

$$r_K = \frac{C_\mu^{1/2}}{\beta_0 \pi^{2/3} C_\kappa^{2/3}} \left(\frac{\Delta}{d_w}\right)^{2/3} \tag{2.30}$$

which is only dependent on the mesh size and independent of the Reynolds number. This is in line with the hybridization strategy of forcing the RANS mode in viscous and buffer sub-layers, transitioning in the log layer and the rest in LES mode. But using the present formulation for r as Eq. (2.29), the transition to LES occurs too early, which leads to modeled stress depletion (MSD) and grid induced separation as shown by (Spalart et al., 2006).

Since, it is important for the model not to switch to LES when the mesh is ambiguous, the shielding must be independent of the grid. Hence a grid-independent shielding of the viscous wall region depending on the Kolmogorov length scale is defined (ξ_K). Which means a global shielding function irrespective of the closure.

$$f_s(\xi_K) = 1 - \tanh\left[\xi_K^{p_1}\right], \qquad \text{where} \quad \xi_K = C_1 \frac{\left(\nu^3/\varepsilon\right)^{1/4}}{d_w} \tag{2.31}$$

where C_1 and p_1 are the coefficients. Their values are 45 and 8, respectively. This parameter activates the shielding up to $y^+ \simeq 100$. The purpose of the hyperbolic tangent function is to

provide a continuous transition from 0 to 1.The comparison based on the turbulent length scale and wall distance ensure the grid independency. Because of this grid independent shielding, the RANS behaviour is correctly recovered in the near-wall region but in the LES region because of mesh being not fine enough for LES an over-estimation is observed which is interrelated to the log-layer mismatch (Nikitin et al., 2000). Hence, a grid dependent shielding to address the log-layer mismatch (ξ_D) is introduced.

In the present model, as the energy ratio is dependent on the grid step, it is relevant to enforce the RANS mode based on the maximum dimension of the cell $\Delta_{\max} = \max[\Delta_x, \Delta_y, \Delta_z]$ in any directions. It is specified by the works in WMLES (Larsson et al., 2016) and IDDES (Han et al., 2020) that the integral length scale L must be at least two times the mesh size (Nyquist-Shannon theorem): $L \geq 2\Delta_{\max}$, in order to properly resolve the large-scale fluctuations to be treated in LES mode in the near-wall region. Pope et al. (2000) showed that in the log layer L can be explicitly related to the wall distance: $L = k^{3/2}/\varepsilon = C_\kappa / C_\mu^{3/4} d_w$. Hence, to avoid log-layer mismatch a shielding function depending on $\Delta_{\max}$ and d_w:

$$f_s(\xi_D) = 1 - \tanh\left[\xi_D^{p_2}\right], \qquad \text{where} \quad \xi_D = C_2 \frac{\Delta_{\max}}{d_w} \tag{2.32}$$

where C_2 and p_2 are the coefficients. Their values are 1.2 and 6, respectively. Hence, the energy ratio is defined as follows:

$$\begin{aligned} r &= (1 - f_s) \times 1 + f_s \times \min[1, r_K] \\ \text{where } f_s &= 1 - \tanh\left[\max\left[\xi_K^{p_1}, \xi_D^{p_2}\right]\right] \end{aligned} \tag{2.33}$$

Furthermore, In order to provide a continuous correction of the time scale T_m, the internal consistency constraint is modified:

$$c_r = \begin{cases} 0 \text{ if } r = 1, \\ f_s \text{ if } r < 1. \end{cases} \tag{2.34}$$

The introduction of these two shielding functions in association with the ICC is critical, in order to control the RANS to LES transition or vice-versa.

2.4 Applications

In this section, the test cases studied during the thesis (flow in a channel, flow over periodic hills, and flow over suddenly expanding channel) and the numerical methodology used is explained. This section also shows the performance of the state-of-the-art HTLES (Duffal et al., 2022) in comparison with reference data (DNS, fine LES). Note that these HTLES solutions will serve as the reference in other chapters. These comparisons highlight the limitations of HTLES in spatially-developing flows, which motivates the work done in the thesis.

The calculations are performed using code_Saturne (Archambeau et al., 2004), the open-source general purpose CFD software developed by Electricité de France (EDF) and distributed under Gnu GPL license (`https://www.code-saturne.org`). It is based on a co-located finite-volume approach that accepts meshes with any type of cell and any type of grid structure.

For hybrid calculations, the Crank-Nicolson scheme is used in time. In order to avoid the pseudo-relaminarization of the flow, the use of a second-order scheme in time is essential for unsteady calculations.

The velocity-pressure system is solved using a SIMPLEC scheme. It is important to pay attention to the convection scheme used for the resolved velocity because it is crucial in LES mode that a centered scheme is used but it can cause numerical instabilities (not refined enough mesh or too high Péclet number leads to significant numerical oscillations) in RANS mode. Hence, a hybrid of second-order upwind scheme (SOLU) and centered difference scheme (CDS) is utilized, using c_r from Eq. (2.34) as a blending co-efficient to be in line with the RANS-LES transition, such that

$$\phi_{HYB} = (1 - c_r)\,\phi_{SOLU} + c_r \phi_{CDS} \quad \text{with} \quad c_r = \begin{cases} 0 \text{ if } r = 1 \quad \text{(RANS)} \\ 1 \text{ if } r < 1 \quad \text{(LES)}. \end{cases} \tag{2.35}$$

To the other less sensitive terms of the transport equations of turbulent quantities, a first order upwind scheme is applied to promote the numerical stability. To estimate the statistically averaged quantities an exponentially weighted average is used (Pruett et al., 2003) (Note that this is to estimate the statistical quantities used in the model, such as k_r, k_m, U, τ_{ij}, etc.). To ensure the convergence of the statistical estimates, the time filter width corresponds to the several tens of flow through times. For more detailed comparison of Hybrid scheme and development of HTLES refer to the thesis of Duffal (2020). For RANS calculations, the results are saved when statistical calculations are converged. Whereas for unsteady LES and hybrid calculations, the calculations run over several tens of flow through time to pass the transient period as the turbulent fluctuations may take some time to develop after an initialization on an statistical field, then the instantaneous fields are again averaged over several flow through times. At the end of the calculations, these time averaged fields are spatially averaged in the homogeneity direction to determine the statistical means of the variables.

2.4.1 Flow in a periodic channel

2.4.1.1 Description of the test case

The study of turbulent flow in an infinite channel serves as a support for the analysis of the characteristics of turbulent boundary layers. This test case consists of two infinite plates parallel to each other with the distance of $2h$ between them where a fluid flows. The mean flow is oriented in the x-direction, with y being the wall normal direction, and z is the spanwise direction. In a steady state, statistical properties are independent of the x and z coordinates (directions of statistical homogeneity), and of the time t because the velocity field is statistically 1D and stationary.

In order to obtain a fully developed flow in a minimal domain, the flow is computed periodic, i.e., all the variables in the inlet plane are imposed equal to the variables in the outlet plane. Because of the presence of a mean pressure gradient, the pressure at the outlet cannot be equal to the pressure at the inlet. To circumvent this issue, an instantaneous pressure to which inlet-outlet periodicity can be applied, a modified pressure $p^\star$ must be defined by subtracting the linear variation of the mean pressure.

If U^* and p^* denotes the instantaneous velocity in x-direction and pressure, and $U = \overline{U^*}$ and $P = \overline{p^*}$ the Reynolds-averaged mean velocity and pressure, the mean momentum balance in a control volume of $[x, x + \mathrm{d}x] \times [0, 2h] \times [z, z + \mathrm{d}z]$ can be written as:

$$P(x)2h\mathrm{d}z - P(x + \mathrm{d}x)2h\mathrm{d}z = 2\tau_w \mathrm{d}x\mathrm{d}z, \tag{2.36}$$

such that

$$\frac{\partial P}{\partial x} = -\frac{\tau_w}{h}. \tag{2.37}$$

which leads to the modified pressure

$$p^\star = p^* - \frac{\partial P}{\partial x}x = p^* + \beta x, \quad \text{with} \quad \beta = \frac{\tau_w}{h}. \tag{2.38}$$

with Eq. (2.38), $p^\star$ is periodic and β is added as a source term. In order to perform computations that are not linked to a particular fluid and a particular channel dimension, it is usual to work in non-dimensional variables. DNS of a turbulent channel flow has always been performed in non-dimensional variables (Kim et al., 1987; Moser et al., 1999; Hoyas et al., 2006; Lee et al., 2015) with the main idea of computing the flow at a given frictional Reynolds number $Re_\tau = hu_\tau/\nu$, where $\nu = \mu/\rho$ is the kinematic viscosity of the fluid and u_τ the frictional velocity, defined by:

$$\tau_w = \rho u_\tau^2, \quad \text{with} \quad \tau_w = \mu \frac{\partial U}{\partial y}\bigg|_{\text{wall}}. \tag{2.39}$$

The particular system of units:

$$L = h;\ T = \frac{h}{u_\tau};\ M = \rho h^3 \tag{2.40}$$

is chosen, which yields

$$\begin{gathered} \widetilde{y} = \frac{y}{h};\ \widetilde{U} = \frac{U}{u_\tau};\ \widetilde{t} = \frac{tu_\tau}{h};\ \widetilde{\rho} = 1;\ \widetilde{k} = \frac{k}{u_\tau^2}; \\ \widetilde{p^\star} = \frac{p^\star}{\rho u_\tau^2};\ \widetilde{\beta} = \frac{\beta}{\rho u_\tau^2 h^{-1}} = 1;\ \widetilde{\nu} = \frac{\nu}{hu_\tau} = \frac{1}{Re_\tau};\ u_\tau = 1. \end{gathered} \tag{2.41}$$

2.4.1.2 Numerical parameters

The numerical test case is implemented using the imposed friction Reynolds number approach, same as the reference DNS case (Moser et al., 1999). The motion, imposed by the longitudinal pressure gradient, is imposed by implementing the source term β in the Navier-Stokes equations. The channel extension is L_x in x-direction and L_z in z-direction chosen large enough to avoid the auto-correlations of the velocity fields. The size of the computational domain corresponds to $L_x \times L_y \times L_z = 2\pi h \times 2h \times \pi h$. Smooth walls are considered in the plane normal to the y-direction on which no slip boundary conditions are imposed.

Model	Re_τ	$\Delta_{y_w^+}$	L_x	L_y	L_z	N_x	N_y	N_z	Δ_{x^+}	Δ_{z^+}	$\Delta_{y_c^+}$
HTLES	590	1	$2\pi h$	2h	πh	64	96	64	60	30	30
DNS	590		$2\pi h$	2h	πh	384	257	384	9.7	4.8	7.2

Table 2.1 – Numerical settings of the grid for the channel flow.

The characteristics of the mesh used is summarized in Table 2.1. The simple geometrical configuration makes it possible to produce a structured orthogonal mesh shown in Fig. 2.4. The parameters $(\Delta_x,\ \Delta_y,\ \Delta_z)$ represent the mesh sizes in the longitudinal (x), wall normal (y) and transverse (z) directions, whereas $(N_x,\ N_y,\ N_z)$ represents the number of cells in each direction. The expansion of the mesh in the wall normal direction is carried out by implementing the law:

$$y_i = 1 + \frac{\tanh[\gamma(2i/N_y - 1)]}{\tanh[\gamma]}, \tag{2.42}$$

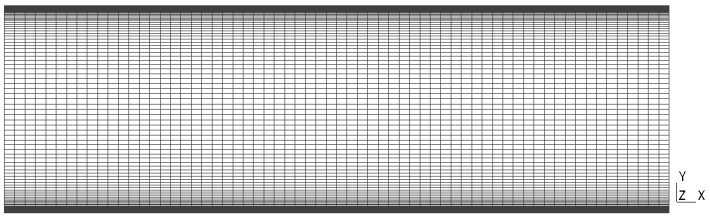

Figure 2.4 – Representation of the mesh for the periodic channel configuration.

with $\gamma = 2.41$. To keep the courant number below 1 throughout the domain a small enough time step is chosen ($dt = 0.001h/u_\tau$). The statistically averaged quantities involved in the model are estimated during the computation by using the exponential temporal filter (Pruett et al., 2003) with the filter size of Δ_T. The size of the filter Δ_T is chosen to be several flow through times. Exponentially filtered quantities are computed as:

$$\frac{\partial}{\partial t}\overline{\phi}(t,\Delta_T) = \frac{\overline{\phi}(t) - \overline{\phi}(t,\Delta_T)}{\Delta_T} \quad \Longrightarrow \quad \overline{\phi}^{n+1} = \overline{\phi}^{n} + \frac{dt}{\Delta_T}\left(\phi^{n+1} - \overline{\phi}^{n}\right). \tag{2.43}$$

2.4.1.3 Results

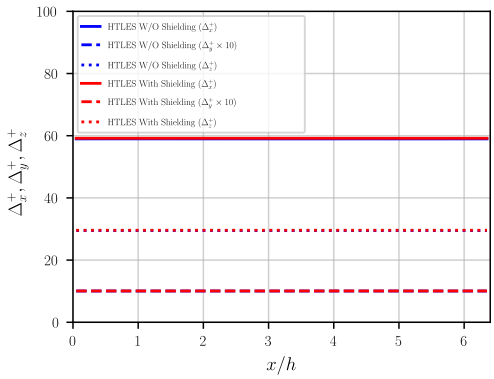

Figure 2.5 – Profiles for dimensionless grid spacing at $Re_\tau = 590$.

Fig. 2.5 describes the dimensionless grid spacing, where Δ_{y^+} is multiplied by the factor of 10 for the purpose of better visualization. The meshing strategy is of particular importance in hybrid approaches. The mesh sizes $\Delta_x = 0.1h$ and $\Delta_z = 0.05h$ are set independently of the Reynolds number. In the direction normal to the wall, $\Delta_{y_w^+} = 1$ at the wall, and increases up to $\Delta_{y_c} = 0.05h$ at the center of the channel. This is in line with the expectations of the hybrid RANS-LES approaches, which are to use the RANS-type meshes in the near wall region, and for the rest:

→ meshes sizes as a function of the Reynolds number in the wall normal direction y, in competence with the near-wall RANS model,

→ meshes sizes as a function of the characteristic size of the geometry (here h) in the tangential directions (x and z), independent of the Reynolds number.

The use of these criteria for the mesh is made possible due to the introduction of the shielding function based on the maximum dimension of the cell (refer to Eq. (2.32)) and a shielding function based on the Kolmogorov length scale (refer to Eq. (2.31)), which make it possible to control the RANS-LES transition. The influence of introducing these functions can be clearly observed in Fig. 2.6, which is the visualization of the modeled-to-total energy ratio. When these shielding functions are not used, the model transitions

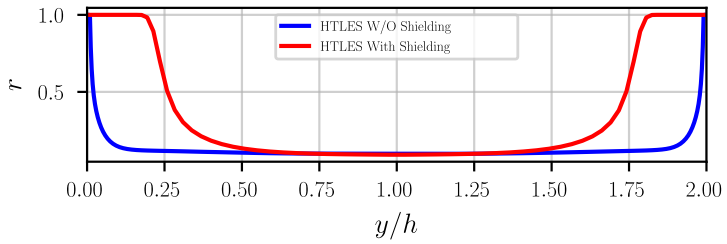

Figure 2.6 – Energy ratio r.

to LES very close to the wall, where the resolution of the mesh is not fine enough for the structures to be solved in LES mode. On the contrary, the introduction of these functions unable us to control the transition effectively.

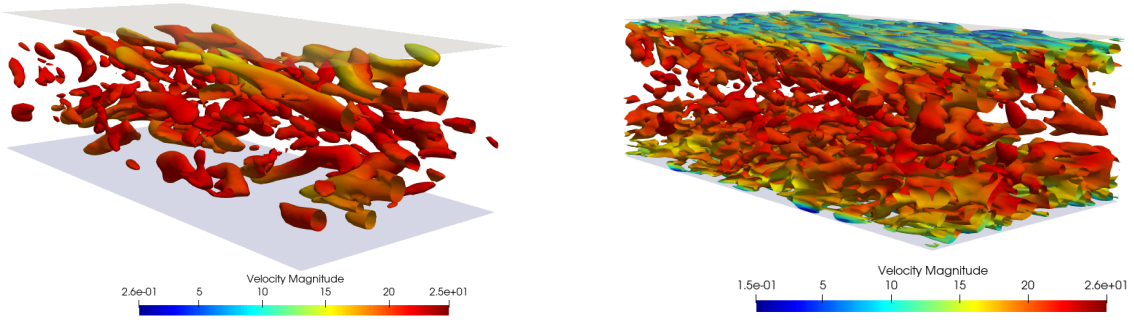

(a) (b)

Figure 2.7 – Iso-surface of the Q-criterion, $Q = 35u_\tau^2/h^2$, coloured by the velocity magnitude for the channel flow at $Re_\tau = 590$ for (a) Model with the shielding functions (b) Model without the shielding functions.

Q-criterion iso-surfaces in Fig. 2.7(a) at $Re_\tau = 590$ shows that the large-scale turbulent structures are explicitly resolved in the central region of the flow. With the activation of LES mode in this region, it is possible to preserve the resolved turbulent fluctuations. On the other hand, the resolved turbulent fluctuations are not visible in the near wall region because of the fact that it is forced to be treated in RANS mode with the help of the shielding functions. On the contrary, in Fig. 2.7(b) when the shielding functions are turned off, we can see the resolved structures in the near wall region.

	Without shielding	With shielding	DNS
C_f	0.00526	0.00551	0.00575

Table 2.2 – Value of skin friction coefficient C_f at the lower wall for different configurations studied.

Table 2.2 shows the values of the friction co-efficient at the bottom wall for both the configurations that has been shown and discussed till now in the chapter, which shows that the results are better with shielding activated than without shielding.

Fig. 2.8 shows the comparison of the mean velocity profiles produced by the HTLES with the reference DNS. Thanks to the ICC, the profiles produced by the HTLES recovers the behaviour of the RANS closure model very close to the wall. In the LES zone, when the shielding functions are used, an appropriate transition with respect to the mesh refinement is imposed to capture the turbulent structures ($y > 0.8\Delta_{\max}$). Although there is a slight overestimation in the transition zone, the results at the center of the channel are in close

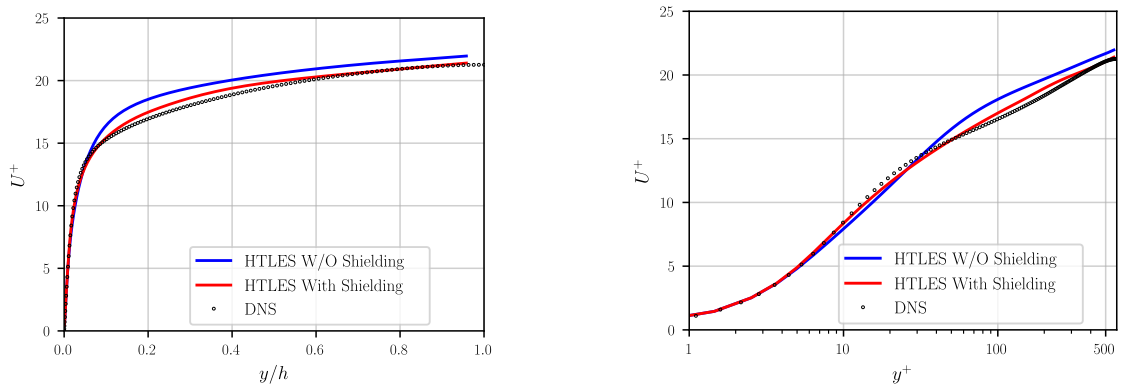

(a) (b)

Figure 2.8 – Mean velocity profiles (a) linear scale (b) semi-log scale.

agreement with the reference DNS. On the other hand, when the shielding functions are not used, we can observe the log-layer mismatch, i.e., an over-estimated velocity profile in the log layer.

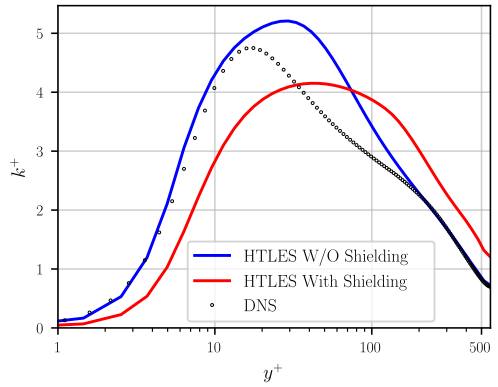

Figure 2.9 – Total turbulent kinetic energy profile.

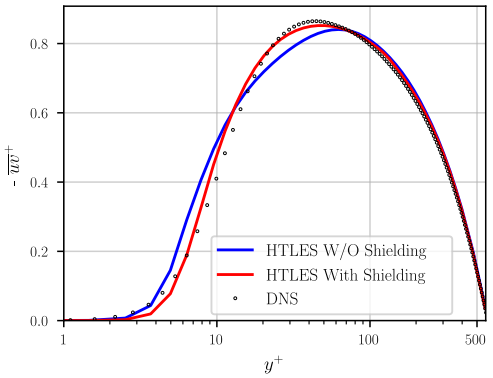

Figure 2.10 – Total shear stress profile.

In Fig. 2.9, the turbulent kinetic energy k is not very well reproduced in the RANS zone which is characteristic of the $k-\omega$ SST model. We also observe a small overestimation in the LES zone. When the shielding functions are turned off, the turbulent kinetic energy is in close agreement with the reference DNS, because without shielding, LES is activated almost down to the wall (refer to Fig. 2.6). In LES mode, k is better predicted than in RANS mode, which is evident from Fig. 2.9. However, near wall grid is not sufficiently fine for a good LES, which leads to a wrong estimation of the shear stress (refer to Fig. 2.10), which in turn leads to wrong velocity profile (refer to Fig. 2.8). This shows why the shielding functions are introduced.

2.4.2 Flow over periodic hills

2.4.2.1 Presentation of the test case

For hybrid approaches, a periodic arrangement of 2D hills in a plane channel constitutes a standard benchmark case. Because a large-scale time dependent phenomenon governs the characteristics of the flow, including moving separation and reattachment points, and

large-scale structures are generated in the detached shear layers above the recirculation region, such that the statistics of this flow are difficult to be satisfactorily reproduced by RANS models.

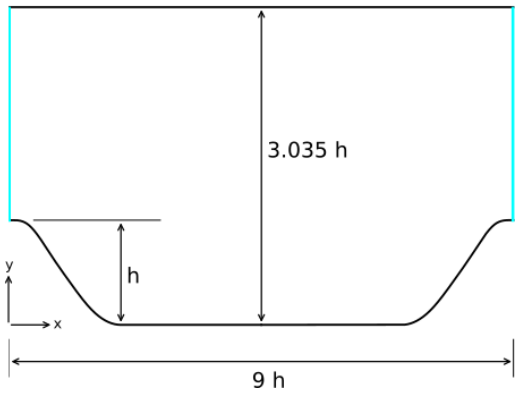

Figure 2.11 – Geometrical representation of a periodic hill case.

As shown in Fig. 2.11, the test case consists of an infinite channel whose lower wall is composed of a succession of hills at regular intervals. Following the numerical studies with LES model carried out by several authors, the test case was studied experimentally by Rapp and Manhart (Rapp et al., 2007; Rapp et al., 2011) providing the reference data for the validation of the turbulence models.

The turbulent flow is statistically 2D and stationary, driven by a longitudinal pressure gradient $\partial P/\partial x$. The flow is oriented in the x-direction, with y being the wall normal direction (with respect to the upper wall) and z the direction of homogeneity. The spacing between the two walls is $L_y = 3.035h$, with h being the height of the hill. The hills are spaced by $L_x = 9h$, with $\approx 1.93h$ being the extension upstream and downstream of the hill. The flow is characterized by the bulk Reynolds number, $Re_b = U_b h/\nu = 10595$, where U_b is the bulk velocity measured at the top of the hill here:

$$Re_b = \frac{U_b h}{\nu}, \quad \text{with} \quad U_b = \frac{1}{2.035h}\int_h^{3.035h} U(y)dy \tag{2.44}$$

The statistical flow is described by the velocities $U = \overline{U*}$, $V = \overline{V*}$ and $W = \overline{W*} = 0$. In the LES computations that has been carried out till now, a boundary layer separation is observed at the top of the hill. The instantaneous position of this separation varies as a function of time, with $x_s/h \in [0, 0.5]$ (Mellen et al., 2000; Temmerman et al., 2003; Breuer et al., 2005; Fröhlich et al., 2005). The flow reattaches in the center of the two hills, with an average of $x_r/h = 4.64 \pm 0.08$ according to the LES data, whereas according to the experimental data $x_r/h = 4.24$ (Rapp et al., 2011). As mentioned earlier the flow over the periodic hills is characterized by unsteady and large-scale phenomena, the RANS statistical description encounters difficulties in dealing with the test case and fails to reproduce the length of recirculation zone.

Also, the classic near-wall models, developed for attached flows, do not allow to describe the near-wall mechanisms in a satisfactory manner. Therefore, this test case is a reference for developing wall improved models. LES models are able to describe the flow on periodic hills satisfactory, but at a really high computational cost.

2.4.2.2 Numerical parameters

The flow is simulated by imposing the mass flow rate as opposed to the channel case where the flow is simulated by imposing the friction. A source term is adjusted at each time step,

corresponding to the longitudinal average pressure gradient $\partial P/\partial x$, in order to keep the constant mass flow rate.

$$\frac{1}{\rho}\left(\frac{\partial P}{\partial x}\right)^{n+1} = \frac{1}{\rho}\left(\frac{\partial P}{\partial x}\right)^{n} + \beta\frac{U_b - 2U_s^n + U_s^{n-1}}{2dt} \tag{2.45}$$

where dt is the time step, $\beta = 0.1$ a relaxation coefficient, U_b is the imposed bulk velocity and U_s is the bulk velocity estimated during the computation. Periodic boundary conditions are used in the direction of the flow, to simulate the infinite extension of the channel with the periodic hills. Periodicity is also considered in the spanwise direction, with $L_z = 4.5h$, following the recommendations of Mellen et al. (2000). The walls are considered smooth.

The particular system of units for the non-dimensionalization of the variables is:

$$L = h;\ T = \frac{h}{U_b};\ M = \rho h^3 \tag{2.46}$$

which yields

$$\begin{gathered}\widetilde{U} = \frac{U}{U_b};\ \widetilde{t} = \frac{tU_b}{h};\ \widetilde{\rho} = 1;\ \widetilde{k} = \frac{k}{U_b^2};\\ \widetilde{p} = \frac{p}{\rho U_b^2};\ \widetilde{\nu} = \frac{1}{Re_b};\ U_b = 1.\end{gathered} \tag{2.47}$$

Re_b	Grid	$\Delta_{y_w^+}$	Δ_x/h	Δ_z/h	N_x	N_y	N_z	No. of cells
10595	M1	1	0.1125	0.1125	80	80	40	0.256 M
	M2	1	0.075	0.075	120	120	60	0.864 M

Table 2.3 – Numerical settings for the grids for the Hill flow.

The main characteristics of the meshes are described in the Table 2.3. As seen in Fig. 2.12, very fine refinement is obtained in the planes parallel to the walls, with $\Delta_{\max} = \Delta_x = \Delta_z$. Moreover, outside of the boundary layer, the cells are globally isotropic.

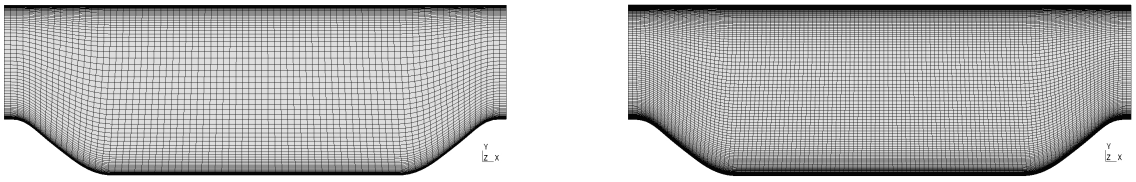

(a) Grid M1 (b) Grid M2

Figure 2.12 – Representation of the different mesh configurations for the periodic hill case.

The computational domain is given as $L_x \times L_y \times L_z = 9h \times 3.035h \times 4.5h$. The periodic hill flow is studied using a coarse mesh M1 ($N_x \times N_y \times N_z = 80 \times 80 \times 40$) and a more than 3 times finer mesh M2 ($N_x \times N_y \times N_z = 120 \times 120 \times 60$) both satisfying $\Delta_{y^+} \simeq 1$ at the wall.

2.4.2.3 Results

Fig. 2.13 describes the dimensionless grid spacing, where Δ_{y^+} is multiplied by the factor of 10 for the purpose of better visualization. The time step is estimated at $dt = 0.005h/U_b$,

so that the courant number is less than unity. To estimate the statistical means of the turbulent variables during the computation, the exponential filter described in the previous section is used, the filter size Δ_T corresponds to a several flow through times to obtain a well-converged estimates. As a reference, the highly resolved LES produced by Breuer et al. (2006) and Breuer et al. (2009) with 13.1 million cells and the experimental study by (Rapp et al., 2007) are considered.

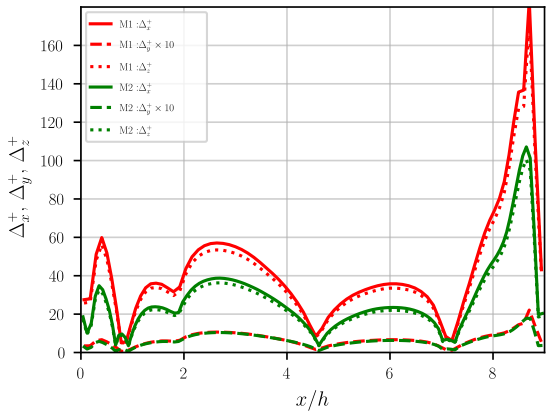

Figure 2.13 – Dimensionless grid spacing on the lower wall of the periodic-hill.

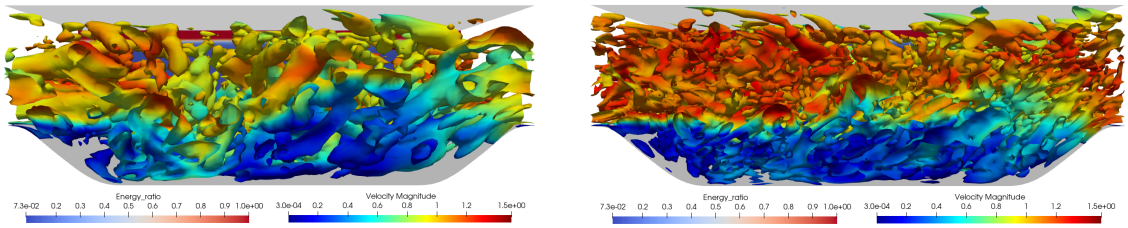

Figure 2.14 – Isocontours $Q = 0.2U_b^2/h^2$ colored with the velocity magnitude and in the background, modeled-to-total turbulent energy ratio r, indicating the regions solved in RANS ($r = 1$) and in LES ($r < 1$). Left: Case solved with the M1 grid; Right: Case solved with the M2 grid.

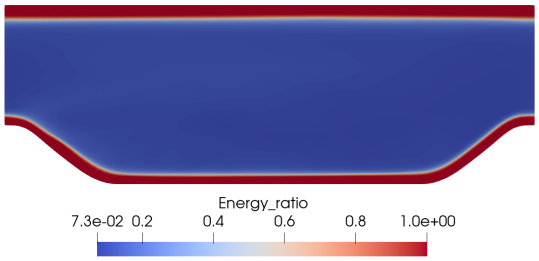

Figure 2.15 – Modeled-to-total turbulent energy ratio r, indicating the regions solved in RANS ($r = 1$) and in LES ($r < 1$).

The Q-criterion iso-surfaces in Fig. 2.14 show that the turbulent fluctuations are resolved in the LES zone. The case resolved with the finer grid allows to describe the structures more finely. We observe that the estimated energy ratio r (refer to Eq. (2.33)) is indeed equal to unity in the near wall region (RANS zone), before decreasing to the values corresponding to the LES values in the center, as expected (refer to Fig. 2.15).

As can be verified from Fig. 2.16, the streamlines are in very good agreement with each other. Even though grid M1 is considerably coarser than grid M2, the overall results are well reproduced.

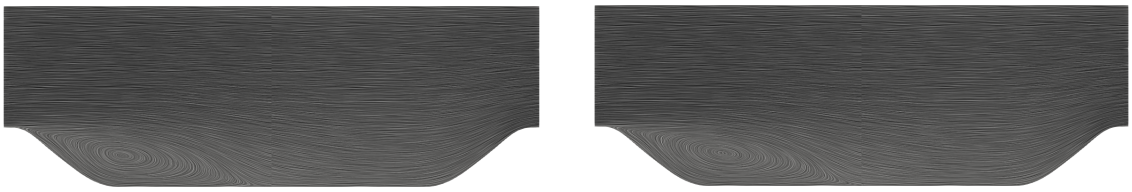

Figure 2.16 – Averaged streamlines obtained with HTLES. Left: M1 grid, Right: M2 grid.

The distribution of skin friction on the periodic-hill lower wall is an interesting way to highlight the behavior of HTLES and LES models. From Fig. 2.17(a), it is quite evident that the $k-\omega$ SST HTLES model reproduces the results similar to the reference data, using both the grids. With both the meshes the results are in close agreement in identifying the main recirculation zone with accurate predictions of separation and reattachment points. Also $C_f \simeq 0$ is identified correctly at the top of the hill ($x/h = 0$) and upstream of the hill ($x/h \simeq 7$). Globally the results are quite satisfactory, even though with the coarser grid M1 compared to the M2 grid the separation point is not as accurately located due to the lack of precision but it does not affect the predictions of the reattachment (refer to Table 2.4).

	LES(Breuer et al., 2005)	HTLES-M1	HTLES-M2
Separation point, x_s/h	0.19	0.18	0.21
Reattachment point, x_r/h	4.69	4.69	4.69

Table 2.4 – Predictions of the separation and reattachment positions for flow over periodic hills at $Re_b = 10595$ with different models and meshes.

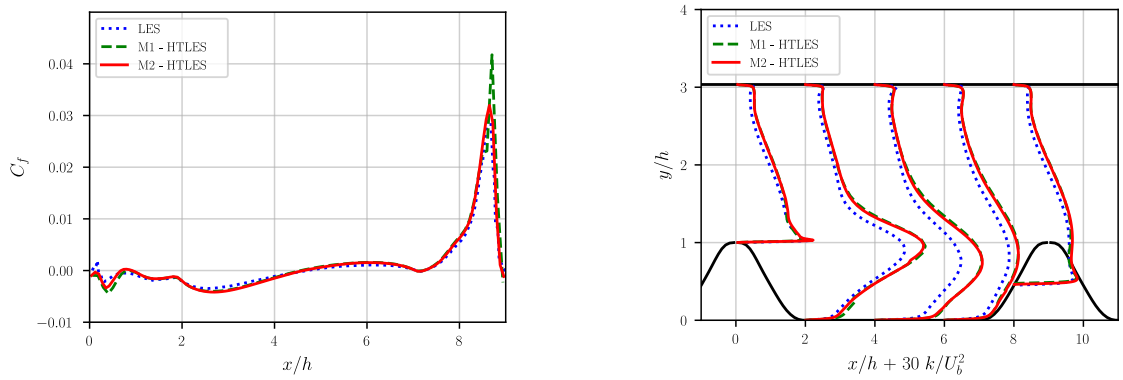

(a) (b)

Figure 2.17 – Profiles for (a) Skin friction coefficient on the lower wall and (b) total turbulent kinetic energy at $Re_b = 10595$.

We now focus on profiles extracted at different streamwise locations ($x/h = 0$, 2, 4, 6 and 8). Regarding mean velocity and total shear stress profiles, the reference data are well reproduced for both grids as shown in Figs. 2.19 and 2.21(b), respectively. It is fundamental to have some minor differences in the profiles depending on the resolution of the grid, but they remain in close accord with each other. Fig. 2.20(a), (b) and Fig. 2.21(a) focus on the total Reynolds stresses. It is interesting to note that, even when observing the overestimation of the total turbulent kinetic energy Fig. 2.17(b), the shapes of the profiles

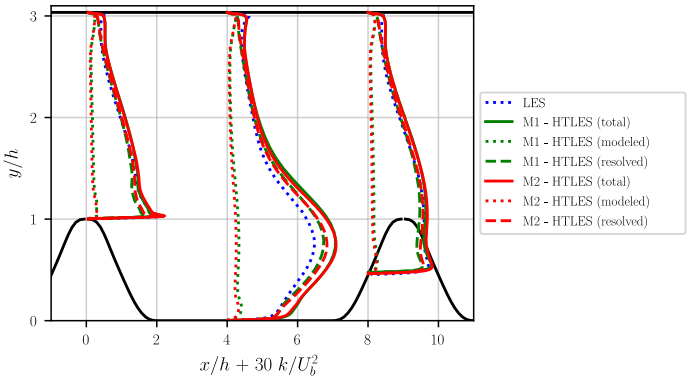

Figure 2.18 – Breakdown of total energy into modeled and resolved components.

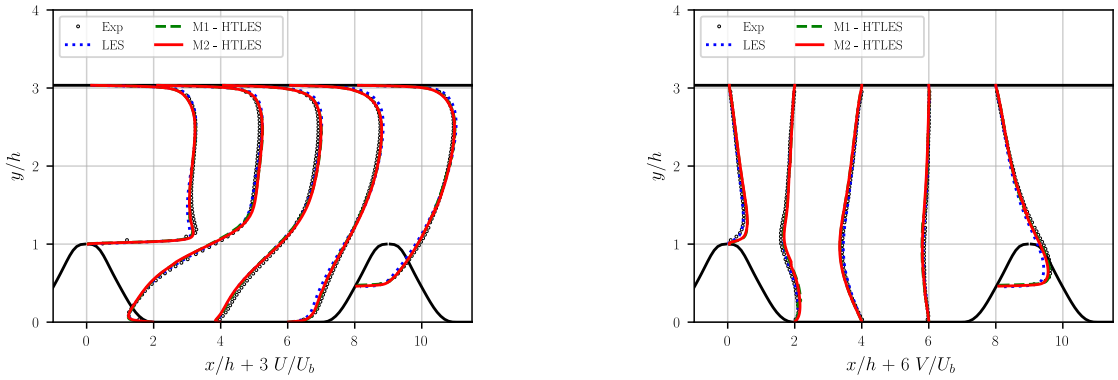

(a) (b)

Figure 2.19 – Velocity profiles: (a) Streamwise velocity profiles and (b) normal velocity profiles at $Re_b = 10595$.

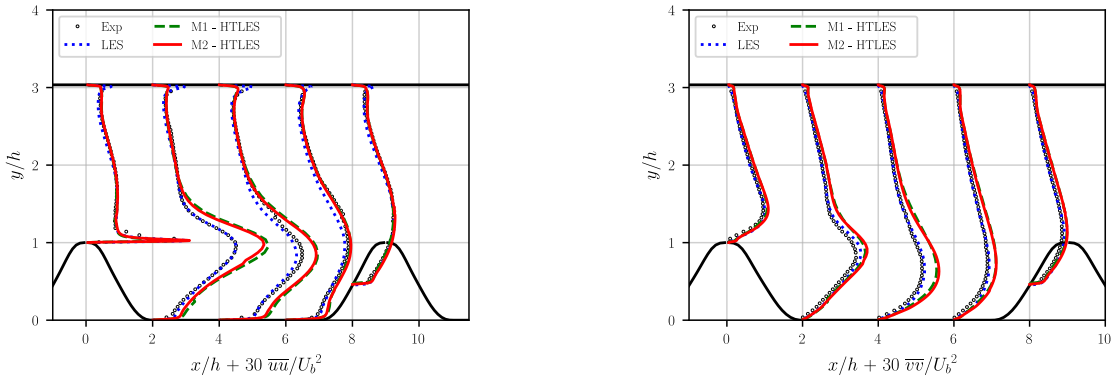

(a) (b)

Figure 2.20 – Profiles for (a) Streamwise and (b) normal components of the Reynolds stresses at $Re_b = 10595$.

are qualitatively reproduced in the detached shear layer and at the approach of the walls. Of course, there are some discrepancies between the two grids, but the agreement between them is quite impeccable considering the large difference in the resolution. Fig. 2.18 shows the breakdown of the total energy into modeled and resolved components for both the meshes. This highlights the difference in resolution of the components while the total

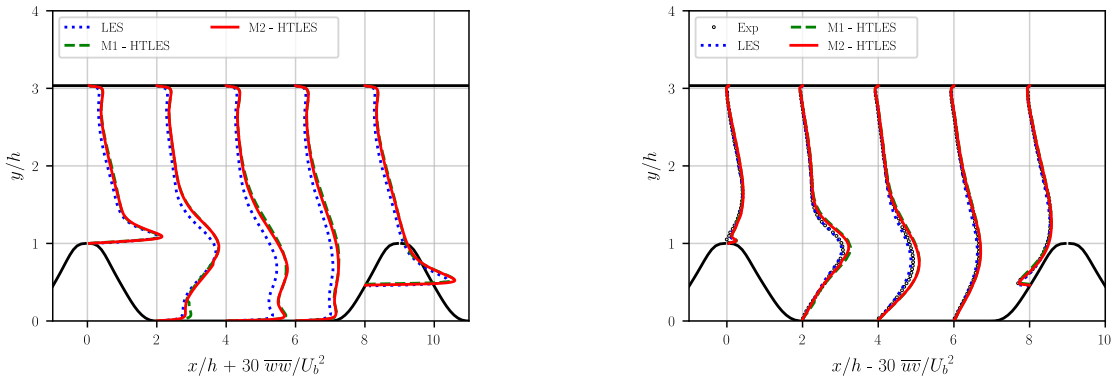

(a) (b)

Figure 2.21 – Profiles for (a) spanwise component of the Reynolds stress and (b) shear stress at $Re_b = 10595$.

(modeled + resolved) is virtually constant. Moreover, note that averaged HTLES results approach reference averaged LES results when the grid is refined, although RANS is still used to solve the near-wall region due to shielding functions.

The analysis of the total turbulent kinetic energy profiles k in Fig. 2.17(b) leads to the same conclusion as before that the overall shape of the profiles are reproduced accurately, but an over-estimation of the energy is observed in the detached shear layer. The modeled energy remain in very close proximity for both the meshes. The over-estimation of the total turbulent energy is mainly related to the over-estimation of the resolved energy in the shear layer, whose profiles are globally in agreement with the references.

2.4.3 Flow over spatially developing hills

Till now we have talked about implementing the HTLES methodology to periodic cases only. This tends to give the validation to the model by addressing the problem of lowering the computing cost by reducing the resolution and reproducing the reference results. But in industrial applications, imposing periodic boundary condition is usually not possible or in many cases reducing the computation to just the area of interest may not be possible. For those scenarios it is then necessary to consider a much larger computational domain to replicate the situation. It is important to analyze the behaviour of this model in such scenarios.

This section tries to address a more realistic scenario. To do so, instead of considering the periodicity in the streamwise direction, we now have a very long channel with periodic hills such that the computing domain is now $L_x \times L_y \times L_z = 45h \times 3.035h \times 4.5h$ i.e. 5 sub-domains or 6 hills in total with each sub-domain's dimensions being $L_x \times L_y \times L_z = 9h \times 3.035h \times 4.5h$. The periodicity is considered only in the direction of homogeneity (z). Note that here, the term sub-domain is used for convenience in describing a region between two successive hills, but there is only one computational domain. To avoid the problems associated with connecting the areas that are refined differently by unstructured or non-conforming meshes, all the sub-domains have the same mesh which is fine enough for the LES mode of HTLES.

As illustrated in Fig. 2.22, out of the 5 sub-domains, the first and the last sub-domains are treated purely in RANS mode. At the end of the first sub-domain, i.e., from the top of the second hill, there is a transition region extending from $x/h = 0$ to $x/h = 2$, to have a smooth transition from RANS to LES mode. The transition with similar length is

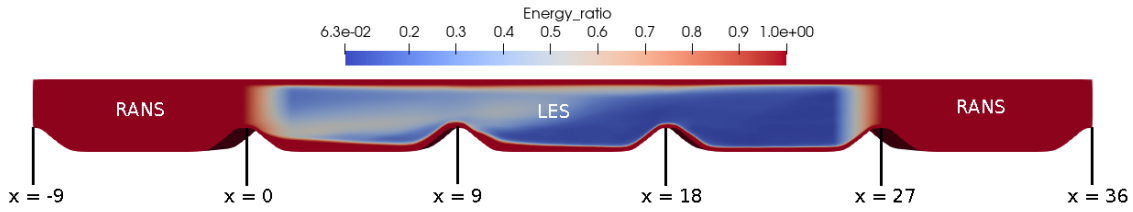

Figure 2.22 – Representation of the different sub-domains, colored with the energy ratio r.

also imposed upstream of the 5th hill (end of the 4th sub-domain) to facilitate the smooth transition between LES and RANS from $x/h = 25$ to $x/h = 27$. The transition between the modes are imposed by prescribing a spatial evolution of the resolution parameter r in the model. In the LES zone, r is still given by the Eq. (2.33). The exact same numerical settings have been used here to simulate the flow as mentioned in Table 2.3. As periodicity is not used in the streamwise direction (x), profiles extracted from periodic RANS computations act as the inlet boundary condition. Periodic HTLES computations, validated against the reference LES computations act as reference in this case.

At the input (first sub-domain) and output (fifth sub-domain), the RANS mode is activated by imposing the energy ratio $r = 1$ in the model. A transition from RANS-to-LES and LES-to-RANS is imposed gradually by enforcing a modified energy ratio r_{mod}.

$$r_{\text{mod}} = (1 - f)r + f \quad \text{with} \quad f\left(\frac{x}{h}\right) = \begin{cases} 1 - \dfrac{x}{2h} & \text{if } \dfrac{x}{h} \in [0, 2] \\ \dfrac{1}{2}\left(\dfrac{x}{h} - 25\right) & \text{if } \dfrac{x}{h} \in [25, 27] \end{cases} \tag{2.48}$$

From the isocontours $Q = 0.2U_b^2/h^2$ plotted in Fig. 2.23, compared with Fig. 2.14, it can be seen that the spatial development of the resolved structures is very slow when the periodic boundary conditions are not provided.

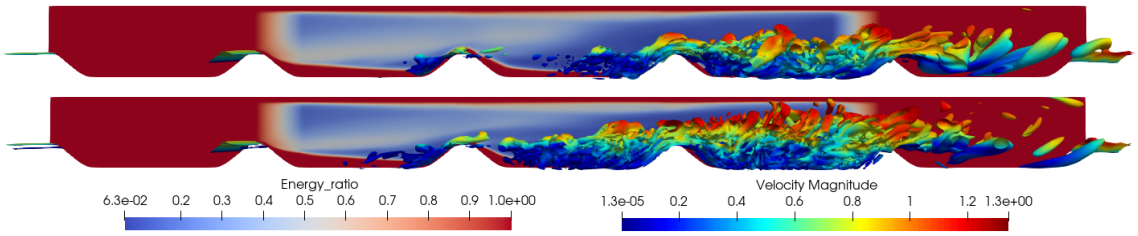

Figure 2.23 – Isocontours $Q = 0.2U_b^2/h^2$ colored with velocity magnitude and energy ratio r in the background. Top: grid M1, Bottom: grid M2.

From the profiles of skin friction coefficient plotted at the bottom wall for both the meshes in Figs. 2.24 and 2.25, it is evident that when we are in the RANS region (first sub-domain) the model replicates the exact results as the reference data (periodic RANS), which confirms that the imposed fields are corresponding well to that of the reference fields. But when we transition to the LES region, in particular in the second and the third sub-domains, the prediction is very degraded compared to the reference dataset (periodic HTLES). The reason behind the degradation is the lack of resolved stresses in the LES mode of the model. HTLES model is developed such a way that when transitioning from RANS mode to LES mode, it reduces the modeled energy. But the model lacks a mechanism for transferring this reduced modeled energy to the resolved energy. The growth of the resolved fluctuations relies entirely on natural instabilities, and is not fast enough to compensate for the stress decay imposed in the model, a phenomenon known as Modeled Stress Depletion

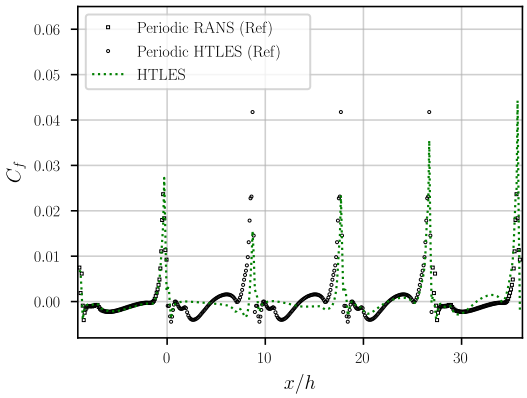

Figure 2.24 – Friction coefficient on the lower wall for M1 grid.

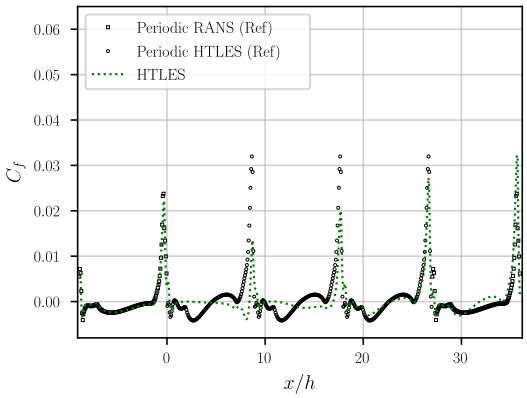

Figure 2.25 – Friction coefficient on the lower wall for M2 grid.

(MSD). This can be verified from the breakdown of total energy into modeled and resolved component plotted in Fig. 2.26, which shows the rapid decrease in the modeled energy but the resolved energy remains zero, causing the underestimation of the total energy. We converge towards the correct approximation in the fourth sub-domain because the resolved structures have been generated. But when we transition again from the LES-to-RANS in the fifth sub-domain the quality of the result is degraded downstream of the hill.

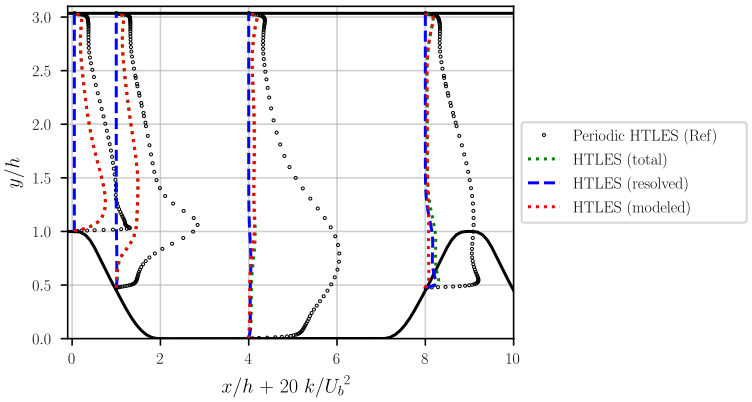

Figure 2.26 – Breakdown of total energy into modeled and resolved components in the second sub-domain.

When we focus on the profiles extracted at different streamwise locations, Figs. 2.27, 2.28, 2.29, 2.30, 2.31, 2.32, 2.33 for turbulent energy, mean velocity and Reynolds stresses, respectively, show that in the first sub-domain, treated in RANS mode, the model preserves the solution almost perfectly since the inlet conditions corresponds to the periodic RANS solution. The small difference is due to the fact that instead of periodic boundary condition at the end of sub-domain 1, we have a RANS to LES transition, which influences the results upstream. Note that in the first and the fifth sub-domain periodic RANS solution is used as a reference and periodic HTLES as a reference in rest of the sub-domains. It is also important to note that, here the comments are primarily made on the profiles plotted for M1 gird, as both the grids yield similar results, as the comparison of periodic computations for different mesh configurations have shown in the previous section.

Figs. 2.27 and 2.28 for the total turbulent energy show that in the second sub-domain and the majority of the third sub-domain, the total energy is highly underpredicted. We

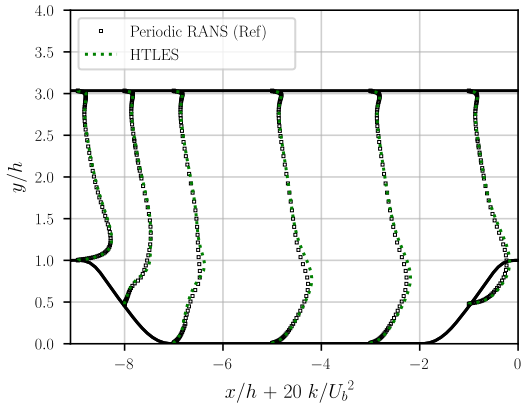

(a) sub-domain 1

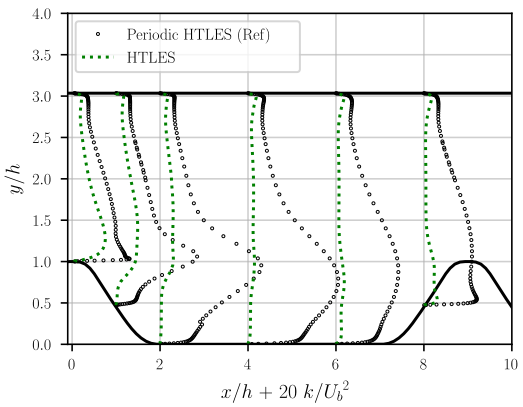

(b) sub-domain 2

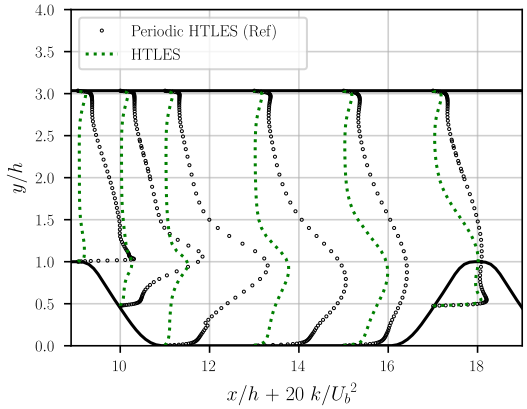

(c) sub-domain 3

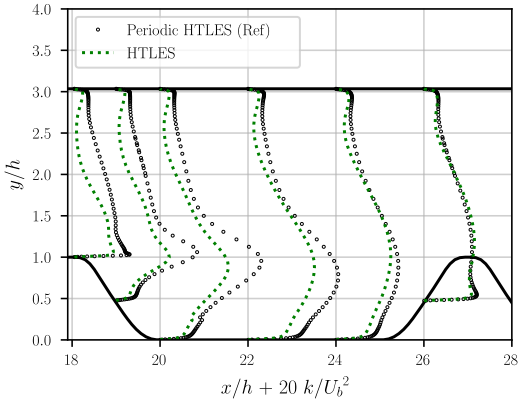

(d) sub-domain 4

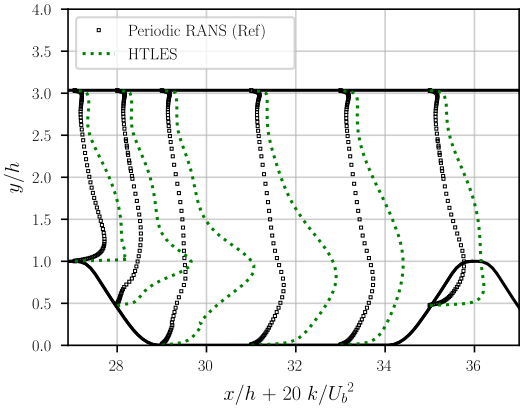

(e) sub-domain 5

Figure 2.27 – Profiles of total turbulent kinetic energy k at $Re_b = 10595$ for M1 grid at different spatial locations.

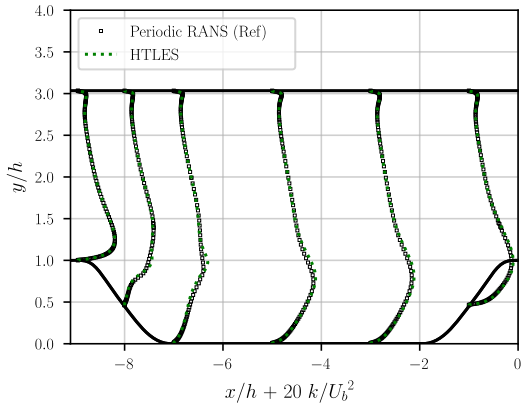

(a) sub-domain 1

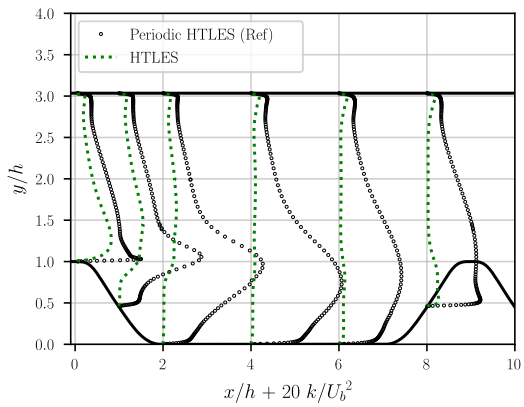

(b) sub-domain 2

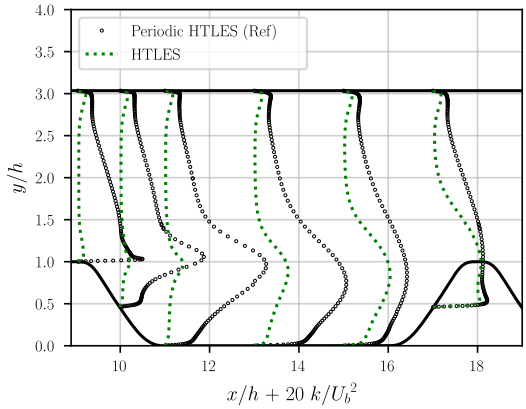

(c) sub-domain 3

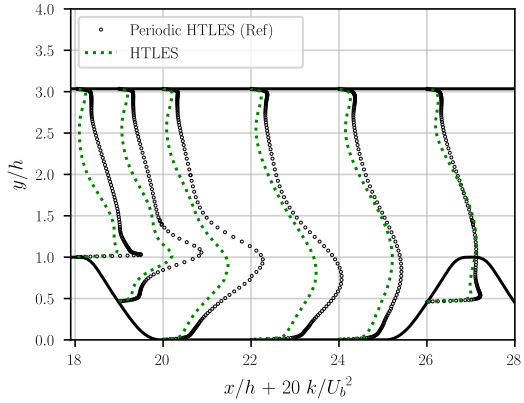

(d) sub-domain 4

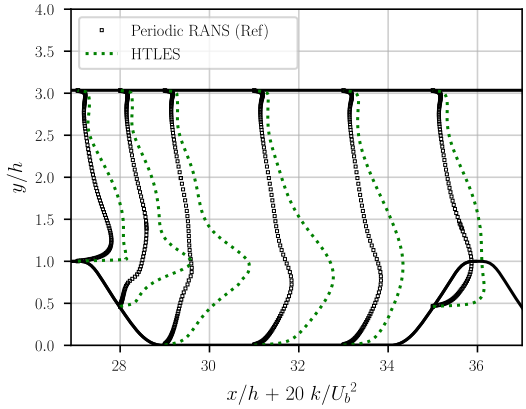

(e) sub-domain 5

Figure 2.28 – Profiles of total turbulent kinetic energy k at $Re_b = 10595$ for M2 grid at different spatial locations.

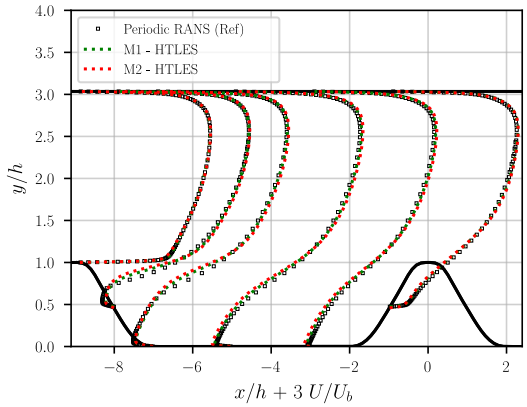

(a) sub-domain 1

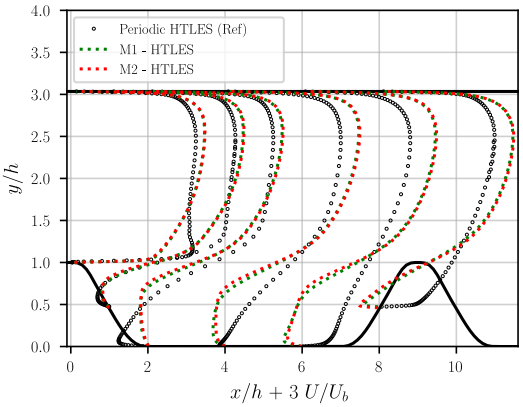

(b) sub-domain 2

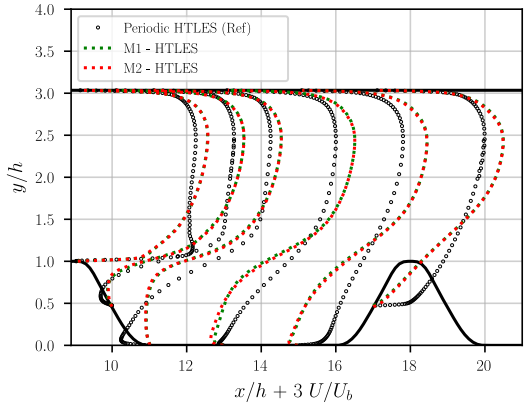

(c) sub-domain 3

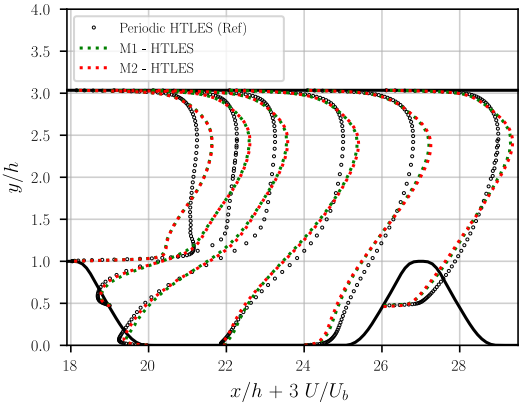

(d) sub-domain 4

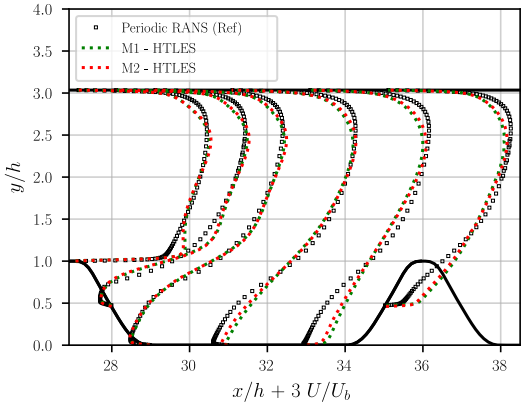

(e) sub-domain 5

Figure 2.29 – Profiles of streamwise velocity at $Re_b = 10595$ for both the grids at different spatial locations.

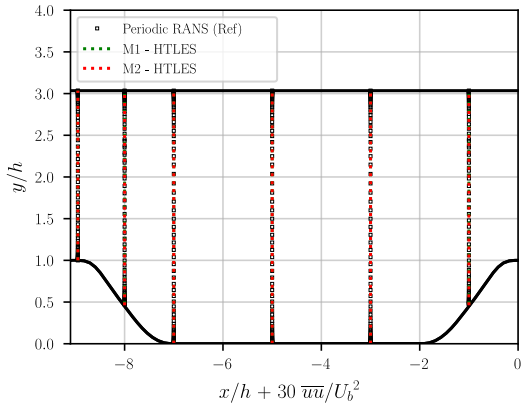

(a) sub-domain 1

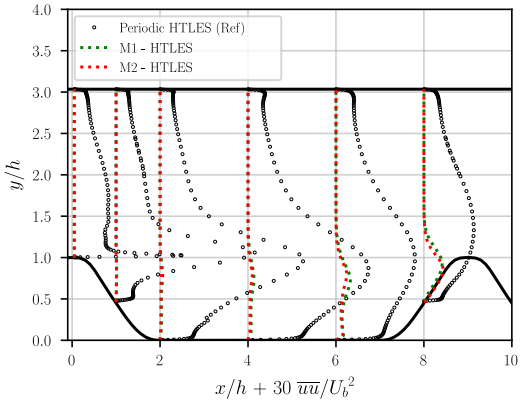

(b) sub-domain 2

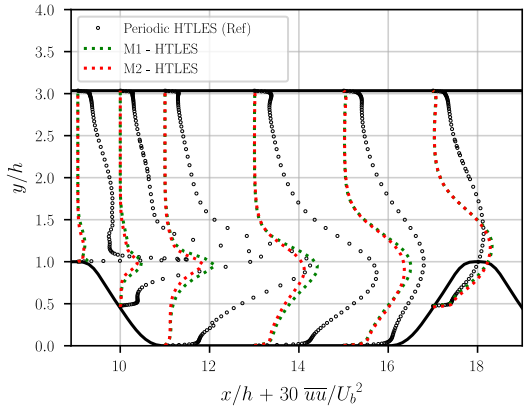

(c) sub-domain 3

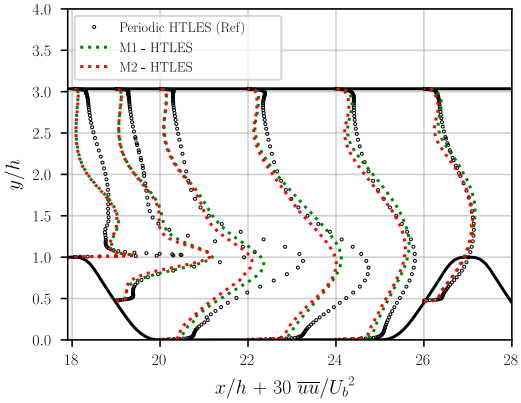

(d) sub-domain 4

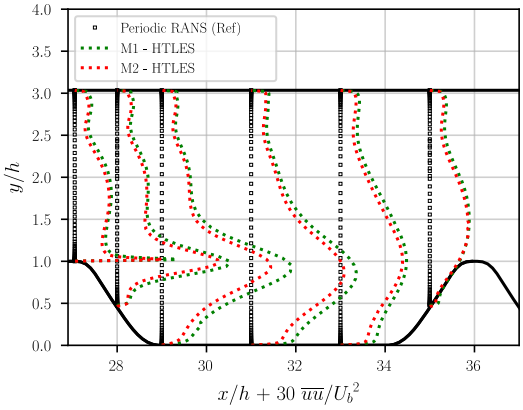

(e) sub-domain 5

Figure 2.30 – Profiles of streamwise component of the Reynolds stresses at $Re_b = 10595$ for both the grids at different spatial locations.

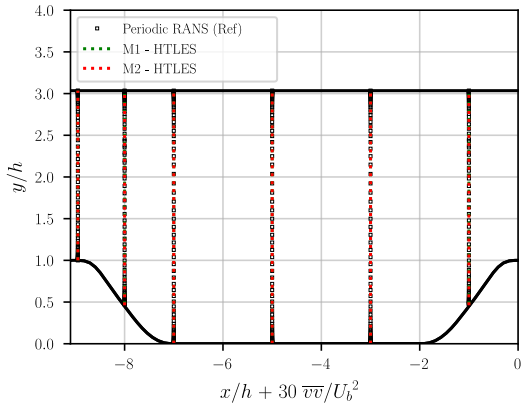

(a) sub-domain 1

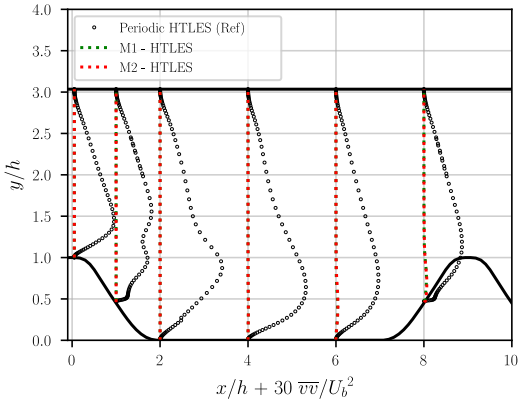

(b) sub-domain 2

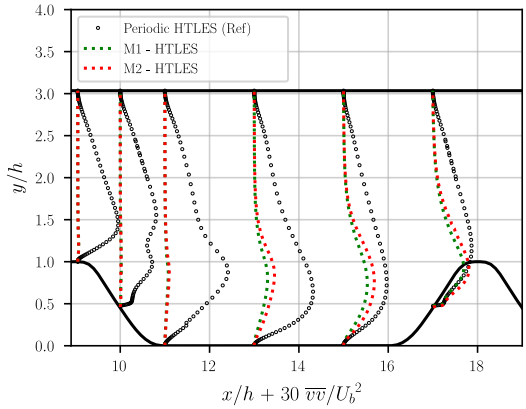

(c) sub-domain 3

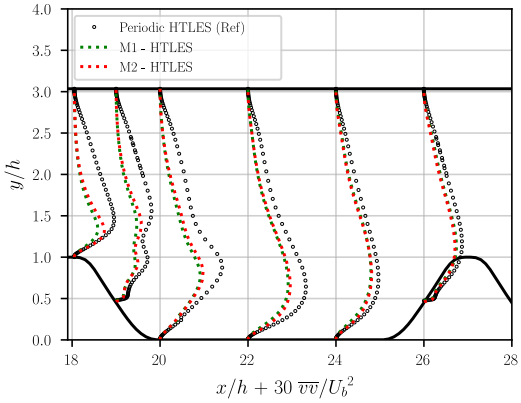

(d) sub-domain 4

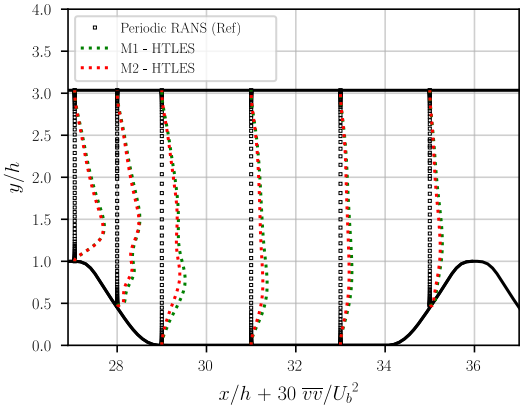

(e) sub-domain 5

Figure 2.31 – Profiles of normal component of the Reynolds stresses at $Re_b = 10595$ for both the grids at different spatial locations.

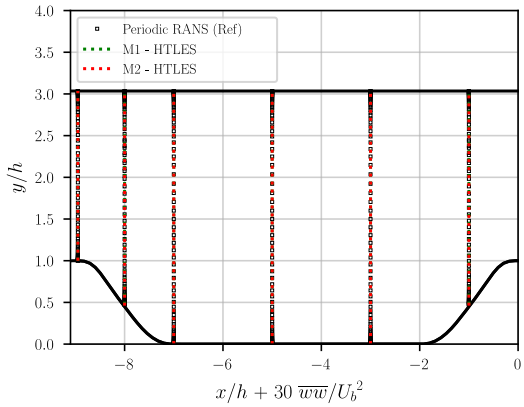

(a) sub-domain 1

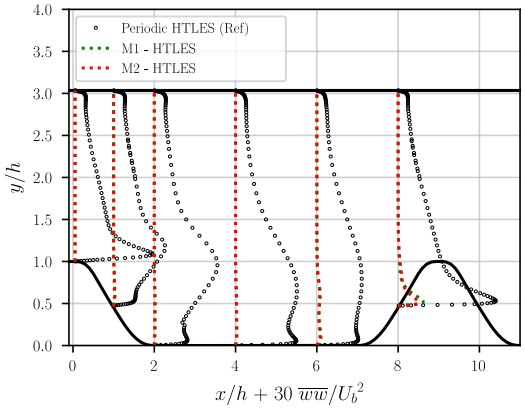

(b) sub-domain 2

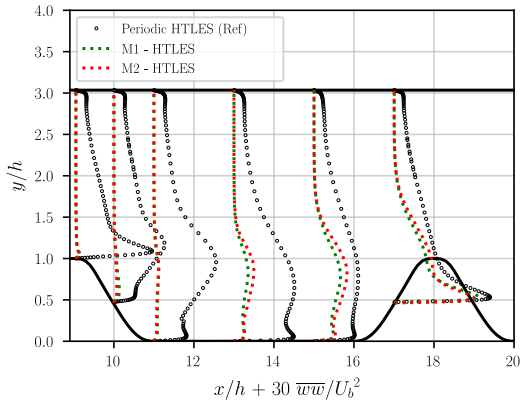

(c) sub-domain 3

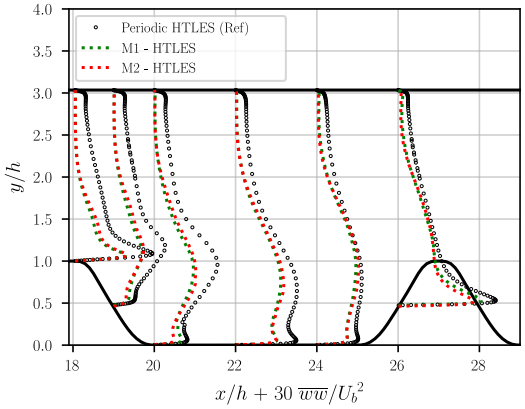

(d) sub-domain 4

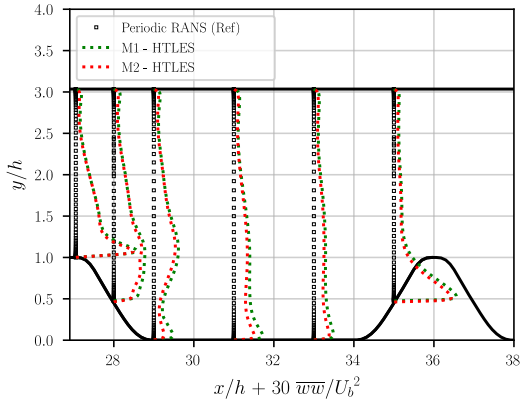

(e) sub-domain 5

Figure 2.32 – Profiles of spanwise component of the Reynolds stresses at $Re_b = 10595$ for both the grids at different spatial locations.

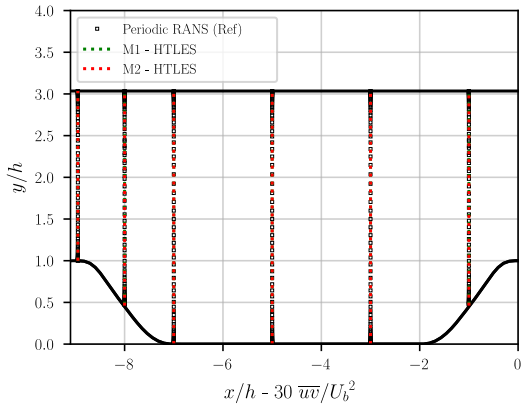

(a) sub-domain 1

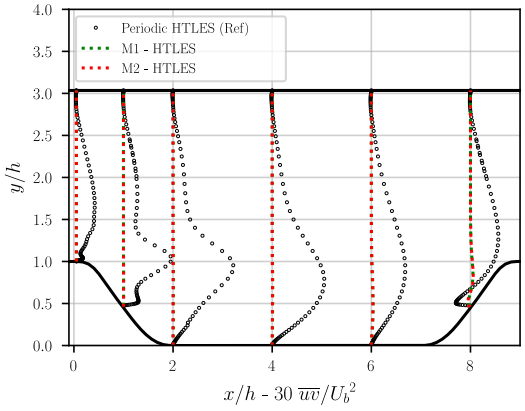

(b) sub-domain 2

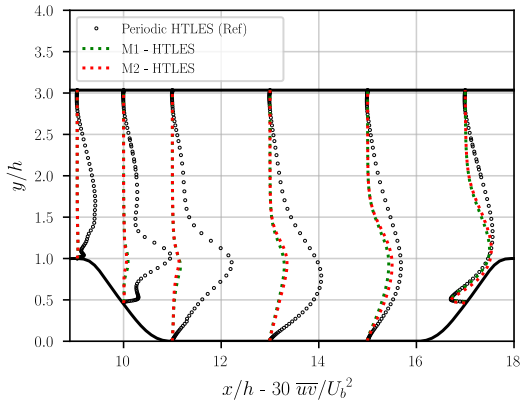

(c) sub-domain 3

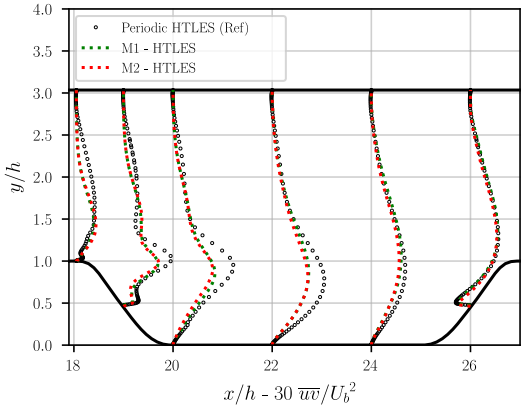

(d) sub-domain 4

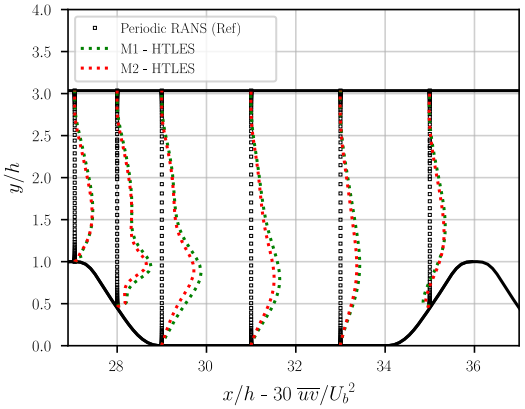

(e) sub-domain 5

Figure 2.33 – Profiles of shear stresses at $Re_b = 10595$ for both the grids at different spatial locations.

can observe a slight increase of the energy in the lower half of the hill ($y/h < 1.5$) upstream of the third hill at $x/h = 8$. This increase of energy is observed throughout the third sub-domain in the shear layer and in the lower half of the domain ($y/h < 2$), but the upper half still remains unchanged. By the end of the third sub-domain, the values start to converge towards the reference values with the total energy still growing in the fourth sub-domain. Finally, towards the end of the fourth sub-domain, a similar energy level as the reference is found ($x/h = 26$) for both the grids. Upon transitioning back to RANS from LES in the fifth sub-domain, a huge over-estimation of the total energy is observed. The main reason behind this underestimation at the RANS-to-LES transition and over-estimation at the LES-to-RANS transition is the inability of the model to increase the resolved stresses when transitioning to LES and to decrease the resolved stresses when transitioning back to RANS. However, somewhat similar values of the total energy as the reference is observed in the upper half ($y/h > 2$) of the fifth sub-domain.

Similar observations are made when the averaged streamwise velocity profiles are plotted against the reference data in Fig. 2.29. The results are very degraded throughout the first regions treated in LES mode. In the second sub-domain, in the recirculation zone the reverse flow velocity is very low. In addition to that, when we breakdown the total energy in the second sub-domain into the resolved and modeled part, the resolved energy is nearly zero with modeled energy also going to zero (refer to Fig. 2.26). This causes the complete flow relaminarization. Towards the later half of the fourth sub-domain the profiles can be seen close to the reference but they are always underestimated towards the lower wall and that underestimation is compensated by the over-estimation towards the upper wall throughout the entirety of the computational domain which is treated in LES. Whereas when we transition from LES-to-RANS in the fifth sub-domain, the velocity is over-estimated towards the lower wall and underestimated towards the upper wall. Figs. 2.30, 2.31, 2.32 and 2.33 lead to the similar predictions for both the grids. Domains treated in LES mode always under-predict the variable we are observing till we reach the upstream of the fifth hill, then the profiles are close to that of the reference. But when we transition back to the RANS mode due to the presence of resolved structures, over-prediction of the variables is observed. It is important to note that the small discrepancies observed in Figs. 2.29 to 2.33 is due to the difference in the mesh utilized, as discussed in the previous section, also here only references for M1 grid is plotted.

Hence, it is safe to say that HTLES fails in generating resolved stresses rapidly, which provides a major motivation to develop a mechanism to compensate for this loss of energy in transition.

2.4.4 Flow over suddenly expanding channel (backstep)

2.4.4.1 Presentation of the test case

The influence of recirculation on turbulent flows can be observed in many geophysical or industrial situations. The efficiency of devices like pumps, turbines and compressors depends significantly on how well the turbulent characteristics are captured in these zones. The flow in suddenly expanding channel or in other words flow over a backward facing step is a classical test case in turbulence modeling due to the challenge it provides and the inability of RANS models to correctly predict the statistics of the flow. A few studies to refer concerning this particular geometry due to the difficulties it present in simulating the flow (DNS: (Le et al., 1997; Barri et al., 2010a; Lamballais, 2014), Experimental: (Barri et al., 2010b; Visscher et al., 2011)).

A schematic view of the flow configuration is presented in Fig. 2.34. The geometry represents only half of the domain as we can assume the symmetry in flow for the other

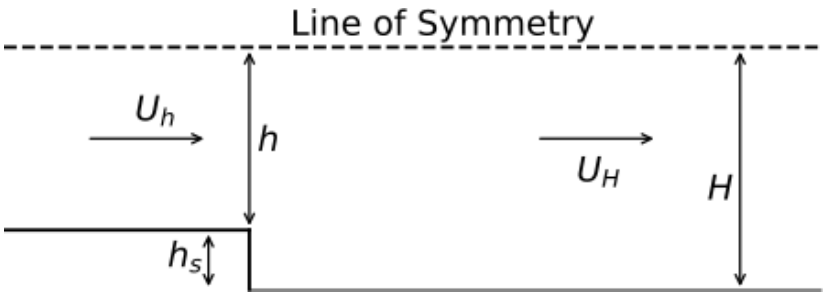

Figure 2.34 – Schematic representation of the geometry.

half. The width of the upstream channel is represented as h and the downstream channel as H, with h_s being the height of the backward facing step. These parameters always respect the relation $H > h$, leading to $h_s = H - h$ and the expansion ration $Er = H/h$. A flow rate is used to drive the flow.

2.4.4.2 Numerical parameters

The flow is characterized by the bulk Reynolds number of the upstream channel, $Re_h = U_h h/\nu = 5000$, where U_h is the bulk velocity measured in the upstream channel; and the expansion ratio $Er = H/h = 3/2$. Bulk velocity downstream of the expansion is given by $U_H = U_h h/H$ because of the mass conservation, which leads to the Reynolds number in the downstream channel given by $Re_H = U_H H/\nu = 5000$.

The particular system of units for the non-dimensionalization of the variables:

$$L = H;\ T = \frac{H}{U_H};\ M = \rho H^3; \tag{2.49}$$

which yields

$$\begin{gathered} \widetilde{U} = \frac{U}{U_h};\ \widetilde{t} = \frac{tU_h}{h};\ \widetilde{\rho} = 1;\ \widetilde{k} = \frac{k}{U_h^2}; \\ Re_h = \frac{U_h h}{\nu};\ \widetilde{p} = \frac{p}{\rho U_h^2};\ \widetilde{\nu} = \frac{1}{Re_h};\ U_h = 1. \end{gathered} \tag{2.50}$$

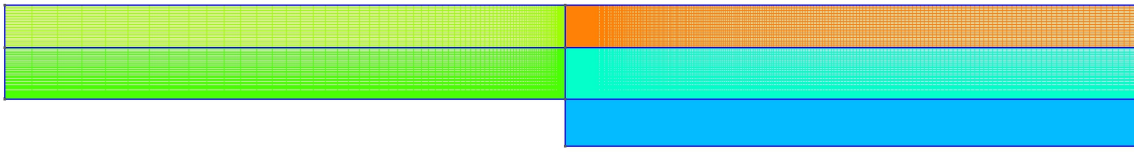

Figure 2.35 – Representation of the mesh.

The main characteristics of the mesh used for the computation with the HTLES model is described in the Table 2.5. As can be seen in Fig. 2.35, cells are isotropic at the expansion of the channel (at $x/h = 0$).

Re_h	$\Delta_{y_w^+}$	N_z	$N_{x_{\text{upstream}}}$	$N_{x_{\text{downstream}}}$	$N_{y_{\text{upstream}}}$	$N_{y_{\text{downstream}}}$
5000	1	42	86	436	100	200

Table 2.5 – Numerical settings for the grid.

The computational domain is given as $L_x \times L_y \times L_z = 24H \times 1H \times 1H$, which corresponds to $x/H \in [-4, 20]$, $y/H \in [0, 1]$ and $z/H \in [0, 1]$. The mesh is created such a way that

it satisfies $\Delta_{y^+} \simeq 1$ at the wall. Here, the grid independent shielding is activated up to $y^+ = 20$, instead of $y^+ = 100$, to account for the low Reynolds number so that we do not treat regions very far from the wall in RANS mode. This setup directly corresponds to the DNS setup studied by Lamballais (2014) without rotation, which will act as the reference for our computations. Periodic boundary conditions are applied in the spanwise direction (z-direction). A precursor periodic RANS computation is performed on the same geometry as the upstream channel to extract the statistically-averaged profiles to impose as the inlet boundary condition in the main computation. The computational domain for the reference DNS is given by $L_x \times L_y \times L_z = 24H \times 2H \times 6H$ discretized on a Cartesian grid of $n_x \times n_y \times n_z = 1441 \times 513 \times 768$. The time step in HTLES computation is kept constant at $dt = 0.0012h/U_h$, so that the Courant number is less than unity throughout.

2.4.4.3 Results

From the isocontours $Q = U_H^2/H^2$ plotted in Fig. 2.37 with modeled-to-total turbulent energy ratio r plotted in background showing the RANS to LES regions, it is seen that the resolved structures take a long time to develop after the RANS to LES transition located at $x/H = -4$. The prediction of the friction coefficient at the bottom wall shows very degraded results compared to the reference (refer to Fig. 2.36).

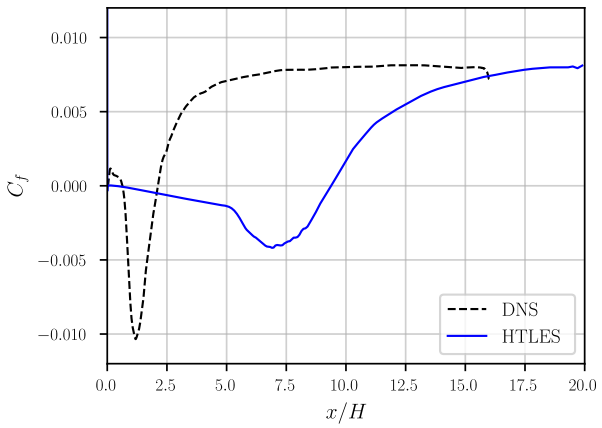

Figure 2.36 – Skin friction coefficient on the lower wall at $Re_H = 5000$.

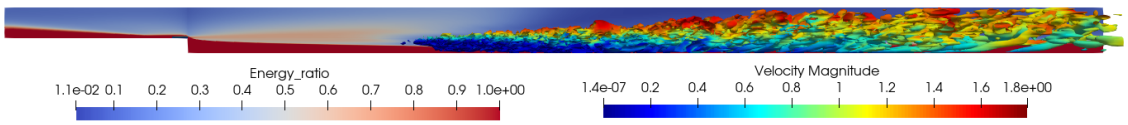

Figure 2.37 – Isocontours $Q = U_H^2/H^2$ colored with the velocity magnitude, and modeled-to-total turbulent energy ratio r in the background.

Focusing on profiles extracted at different streamwise locations, the comparison of profiles plotted in Figs. 2.38, 2.39, 2.40, 2.41, 2.42, 2.43 for velocity, total turbulent energy, diagonal components of the Reynolds stress tensor and shear stress, respectively, show that the results are very far from the correct values. Profiles plotted for the streamwise velocity in Fig. 2.38 show that the profiles are in agreement with the reference till $x/H = 0$, where the separation of the flow takes place. Due to the weakness of the reverse flow in the recirculation zone, the relaminarization of the flow happens.

As the profiles extracted from precursor RANS computation act as the inlet boundary condition, the turbulent kinetic energy plotted in Fig. 2.39 is underpredicted, which is a usual issue observed with the $k - \omega$ SST RANS model. Further along in the streamwise

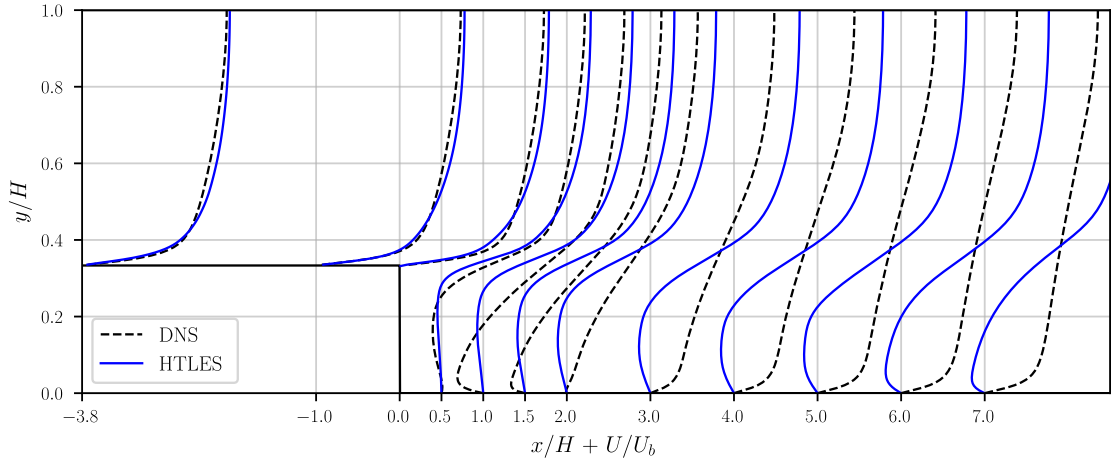

Figure 2.38 – Profiles of streamwise velocity at $Re_H = 5000$.

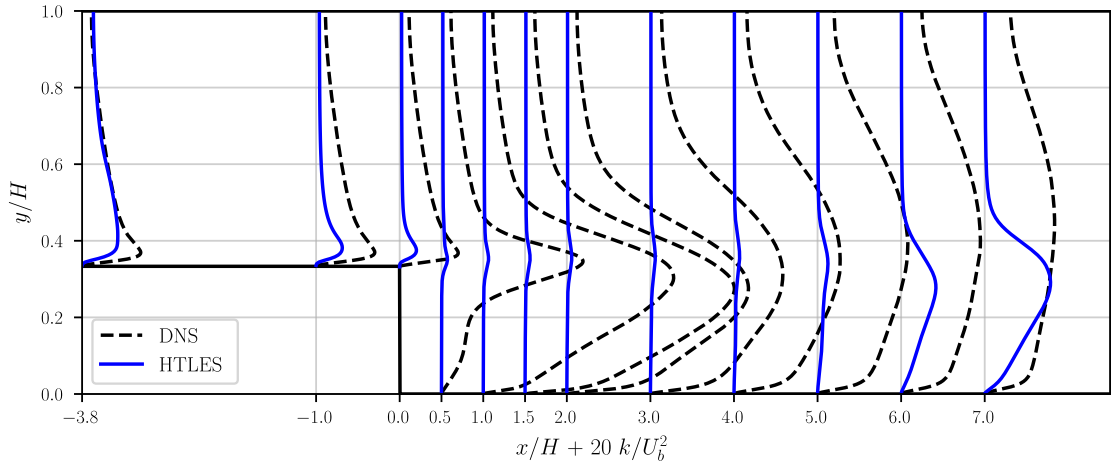

Figure 2.39 – Profiles of total turbulent kinetic energy at $Re_H = 5000$.

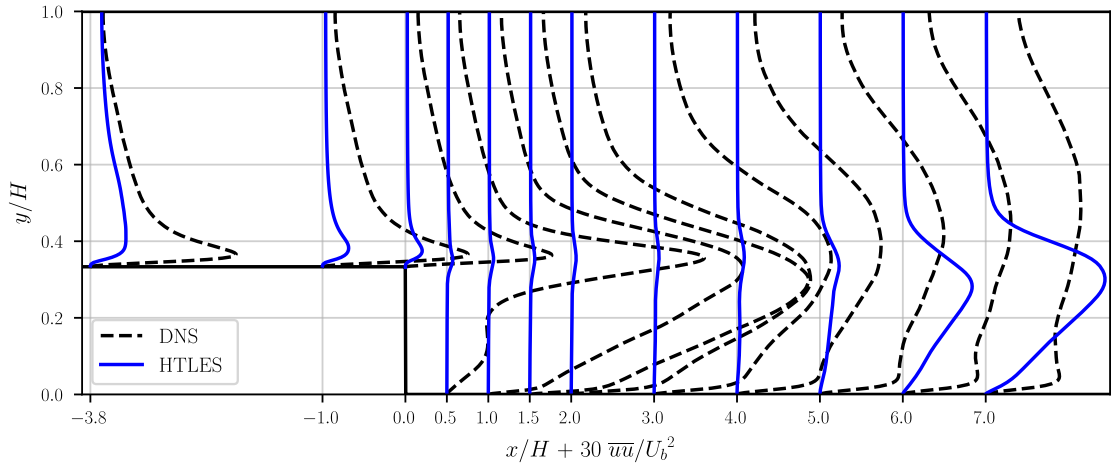

Figure 2.40 – Profiles of the streamwise component of the Reynolds stress at $Re_H = 5000$.

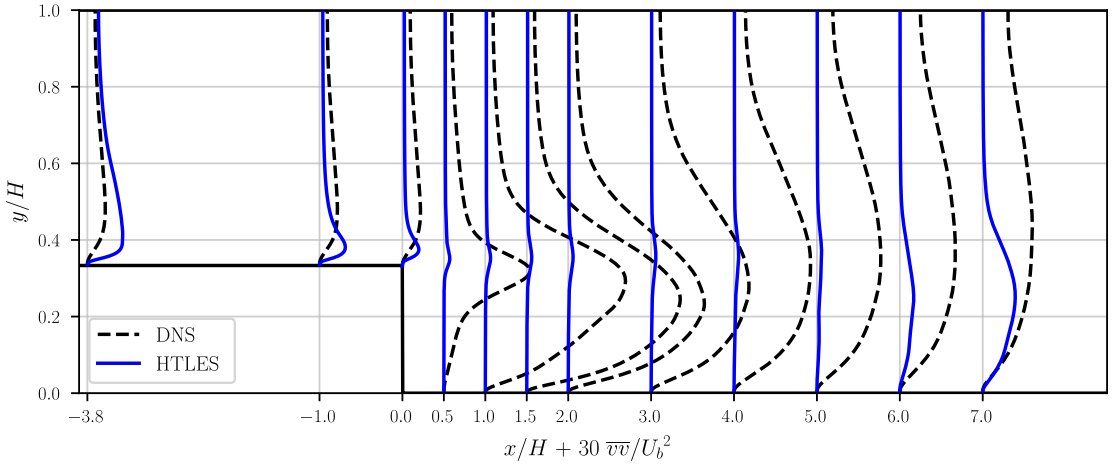

Figure 2.41 – Profiles of the vertical component of the Reynolds stress at $Re_H = 5000$.

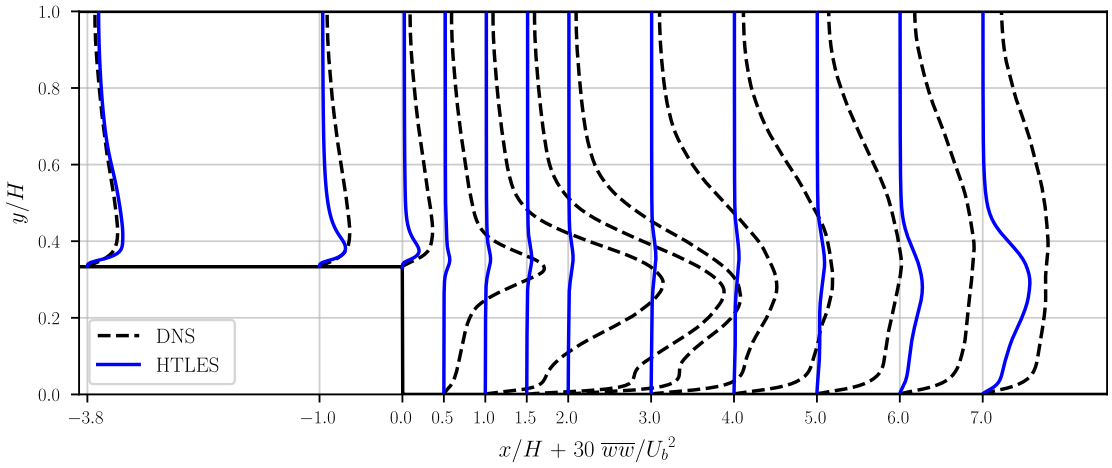

Figure 2.42 – Profiles of the spanwise component of the Reynolds stress at $Re_H = 5000$.

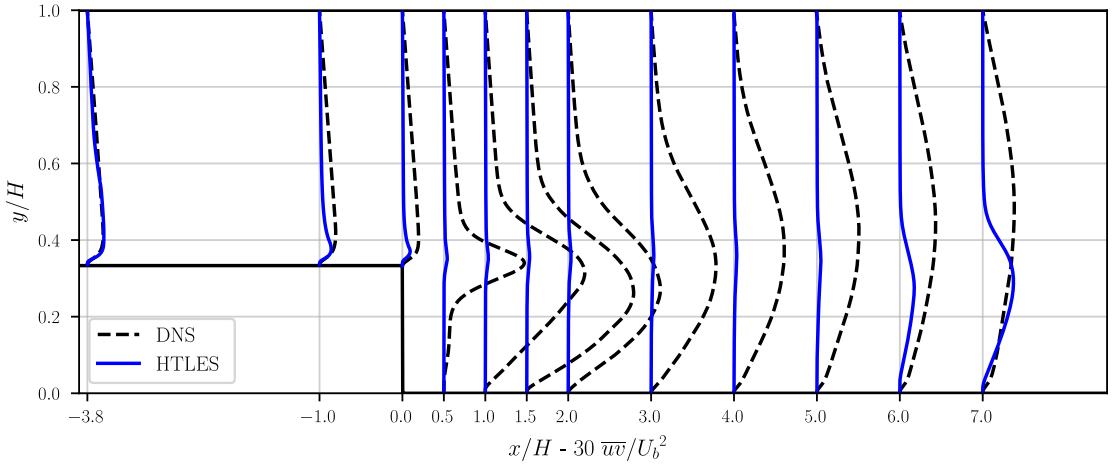

Figure 2.43 – Profiles of the shear stress at $Re_H = 5000$.

direction, the HTLES model reduces the modeled energy but the resolved energy is still zero, which leads to a severe under-prediction of the total energy (almost zero up to $x/H = 5$). From $x/H = 6$ onwards we can see the increase in the total energy in the shear layer, exactly the point where we start seeing the development of the resolved structures in the isocontours (refer to Fig. 2.37). But in the core of the channel the total energy ($k = 0$) is still highly underpredicted. Similar observations for the components of the Reynolds stresses can be made from Figs. 2.40, 2.41, 2.42, and 2.43.

2.5 Conclusion

The first part of the chapter recalls the interest of temporal filtering in the context of hybrid models. The definition of the uniform temporal filter is given, highlighting the main advantages of this definition, in particular satisfying Galilean invariance. Ensuring the H-equivalence criterion, the Hybrid temporal LES model is presented, which has the hybridization function in the transport equation of the turbulent energy, unlike other hybrid models discussed before which have the hybridization function in the transport equation of dissipation rate. However, the formulation of the HTLES model is more complex due to the appearance of the hybridization function in many terms.

The hybrid HTLES method provides very satisfactory predictions for the flow in the infinite plane channel at $Re_\tau = 590$ and flow in the channel with periodic hills at $Re_b = 10595$ with a mesh just fine enough for the LES mode of HTLES, when the periodic boundary conditions are applied in streamwise direction along with the spanwise direction.

→ The quantities of interest such as the friction coefficient on the lower wall and the velocity field are predicted with good accuracy. The turbulent kinetic energy and the components of the Reynolds stress tensor are qualitatively reproduced with an over-estimation.

→ The robustness of the formulation near the wall is ensured by implementing the near-wall shielding function, which ensures that the near wall region is treated in RANS mode. The importance and effectiveness of this function can be seen in the flows with higher Reynolds number (Duffal et al., 2022).

When it comes to the more realistic cases with an inlet and an outlet boundary condition, the results produced by the HTLES model for the flow in spatially developing channel with periodic hills with $Re_b = 10595$ and the flow in suddenly expanding channel (backward-facing step) with $Re_h = 5000$, are not satisfactory.

→ In continuous hybrid RANS-LES modeling, when the fluid flows from a RANS to a LES zone, the modeled stresses decrease drastically but the resolved stresses do not grow fast enough, which creates the imbalance in the total stresses. This phenomena is know as the "Modeled-stress depletion". This problem is due to the fact that there is a mechanism to reduce the modeled energy when the resolution is refined, but absence of a mechanism to transfer this reduced energy to the resolved energy. In a simplified case of a RANS-to-LES transition in grid turbulence, if an eddy-viscosity model is used for the subfilter stress, the molecular and turbulent diffusion terms in the resolved momentum equation is written as:

$$\frac{\partial}{\partial x_j}\left[(\nu + \nu_{\text{sfs}})\,\frac{\partial \widetilde{u}_i}{\partial x_j}\right] . \tag{2.51}$$

If we think logically, in the RANS region, the resolved velocity is the mean velocity and the diffusion terms are zero due to the absence of velocity gradient. That reduces

the resolved momentum equation to the form:

$$\widetilde{u_j}\frac{\partial \widetilde{u_i}}{\partial x_j} = -\frac{1}{\rho}\frac{\partial \widetilde{p}}{\partial x_i} \tag{2.52}$$

which satisfies the solution of $0 = 0$ for uniform flows. When the mesh is refined to match the LES like resolution, the hybrid model (HTLES) strongly reduces the turbulent viscosity ν_t. Since we've considered the homogeneity, there is no term representing the turbulent viscosity in Eq. (2.52). Hence, the solution we got in RANS remains the solution of the equation.

→ The aim of keeping the total turbulent kinetic energy constant during the RANS-to-LES transition fails due to the lack of a mechanism. Instead what happens due to the refinement is that the modeled energy k_m decreases drastically and the resolved energy k_r remains zero in this particular example. It is obvious that no modification in the model which solves for the unresolved part can correct this fundamental problem of violation of the conservation of the mechanical energy. In reality, the decrease of the modeled energy corresponds to a modification in the partition of the modeled and the resolved energy, which generate terms in the momentum equation that are not accounted for here in this model. Therefore, in the next chapters, a new methodology for this missing mechanism is proposed and tested on various test cases.

CHAPTER 3

Active HTLES

In this chapter, the first half is dedicated to the bibliographical study of pre-existing methods to generate the fluctuations and add needed energy to drive the flow towards the correct solution. Then in the second half of the chapter, the development of a methodology called *active* approach is presented to eliminate the case dependency and need for the target statistics in order to drive the flow.

Contents

3.1 Introduction

In continuous hybrid RANS/LES modeling, while transitioning from RANS-to-LES, we go from fully modeled to partially resolved quantities and by doing so the reduction in modeled energy should be compensated by the increase in the resolved energy. However, the modeled stresses decrease drastically but the resolved stresses do not grow fast enough due to the fact that the growth of the resolved fluctuations relies completely on the natural instabilities. This phenomena of stress decay imposed in the model is known as "Modeled Stress Depletion (MSD)". This problem can be traced back to the fact that there is a mechanism to reduce the modeled energy when the mesh is refined but no mechanism for transferring this energy to the resolved motion. This lack of resolved energy in the transition zone is also known as the "*grey area*" problem. This problem can be alleviated by decreasing the subgrid viscosity in the initial region of the sheared detached layer to zero, in order to avoid the delay in the development of the instabilities. However, this solution is not general enough as it only works in the flow with inflectional velocity profiles due to the fact that it does not inject energy into the resolved motion (Mockett et al., 2018).

Over the years a few methods have been developed that introduce resolved fluctuations into the resolved motion, one way or the other. They are mainly divided into two categories:

- → **Injection of synthetic turbulent fluctuations:** This method superimposes some artificially generated turbulent velocity fluctuations onto a RANS velocity field at the RANS/LES interface. The simplest method of generating the fluctuations consist of introducing a random white noise. However, many other approaches were developed to inject more realistic fluctuations.

- → **Volume forcing of the momentum equation:** This method is based on introducing a volume source term in the governing equations of the flow, which is activated in the transition zone. Due to the control over the intensity of this volume source term (possibility of gradual increase), this method does not encounter spurious noise due to the sudden emergence of turbulence.

A brief study about these methods is presented in section 3.2 before presenting a new more general "*active approach*", which is a mechanism to inject energy into the resolved motion in section 3.3.

It is important to note that the growth of the resolved structure due to natural instabilities in a flow upon transitioning takes time, which is referred to as "Transitioning zone" or "grey area". Introducing external elements to introduce resolved fluctuations, reduces this transition zone. But completely eliminating this zone is hardly possible.

Apart from the categories mentioned above to generate resolved fluctuations, researchers have identify a few more categories. But they cannot be categorized under the energy injection methods.

- → **Precursor DNS or LES:** In this method the velocity fluctuations at the RANS/LES interface are set to rescaled fluctuations from a precursor DNS or well-resolved LES computation. Given that the rescaling laws used are correct, this method ensures a high accuracy of the simulation. Due to the reliance on the precursor DNS, this method is restricted to very simple flow configurations. See Schlüter et al. (2004) for a reference.

- → **Recycling of turbulence:** This method proposed on transferring the unsteady information available in the same simulation at some downstream section of the

flow to the RANS/LES transition (LES inlet). This requires appropriate rescaling of the transferred turbulence. Because of the difficulty in rescaling, this method is applicable to the flow with simple characteristics. In addition to that, it also demands for some special initialization to establish mature turbulence within the recycling region. This method was originally proposed by Lund et al. (1998).

3.2 Turbulence generation methods

3.2.1 Synthetic Eddy Method (SEM)

The synthetic Eddy Method is based on superimposing the flow field by coherent structures. The method was proposed by Jarrin (Jarrin et al., 2006; Jarrin et al., 2009). The brief outline of the theory is presented below. SEM uses the statistics available from the upstream RANS computation i.e. streamwise mean velocity U_i, Reynolds stress tensor R_{ij} and a turbulent length scale. The velocity fluctuations to impose on the LES inflow plane is a finite set of N artificial eddies given by:

$$u_i = U_i + \frac{1}{\sqrt{N}} \sum_{k=1}^{N} a_{ij} \varepsilon_j^k f_{\sigma(x)} \left(\mathbf{x} - \mathbf{x}^k \right), \quad \text{with} \quad N = \max \left(\frac{V_B}{\sigma^3} \right) \tag{3.1}$$

where $\mathbf{x}^k$ are the locations of the eddies with ε_j^k being their intensity at those locations, a_{ij} determines the magnitude of the velocity fluctuation as a function of Reynolds stresses and $f_\sigma \left(\mathbf{x} - \mathbf{x}^k \right)$ is the velocity distribution of the eddy located at $\mathbf{x}^k$. The location and the intensity of each eddy are independent random variable.

The synthetic eddies are randomly generated in a virtual domain. The LES inflow plane has a finite set of points $S = \{\mathbf{x}_1, \mathbf{x}_2, ..., \mathbf{x}_s\}$ (forcing region). A box (virtual domain) of eddies B is created which surrounds S points and contains synthetic eddies. The minimum and maximum coordinates of the domain are defined by:

$$x_{i,\min} = \max_{\mathbf{x} \in S} \left(x_i - \sigma(\mathbf{x}) \right) \quad \text{and} \quad x_{i,\max} = \max_{\mathbf{x} \in S} \left(x_i + \sigma(\mathbf{x}) \right) \tag{3.2}$$

where σ is a characteristic length scale which controls the size of the structures. The number of eddies N is set constant to ensure the constant density inside of the box of eddies. V_B is the volume of the box of eddies. The eddies are convected through the virtual domain with a constant characteristic velocity U_c (averaged mean RANS velocity over LES inflow plane).

$$\mathbf{x}^k(t + dt) = \mathbf{x}^k(t) + U_c \mathrm{d}t \tag{3.3}$$

Eq. (3.3) gives the new position of the eddy at each iteration, where dt is the time step of the simulation. It also represent the way time correlation of the fluctuating velocity is imposed. Eddies convected outside the virtual domain are randomly regenerated at the inlet side of the virtual domain.

In Eq. (3.1) the shape function $f_\sigma \left(\mathbf{x} - \mathbf{x}^k \right)$ represents the velocity distribution of the eddy located at $\mathbf{x}^k$, defined as:

$$f_\sigma \left(\mathbf{x} - \mathbf{x}^k \right) = \frac{\sqrt{V_B}}{\sigma^3} f \left(\frac{x - x^k}{\sigma} \right) f \left(\frac{y - y^k}{\sigma} \right) f \left(\frac{z - z^k}{\sigma} \right) \tag{3.4}$$

f is a tent function which satisfies the normalization condition.

$$f(x) = \begin{cases} \sqrt{\frac{3}{2}} \left(1 - |x| \right) & \text{if } |x| < 1 \\ 0 & \text{otherwise} \end{cases} \tag{3.5}$$

The length scale σ is estimated by the turbulent information obtained from the RANS computation and the maximum mesh size.

$$\sigma = \max\left\{\min\left\{\frac{k^{3/2}}{\varepsilon}, \kappa\delta\right\}, \Delta\right\} = \max\left\{\min\left\{l_{\mathrm{RANS}}, \kappa\delta\right\}, \Delta\right\} \tag{3.6}$$

where $\kappa = 0.41$.

Jarrin et al. (2009) implemented the SEM method with success to a wide variety of configurations from a simple channel and square duct flow to the flow over an airfoil trailing edge. Later, Skillen et al. (2016) proposed a modified version with a correction in normalisation procedure to ensure that the prescribed statistics are correctly recovered and implemented it with success in channel flow and two-dimensional asymmetric diffuser. Recently, Schau et al. (2022) proposed an improved SEM called Ensemble Synthetic Eddy Method (ESEM) to provide flexibility and more importantly extending the original SEM to inhomogeneous turbulence.

3.2.2 Synthetic Turbulence Generator (STG)

This approach of generating artificial turbulent velocity fluctuations is based on Fourier reconstruction techniques employing the time and space correlations in addition to the available information of the averaged characteristics and turbulence statistics available from the RANS computation. Depending on the specific properties used, there are many versions of available STG. Here, we will in brief discuss a STG method proposed by Shur et al. (2014). The velocity vector at any point $\mathbf{r} = \{x, y, z\}$ in the RANS-LES interface is defined as:

$$U(\mathbf{r}, t) = U_{\mathrm{RANS}}(\mathbf{r}) + u'(\mathbf{r}, t) \tag{3.7}$$

U_{RANS} is the mean velocity vector and $u'(\mathbf{r}, t)$ is the velocity fluctuation vector which is expressed as:

$$u_i'(\mathbf{r}, t) = a_{ij} v_j'(\mathbf{r}, t) \tag{3.8}$$

where v_j' is the auxiliary vector of fluctuations defined by super-positioning the weighted spatio-temporal Fourier modes. For the STG, as well as the SEM, a_{ij} determines the magnitude of the velocity fluctuations as a function of the Reynolds stresses taken from the RANS computation.

$$\begin{bmatrix} \sqrt{R_{11}} & 0 & 0 \\ R_{21}/a_{11} & \sqrt{R_{22} - a_{21}^2} & 0 \\ R_{31}/a_{11} & (R_{32} - a_{21}a_{31})/a_{22} & \sqrt{R_{33} - a_{31}^2 - a_{32}^2} \end{bmatrix} \tag{3.9}$$

$$v'(\mathbf{r}, t) = \sqrt{6} \sum_{n=1}^{N} \sqrt{q^n} \left[\sigma^n \cos\left(k^n d^n \cdot \mathbf{r}' + \varphi^n\right)\right] \tag{3.10}$$

where N is the number of modes; d^n is the random vector which is uniformly distributed over a unit sphere and σ^n is a unit vector normal to d^n ($\sigma^n \cdot d^n = 0$). The intervals for these uniformly distributed random variables are defined in table 3.1:

variable	φ^n	d^n
interval	$[0, 2\pi)$	$[0, 2\pi)$

Table 3.1 – Distribution of random variables

All these random numbers have to be defined only once as they are time-independent. The normalized amplitudes of the modes in the modified von Karman spectrum is defined by:

$$q^n = \frac{E(k^n)\Delta k^n}{\sum_{n=1}^{N} E(k^n)\Delta k^n}, \sum_{n=1}^{N} q^n = 1 \tag{3.11}$$

where k^n is the wave number magnitude of the vector d^n. To introduce the time-dependent fluctuations, a modified position vector $\mathbf{r}'$ is defined with the assumption of x-direction being the streamwise direction, such that:

$$\begin{bmatrix} \frac{2\pi}{k^n \max\{l_e(\mathbf{r})\}} (x - U_0 t) \\ y \\ z \end{bmatrix} \tag{3.12}$$

with U_0 being the maximum or bulk velocity over the RANS-LES interface. $l_e(\mathbf{r})$ corresponds to the local scale of eddies with the most energy. Defining the local scale properly is of utmost importance due to the fact that based on this length scale the development of the synthetic fluctuating velocity field achieves the closeness to the physically realistic ones. The formulation used is

$$l_e = \min\left(2d_w, C_l l_{\mathrm{RANS}}\right) \ , \tag{3.13}$$

Here $C_l = 3.0$ is an empirical constant, d_w is the distance to the wall, and l_{RANS} is the length scale of the background RANS model. The set of wave numbers k^n is fixed and common for the entire interface and it forms a geometric series:

$$k^n = k^{\min}(1+\alpha)^{n-1}, n = 1, 2, ..., N; \ 0.01 \leq \alpha \leq 0.05. \tag{3.14}$$

The spatial spectrum of the energy of turbulence is the von Karman spectrum $E(k)$, modified by introducing two empirical functions f_n and f_{cut}. Both functions act as damping function: f_n ensures the damping of the spectrum in the vicinity of the wavenumber corresponding to the Kolmogorov length-scale, whereas f_{cut} dampens the spectrum at wavenumbers larger than the Nyquist frequency.

Schmidt et al. (2015) showed a successful application of STG based on digital filter approach (Klein et al., 2003) to generate inlet boundary conditions for a hybrid LES-URANS methodology, in the plane channel flow and the periodic hill flow test cases. Schmidt et al. (2017) extended this idea further to analyze the influence of the inflow conditions on the external wall-bounded flow, and presented a modification of STG which is based on source terms. Recently, Janin et al. (2021) proposed a linear forcing method for isotropic turbulence based on a reconstruction approach which builds velocity fluctuations with a prescribed energy spectrum model, which successfully drives the resolved energy towards its target value while preserving the length and the time scales.

3.2.3 SKK approach

The SKK approach proposed by Spille-Kohoff et al. (2001) aims at promoting turbulent fluctuations in a set of planes close to the LES inlet by adding a forcing term to the wall-normal momentum equation, in order to amplify the velocity fluctuations in that direction. The body force f acts in the wall normal direction according to

$$\frac{\partial \overline{u_i}}{\partial t} + u_j \frac{\overline{u}_i}{\partial x_j} = -\frac{1}{\rho}\frac{\partial \overline{p}}{\partial x_i} - \frac{\partial \overline{u_i' u_j'}}{\partial x_j} + \frac{1}{\mathrm{Re}}\frac{\partial^2 \overline{u_i}}{\partial x_j \partial x_j} + f e_2 \tag{3.15}$$

This forcing enhances the local flow events that contribute to the production of the resolved shear stress. Indeed, in the zero-pressure gradient boundary layer flows (flat plate boundary layer flows):

$$P_{-\rho\overline{u'v'}} = \overline{v'v'}\frac{\mathrm{d}u}{\mathrm{d}y} \ , \tag{3.16}$$

such that generating wall-normal fluctuations promotes the resolved shear stress. A PI (proportional and integral) controller adjust the magnitude of the body force such that the shear stress profiles tends towards the target shear stress profile at a given streamwise location (x_0). The target profile $g\left(x_0, y\right)$ can be taken from an experiment or a RANS calculation.

The input of the PI controller at the location x_0 is computed based on the error between actual and target shear stresses:

$$e\left(y,t\right) = -\rho\overline{u'v'}^{z,t}\left(x_0,y,t\right) - g\left(x_0,y\right) \tag{3.17}$$

Here, $\overline{(\cdot)}^{z,t}$ denotes the averaging in the spanwise direction and in time to speed-up the convergence of the statistics. The integral term in the computation of the amplitude of the error, helps to avoid sudden jump, which could make the system unstable:

$$r\left(y,t\right) = \alpha e\left(y,t\right) + \beta\int_0^t e\left(y,t'\right)\mathrm{d}t' \tag{3.18}$$

The α and β parameters are chosen such that the error signal can decrease fast enough without causing instabilities. The instantaneous body force is computed as

$$f\left(x_0,y,z,t\right) = r\left(y,t\right)\left[u\left(x_0,y,z,t\right) - \overline{u}^{z,t}\left(x_0,y\right)\right] \tag{3.19}$$

In order to prevent from computing for unrealistic large shear stress events, a few constraints for the instantaneous local quantities are applied:

$$\left|u'\right| < 0.6U_\infty, \ \left|v'\right| < 0.4U_\infty, \ u'v' < 0 \ \text{ and } \ \left|u'v'\right| > 0.0015U_\infty^2 \tag{3.20}$$

where U_∞ is the free-stream velocity.

Keating et al. (2004a) showed successful implementation of this approach in generating inflow conditions for large-eddy simulation in spatially developing channel flow. Furthermore, Keating et al. (2004b) presented a modified version by coupling the original method with the synthetic turbulence method of Batten et al. (2004) and implemented it successfully in spatially developing channel flow and boundary-layer flow over a flat plate. More recently, Haywood et al. (2019) illustrated a modification which only modifies fluctuations that already exist and does not generate its own fluctuations. In case of grid sensitivity, the SKK approach is quite good when the grids are fine but when a coarse grid resolution is used, the efficiency of the method is less satisfactory.

3.2.4 LDS approach

In order to improve the efficiency of the SKK approach for coarse grid resolution to handle complex flows with high Reynolds number, Laraufie et al. (2011) proposed a new approach to control the intensity of the forcing by the wall-normal turbulent stress rather than the shear stress. The use of the wall-normal Reynolds stress in the derivation of the error function would allow for a better reactivity in the LDS approach.

$$\left(x_0,y,t\right) = -\rho\overline{v'^2}^{z,t}\left(x_0,y,t\right) - g\left(x_0,y\right) \tag{3.21}$$

where $g\left(x_0, y\right)$ is the target wall-normal Reynolds stress.

The LDS approach is developed around the RANS-SA hybrid model, which just allows direct access to the shear stress. To link the wall-normal Reynolds stress to the turbulent kinetic energy k, a reconstruction of the wall-normal Reynolds stress from a time averaged field is necessary. This leads to a good approximation in the log layer (Wilcox et al., 1998).

$$\overline{v'^2}^t = \frac{4}{9}k \tag{3.22}$$

Since the turbulent energy is not given by the SA model either, it is made use of the fact that the ratio between the shear stress and turbulent kinetic energy in a boundary layer is (Bradshaw et al., 1967):

$$-\frac{\overline{u'v'}^t}{k} = 0.3\ . \tag{3.23}$$

Finally, the Boussinesq approximation provides the link between the shear stress and the turbulent viscosity provided by the RANS-SA hybrid calculation.

$$-\overline{u'v'}^t = \nu_t \left(\frac{\partial \overline{u}^t}{\partial y} + \frac{\partial \overline{v}^t}{\partial x} \right) \tag{3.24}$$

where $\overline{(\cdot)}^t$ indicates that the quantities are time averaged.

3.2.5 Anisotropic Linear Forcing (ALF)

The Anisotropic Linear Forcing is a generalization of the SKK and LDS approaches based on the imposition of a complete target Reynolds-stress tensor and a target mean velocity at the beginning of the LES region in a zonal hybrid RANS/LES approach, with an overlap of the RANS and LES zones. The method was first introduced by De Laage de Meux et al. (2015). The intensity of the forcing in the LES region is driven by the statistics given by the RANS. To do this, a fluctuating force defined as follows:

$$\widetilde{f_i} = A_{ij}\widetilde{u_j} + B_i \tag{3.25}$$

with A_{ij} being a symmetrical second-order tensor and B_i a vector, which are independent of time when the steady state is reached. The filtered momentum equation for an incompressible flow can be written as:

$$\frac{\partial \widetilde{u_i}}{\partial t} + \widetilde{u_j}\frac{\partial \widetilde{u_i}}{\partial x_j} = -\frac{1}{\rho}\frac{\partial \widetilde{p}}{\partial x_i} + \nu \frac{\partial^2 \widetilde{u_i}}{\partial x_j \partial x_i} - \frac{\partial \tau_{ij}}{\partial x_j} + f_i \tag{3.26}$$

where the tilde $\widetilde{\cdot}$ denotes the filtering operator, $\tau_{ij} = \widetilde{u_i u_j} - \widetilde{u_i}\widetilde{u_j}$ the subgrid scale tensor. In order to analyze the effect of this force f_i on the mean and fluctuating flow separately, fluctuating body force can be split into Reynolds averaged part $\overline{f_i}$ and fluctuating part f_i' such as

$$f_i = \overline{f_i} + f_i' \tag{3.27}$$

The volumic forcing in Eq. (3.25) is then decomposed into a mean and a fluctuating part in order to analyze the effect of the force, but is it not done in practice:

$$\overline{f_i} = A_{ij}\overline{\widetilde{u_j}} + B_i \quad \text{and} \quad f_i' = A_{ij}u_j' \tag{3.28}$$

Applying the Reynolds decomposition to the filtered momentum equation, the contribution of the body force to the mean momentum equation and the transport equation of the resolved stress can be written as:

$$\frac{\partial \overline{\widetilde{u_i}}}{\partial t} + \overline{\widetilde{u_j}}\frac{\partial \overline{\widetilde{u_i}}}{\partial x_j} = -\frac{1}{\rho}\frac{\partial \overline{\widetilde{p}}}{\partial x_i} + \nu \frac{\partial^2 \overline{\widetilde{u_i}}}{\partial x_j^2} - \frac{\partial \overline{\tau_{ij}}}{\partial x_j} + \overline{f_i} - \frac{\partial}{\partial x_j}\overline{u_i' u_j'} \tag{3.29a}$$

$$\frac{\partial \overline{u_i' u_j'}}{\partial t} + \overline{\widetilde{u}_j} \frac{\partial \overline{u_i' u_j'}}{\partial x_j} = P_{ij}^r + \phi_{ij}^r + \mathcal{X}_{ij} + D_{ij}^{T^r} + D_{ij}^{\tau} + D_{ij}^{\nu^r} - \varepsilon_{ij}^r + T_{ij}^f \tag{3.29b}$$

where

$$u_i' = \widetilde{u}_i - \overline{\widetilde{u}_i} \tag{3.30}$$

$$\mathcal{X}_{ij} = \overline{\tau_{il}' \frac{\partial u_j'}{\partial x_l} + \tau_{jl}' \frac{\partial u_i'}{\partial x_l}} \tag{3.31}$$

$$D_{ij}^{\tau} = -\frac{\partial}{\partial x_l} \left(\overline{\tau_{il}' u_j' + \tau_{jl}' u_i'} \right) \tag{3.32}$$

such that $\overline{u_i' u_j'}$ is the resolved part of the Reynolds stress tensor. The different terms of the Eq. (3.29) are not detailed here. They are the counterpart for the resolved scales of the terms of Eq. (1.26), except for T_{ij}^f which represents the production term due to the fluctuating force f_i. It is noticeable from Eq. (3.29a), that only the averaged part of the body force $\overline{f_i}$ acts on the mean flow. This body force introduces an additional term in Eq. (3.29b) depending on the fluctuating part of the force through which it contributes to the budget of the resolved stresses $\overline{u_i' u_j'}$:

$$T_{ij}^f = \overline{f_i' u_j'} + \overline{f_j' u_i'} = A_{ik} \overline{u_j' u_k'} + A_{jk} \overline{u_i' u_k'} \tag{3.33}$$

Depending on the sign, this term increases or decreases the resolved stresses. Upon constructing the transport equation for the resolved energy, by taking the half trace, it can be easily shown that the introduction of this force introduces a production term:

$$T^f = A_{ik} \overline{u_i' u_k'} \ , \tag{3.34}$$

where u_i' is the fluctuating part of the resolved velocity. Only the mean part of the fore acts on the mean momentum equation. To drive the average filtered velocity $\overline{\widetilde{u}_j}$ and the resolved stresses $\overline{u_i' u_j'}$ towards the target $\overline{u_i}^\dagger$ and $\overline{u_i' u_j'}^\dagger$, the model is written as follows:

$$A_{ik} \overline{u_j' u_k'} + A_{jk} \overline{u_i' u_k'} = \frac{1}{\tau_r} \left(\overline{u_i' u_j'}^\dagger - \overline{u_i' u_j'} \right) \tag{3.35a}$$

$$A_{ij} \overline{\widetilde{u}_j} + B_i = \frac{1}{\tau_v} \left(\overline{u_i}^\dagger - \overline{\widetilde{u}_i} \right) \tag{3.35b}$$

It is a linear system with nine equations for nine unknowns. The necessary quantities, i.e., the mean resolved velocity and the resolved stresses have to be estimated, which is done by the means of spatial filtering in the direction of homogeneity or a temporal filter for a statistically stationary flows. The target values are obtained from the RANS results in the overlap region.

Forcing time scales τ_v and τ_r, which are relaxation times for the mean velocity and the resolved stress tensor, respectively, were defined by studying the behaviour of the ALF on the flow in a flat channel:

$$\tau_r = \max \left(2\tau, 0.01 \frac{k^\dagger}{\varepsilon^\dagger} \right) \quad \text{and} \quad \tau_v = \frac{5h}{U_b} \tag{3.36}$$

where τ is the time step and U_b is the bulk velocity.

De Laage de Meux et al. (2015) showed the successful application of this method in case of homogeneous turbulence in LES, also with the example of a channel flow in zonal

hybrid RANS/LES approach it successfully displays the reduction obtained in the adaptation region. In addition to that, for isotropic turbulence, the ALF reduces to the isotropic linear forcing proposed by Lundgren (2003). In case of passive noise gap (acoustic excitation of a partially covered cavity), Erbig et al. (2018) showed that a hybrid RANS/LES approach consisting of EB-RSM and ALF produces a transient turbulent boundary layer upstream of the cavity whose mean velocity profile and wall pressure spectra compare well with the experimental data. Kempf et al. (2022) utilized a combination of a traditional recycling rescaling approach and an ALF, called recycling rescaling anisotropic linear forcing (RRALF) proposed by Kuhn (2021), to produce a high-quality turbulent flow needed to predict the acoustic sources.

Introducing a body force allows acting directly inside the flow unlike the synthetic turbulent fluctuations which acts only at the boundary. Compared to other forcing methods, volumic forcing presents a simpler way of implementation even for complex geometries and it is less CPU-consuming. This need for injecting turbulence in hybrid models at the RANS/LES interface is due to the fact that there is a region of adaptation to establish mature turbulence downstream of the interface. Without the injection, this region is too long (as seen in sections 2.4.3 and 2.4.4) and damages the whole solution. Implementation of these methods reduce the adaptation region but completely eliminating it is impossible. All the forcing methods discussed till now are based on the zonal RANS/LES approach rather than the global approach. In addition to that they require the target statistics to drive the force. This necessity of providing with the target statistics raises the need for the precursor DNS or well-resolved LES or in some case RANS computation, which increase the computational cost. In addition to this, the problem with these methods are that they are not compatible with continuous approaches.

3.3 Methodology for the Active Hybrid RANS/LES approach

The main objective of the filtering is to compute only the so-called large scale component of each variable of the flow, which eliminates from the instantaneous field any contribution of a scale smaller than the characteristic length scale of the filter. As can be seen from Fig. 3.1, upon changing the filter size or refining the mesh, there is a part of energy that was in the modeled part which goes to the resolved part.

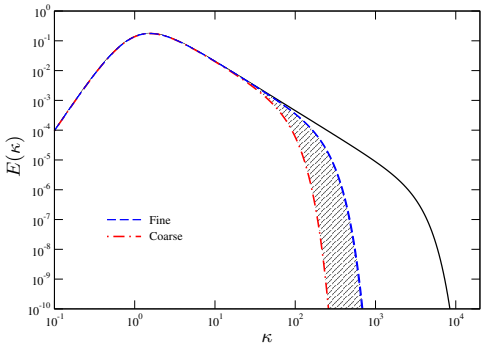

Figure 3.1 – Illustration of the transfer of energy from the modeled to the resolved part in hybrid RANS/LES due to a change in resolution, in spectral space.

Several authors (Ghosal et al., 1995; Germano, 2004; Fadai-Ghotbi et al., 2010; Wallin et al., 2011; Chaouat et al., 2013b; Davidson, 2016) have shown that when you derive an

equation for a filtered quantity, you have a term which arises due to the variation of the filter size in the equation. This term arises due to the fact that the filter does not commute with the derivatives. This term corresponds to the transfer of energy, which does not exist and missing in the model. We believe that this lack is the cause for not having fast enough growth in the resolved turbulent kinetic energy k_r. This section is dedicated to developing a model which corresponds to this mechanism.

3.3.1 Theoretical framework

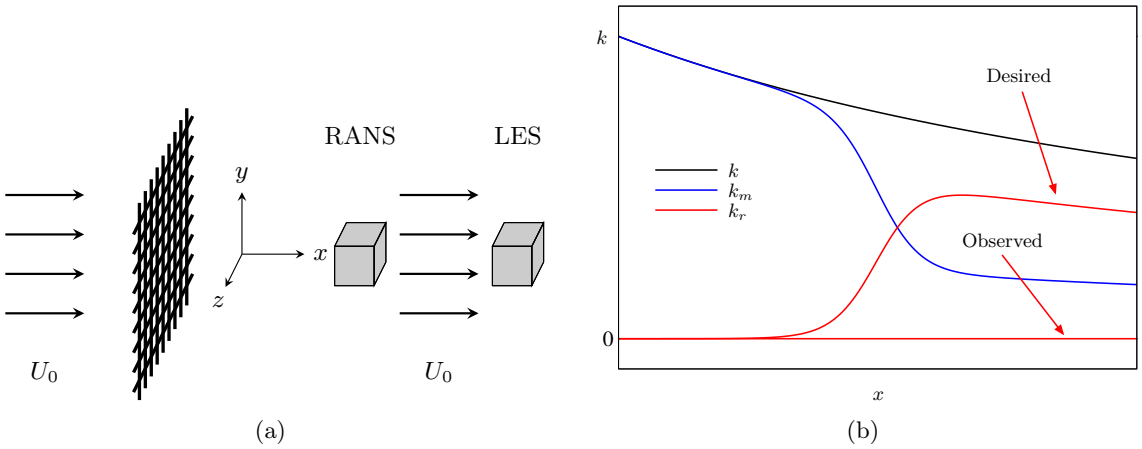

Figure 3.2 – Illustration of the problem of the absence of turbulent energy transfer between modeled and resolved part in grid turbulence. (a) Schematic view of a grid turbulence experiment. (b) Expected and observed behaviour of the turbulent energy partition in hybrid RANS/LES.

The simplified case of a RANS-to-LES transition in grid turbulence, as shown in Fig. 3.2(a), can be useful to illustrate the problem of the absence of energy transfer between modeled and resolved part via a thought experiment. In the RANS region, the resolved velocity is the mean velocity and the diffusion terms being zero due to the absence of velocity gradient, the momentum equation reduces to

$$\widetilde{u_j}\frac{\partial \widetilde{u_i}}{\partial x_j} = -\frac{1}{\rho}\frac{\partial \widetilde{p}}{\partial x_i} \tag{3.37}$$

whose solution is $0 = 0$. When the model is switched to LES by refining the mesh at a given position, the hybrid RANS/LES model strongly decrease the turbulent viscosity. However, the turbulent viscosity does not appear in Eq. (3.37), The RANS solution remains the solution even in the LES zone. This gives no reason for the resolved structures to appear earlier in the domain. Only the natural instability of the flow will make the resolved structures appear, which takes time. Fig. 3.2(b) shows the desired results for the resolved energy. It is obvious that modifying the model for the unresolved part can not correct this problem of not having enough resolved energy, since the model is not involved in Eq. (3.37). This loss of turbulent energy and decrease of total turbulent stresses which drives the mean momentum equation, affects the mean velocity profiles in the turbulent shear flows.

If one considers a flow without variation along the trajectories, for example a fully developed channel flow, the total turbulent kinetic energy is constant.

$$\frac{dk}{dt} = 0 \tag{3.38}$$

The instantaneous solution is of no interest for the moment, but only the averaged quantities: k_r and k_m are the Reynolds-averaged resolved and modeled turbulent kinetic energies,

respectively, and the total turbulent kinetic energy is $k = k_r + k_m$. If the grid spacing is constant, as in Fig. 3.4(a), then the energy partition does not change and the two contributions k_r and k_m are constant. Fig. 3.3(a) shows three different solutions that a hybrid RANS-LES model is supposed to give on three different meshes: a coarse constant mesh, a finer constant mesh and a mesh with an abrupt refinement. For an ideal hybrid method, one should obtain the same total turbulent energy in all three cases (partition of energy may vary but the total energy should remain the same). In practice, hybrid RANS-LES models are not "ideal", but this consideration must not interfere with the present analysis. Here, it is very important to note that we are only interested in the theoretical dependence of the variables on the grid step on which the filter size depends, independently of the discretization errors. It is therefore assumed, in an idealized way, that there is no numerical error, or in other words, that the numerical scheme is of infinite accuracy. Taking into account the numerical errors would not allow to consider that k is perfectly independent of Δ.

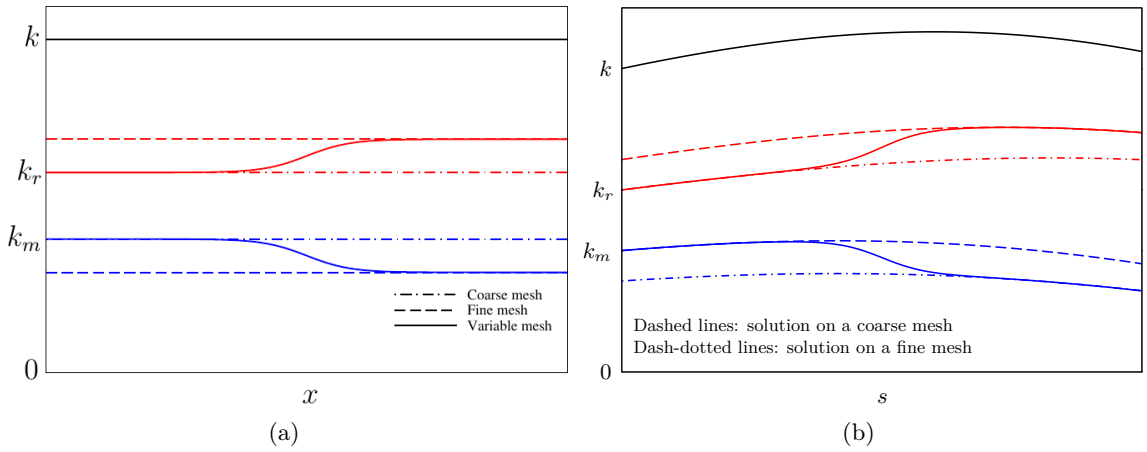

Figure 3.3 – Evolution of the energy partition in the flow direction with mean resolved energy k_r, mean modeled energy k_m and total energy $k = k_r + k_m$. (a) case of a flow invariant in the x-direction (fully developed channel flow). (b) general case. The dashed lines indicate the solutions obtained for a constant grid step. The solid lines indicate the solution obtained in the case of an abrupt refinement.

On the other hand, the energy partition between resolved and modeled parts is different on a coarse and a fine mesh. On the mesh with an abrupt refinement, the solution that would be obtained on the coarse mesh is abruptly replaced by the one that would be obtained on the fine mesh. What is plotted in the Fig. 3.3(a) is what we would ideally like to see, i.e., rapid compensation of reduced modeled energy k_m by the increased resolved energy k_r, such that the total energy k remains constant, when going from a coarse mesh to a fine mesh. This simplified analysis in the case of a flow invariant along the x-direction can be easily extended to a more general case, as shown in Fig. 3.3(b). All quantities now evolve in the direction of the flow, but it is still expected that the solution obtained for the total turbulent kinetic energy k is independent of the energy partition, and that, in the case of a mesh with abrupt refinement, the quantities k_r and k_m abruptly change from the solution on the coarse mesh to the solution on the fine mesh. In practice, this decrease of the modeled energy corresponds to a modification of the partition of the energy, which generates terms in the momentum equation that are not taken into account. This is exactly the issue addressed in this thesis.

In filtered approaches, it is easy to demonstrate (Fadai-Ghotbi et al., 2010) that when the filter size is varied (by refining the mesh), the equations display a term of energy

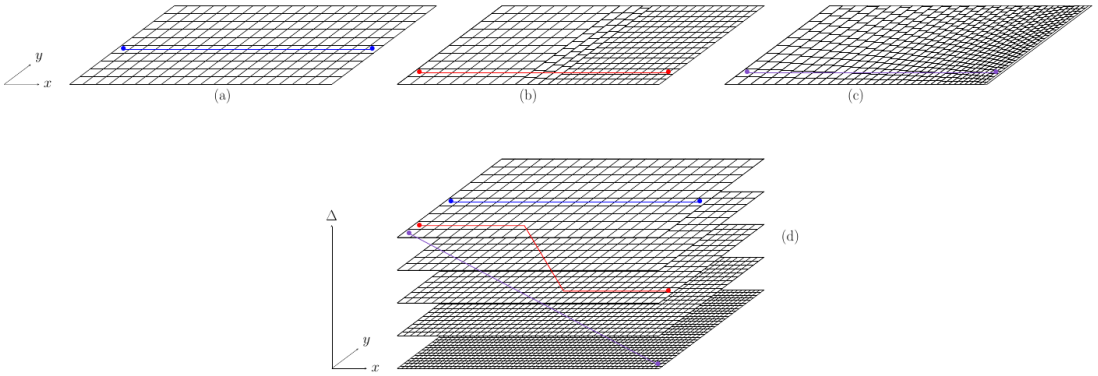

Figure 3.4 – Mesh in the (x-y) plane of a channel. (a) Uniform mesh; (b) Mesh with a sudden refinement; (c) Mesh with a gradual refinement; (d) View in the (x-y-Δ) space of the three trajectories shown in figures (a), (b) and (c).

transfer from the modeled part to the resolved part. Here, a different and simpler way of viewing this problem is used, which emphasizes the generality of the approach by not referring to a particular formalism. It simply considers that when the mesh size varies, the solution is changed. It is not a question of a dependence on the numerical scheme, but of a dependence of the model on the grid step. Thus, it is proposed to express any filtered field ϕ depending not only on the coordinates t and x_i, but also on the grid step Δ:

$$\phi\left(t, x_i, \Delta\right), \tag{3.39}$$

i.e., to describe the solutions as being part of a hyperspace of dimension five. Note that one could, in a completely equivalent way, express ϕ not as a function of Δ but as a function of the cut-off frequency ω_c or wavenumber κ_c, or of the energy ratio r as will be shown later on, but it is easier to visually represent a dependence on the grid step. As mentioned earlier in chapter 2, for the particular case of HTLES, the cut-off frequency ω_c is fixed by mesh size Δ only (refer to Eq. (2.23)). Note that for an anisotropic mesh, Δ can be computed in various ways (Piomelli, 2021), which does not interfere with the following analysis. In HTLES (Hybrid method used throughout the thesis), Δ is computed as the cubic root of the volume of the cell.

Fig. 3.4(d) provides a representation of this hyperspace, in which here, for obvious reasons, the two dimensions z and t are not represented. If we follow a fluid particle (blue trajectory) crossing a domain meshed with a constant grid step Δ, Fig. 3.4(a), its representation in the hyperspace (blue trajectory in Fig. 3.4(d)) remains in the subspace $\Delta = const$ represented by a horizontal plane. On the other hand, if we follow the fluid particle (red trajectory) in Fig. 3.4(b), where the mesh is suddenly refined, as in Fig. 3.3, the solution changes from a coarse-mesh solution to a fine-mesh solution, which, in the hyperspace, corresponds to the red trajectory that moves downward in the direction of small Δ's. The purple trajectory of Figs. 3.4(c) and (d) corresponds to the solution obtained on a gradually refined mesh.

This description in a five-dimensional hyperspace will allow us to distinguish, in the evolution of the different physical quantities, what is due to the dynamics of the flow from what is due to the changes in grid step. The total variation $\mathrm{d}\phi$ of the variable ϕ is expressed as

$$\mathrm{d}\phi = \frac{\partial \phi}{\partial t}\mathrm{d}t + \frac{\partial \phi}{\partial x_i}\mathrm{d}x_i + \frac{\partial \phi}{\partial \Delta}\mathrm{d}\Delta, \tag{3.40}$$

such that

$$\begin{aligned}\frac{\mathrm{d}\phi}{\mathrm{d}t} &= \frac{\partial \phi}{\partial t} + \frac{\partial \phi}{\partial x_i}\frac{\mathrm{d}x_i}{\mathrm{d}t} + \frac{\partial \phi}{\partial \Delta}\frac{\mathrm{d}\Delta}{\mathrm{d}t} \\ &= \frac{\partial \phi}{\partial t} + \nabla\phi \cdot U + \underbrace{\frac{\partial \phi}{\partial \Delta}\frac{\mathrm{d}\Delta}{\mathrm{d}t}}_{\text{Extra term}}\end{aligned} \tag{3.41}$$

which is nothing but the summation of the classical material derivative and the extra term due to the mesh variation. For the particular case of a constant grid step, this extra term disappears. Hence the material derivative of the filtered quantity can be decomposed into two parts:

$$\frac{\mathrm{d}\phi}{\mathrm{d}t} = \left.\frac{\mathrm{d}\phi}{\mathrm{d}t}\right|_{\Delta} + \left.\frac{\mathrm{d}\phi}{\mathrm{d}t}\right|_{t,x_i} \tag{3.42}$$

Following this standard notations, the derivative of the variable ϕ at constant Δ can be defined as:

$$\left.\frac{\mathrm{d}\phi}{\mathrm{d}t}\right|_{\Delta} = \frac{\partial \phi}{\partial t} + \nabla\phi \cdot U \tag{3.43}$$

It is the derivative taken in an horizontal plane in Fig. 3.4. Now,

$$\left.\frac{\mathrm{d}\phi}{\mathrm{d}t}\right|_{t,x_i} = \frac{\partial \phi}{\partial \Delta}\frac{\mathrm{d}\Delta}{\mathrm{d}t} \tag{3.44}$$

is the derivative at constant t and x_i. In other words, it is the part due only to the variations of Δ. It is the derivative taken in the vertical direction in Fig. 3.4. It is easy to interpret this term by looking at the quantities k, k_r and k_m. Indeed, as illustrated by Fig. 3.3(a) and (b), the total turbulent energy is independent of the grid step, and thus

$$\frac{\partial k}{\partial \Delta} = 0\ . \tag{3.45}$$

Since, $k = k_r + k_m$

$$\frac{\partial k_r}{\partial \Delta} = -\frac{\partial k_m}{\partial \Delta}\ , \tag{3.46}$$

which reflects the fact that a variation of the grid step leaves the total energy unchanged but changes the energy partition. As illustrated by Fig. 3.3, when the grid is refined, the increase of resolved energy and decrease of the modeled energy are expected to be by the same amount. The term

$$\frac{\partial k_r}{\partial \Delta}\frac{d\Delta}{dt} = -\frac{\partial k_m}{\partial \Delta}\frac{d\Delta}{dt} \tag{3.47}$$

then represents the rate of energy transfer from the modeled part to the resolved part. It is therefore clear that this term must appear in the evolution equations of these quantities. However, this mechanism does not exist in the models and therefore must be introduced (It is important to note here that the mechanism to reduce the modeled energy k_m exists in the models, but not the counterpart to increase the resolved energy k_r.). For the moment, we are relying on the natural growth of resolved energy, mostly due to shear instabilities, which is not sufficient. We believe that this is the main cause for the grey area issue. Hence, this missing mechanism for generating resolved energy must be introduced. Interestingly, by deriving the subfilter energy equations in the case of a variable filter, Chaouat (2017) showed that different terms appear related to the non-commutativity of the filter with

the differential operators, and that the term Eq. (3.47), originating from the material derivative, is the dominant term. Our analysis shows that this additional term arises from the variations of the grid step, independent of any underlying formalism and is therefore valid for any scale-resolving approach in which the partition of energy is related to the grid step (or any other resolution parameter), such as the widely spread DES, DDES or PANS approaches, and even pure LES.

In the framework of the HTLES model, the size of the filter can, possibly, be related to the time step τ , according to Eq. (2.23). Thus, there is also a sensitivity of the solution to the time step, and the extra term must be replaced by

$$\left.\frac{\mathrm{d}\phi}{\mathrm{d}t}\right|_{t,x_i} = \frac{\partial\phi}{\partial\Delta}\frac{\mathrm{d}\Delta}{\mathrm{d}t} + \frac{\partial\phi}{\partial\tau}\frac{\mathrm{d}\tau}{\mathrm{d}t} \tag{3.48}$$

In regions where the temporal filter width Δ_T is fixed by τ , the term $\partial\phi/\partial\Delta$ is zero and in regions where Δ_T is fixed by Δ, the term $\partial\phi/\partial\tau$ is zero. Note that, in most of the usual simulations, the time step is constant and thus $d\tau/dt = 0$. However, since the material derivatives inherently involves time derivatives, Eq. (3.48) encompasses cases where the time step or the grid step vary in time, such as with automatic mesh refinement methods.

3.3.2 Modelling of the energy transfer due to variations of the resolution

In the situation described in Fig. 3.3, where the mesh is abruptly refined, the HTLES turbulence model is sensitized to the variation of Δ because the transport equation of the subfilter energy

$$\frac{\mathrm{d}k_{\mathrm{sfs}}}{\mathrm{d}t} = P_{\mathrm{sfs}} + D_{\mathrm{sfs}} - \frac{k_{\mathrm{sfs}}}{T_m} \tag{3.49}$$

involves T_m which depends on the energy ratio r, which in turn depends on Δ as shown in Eq. (2.27). In other words, due to this dependence on Δ, the lhs of Eq. (3.49) represents the total variation of k_{sfs}, i.e., both the terms of Eq. (3.42).

$$\frac{\mathrm{d}k_{\mathrm{sfs}}}{\mathrm{d}t} = \left.\frac{\mathrm{d}k_{\mathrm{sfs}}}{\mathrm{d}t}\right|_{\Delta} + \left.\frac{\mathrm{d}k_{\mathrm{sfs}}}{\mathrm{d}t}\right|_{t,x_i} \tag{3.50}$$

A refinement of the mesh results in a decrease of r and T_m, and consequently a decrease of k_{sfs}. The Reynolds average $k_m = \overline{k_{\mathrm{sfs}}}$ will therefore decrease. It is well known that in the case of abrupt refinement, one cannot rely on a rapid increase in resolved fluctuations to create resolved energy, so that in the situation of Fig. 3.3, the increase of k_r will not be rapid enough to compensate for the decrease of k_m. This phenomenon is known as modelled stress depletion (MSD). The reason being the absence of the term which corresponds to the transfer of energy between modeled and resolved parts (the second term of Eq. (3.50)).

As the resolved momentum equation does not contain this corresponding term, the only way to introduce a source of resolved energy is to add a force to the resolved momentum equation. It is therefore proposed here to use a fluctuating force similar to the one used in the ALF method of De Laage de Meux et al. (2015) to generate fluctuations and introduce the required energy into the resolved motion.

A fluctuating force of the form:

$$f_i = A_{ij}\widetilde{u_i} + B_i, \tag{3.51}$$

which linearly depends on the resolved(filtered) velocity $\widetilde{u_i}$ is introduced. As mentioned in section 3.2.5 about the ALF, the averaged effect of the force can be analyzed by looking at the mean momentum equation and the equation for the mean resolved stress. A mean

force appears in the mean momentum equation, which must be equal to zero, because one does not want to influence the mean velocity. Hence,

$$\overline{f_i} = A_{ij}\overline{\widetilde{u_j}} + B_i = 0 \tag{3.52}$$

The production term of the resolved turbulent kinetic energy k_r being half the trace of the resolved stresses $\overline{u_i'u_k'}$, can be written as

$$T^f = A_{ik}\overline{u_i'u_k'} \tag{3.53}$$

which is nothing else than the average work done by the force per unit time. If we want this power to be equal to the energy decrease in the modeled part due to the variations of Δ, the relation to satisfy is

$$A_{ik}\overline{u_i'u_k'} = -\frac{\partial k_m}{\partial \Delta}\frac{\mathrm{d}\Delta}{\mathrm{d}t} \ . \tag{3.54}$$

Individually, each component must satisfy

$$T_{ij}^f = A_{ik}\overline{u_j'u_k'} + A_{jk}\overline{u_i'u_k'} = -\frac{\partial \tau_{ij}^m}{\partial \Delta}\frac{\mathrm{d}\Delta}{\mathrm{d}t} \tag{3.55}$$

where τ_{ij}^m is the Reynolds average of the modeled subfilter-stress tensor, $\tau_{ij}^m = \overline{\tau_{ij\mathrm{sfs}}}$. Anisotropy is simply accounted for by assuming

$$\frac{\partial \tau_{ij}^m}{\partial \Delta} \simeq \frac{\tau_{ij}^m}{k_m}\frac{\partial k_m}{\partial \Delta} \tag{3.56}$$

which is compatible with the Eq. (3.54). Now, the modeled turbulent kinetic energy k_m is defined as Eq. (2.25) such that

$$\frac{\partial k_m}{\partial \Delta} = \frac{2\varepsilon^{2/3}}{3\beta_0\pi^{2/3}}\Delta^{-1/3} \tag{3.57}$$

Here, we have assumed that the time step τ is sufficiently small. Finally,

$$\frac{1}{k_m}\frac{\partial k_m}{\partial \Delta} = \frac{2}{3\Delta} \tag{3.58}$$

which leads to

$$\frac{\partial \tau_{ij}^m}{\partial \Delta} = \frac{2}{3}\frac{1}{\Delta}\tau_{ij}^m \tag{3.59}$$

The conclusion of this analysis is that, at each point in the domain, the following system of equations must be resolved to determine the values of A_{ij} and B_i, which defines the fluctuating force f_i at each point.

$$A_{ij}\overline{\widetilde{u_j}} + B_i = 0 \tag{3.60a}$$

$$A_{ik}\overline{u_j'u_k'} + A_{jk}\overline{u_i'u_k'} = -\frac{2}{3}\mathcal{C}\tau_{ij}^m\frac{1}{\Delta}\frac{\mathrm{d}\Delta}{\mathrm{d}t} \tag{3.60b}$$

Note that a coefficient $\mathcal{C}$ has been introduced in the right hand side of Eq. (3.60). The analytical derivation above shows that $\mathcal{C} = 1$, but in practice, this coefficient introduces a degree of freedom to adjust the intensity of the forcing. Finally, it can be noticed that, since T^f is an energy transfer from k_m to k_r, the term

$$\frac{2}{3}k_m\frac{1}{\Delta}\frac{d\Delta}{dt} \tag{3.61}$$

appears in the transport equation for the modeled energy. However, the theoretical framework of HTLES shows that the reduction of modeled energy can be accounted for by substituting k_{sfs}/T_m for the dissipation in Eq. (3.49), which means that the effect of the term in Eq. (3.61) is already represented in the model.

3.3.3 Accounting for the shielding functions

The forcing given by Eq. (3.60) is general and applicable to any mesh-dependent hybrid RANS/LES approach, since Eq. (3.58) simply assumes a Kolmogorov spectrum. Like in the HTLES model, many hybrid RANS/LES approaches introduce shielding functions such that, the dependence of the solution on the grid step Δ is disrupted near the walls. Therefore, it makes more sense in this case to consider the dependence of the solution on the energy ratio r directly,

$$\phi\left(t, x_i, r\right) \tag{3.62}$$

which yields

$$\frac{\mathrm{d}\phi}{\mathrm{d}t} = \frac{\partial\phi}{\partial t} + \nabla\phi \cdot U + \frac{\partial\phi}{\partial r}\frac{\mathrm{d}r}{\mathrm{d}t} \ . \tag{3.63}$$

Upon following the same analytical procedure as section 3.3.2,

$$T^f = -\frac{\partial k_m}{\partial r}\frac{\mathrm{d}r}{\mathrm{d}t} \ . \tag{3.64}$$

Now, $k_m = rk$ and k is independent of the energy ratio r, such that

$$T^f = -k\frac{\mathrm{d}r}{\mathrm{d}t} \ . \tag{3.65}$$

Subsequently, Eq. (3.60) is simply replaced by

$$A_{ik}\overline{u_j' u_k'} + A_{jk}\overline{u_i' u_k'} = -\mathcal{C}\tau_{ij}^m \frac{1}{r}\frac{\mathrm{d}r}{\mathrm{d}t} \ . \tag{3.66}$$

This expression thus makes it possible to take into account a more complex formulation of r than a simple dependence on the grid step Δ.

However, in the case when r directly depends on Δ through

$$r = \frac{1}{\beta_0}\left(\frac{\pi}{\Delta}\frac{k^{3/2}}{\varepsilon}\right)^{-2/3} \ , \tag{3.67}$$

which is the case in most of the domain, the two formulations are strictly equivalent. Indeed,

$$\frac{1}{r}\frac{\mathrm{d}r}{\mathrm{d}t} = \frac{1}{r}\frac{\partial r}{\partial\Delta}\frac{\mathrm{d}\Delta}{\mathrm{d}t} = \frac{2}{3}\frac{1}{\Delta}\frac{\mathrm{d}\Delta}{\mathrm{d}t} \ . \tag{3.68}$$

To summarize, the system of equations to be solved is

$$A_{ij}\widetilde{u_j} + B_i = 0 \ , \tag{3.69a}$$

$$A_{ik}\overline{u_j' u_k'} + A_{jk}\overline{u_i' u_k'} = -\mathcal{C}\tau_{ij}^m \frac{1}{r}\frac{\mathrm{d}r}{\mathrm{d}t} \ . \tag{3.69b}$$

Similarly, the model can be extended to any resolution parameter.

3.4 Conclusion

In hybrid RANS/LES methods, when the flow transitions from a RANS zone to a LES zone, there is a shift from fully modeled to partially resolved quantities. This transition necessitates compensating for the reduction in modeled energy with an increase in resolved energy. Unfortunately, the growth of resolved fluctuations relies solely on natural instabilities and is not sufficiently rapid to counterbalance the stress decay imposed by the model.

A simple analysis in spectral space reveals that the missing element is the transfer of energy from the modeled component to the resolved component, since the momentum equation remains unaffected by variations in grid resolution.

To address this issue, a method is proposed to model the commutation terms resulting from grid step variations, which are responsible for this energy transfer but are commonly disregarded, through the use of a fluctuating volume forcing. It is demonstrated that the intensity of this force can be determined by equating the work done by the force per unit time to the decrease in modeled energy caused by grid step variations.

This novel approach, referred to as *active* hybrid RANS/LES, has the potential to be applied to any hybrid RANS/LES method, provided a parameter driving the RANS-to-LES transition can be identified. Importantly, this method is highly versatile as it does not require information about the interface between RANS and LES regions; it relies solely on local quantities, particularly the material derivative of the resolution parameter.

CHAPTER 4

Validation of Active HTLES methodology

This chapter is dedicated to validate the newly proposed methodology in the previous chapter by testing it against the pre-existing model. The first half of the chapter is dedicated to compare this *active* approach with the Anisotropic Linear Forcing (ALF) method in the 3-hill case to investigate the validity of the new approach. The later half of the chapter is dedicated to test the model against a more realistic scenario (5-hill case) with three regions (RANS-LES-RANS) with continuous transition between them to establish the effectiveness of the model.

Contents

4.1 Introduction

The methodology for the active approach has been established in the previous chapter. It is necessary to test this new methodology (i) against HTLES to see if the *grey area* problem is reduced, and (ii) against the pre-existing volumic forcing method ALF, since it was successfully tested previously. Since the *active* approach is a modification of the Anisotropic Linear Forcing (ALF) method developed by De Laage de Meux et al. (2015), it is necessary to check that the modification of the source term of the system solved to compute the amplitude of the forcing introduces the correct amount of resolved energy. Hence, the ALF method serves as the reference method for generating resolved fluctuations to test against the *active* approach.

4.2 Comparison with Anisotropic Linear Forcing

The Active approach for volumic forcing given in section 3.3 is a modification of the original ALF method. The ALF method was proposed with the purpose of providing the flow with fluctuations at the entrance of a LES domain that satisfy a desired statistical state in a zonal hybrid RANS/LES approach, with an overlap of the RANS and LES zones. In the overlap zone, the intensity of the forcing is driven by the statistics given by the RANS zone.

In order to validate that the active approach, which does not use RANS statistics, works similarly to the original ALF, a configuration that makes it possible to compare the two approaches has to be considered. Unlike the original composition discussed in section 3.2.5, where the flow is driven by the mean velocity, here to make a fair comparison, the ALF is not forced towards an imposed velocity field, hence Eq. (4.1b). The new system of equations for ALF is written as:

$$A_{ik}\overline{u'_j u'_k} + A_{jk}\overline{u'_i u'_k} = \frac{1}{\tau_r}\left(\tau^{\dagger}_{ij} - \overline{u'_i u'_j}\right) , \tag{4.1a}$$

$$A_{ij}\widetilde{u_j} + B_i = 0 . \tag{4.1b}$$

where τ_r is the relaxation time for resolved stress tensor.

$$\tau_r = \max\left(2\tau, 0.01\frac{k^{\dagger}}{\varepsilon^{\dagger}}\right) \tag{4.2}$$

We recall that the system of equations for the active approach is:

$$A_{ik}\overline{u'_j u'_k} + A_{jk}\overline{u'_i u'_k} = -\mathcal{C}\tau^m_{ij}\frac{1}{r}\frac{\mathrm{d}r}{\mathrm{d}t} , \tag{4.3a}$$

$$A_{ij}\widetilde{u_j} + B_i = 0 . \tag{4.3b}$$

where $\mathcal{C}$ is a coefficient.

4.2.1 Comparison using the coefficient $\mathcal{C} = 1$

Three different approaches are compared: i) the standard HTLES; ii) a zonal RANS-LES coupling using the ALF in the overlap region; and iii) the newly proposed *active* HTLES. To compare these different methodologies, a channel simulation with periodic constriction has been performed, this time not in a periodic domain, but in a spatially developing domain, with input and output boundaries. The computational domain contains n inter-hills subdomains bounded by $n+1$ hills. The entrance and the exit of the domain is located

at the tops of the hills. The first and the last hills are in fact half-hills. This is the reason why we call the case with $n = 3$ the 3-hills case and the case with $n = 5$ the 5-hills case. Here for the validation of the active approach against ALF approach, $n = 3$ is used. Note that the term subdomain is used here for the convenience in describing the region between two successive hills, but there is only one computational domain.

In order to decouple the numerical issues from the modeling issue and also to avoid problems of connections between areas refined differently by unstructured or non-conformal meshes, the simulations are performed using the same mesh in each subdomain, which is fine enough for HTLES.

The flow is characterized by the bulk Reynolds number, $Re_b = U_b h/\nu = 10595$, where U_b is the bulk velocity and h is the height of the hill. The size of each subdomain is $L_x \times L_y \times L_z = 9h \times 3.035h \times 4.5h$, discretized such that $N_x \times N_y \times N_z = 80 \times 80 \times 40$, keeping $\Delta y^+ \simeq 1$. It is also important to mention that the shielding is activated, keeping the model in RANS mode up to $y^+ \simeq 100$. The transition between RANS mode at the inlet and downstream LES mode is imposed by prescribing a spatial evolution of the resolution parameter r in the model. On the other hand, in the LES region, r is still given by Eq. (2.33).

The reference solution is the periodic HTLES solution presented in section 2.4.2. Here to get rid of the influence of a RANS solution which introduces an additional deviation from the periodic HTLES, the inlet condition imposed at $x/h = 0$ is the time averaged periodic HTLES solution. The ALF consists of two overlapping zones: the upstream zone, which only contains the flow statistics and provides the target Reynolds-stress tensor $\tau_{ij}^{\dagger}$; and the downstream zone, treated with HTLES in LES mode. In the overlap zone, which covers the region $x/h \in [0, 2]$, the ALF is activated. As mentioned earlier, to get rid of the influence of a RANS model, here the target solution is obtained from averaging in time the periodic HTLES, which is viewed as an ideal RANS computation: the computation in the upstream zone corresponds to the periodic HTLES computation, which in practice is performed in advanced.

In order to make a fair comparison between different approaches, the same input conditions are used, with the averaged velocity profile obtained in periodic HTLES, and also k_{sfs} equal to the total turbulent energy. For the HTLES+ALF approach, since it is zonal, the LES mode of HTLES is activated in all the downstream domain. In contrast, for HTLES and active HTLES, which are continuous approaches, a general RANS-to-LES transition is imposed (refer to Fig. 4.1). At the input, the RANS mode is activated by imposing $r = 1$ in the model. A transition from RANS to LES is imposed gradually from $x/h = 0$ to $x/h = 2$, by enforcing a modified energy ratio r_{mod}:

$$r_{\text{mod}} = f + (1 - f)r \quad \text{with} \quad f\left(\frac{x}{h}\right) = 1 - \frac{x}{2} \quad \text{for} \quad x/h \in [0, 2] \tag{4.4}$$

such that r gradually reduces from $r = 1$ at the inlet to the values in HTLES given by Eq. (2.33). After $x/h = 2$, the LES mode is activated.

From Figs. 4.4 and 4.5, it can be seen that in the case of the standard HTLES, without the introduction of forcing, the recovery of the total turbulent kinetic energy is very slow. Just after the inlet ($x/h \simeq 0$), the turbulent energy is virtually equal to the one of the periodic case, since it is entirely modeled ($r = 1$, RANS mode, refer to Figs. 4.7a and 4.8a) and the periodic profile of the total turbulent energy is imposed as the inlet condition for the modeled energy k_{sfs}. In the RANS-to-LES transition region ($x/h \in [0, 2]$), k_{sfs} is gradually decreased according to the Eq. (4.4). The growth of the resolved turbulent energy is supposed to compensate for this decrease. However, Figs. 4.4, 4.5 and 4.8 show that this compensating mechanism does not work. In reality, the total turbulent energy remains

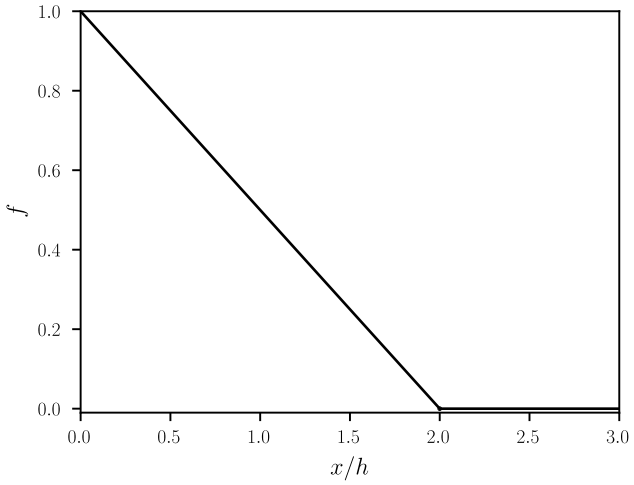

Figure 4.1 – Shape of the function f to impose a gradual transition from RANS-to-LES.

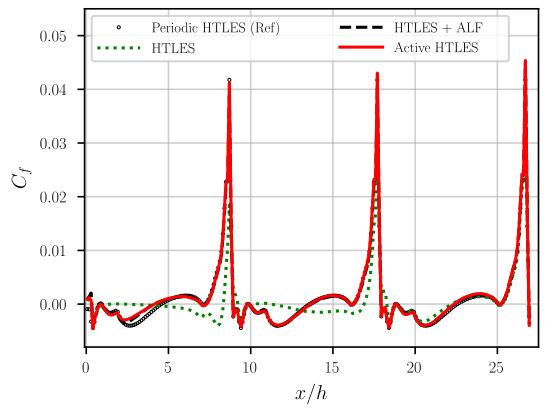

Figure 4.2 – Skin friction coefficient along the lower wall. Comparison of Periodic HTLES, HTLES without forcing, HTLES+ALF and Active HTLES with $\mathcal{C} = 1$.

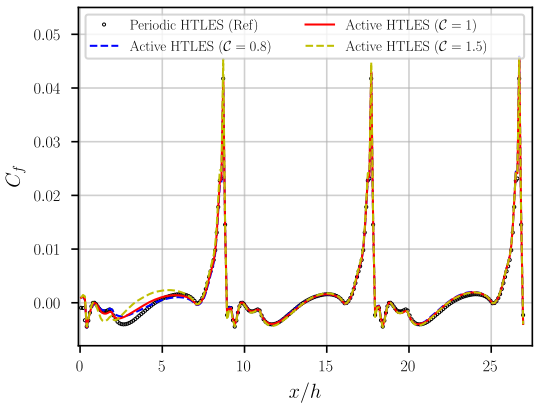

Figure 4.3 – Skin friction coefficient along the lower wall for different coefficient $\mathcal{C}$ values.

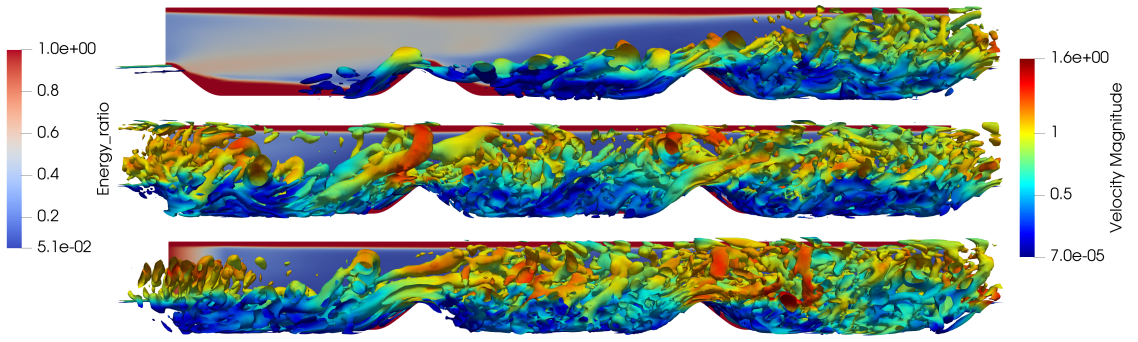

Figure 4.4 – Isocontours $Q = 0.2U_b^2/h^2$ colored with the velocity magnitude and, in the background, modeled-to-total turbulent energy ratio r, indicating the regions solved in RANS ($r = 1$) and in LES ($r < 1$). Top: Without forcing, Middle: HTLES + ALF, Bottom: Active HTLES. For ALF and active HTLES, the RANS-to-LES transition in $x/h \in [0, 2]$ is forced.

very small in the first subdomain ($x/h \in [0, 9]$). The energy starts increasing essentially in the detached sheared layer, only in the second subdomain ($x/h \in [9, 18]$); and eventually recovers the expected level towards the end of the third subdomain ($x/h > 24$). It is important to recall that there is only one computational domain and the term subdomain is used to identify the regions between two successive hills. From Figs. 4.7 and 4.8, it is observed that the model takes very long time to reach the correct energy ratio ($x/h > 24$), which is in sync with the behaviour of the total turbulent energy and its development. Fig. 4.7 shows the desired (or target) energy ratio, i.e., the ratio r imposed in the model given by Eq. (4.4). Fig. 4.8 shows the observed energy ratio, i.e. the ratio of the modeled to the total turbulent energy actually measured during the computation. Ideally, the desired and observed ratios match, but there is no mechanism to impose it in the computation. Here, the two ratios don't matter at all in the first two subdomains. The overestimation of r_{observed} is due to the very slow development of the turbulent structures and thus of the resolved energy.

This has a great influence on the velocity profiles, presented in Fig. 4.6. The lack of mixing of momentum by the turbulent structures is at the origin of a too weak entrainment and thus of an underestimation of the backward velocity and an overestimation of the size of the recirculation zone. As a result, the friction coefficient C_f is very poorly reproduced until the end of the subdomain 2 (refer to Fig. 4.2). When the turbulent energy in the third subdomain reaches the correct level, the velocity profiles are much better predicted and C_f also tends towards the value obtained in the periodic computations when approaching the last hill.

In contrast, it can be seen that the ALF is very efficient in generating resolved energy quickly and thus maintaining a total turbulent energy level along with the observed energy ratio in close proximity with the periodic computations (refer to Figs. 4.5, 4.6, and 4.8). This is achieved by forcing at each point in the region $x/h \in [0, 2]$ towards the target values according to Eq. (4.1). However, after the end of the forcing region, (Fig. 4.5a) at $x/h = 4$, a part of the generated fluctuations are dissipated, and the turbulent energy is slightly underestimated. However, at the end of the first subdomain, the total turbulent energy (Fig. 4.5a), the velocity profile (Fig. 4.6a) and the friction coefficient (Fig. 4.2) are very well reproduced. The results are in almost perfect agreement with the periodic results from the middle of the second subdomain (refer to Figs. 4.2, 4.5b, 4.6b, 4.7b and 4.8b). It should be noted here that the coefficient $\mathcal{C} = 1$ is used in Eq. (4.3). A comparative study of various coefficients is presented later in this section.

The challenge for the new forcing method, which has no target field but is simply based on the estimate of the energy rate to be injected into the resolved part of the momentum equation (refer to Eq. (4.3)), is to approach the very good results obtained with the ALF. The activation of the forcing is related to the transition from RANS-to-LES driven by Eq. (4.4), which generates a decrease of energy ratio r along the streamlines. It is observed that in the middle of the RANS-to-LES transition zone, at $x/h = 1$, the total turbulent energy is underestimated (refer to Fig. 4.5a); meaning that the modeled energy has been reduced by the HTLES model (refer to Fig. 4.8a) but the fluctuating energy generated by the forcing is not yet sufficiently developed. On the other hand, a slight overestimation of the turbulent energy in the detached shear layer and in the recirculation zone, with a stronger overshoot in the core of the flow is observed at the end of the transition zone ($x/h = 2$). The velocity profiles (refer to Fig. 4.6a) are slightly less accurate compared to the ALF method. However, it can be seen that from the end of the first subdomain, the results given by the active HTLES method are in close agreement to those given by the ALF and the periodic HTLES. This is true for the turbulent kinetic energy (Fig. 4.5a), the mean velocity (Fig. 4.6a), and the energy ratio (Fig. 4.8a). It is remarkable that the

friction coefficient (refer to Fig. 4.2) remains virtually identical to that obtained with the ALF and tends to the periodic HTLES values as soon as the middle of the first subdomain.

Finally, one can wonder if active HTLES is able to reproduce the anisotropy of turbulence as well as the ALF which is imposing the different components through Eq. (4.1a). It can be seen in Fig. 4.9 that the ALF indeed imposes the correct components individually in a very accurate way at the end of the forcing region (refer to Fig. 4.9b). With active HTLES, the prediction can be considered very satisfactory in the shear layer, considering the fact that there are no target statistics but only an evolution of the transfer of energy, made anisotropic using hypothesis (refer to Eq. (3.56)). It is noticeable that the kinetic energy overshoot in the upper half of the channel is only visible on the diagonal component which are not active in the momentum equation, and not on the shear stress: this explains why this overshoot is not detrimental to the prediction of the mean velocity field. In Fig. 4.9c, it is observed that this overshoot is still visible in the upper half, but in the lower half, the prediction of active HTLES are globally as good as those of the ALF. In the second subdomain (refer to Figs. 4.9d and 4.9e), the two approaches give very similar Reynolds stress components, and the active HTLES is even surprisingly better at $x/h = 11$.

4.2.2 Influence of different coefficient values

In the previous section, results were obtained using the coefficient $\mathcal{C} = 1$ in Eq. (4.3a) for active HTLES. In this section, the influence of the value of the coefficient is investigated.

An increase in the coefficient $\mathcal{C}$ accelerates the production of resolved energy, at the cost of a very strong overshoot at the end of the transition region; a decrease of $\mathcal{C}$ suppresses the overshoot in particular in the upper half of the channel, but finally degrades the results at the exit of the transition region in $x/h = 2$ (refer to Fig. 4.10). A small overshoot is desirable, as a part of the resolved energy generated by the fluctuating force is dissipated. But as the value of the coefficient $\mathcal{C}$ increases, this overshoot of energy becomes larger, which is not desired.

Fig. 4.11 shows that this overshoot has a significant detrimental influence on the velocity profiles, at least in the first subdomain. From Fig. 4.3, it can be seen that when the coefficient is increased above 1, the separation zone and the reattachment zone is highly overestimated in the first subdomain ($x/h < 9$), where as the opposite is true when the coefficient is reduced. In the beginning of the second subdomain slightly deteriorated results are observed, but from $x/h \simeq 13$ onwards, the results are in close agreement with those of the active HTLES with coefficient's value of unity. Considering all the variables, it is considered that the coefficient $\mathcal{C} = 1$ is a good choice. In general, $\mathcal{C} = 1$ provides the best suitable results for all the quantities of interest.

An increase in the coefficient $\mathcal{C}$ accelerates the production of resolved energy, at the cost of a stronger overshoot at the end of the transition region; a decrease of $\mathcal{C}$ suppresses the overshoot but finally degrades the results at the exit of the transition region (refer to Fig. 4.10). A small overshoot is desirable, as a part of the resolved energy generated by the fluctuating force is dissipated. But as the value of the coefficient $\mathcal{C}$ increases, this overshoot of energy becomes larger, which is not desired. Hence, coefficient $\mathcal{C} = 1$ is an ideal choice. Whereas, from the velocity profiles in Fig. 4.11, it is seen that the decreasing the coefficient's value to $\mathcal{C} = 0.8$ predicts the results in closer proximity to the periodic results compared to the other coefficients used. But in general, $\mathcal{C} = 1$ provides the best suitable results for all the quantities of interest.

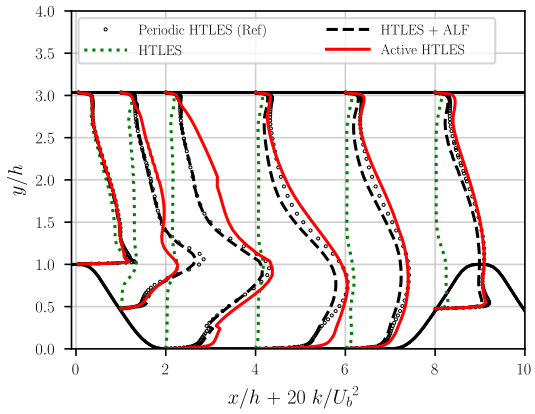

(a) subdomain 1

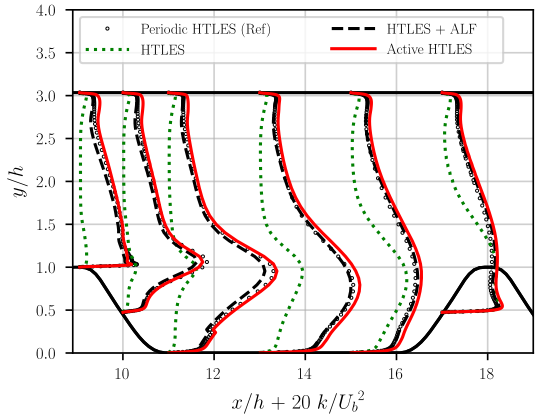

(b) subdomain 2

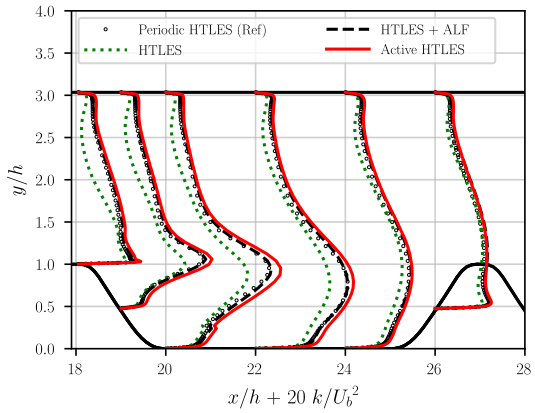

(c) subdomain 3

Figure 4.5 – Profiles of total turbulent kinetic energy in different subdomains. Comparison of periodic HTLES, HTLES without forcing, HTLES with ALF and Active HTLES, both with a forcing in the region $x/h \in [0, 2]$.

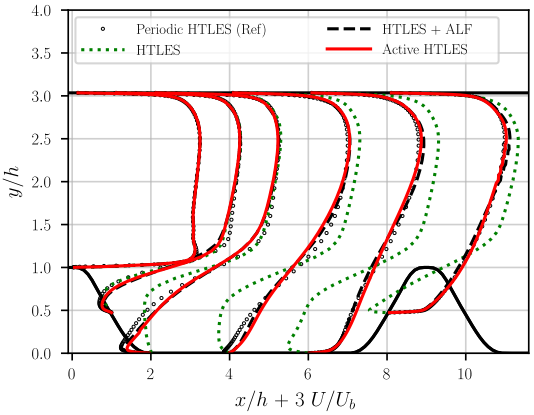

(a) subdomain 1

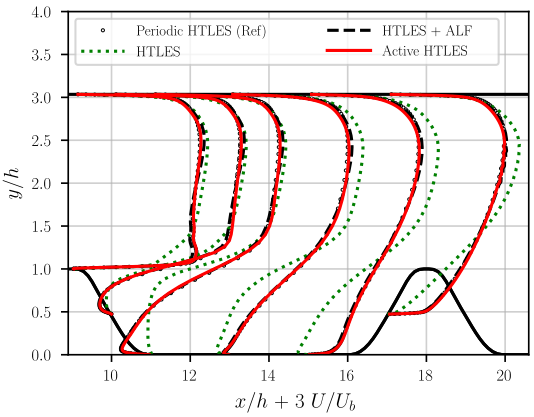

(b) subdomain 2

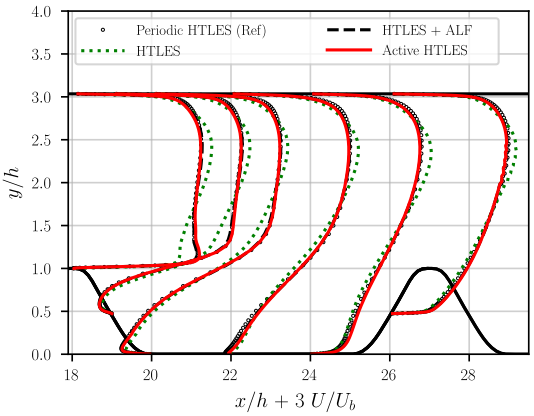

(c) subdomain 3

Figure 4.6 – same figure as Fig. 4.5 for the mean velocity.

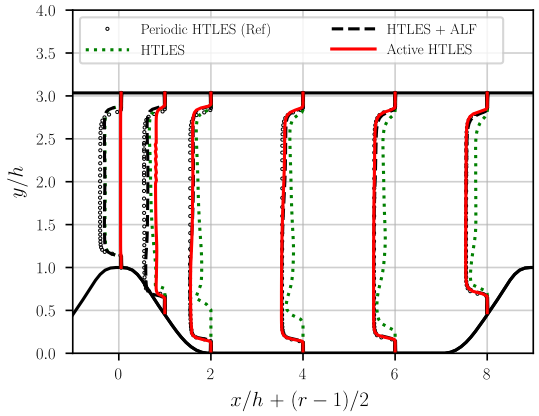

(a) subdomain 1

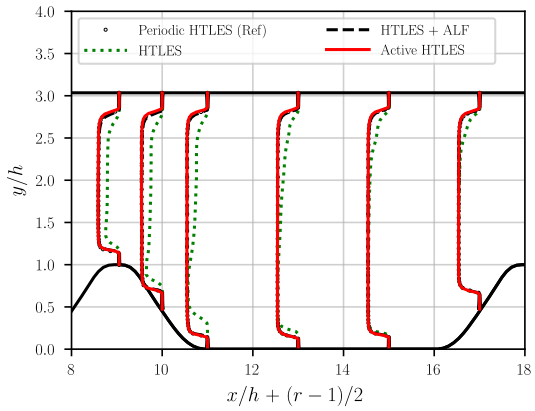

(b) subdomain 2

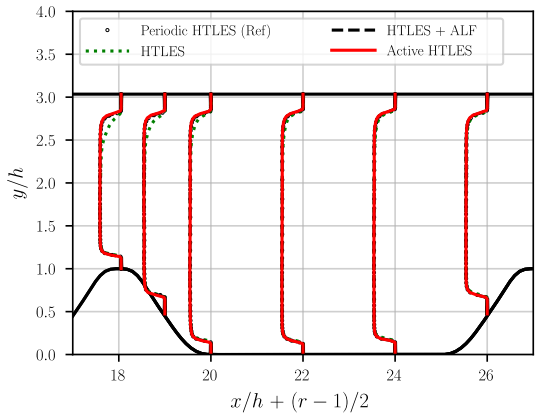

(c) subdomain 3

Figure 4.7 – Profiles of energy ratio (desired) in different subdomains. Comparison of periodic HTLES, HTLES without forcing, HTLES with ALF and Active HTLES, both with a forcing in the region $x/h \in [0, 2]$.

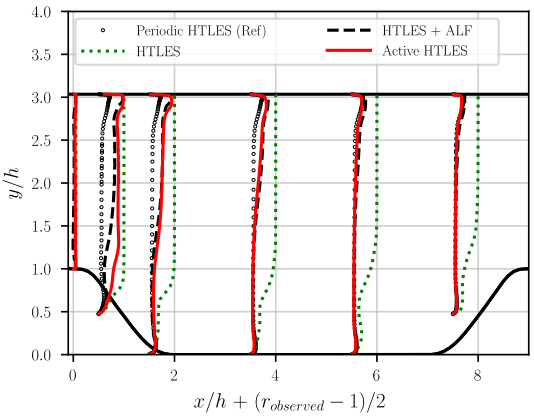

(a) subdomain 1

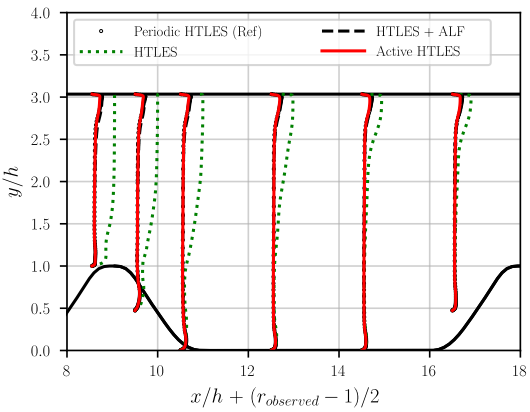

(b) subdomain 2

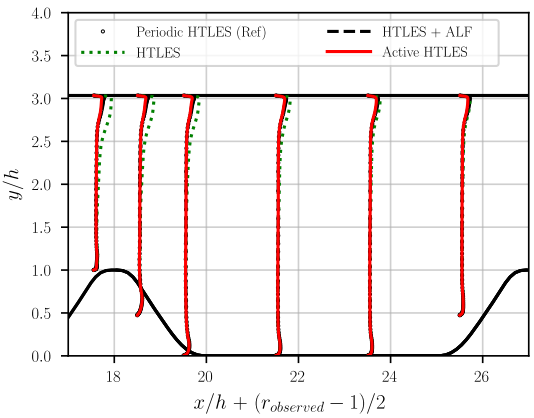

(c) subdomain 3

Figure 4.8 – same figure as Fig. 4.7 for the observed energy ratio k_m/k.

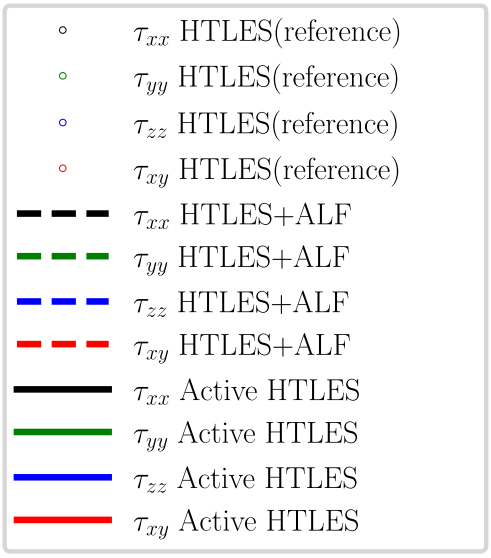

(a) Legends

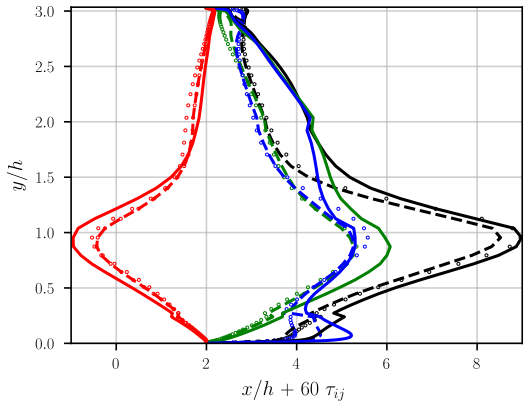

(b) at $x/h = 2$

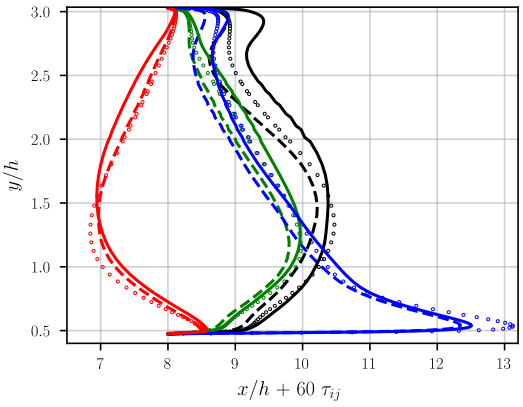

(c) at $x/h = 8$

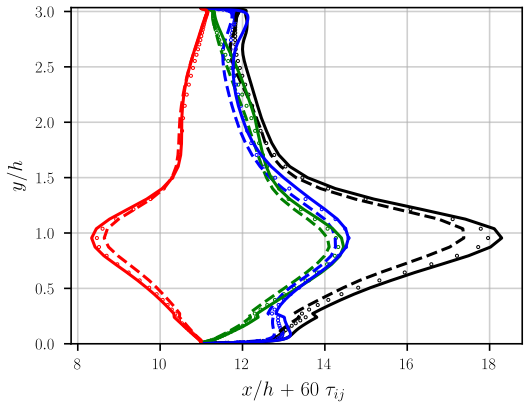

(d) at $x/h = 11$

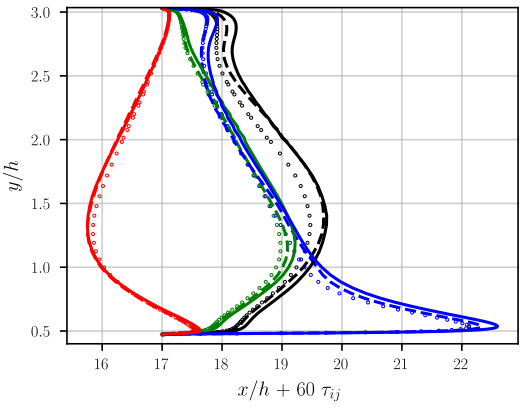

(e) at $x/h = 17$

Figure 4.9 – Profiles of Reynolds stresses at different streamwise locations. Comparision of periodic HTLES, HTLES with ALF and Active HTLES, both with a forcing in the region $x/h \in [0, 2]$.

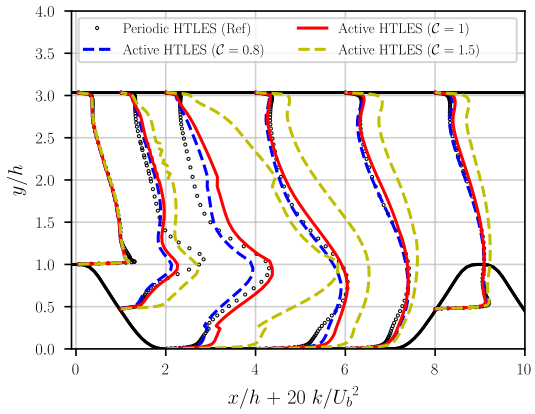

(a) subdomain 1

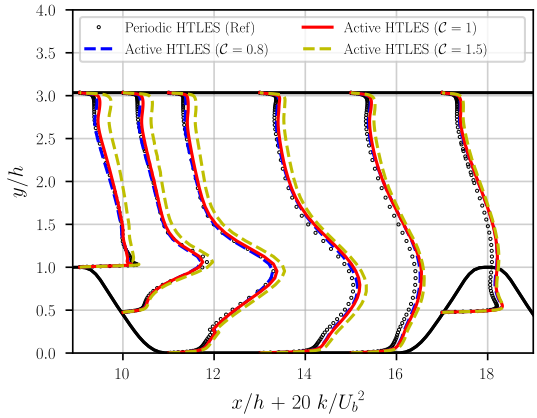

(b) subdomain 2

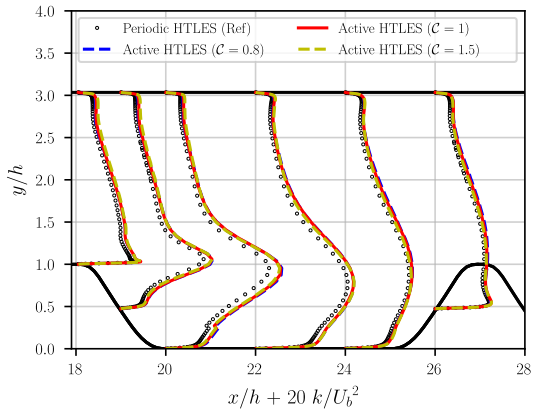

(c) subdomain 3

Figure 4.10 – Profiles of total turbulent kinetic energy in different subdomains with different coefficients for Active HTLES. Comparison of periodic HTLES, HTLES without forcing, HTLES with ALF and Active HTLES, both with a forcing in the region $x/h \in [0, 2]$.

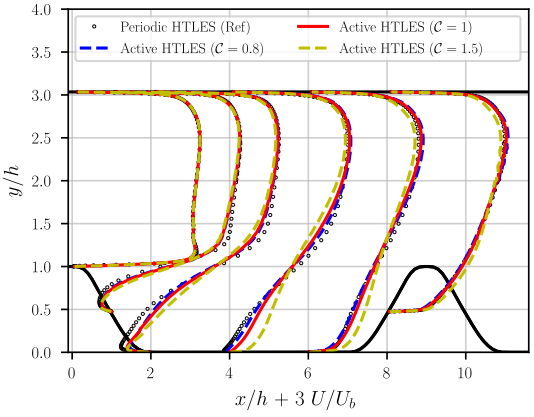

(a) subdomain 1

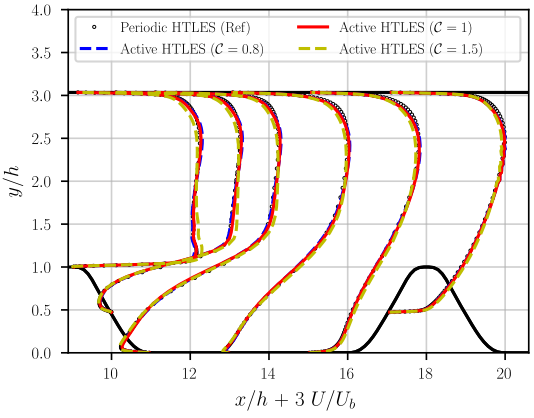

(b) subdomain 2

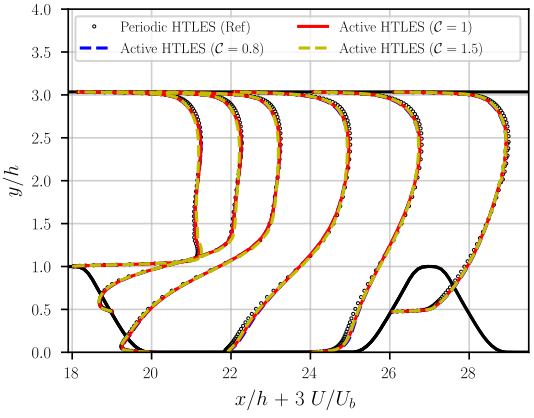

(c) subdomain 3

Figure 4.11 – same figure as Fig. 4.10 for the mean velocity.

4.3 5 Hill case

The active approach is now tested in a more realistic scenario, where the simulation transitions from a fully developed RANS to LES, and back from LES to RANS at the end of the domain. The geometrical representation of the 5-hill test case is shown in Fig. 4.12.

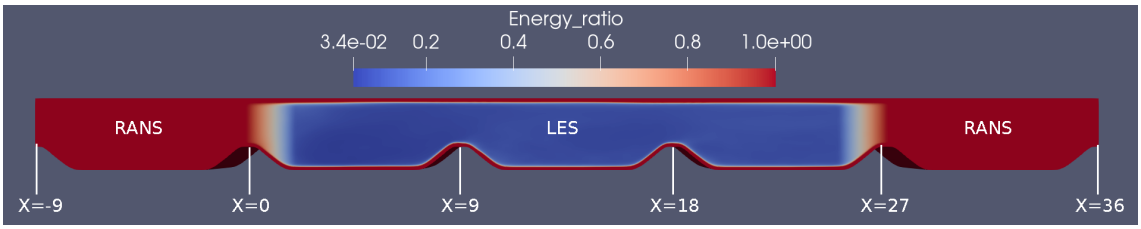

Figure 4.12 – Geometrical representation of the 5-hill test case, showing the isocontours of the modeled-to-total energy ratio r, indicating the regions solved in RANS ($r = 1$) and in LES ($r < 1$).

As indicated in Fig. 4.12, two subdomains (again, there is only one computational domain) are treated in RANS mode, one at the entrance and one at the exit, by imposing the energy ratio r to be unity in these domains; and the other three are treated in LES mode. The RANS-to-LES transition from $x/h = 0$ to $x/h = 2$ and LES-to-RANS transition from $x/h = 25$ to $x/h = 27$ are imposed gradually, by enforcing a modified energy ratio r_{mod}:

$$r_{\text{mod}} = f + (1 - f)r \quad \text{with} \quad f\left(\frac{x}{h}\right) = \begin{cases} 1 - \dfrac{x}{2} & \text{for } \dfrac{x}{h} \in [0, 2] \\ \dfrac{x - 25}{2} & \text{for } \dfrac{x}{h} \in [25, 27] \end{cases} \tag{4.5}$$

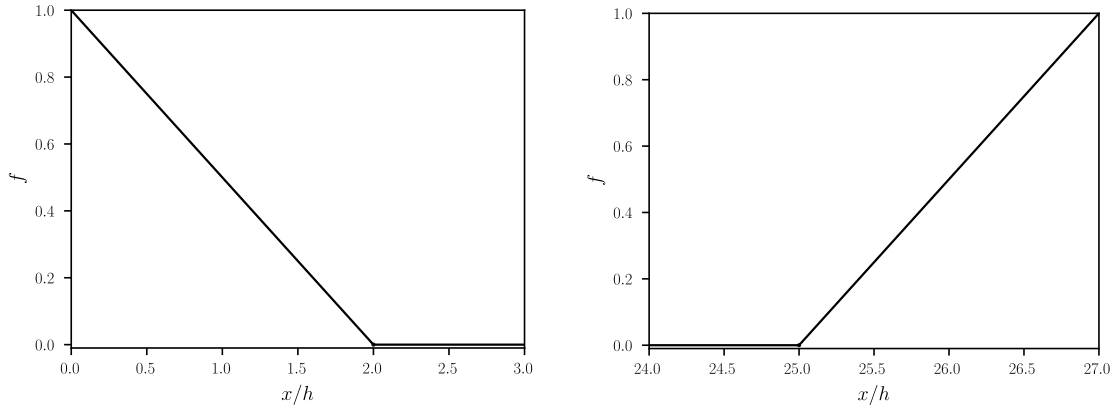

(a) (b)

Figure 4.13 – Shape of the function f to impose a gradual transition from (a)RANS-to-LES and (b) LES-to-RANS.

With this modification, three cases are compared:

→ HTLES without forcing;

→ Active HTLES with forcing activated only in RANS-to-LES transition region;

→ Active HTLES with forcing both the RANS-to-LES and LES-to-RANS transitions.

Re_b	Grid	$\Delta_{y_w^+}$	Δ_x/h	Δ_z/h	N_x	N_y	N_z	No. of cells
10595	M1	1	0.1125	0.1125	80	80	40	0.256 M
	M2	1	0.075	0.075	120	120	60	0.864 M

Table 4.1 – Numerical settings for the grids for the Hill flow

The main characteristics of the meshes are described in the Table 4.1. Each subdomain is treated with the same mesh. With these meshes, an almost isotropic refinement is obtained in the planes parallel to the walls. Moreover, outside the boundary layer, the cells are globally isotropic. The flow is studied using a coarse mesh M1 and a fine mesh M2 containing more than three times more cells, which both satisfy $\Delta y^+ \simeq 1$. Periodic RANS profiles are imposed as the inlet boundary conditions. The results are then compared with the periodic RANS solution in RANS regions and with the periodic HTLES in the transitions and LES regions (for periodic results refer to section 2.4.2). All the computations use the same numerical parameters as in chapters 2 and 4.

4.3.1 Comparison using the coefficient $\mathcal{C} = 1$

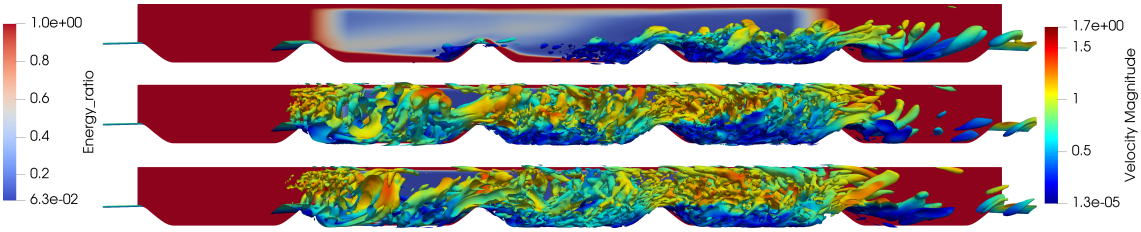

Figure 4.14 – Isocontours $Q = 0.2U_b^2/h^2$. Top: HTLES without forcing Middle: Active HTLES forcing only the RANS-to-LES transition Bottom: Active HTLES forcing both the transition regions.

Figs. 4.14 to 4.25 show, for three cases and for the two grids, the comparison of the Q-isocontours, friction coefficient, turbulent energy profiles, mean velocity profiles, energy ratio profiles and profiles for Reynolds stresses, respectively. In the first subdomain, treated in RANS mode ($r = 1$), since the inlet conditions correspond to the periodic RANS solution, the three approaches preserve the solution almost perfectly. The small discrepancies are due to the fact that at the end of the RANS region at $x/h = 0$, instead of having a periodic condition, the transition zone from RANS to LES begins, which marginally impacts the upstream region.

From the isocontours $Q = 0.2U_b^2/h^2$ plotted in Fig; 4.14, it is seen that when no force is applied, the resolved structures take a long time to develop after the RANS-to-LES transition located between $x/h = 0$ and $x/h = 2$. In contrast, when the forcing is applied, a rapid appearance of the resolved structures is observed. Isocontours plotted in Fig. 4.16 at different times in the simulation suggest the instantaneous nature of the forcing. The visual shape of the resolved structures suggests that the forcing is a rather violent process, which does not produce realistic turbulence. However, it is very efficient in injecting resolved energy, which promotes the appearance of realistic turbulence at the end of the first subdomain. This is not surprising since the forcing does not contain any information about turbulent scales except energy levels and only amplifies preexisting fluctuations. Rapid appearance of the resolved structures makes a huge impact on the total turbulent energy in the LES zones shown in Figs. 4.17 and 4.18. The computation utilizes two

different meshes, but the comparison made with their respective references are identical, which suggests that the coarse mesh used here is fine enough for HTLES computations and that the forcing is robust to a change of grid.

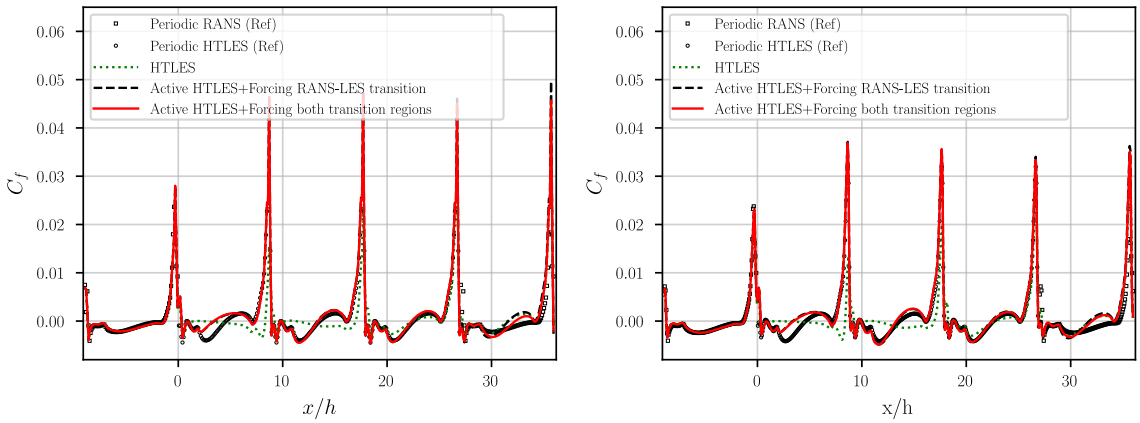

(a) M1 mesh (b) M2 mesh

Figure 4.15 – Skin friction coefficient along the lower wall.

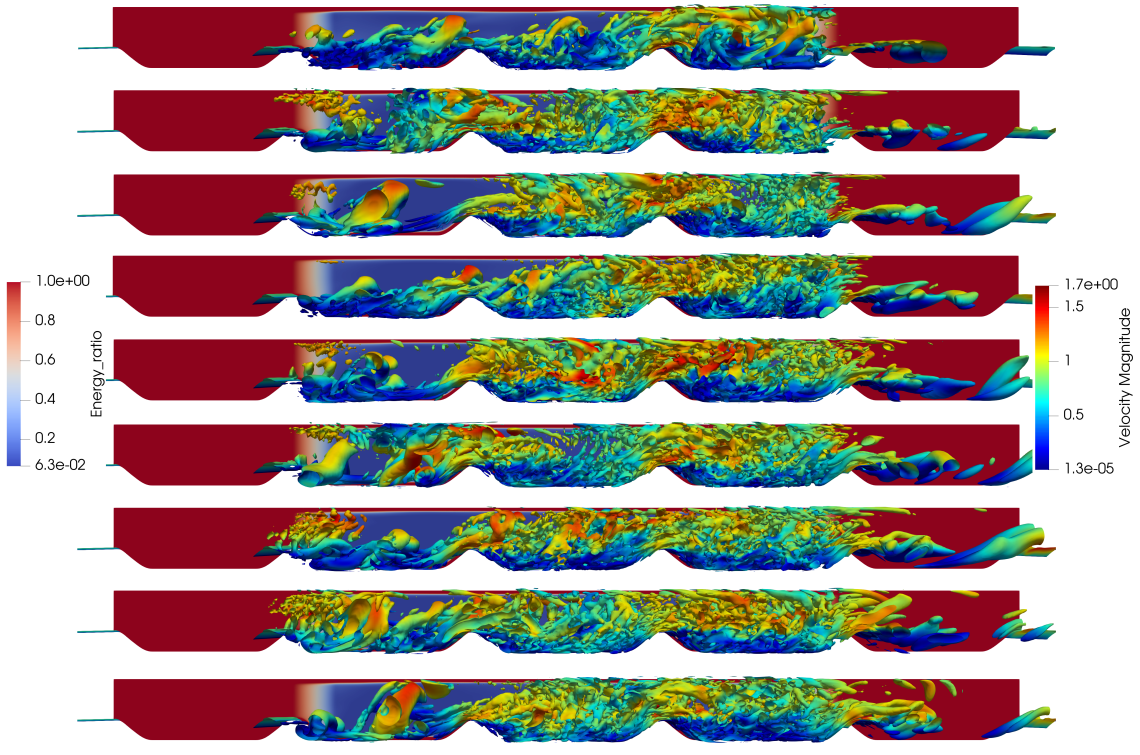

i

Figure 4.16 – Isocontours $Q = 0.2U_b^2/h^2$ for Active HTLES with forcing at both the transition regions. From the top the isocontours are plotted at $tU_b/h = 50$, 550, 1050, 1550, 2050, 2450, 3050, 3500, and 4000 in the simulation.

Without the application of the forcing, the turbulent energy is highly underestimated until the end of the fourth subdomain ($x/h \simeq 24$), in a similar manner to the case studied in section 4.2. The essential difference between these two cases is that at $x/h = 0$, the periodic HTLES solution was used as a boundary condition in the previous section, whereas

here, the values at $x/h = 0$ are advected from the RANS zone. Comparison of velocity profiles in Figs. 4.19 and 4.20, and skin friction coefficient C_f in Fig. 4.15 show that this modification has not changed much the results for pure HTLES, since the results obtained in the LES zone without forcing are equally inaccurate. Figs. 4.23 and 4.24 show how the model fails to reduce the modeled energy efficiently without the forcing in the center of the flow until downstream of the fourth hill ($x/h < 20$).

From Figs. 4.16, 4.17 and 4.18, it is seen that, when the forcing is introduced (regardless of whether it is activated or not in the downstream LES-to-RANS transition zone), the generation of resolved turbulent energy occurs rapidly. However, a larger overshoot is observed compared to the situation discussed in section 4.2 (refer to Figs. 4.17b and 4.18b). This difference in overshoot arises from the fact that the velocity profiles and turbulent variables at the location $x/h = 0$ are no longer the ideal periodic HTLES profiles, but rather those advected from the upstream RANS domain, which are quite different.

Fig. 4.15 shows that in the case of 5-hill configuration, the reproduction of the friction coefficient is less accurate in the region $x/h \in [0, 9]$ compared to the 3-hill case, because the LES mode of HTLES needs to correct the mean fields originating from the RANS region, in addition to developing resolved structures. It is important to note that in the absence of forcing, the resolved energy remains nearly zero throughout the second subdomain (refer to Fig. 4.17b and 4.18b). The reverse flow velocity is very low in the recirculation zone, causing complete relaminarization, with the modeled energy also going to zero (refer to Figs. 4.19b and 4.20b). In contrast, with active HTLES, the resolved energy develops significantly, leading to the aforementioned overshoot. Here, coefficient $\mathcal{C} = 1$ is utilized: later in the section a comparative study of different coefficient values have been performed.

The recovery of the reference HTLES solution is slower in 5-hills case than the idealized scenario discussed in the previous section of 3-hill case, where the periodic HTLES profiles were imposed at the inlet. Although the profiles of turbulent energy, mean velocity and observed energy ratio still exhibit slight deviation from the periodic solution in the middle of the fourth subdomain (refer to Figs. 4.17, 4.18, 4.19, 4.20, 4.23 and 4.24), the friction coefficient is predicted very satisfactory starting from the end of the second subdomain (the first subdomain treated in LES mode).

As the hybrid model is based on the underlying $k-\omega$ SST RANS model, the Reynolds stress tensor is computed based on the Boussinesq approximation. Hence, to look at the anisotropy of the stress tensor, the anisotropy tensor is defined as:

$$a_{ij} = \frac{\tau_{ij}}{k} - \frac{2}{3}\delta_{ij} \tag{4.6}$$

where k is the total turbulent kinetic energy, τ_{ij} the Reynolds stress tensor and δ_{ij} the Kronecker delta. From Fig. 4.25, it can be seen that the anisotropy is in close approximation with the reference values when the forcing is activated. In the first subdomain, which is treated in RANS mode, irrespective of the fact whether the forcing is active or not, the anisotropy is virtually the same as in the periodic RANS computation, due to the fact that the periodic RANS profiles are imposed as the inlet boundary condition.

At $x/h = 2$ (refer to Fig. 4.25c), despite the fact that the turbulent energy is severely underestimated, as seen in Fig. 4.17, the component a_{12}, corresponding to the shear stress, is reasonably well represented by the $k-\omega$ SST closure (modeled part). In contrast, since the model is a linear eddy-viscosity model, the diagonal components of the anisotropy are not correct, in particular in the upper part of the channel. When the forcing is introduced, it can be seen that, thanks to the appearance of significant resolved part, the anisotropy tensor is much better reproduced. Further downstream, at the same location (end of the hill) in subdomains 3 and 4 (refer to Figs. 4.25d and 4.25e), the situation is improved for

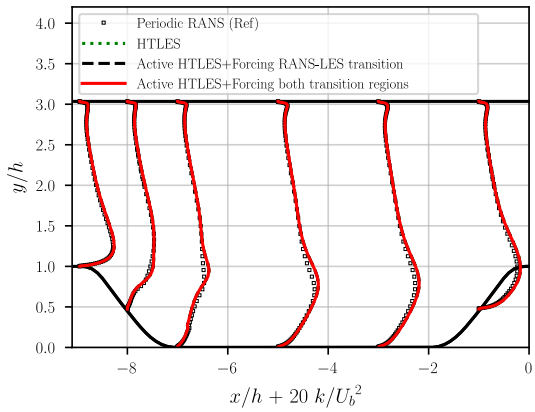

(a) subdomain 1

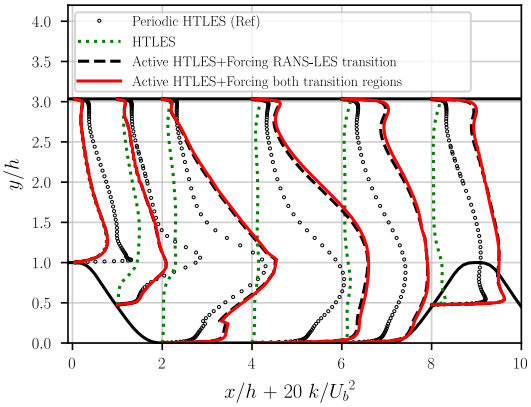

(b) subdomain 2

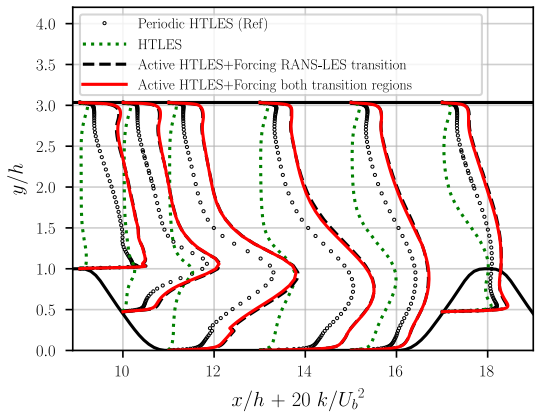

(c) subdomain 3

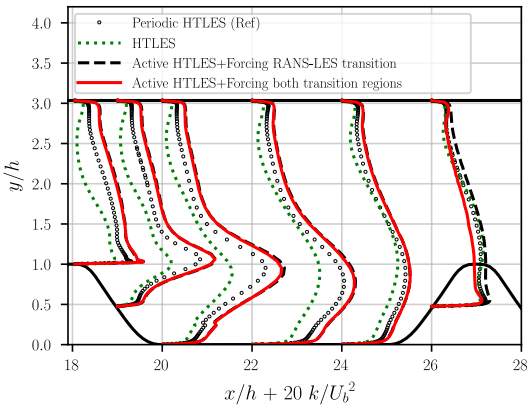

(d) subdomain 4

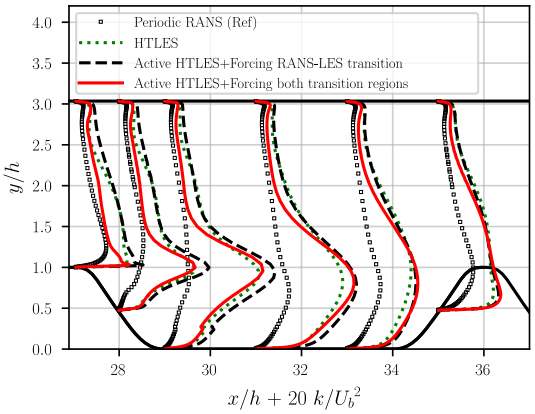

(e) subdomain 5

Figure 4.17 – Profiles of total turbulent kinetic energy in different subdomains. Comparison of periodic RANS, periodic HTLES, HTLES without forcing, Active HTLES forcing RANS-to-LES transition and Active HTLES forcing both RANS-to-LES and LES-to-RANS transition using **M1 mesh**.

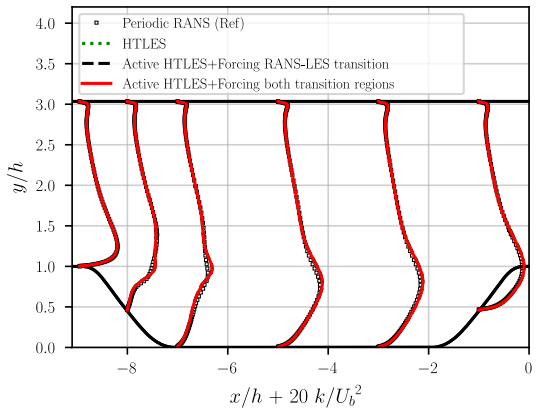

(a) subdomain 1

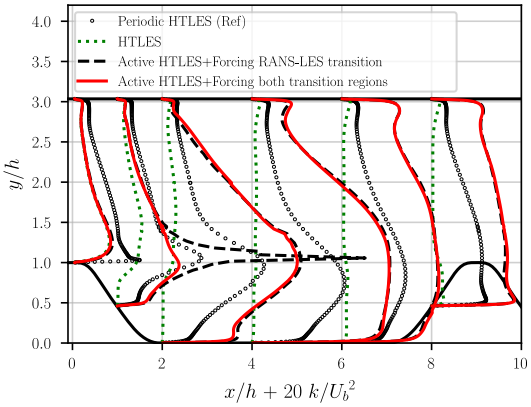

(b) subdomain 2

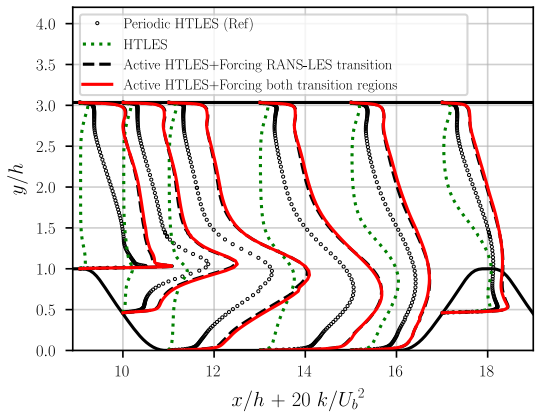

(c) subdomain 3

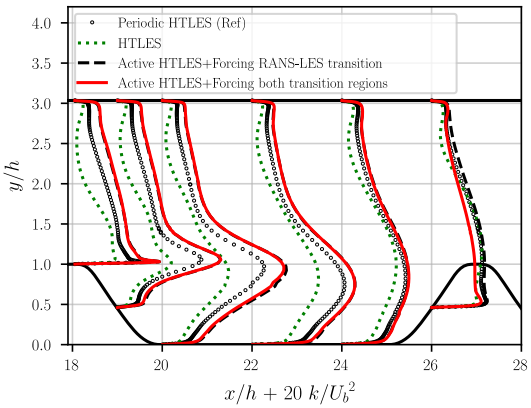

(d) subdomain 4

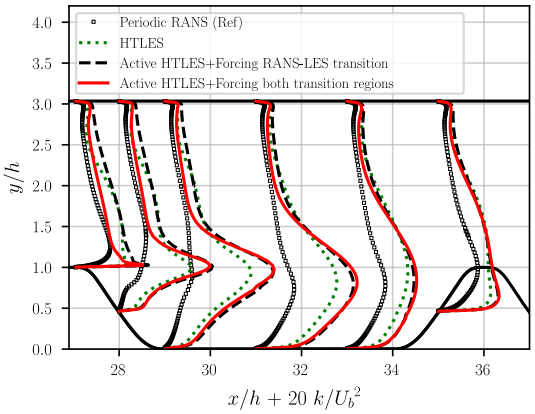

(e) subdomain 5

Figure 4.18 – Profiles of total turbulent kinetic energy in different subdomains. Comparison of periodic RANS, periodic HTLES, HTLES without forcing, Active HTLES forcing RANS-to-LES transition and Active HTLES forcing both RANS-to-LES and LES-to-RANS transition using **M2 mesh**.

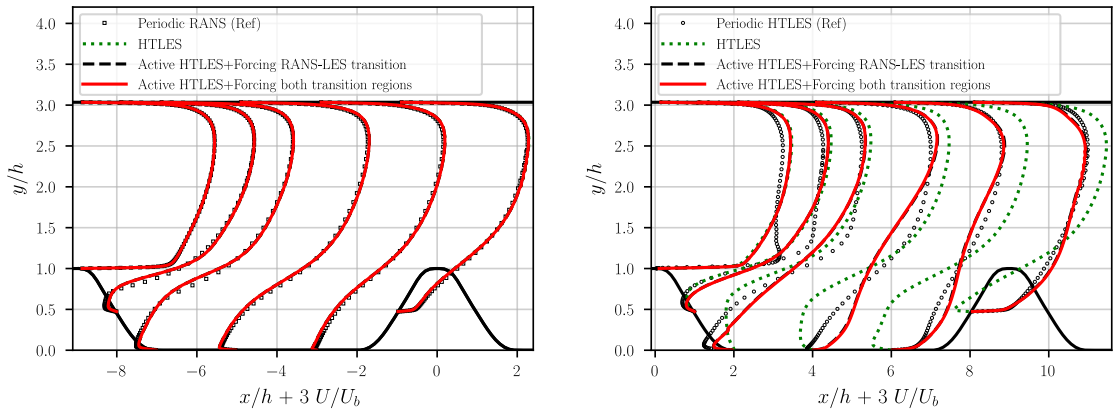

(a) subdomain 1

(b) subdomain 2

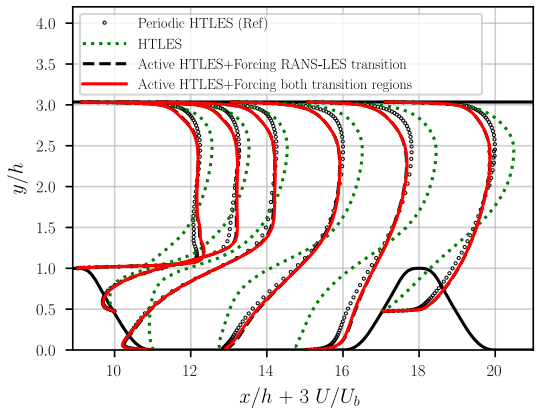

(c) subdomain 3

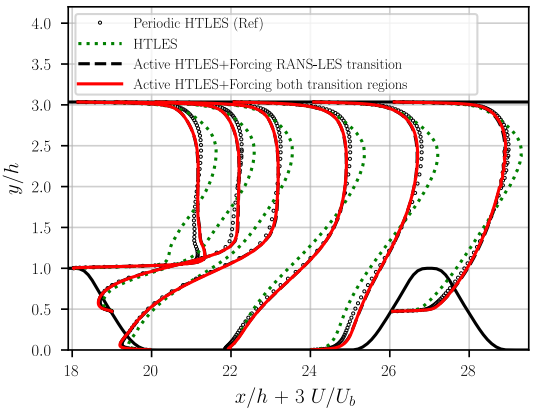

(d) subdomain 4

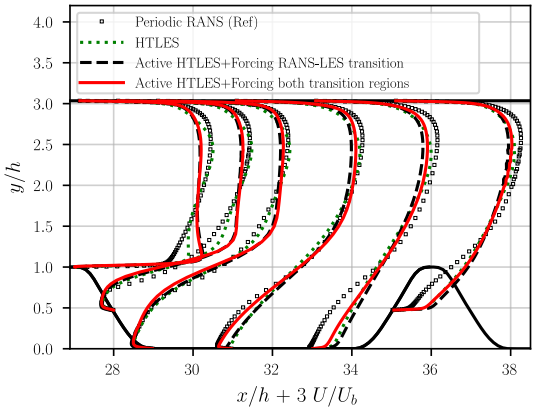

(e) subdomain 5

Figure 4.19 – Profiles of the mean velocity in different subdomains. Comparison of periodic RANS, periodic HTLES, HTLES without forcing, Active HTLES forcing RANS-to-LES transition and Active HTLES forcing both RANS-to-LES and LES-to-RANS transition using **M1 mesh**.

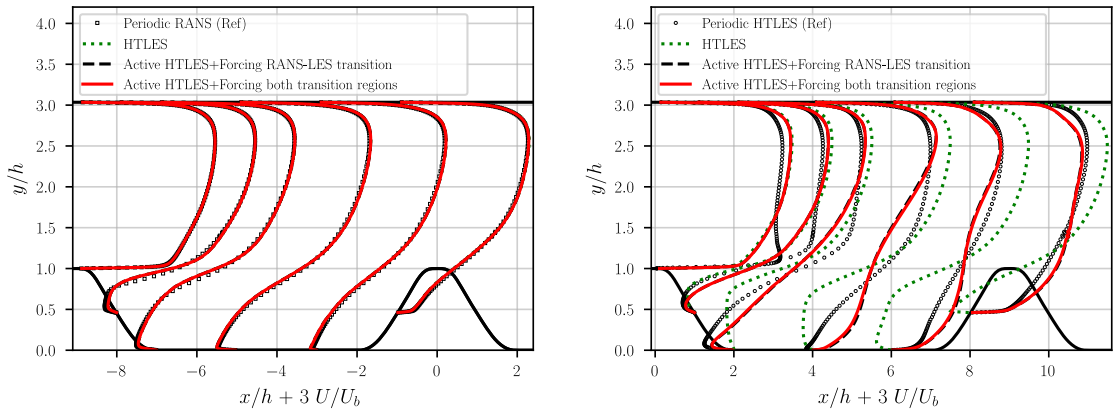

(a) subdomain 1

(b) subdomain 2

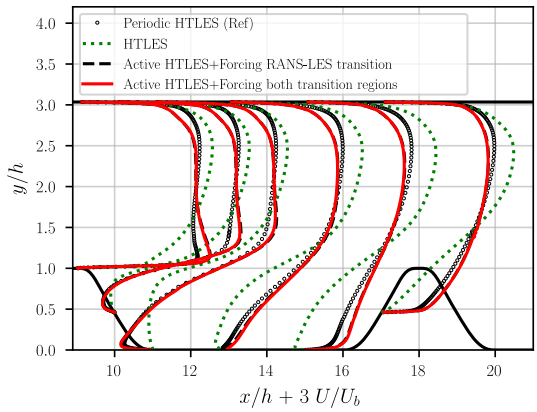

(c) subdomain 3

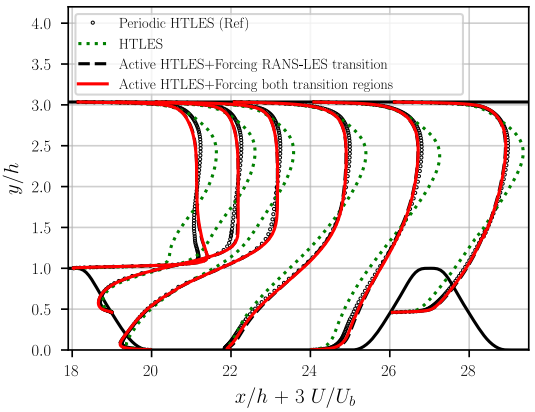

(d) subdomain 4

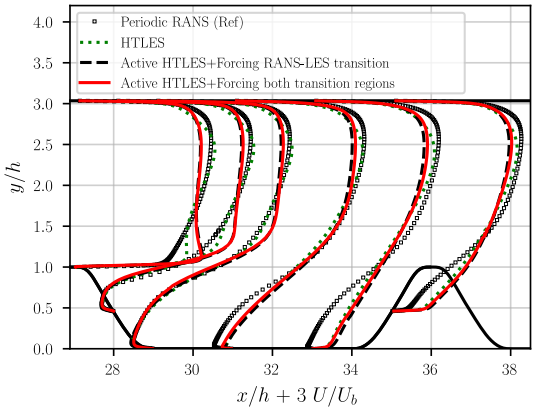

(e) subdomain 5

Figure 4.20 – Profiles of the mean velocity in different subdomains. Comparison of periodic RANS, periodic HTLES, HTLES without forcing, Active HTLES forcing RANS-to-LES transition and Active HTLES forcing both RANS-to-LES and LES-to-RANS transition using **M2 mesh**.

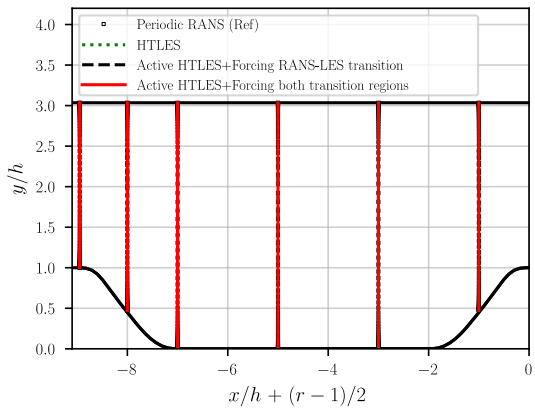

(a) subdomain 1

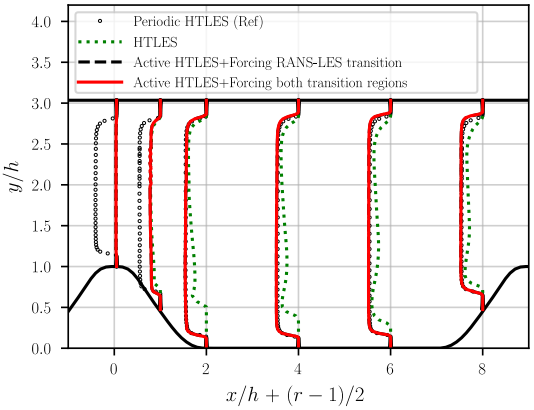

(b) subdomain 2

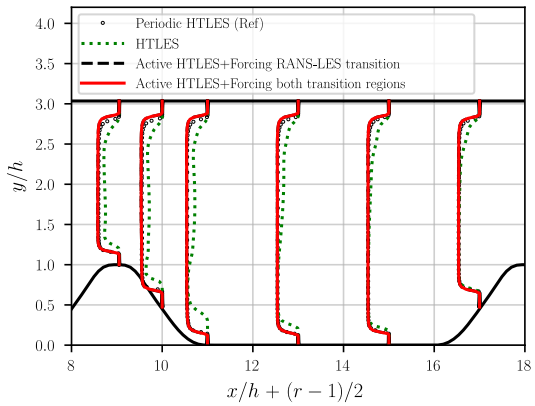

(c) subdomain 3

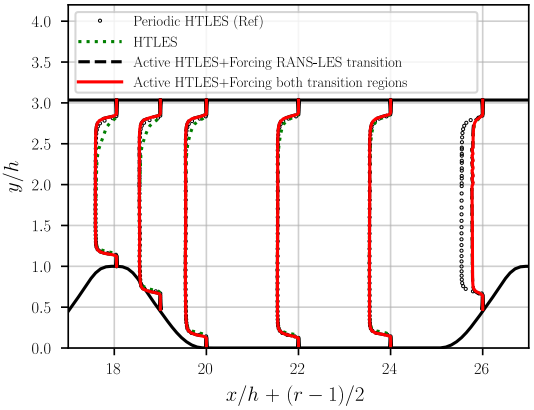

(d) subdomain 4

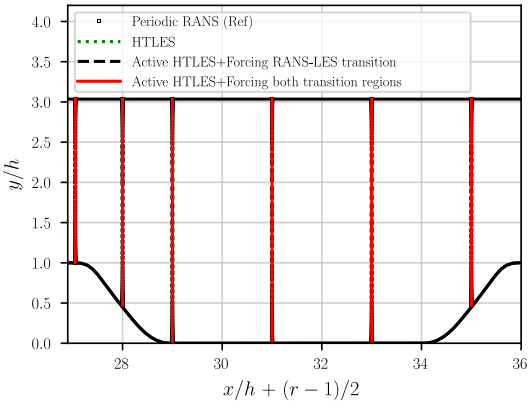

(e) subdomain 5

Figure 4.21 – Profiles of energy ratio imposed (desired) in different subdomains. Comparison of periodic RANS, periodic HTLES, HTLES without forcing, Active HTLES forcing RANS-to-LES transition and Active HTLES forcing both RANS-to-LES and LES-to-RANS transition using **M1 mesh**.

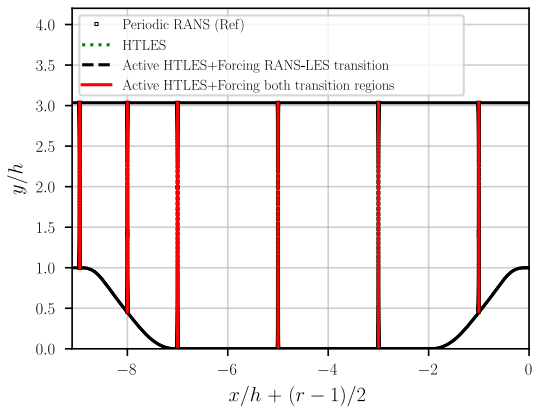

(a) subdomain 1

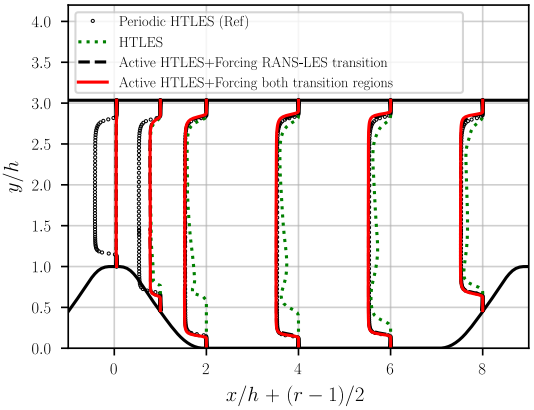

(b) subdomain 2

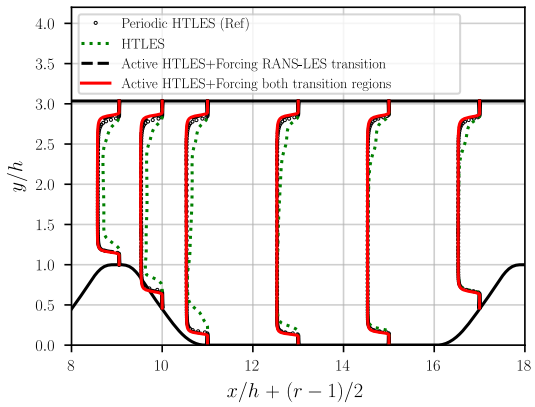

(c) subdomain 3

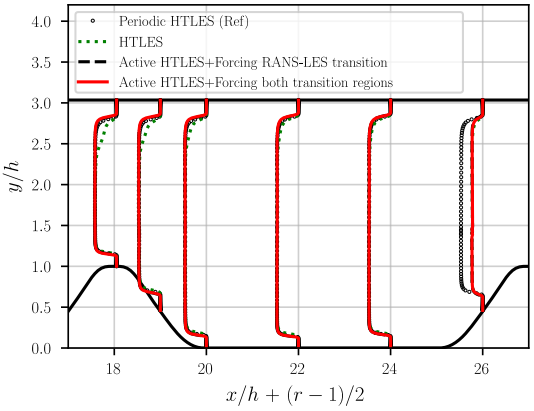

(d) subdomain 4

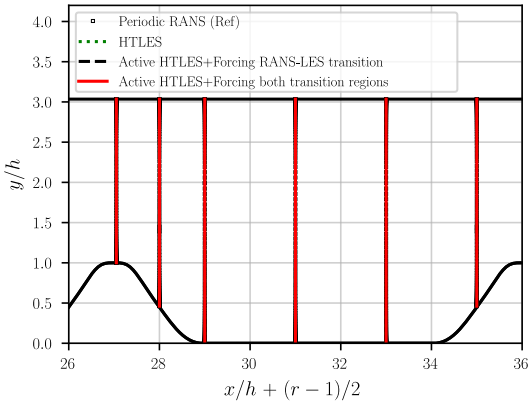

(e) subdomain 5

Figure 4.22 – Profiles of energy ratio imposed (desired) in different subdomains. Comparison of periodic RANS, periodic HTLES, HTLES without forcing, Active HTLES forcing RANS-to-LES transition and Active HTLES forcing both RANS-to-LES and LES-to-RANS transition using **M2 mesh**.

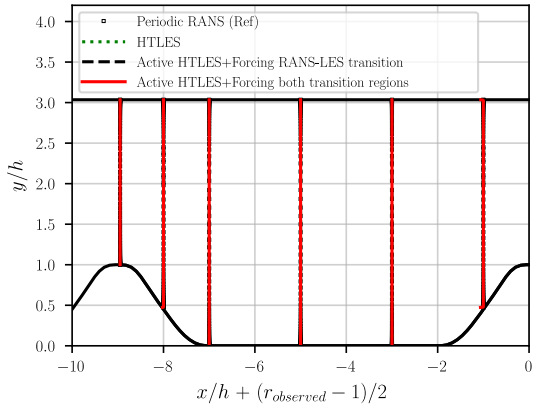

(a) subdomain 1

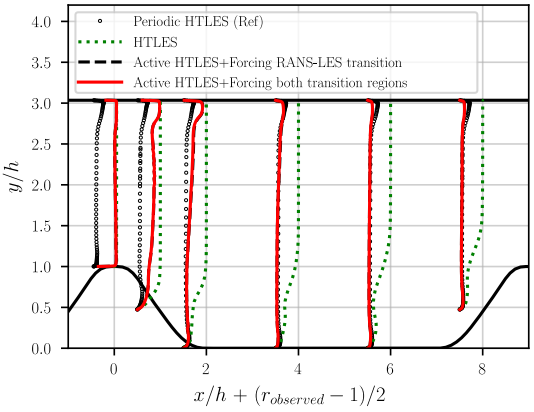

(b) subdomain 2

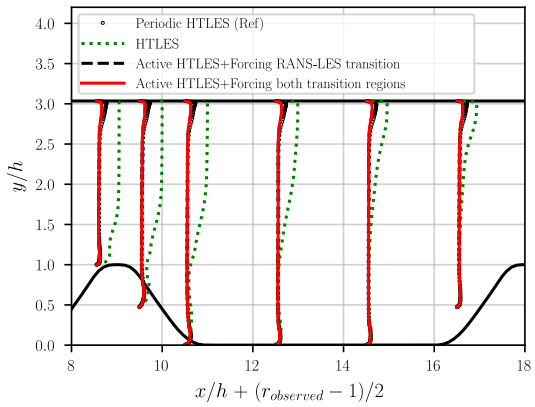

(c) subdomain 3

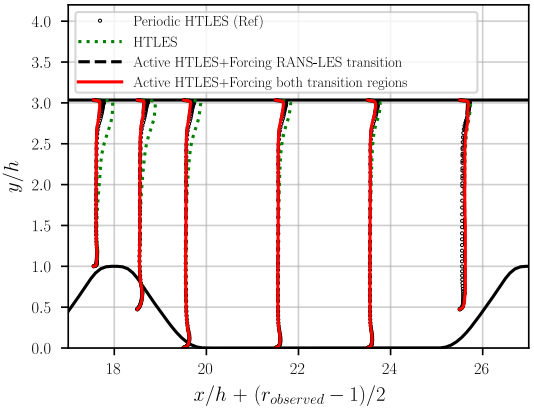

(d) subdomain 4

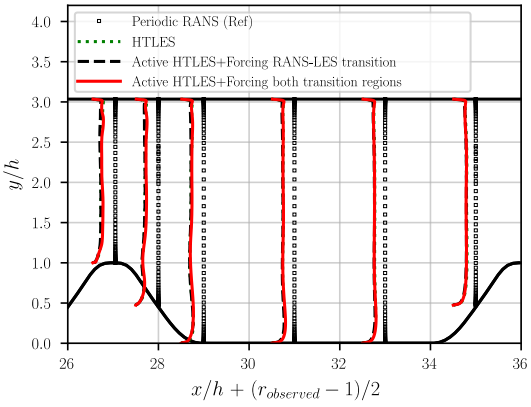

(e) subdomain 5

Figure 4.23 – Profiles of observed energy ratio k_m/k in different subdomains. Comparison of periodic RANS, periodic HTLES, HTLES without forcing, Active HTLES forcing RANS-to-LES transition and Active HTLES forcing both RANS-to-LES and LES-to-RANS transition using **M1 mesh**.

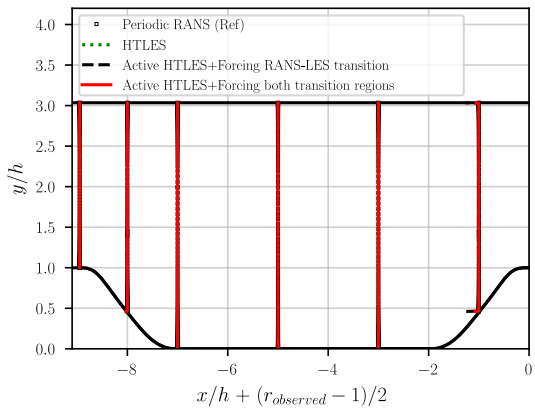

(a) subdomain 1

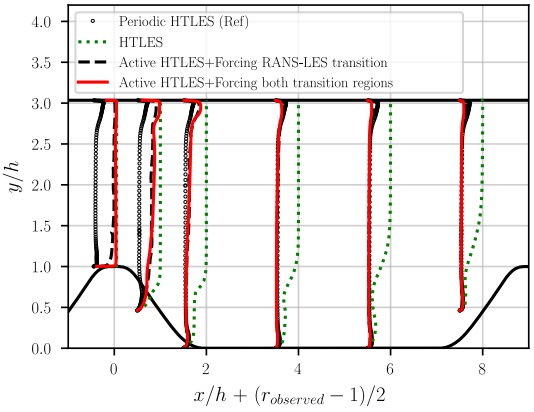

(b) subdomain 2

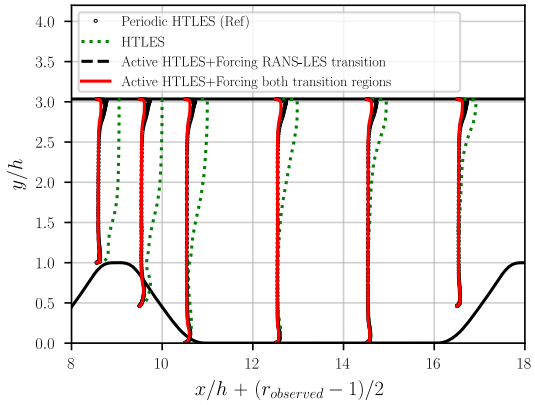

(c) subdomain 3

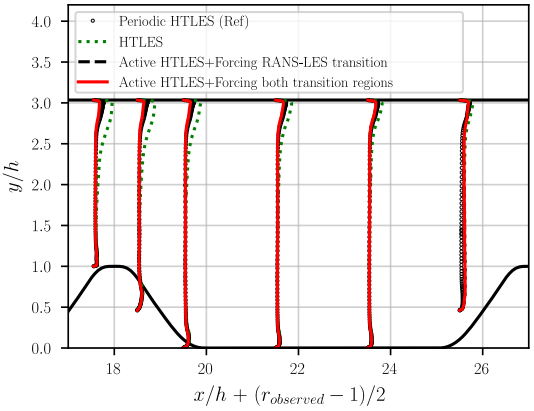

(d) subdomain 4

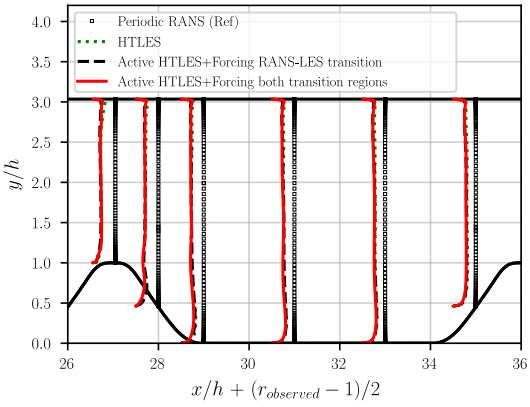

(e) subdomain 5

Figure 4.24 – Profiles of observed energy ratio k_m/k in different subdomains. Comparison of periodic RANS, periodic HTLES, HTLES without forcing, Active HTLES forcing RANS-to-LES transition and Active HTLES forcing both RANS-to-LES and LES-to-RANS transition using **M2 mesh**.

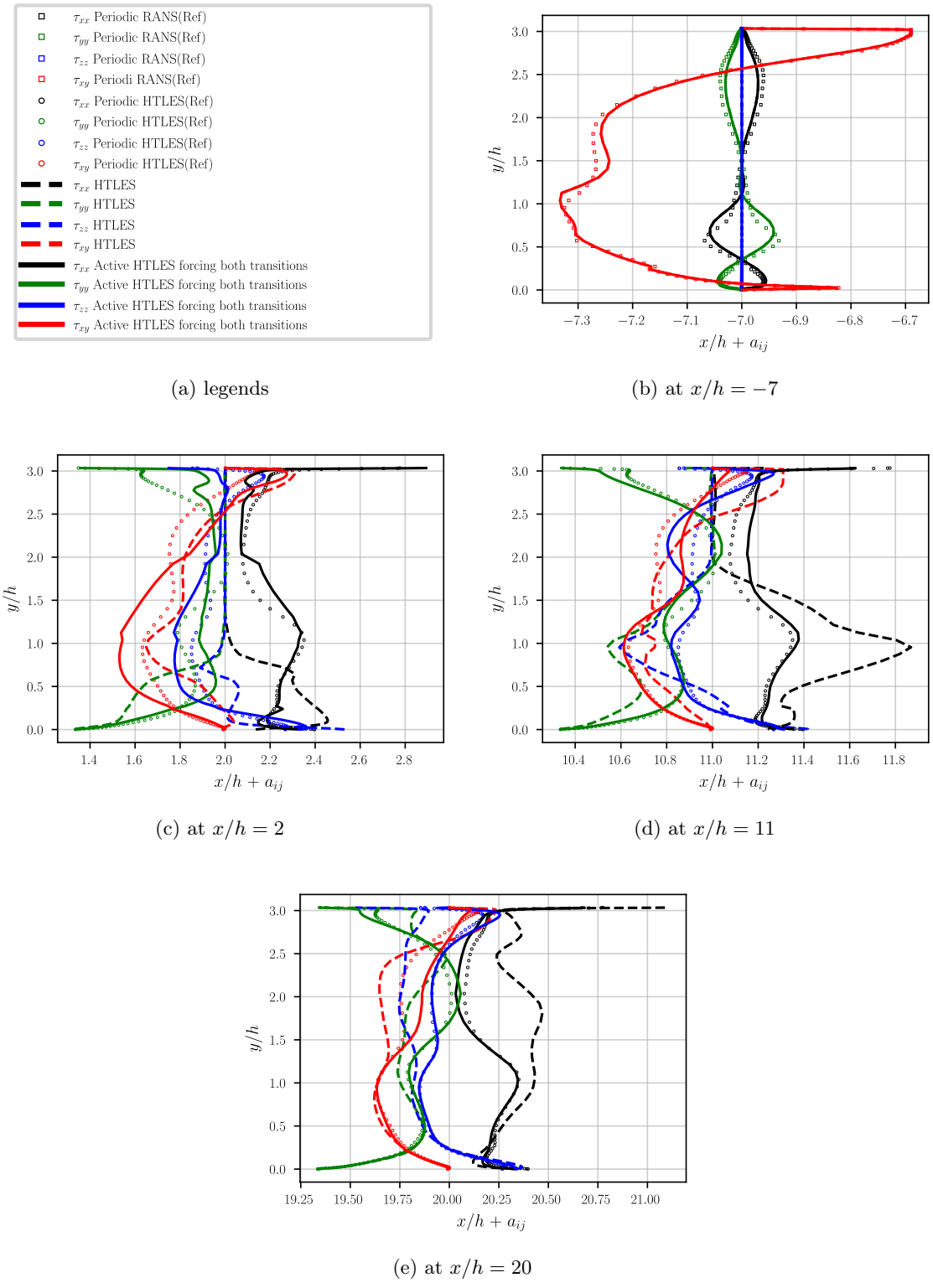

(a) legends

(b) at $x/h = -7$

(c) at $x/h = 2$

(d) at $x/h = 11$

(e) at $x/h = 20$

Figure 4.25 – Profiles of anisotropic tensor at different streamwise locations. Comparison of periodic RANS, periodic HTLES, HTLES without forcing and Active HTLES forcing both RANS-to-LES and LES-to-RANS transition using M1 mesh.

HTLES without forcing, but the anisotropy still does not match that of periodic HTLES. When the forcing is introduced, all the components are very close to the reference in the lower part of the channel, and quite close in the upper half.

An interesting observation is made when the forcing is applied at the LES-to-RANS transition as well, i.e., at the end of the fourth subdomain ($x/h \in [25, 27]$). The direction of forcing is opposite to that of the RANS-to-LES transition meaning that it leads to the destruction of the resolved energy. Figs. 4.17d and 4.18d reveals that the turbulent energy is indeed reduced in the core of the flow due to this negative forcing, but not significantly in the separated shear layer and recirculation zone. Figs. 4.14, 4.17e and 4.18e suggests that resolved structures persist in all cases at the beginning of the RANS domain, irrespective of the forcing, proving it difficult to kill the resolved structure in the RANS zone (it is important to note that in these figures, the reference profiles correspond to those from the periodic RANS simulation).

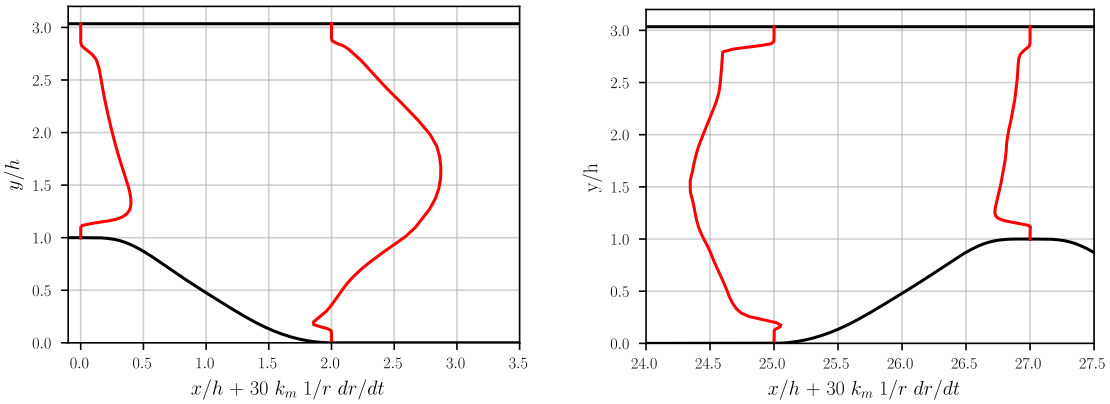

(a) RANS-to-LES transition

(b) LES-to-RANS transition

Figure 4.26 – Profiles of the half-trace of the rhs of the forcing (Eq. (4.3)) in the transition region (mean production of resolved energy). Case of Active HTLES with forcing both RANS-to-LES and LES-to-RANS transitions using M1 mesh.

Fig. 4.26 illustrates the behaviour of the mean production of resolved energy due to the volume forcing. It reveals that the volumic forcing aims to "introduce" resolved turbulent structures in RANS-to-LES transition and "kill" the resolved turbulent structures in LES-to-RANS transition. Specifically, from Fig. 4.26a, the forcing contributes to the resolved motion, except near the lower wall at $x/h = 2$, where the flow reenters the near wall RANS region imposed by the shielding function from LES region. In contrast, from Fig. 4.26b, the forcing contributes to the destruction of resolved structures except for the near wall region at the beginning of the hill $x/h = 25$.

4.3.2 Influence of different coefficient values

Fig. 4.27 shows that increasing the coefficient leads to highly degraded prediction of the skin friction coefficient in the second subdomain and slightly degraded predictions in the third subdomains. However, the main benefit of increasing the coefficient can be seen in the 5th subdomain, which is treated in RANS mode. Increasing the coefficient up to a certain level ($\mathcal{C} = 1.5$) increases the accuracy in capturing the recirculation zone. However, after a certain level ($\mathcal{C} = 2$) the accuracy of predicting the reattachment location decreases.

Increasing the coefficient leads to higher and higher overshoot in the turbulent energy in the second subdomain (refer to Fig. 4.29b), which is not desirable as the correct energy

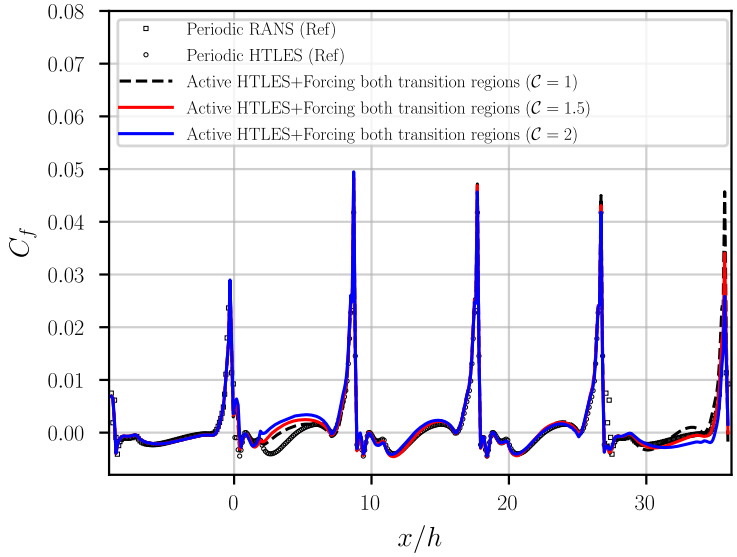

Figure 4.27 – Skin friction coefficient along the lower wall for different coefficients using M1 mesh.

levels are difficult to achieve with such an increasing overshoot. With $\mathcal{C} = 2$, unrealistic energy levels are reached, and numerical oscillations appear. However, in the LES-to-RANS transition, an increased value of the coefficient helps destroying the resolved structures more rapidly and leads the prediction of turbulent energy towards correct level (refer to Fig. 4.29e). In contrast, Fig. 4.30 shows that the predictions for the mean velocity profiles are in close proximity to each other irrespective of the value of the coefficient until the last subdomain (subdomain treated in RANS mode after LES-to-RANS transition). Fig. 4.31 represents the prolific effect of increasing the coefficient on the observed energy ratio r_{observed}. Where the profiles suggest that increasing the coefficient leads to underestimation of the modeled energy throughout the subdomains treated in LES mode in the region close to the upper wall, but leads to the correct levels of modeled energy in the fifth subdomain.

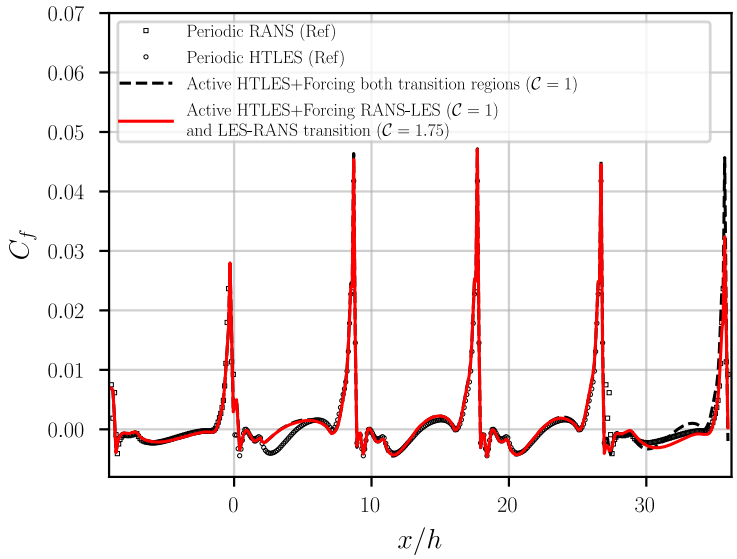

Figure 4.28 – Skin friction coefficient along the lower wall for variable coefficients using M1 mesh.

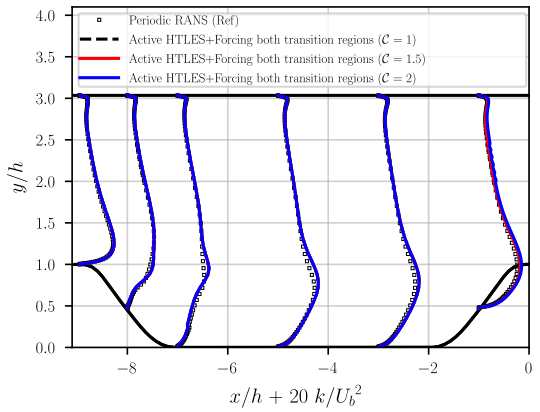

(a) subdomain 1

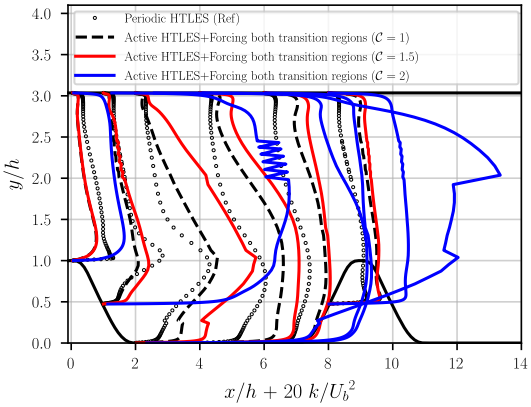

(b) subdomain 2

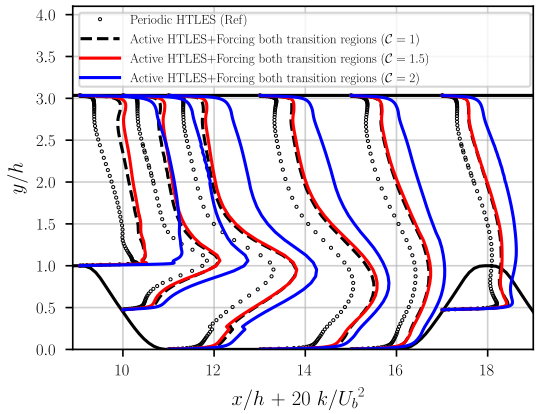

(c) subdomain 3

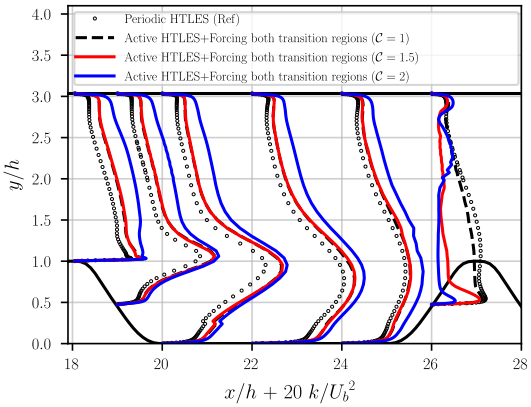

(d) subdomain 4

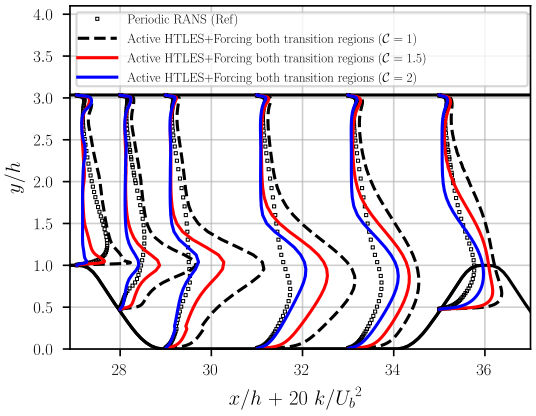

(e) subdomain 5

Figure 4.29 – Profiles of total turbulent kinetic energy in different subdomains. Comparison of periodic HTLES, HTLES without forcing and Active HTLES forcing both RANS-to-LES and LES-to-RANS transitions using M1 mesh for different coefficients.

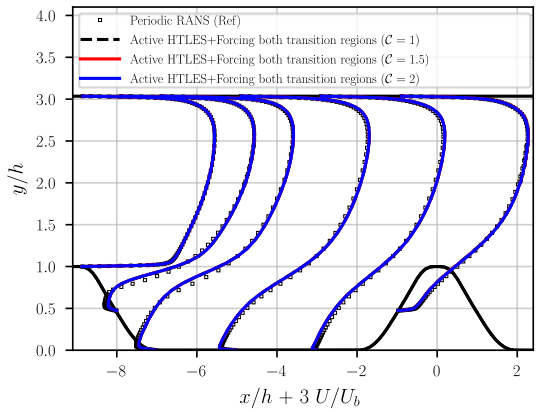

(a) subdomain 1

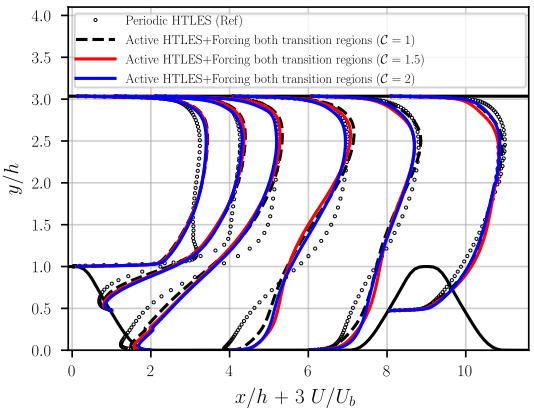

(b) subdomain 2

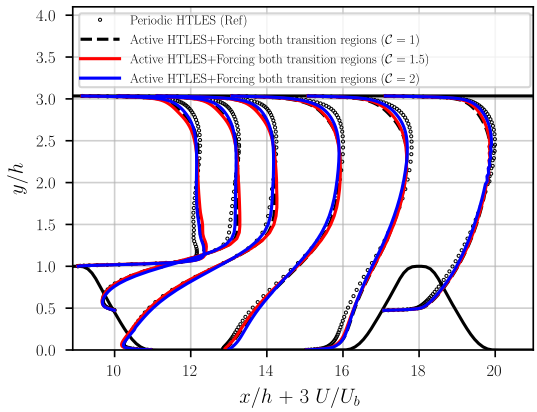

(c) subdomain 3

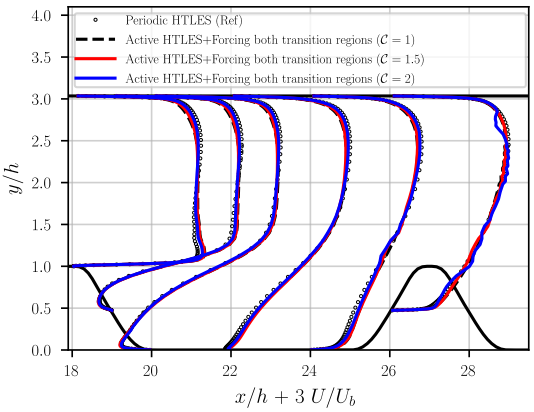

(d) subdomain 4

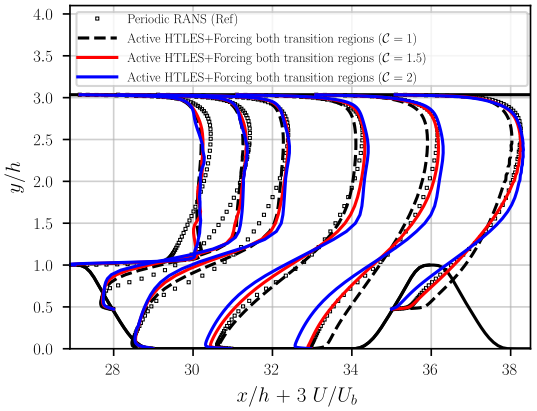

(e) subdomain 5

Figure 4.30 – Profiles of the mean velocity in different subdomains. Comparison of periodic HTLES, HTLES without forcing and Active HTLES forcing both RANS-to-LES and LES-to-RANS transitions using M1 mesh for different coefficients.

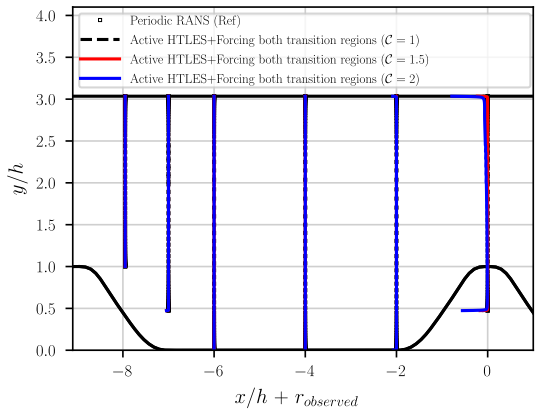

(a) subdomain 1

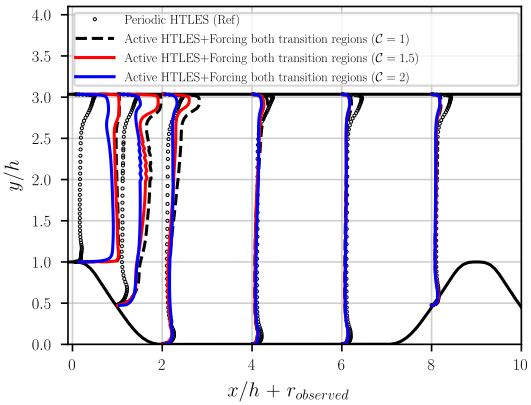

(b) subdomain 2

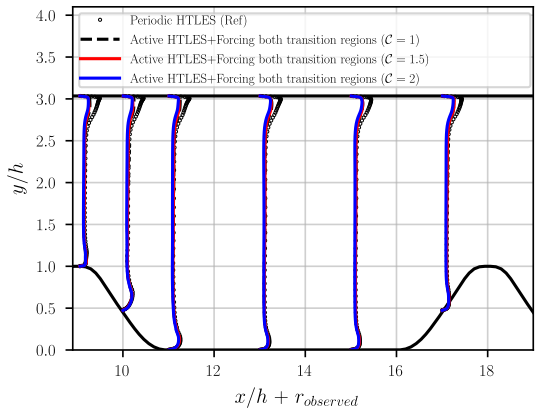

(c) subdomain 3

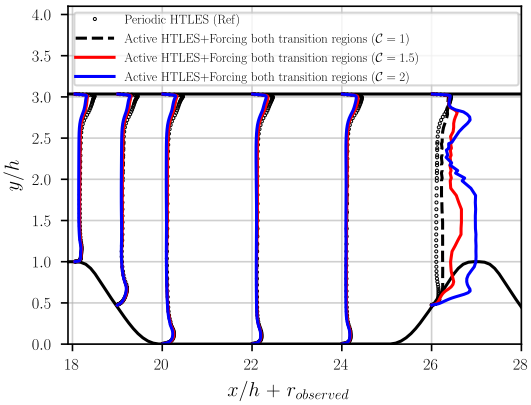

(d) subdomain 4

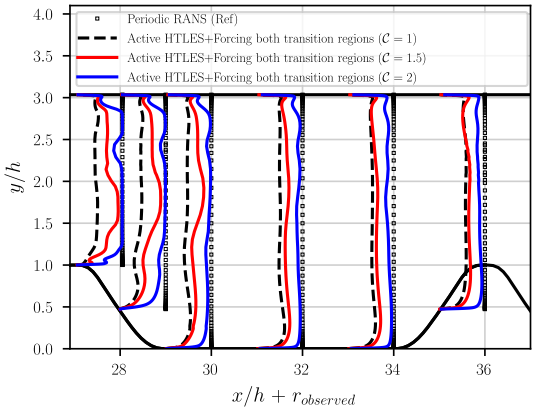

(e) subdomain 5

Figure 4.31 – Profiles of observed energy ratio k_m/k in different subdomains. Comparison of periodic HTLES, HTLES without forcing and Active HTLES forcing both RANS-to-LES and LES-to-RANS transitions using M1 mesh for different coefficients.

4.3.3 Variable coefficients

As discussed in section 4.3.2, increasing the coefficient universally predicts larger overshoot of energy and fails to improve the velocity profiles in the recirculation region when transitioning from RANS-to-LES. In contrast, for the LES-to-RANS transition increasing the value of the coefficient up to a certain level, leads to a faster recovery of the RANS solution. Hence, it seems interesting to test a variable coefficient whose value is different for each transition. For this purpose, the test case presented here has $\mathcal{C} = 1$ for RANS-to-LES transition and $\mathcal{C} = 1.75$ for LES-to-RANS transition.

Fig 4.28 shows, as the coefficient $\mathcal{C}$ is identical in RANS-to-LES transition, prediction of the friction coefficient is equally inaccurate in the second subdomain, but when transitioning from LES-to-RANS at the end of the fourth subdomain ($x/h \in [25, 27]$), increasing the coefficient leads to better prediction in the RANS region (fifth subdomain). From Fig. 4.32d, it can be seen that using the higher coefficient value is killing the resolved structures more rapidly, leading to underestimation of the total energy initially ($x/h < 30$) in the fifth subdomain treated in RANS mode (refer to Fig. 4.32e) due to the fact that the resolved energy is destroyed but the modeled energy at the end of the LES region (fourth subdomain) is very small. But it is desirable because it makes the convergence towards the RANS values in the fifth subdomain faster, in particular as concerns the velocity profiles (refer to Fig. 4.33).

4.3.4 Spectral analysis

The statistical predictions being validated, the main objective of this section is to analyze the spectra of energy in the flow and to evaluate the unsteady information available. To do this, temporal spectra are produced, by recording the signals of the instantaneous variables at the positions explained in Table 4.2, and indicated in Fig. 4.34. It is important to point out that these probes are representative of the different shapes of the energy spectra encountered in the periodic hills.

Probes	P1	P2	P3	P4	P5
x/h	0.35	2.1	2.0	3.5	7
y/h	1.05	0.9	0.53	0.53	0.53

Table 4.2 – Positions of the probes used to record the signals to produce the energy spectra.

It is important to note that these points are repeated in each subdomain, i.e. there are 25 monitoring points in total in the case of an active HTLES computation. Periodic HTLES computation is used as a reference here. Thanks to the streamlines plotted in Fig. 4.34, it is observed that the probe P3 is located in the center of the recirculation zone, where the velocity is very low, while the probes P1, P2 and P4 are located in the detached shear layer, where high velocities are measured. Probe P5 lies after reattachment zone, in the upstream side of the hill, where the velocities are lower. It is important to note that all the points are in the LES zone of the active HTLES calculations, except for probe P1, located at the top of the hill and in the near-wall region, where fluid acceleration involves high velocities, and treated in the RANS mode due to the shielding function. This makes it possible to evaluate the unsteady content penetrating into this zone.

The first step of the study consists in carrying out a Periodic HTLES calculation using M1 mesh, in order to have access to validated reference data. Time signals for velocity are recorded at the positions of the probes defined in Table 4.2. The periodogram method

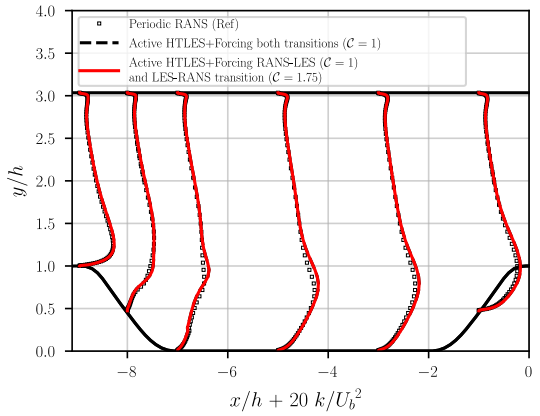

(a) subdomain 1

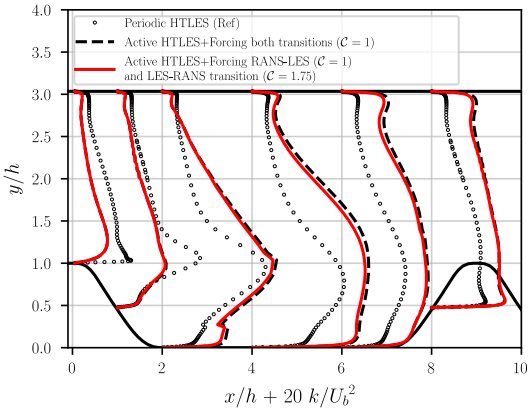

(b) subdomain 1

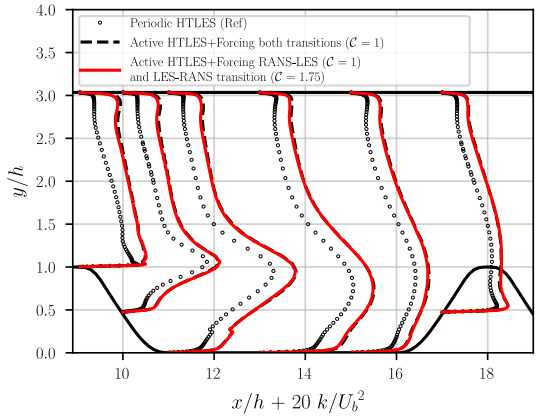

(c) subdomain 3

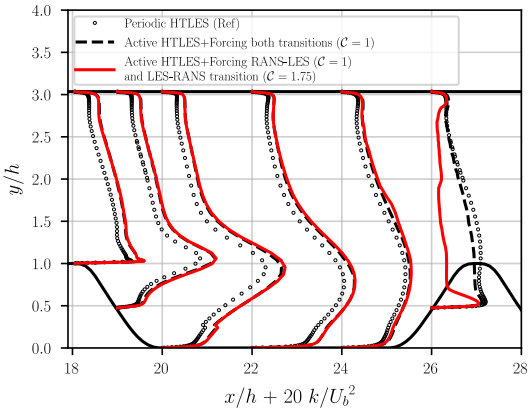

(d) subdomain 4

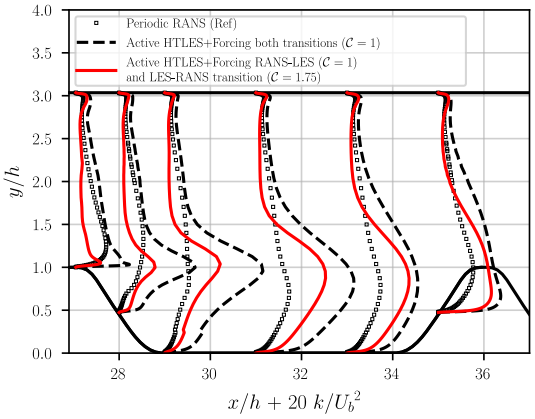

(e) subdomain 5

Figure 4.32 – Profiles of total turbulent kinetic energy in different subdomains. Comparison of Periodic HTLES, HTLES without forcing and Active HTLES forcing both RANS-to-LES and LES-to-RANS transitions using M1 mesh using variable coefficient.

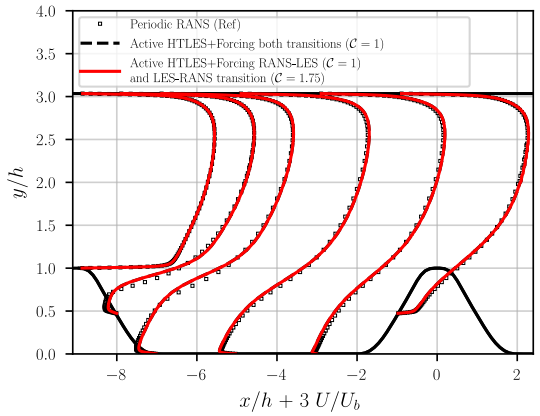

(a) subdomain 1

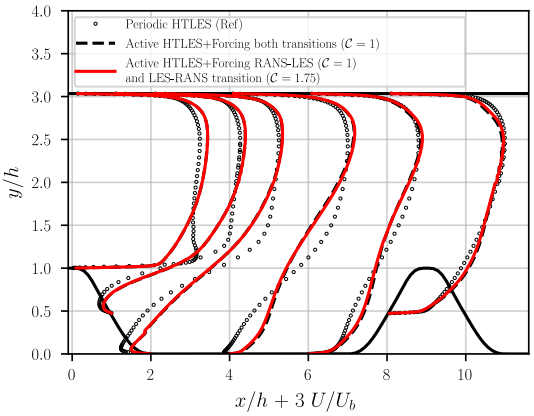

(b) subdomain 1

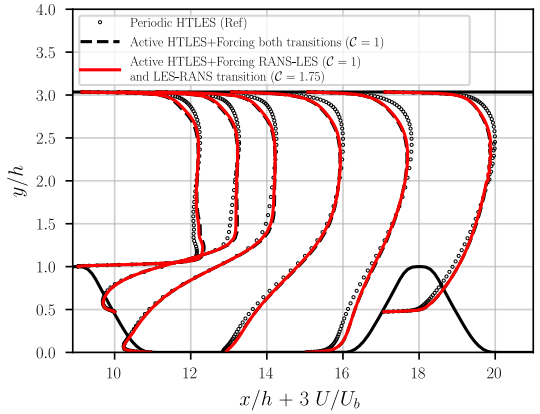

(c) subdomain 3

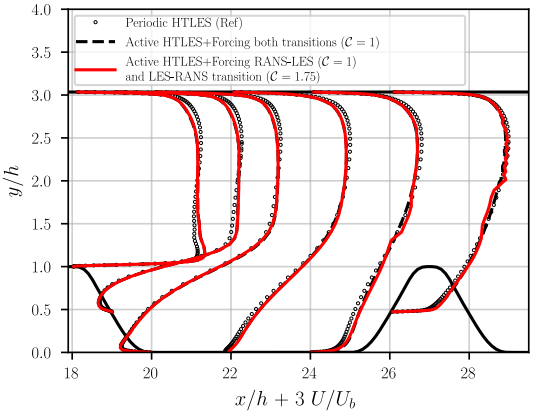

(d) subdomain 4

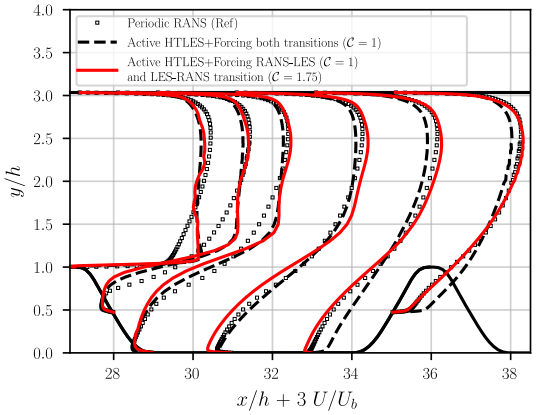

(e) subdomain 5

Figure 4.33 – Profiles of mean velocity in different subdomains. Comparison of Periodic HTLES, HTLES without forcing and Active HTLES forcing both RANS-to-LES and LES-to-RANS transitions using M1 mesh using variable coefficient.

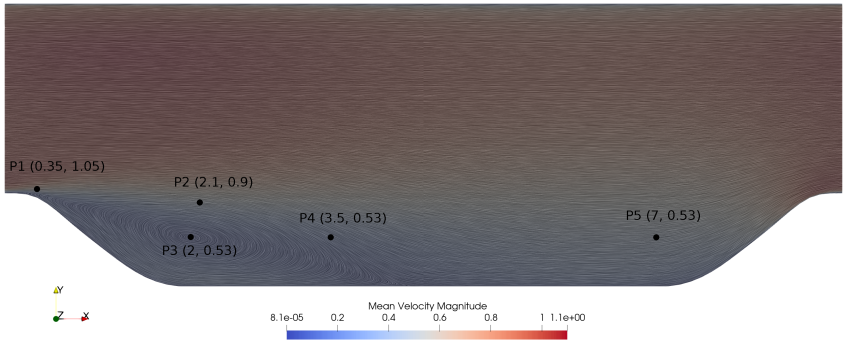

Figure 4.34 – Position of the probes used to capture the temporal spectra, in the background averaged velocity field in a Periodic HTLES computation with M1 mesh is represented.

defined by Welch (1967) is used to estimate the 1D power spectral density for turbulent kinetic energy. The main parameters are described below:

→ The signal is recorded over 800000 time steps, the time step $dt = 0.005h/U_b$ is fixed in the study regardless of the mesh.

→ The signal is decomposed into 4 segments with 50% overlap allowing optimum variance reduction (noise reduction).

→ The Power Spectral Density (PSD) of the turbulent variables is calculated for each of the successive segments using Hann's window (Kahlig, 1993).

→ The overall PSD is estimated by averaging the PSDs calculated for each segment. This leads to the reduction in the variance due to noise and smooth shape of the spectra.

Since the energy spectra are estimated by calculating the power spectral density on time signals, it is important to note that the cutoff frequency of the filter is defined by:

$$f_c = \max\left[\frac{1}{2\mathrm{d}t}, \frac{U_s}{2\Delta}\right] \tag{4.7}$$

where dt is the time step, U_s the sweeping velocity and Δ the characteristic size of the cells. In the case that is studied here $f_c = U_s/2\Delta$, because the time step is sufficiently small.

	Probes	P1	P2	P3	P4	P5
	subdomain 1	6.88	2.53	0.68	1.09	1.76
	subdomain 2	6.82	4.44	3.54	4.38	4.23
f_s	subdomain 3	7.59	3.93	3.23	3.92	3.80
	subdomain 4	8.37	4.47	3.42	3.89	3.59
	subdomain 5	6.13	2.41	1.48	1.98	2.28

Table 4.3 – Cutoff frequency at different probes positions (in Hz).

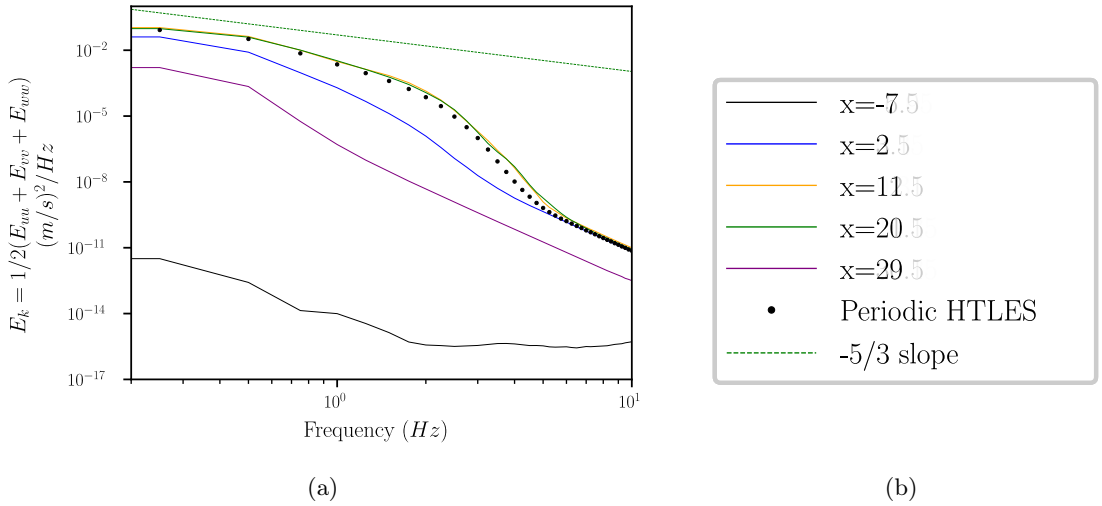

(a) (b)

Figure 4.35 – PSD of the turbulent kinetic energy, for the probe P3 in the recirculation zone. Comparing the Periodic HTLES and Active HTLES forcing both transitions using M1 mesh.

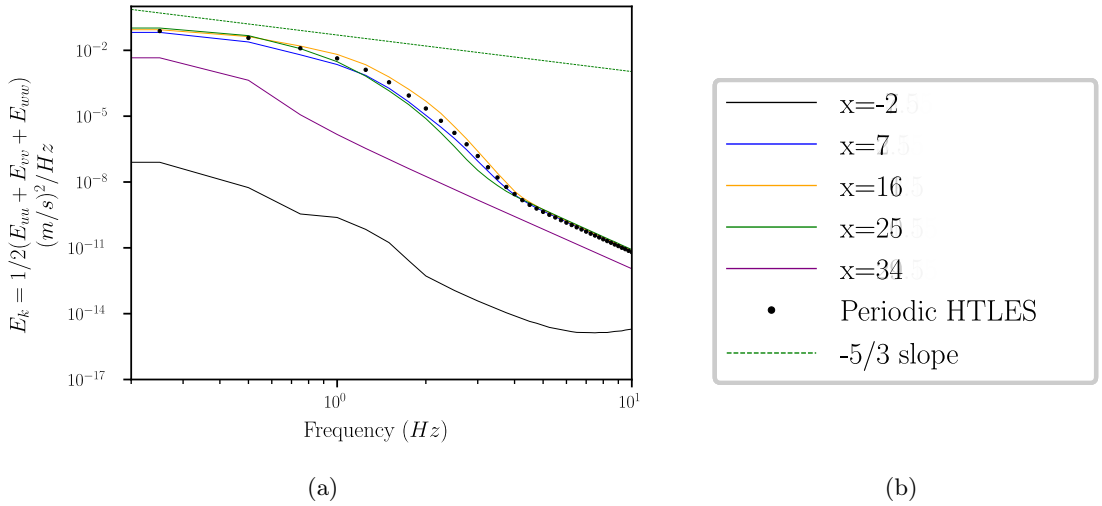

(a) (b)

Figure 4.36 – PSD of the turbulent kinetic energy, for the probe P5 in the reattachment zone. Comparing the Periodic HTLES and Active HTLES forcing both transitions using M1 mesh.

Figs. 4.35, 4.36, 4.37, 4.38 and 4.39 show the temporal spectra for the turbulent kinetic energy E_k for probes at different locations, and comparing them to the reference periodic HTLES calculation using M1 mesh. The use of Welch's periodogram method has made it possible to considerably reduce the variance thus allowing to compare the spectra more precisely.

As the shielding function is activated throughout the study of periodic hills case, it is important to note that probe P1 placed really closed to the wall ($y^+ < 100$) is treated in RANS mode, which will lead to a greater filtering of high frequencies, since the resolved turbulent structures are generated only in the LES zone, and are penetrating into the RANS zone.

In Figs. 4.35, 4.36, 4.37, 4.38 and 4.39, a drop in the turbulent energy is observed.

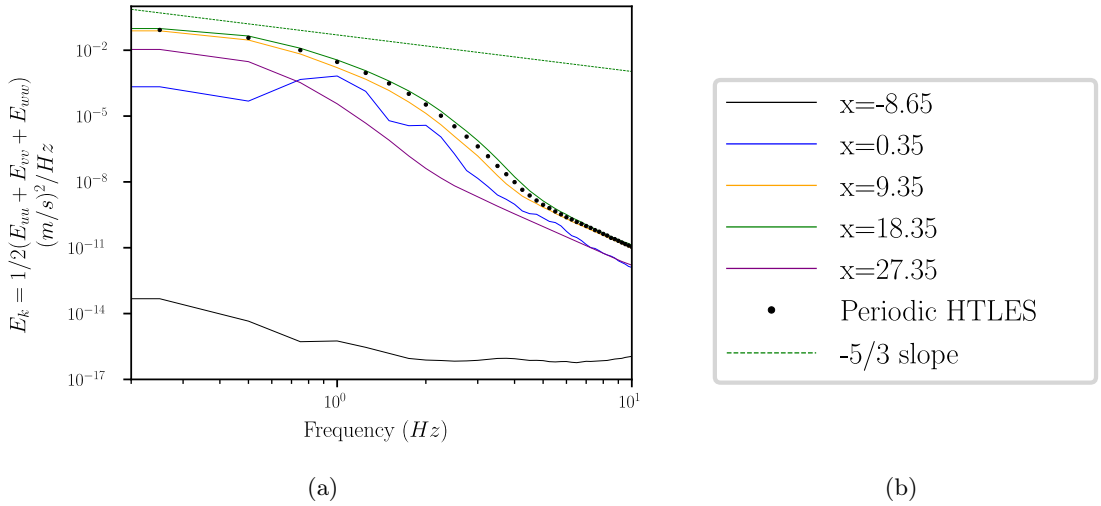

(a) (b)

Figure 4.37 – PSD of the turbulent kinetic energy, for the probe P1 in the detachment zone. Comparing the Periodic HTLES and Active HTLES forcing both transitions using M1 mesh.

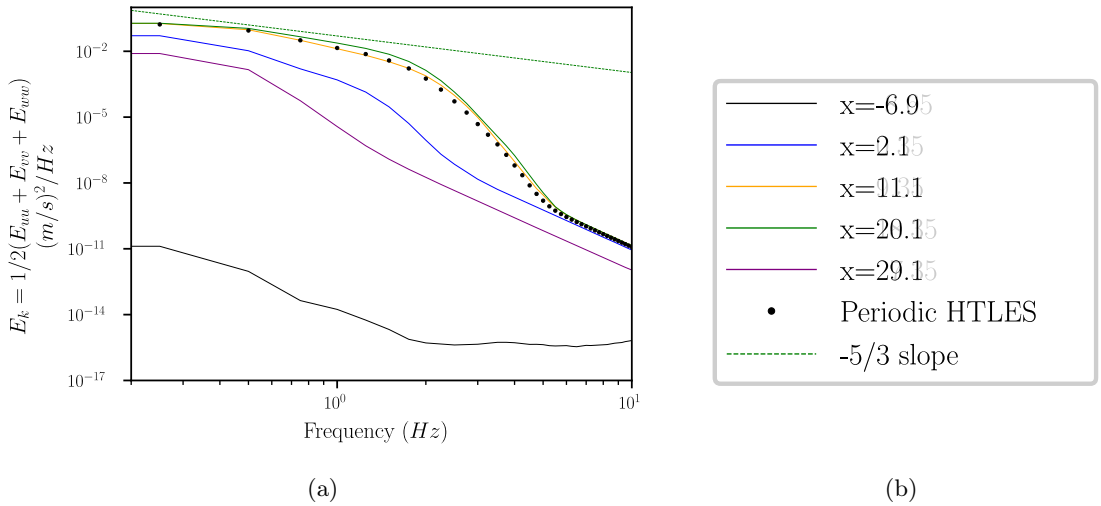

(a) (b)

Figure 4.38 – PSD of the total turbulent energy, for the probe P2 in the detachment zone. Comparing the Periodic HTLES and Active HTLES forcing both transitions using M1 mesh.

This drop is due to the fact that we approach the cutoff frequency. It can be seen that in the RANS region (first subdomain, $x/h < 0$), virtually there is no resolved energy. In the forcing region, very early in the subdomain 2 (blue lines), excellent recovery of the energy is observed.

It is interesting to note that at the beginning of the forcing region (P1), the application of the forcing populates the small scales first, while at the end of the forcing region (P2 and P3), it is the large scales that are generated first. Due to the fact that the forcing introduced is linear, one can not distinguish between different frequencies. Because the equation of forcing (refer to Eq. (3.69)) contains the fluctuating velocity, which is multiplied by A_{ij}, what it does is simply amplifying pre-existing small scale fluctuations. Hence, one cannot control which frequencies are generated. What is observed globally is that all the scales are generated quite well at the end of the second subdomain (P5, blue line).

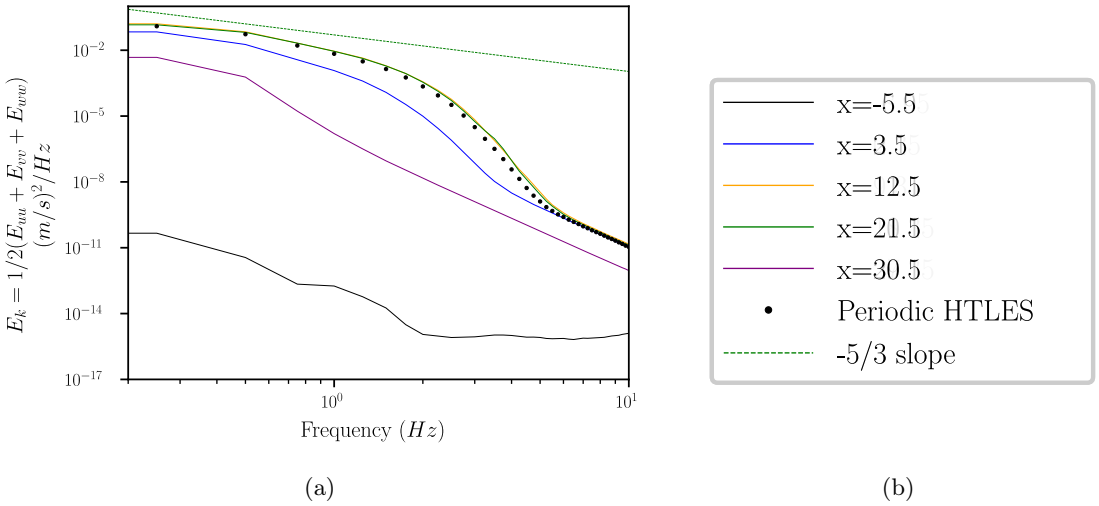

(a) (b)

Figure 4.39 – PSD of the turbulent kinetic energy, for the probe P4 in the detachment zone. Comparing the Periodic HTLES and Active HTLES forcing both transitions using M1 mesh.

For all the probes located at different locations in the computational domain, a similar behaviour is observed. The introduction of the forcing at RANS-to-LES transition, populates rapidly compared to the reference results. Further in the domain (third subdomain onwards, $9 < x/h < 27$), an overestimation of energy is observed which is in agreement with the profiles plotted earlier in the chapter. A more interesting phenomenon is observed during the transition back to RANS from LES; a reduction in total energy is observed but not to the levels of energy expected in RANS region. But it can be seen as a huge improvement due to the fact that it is very difficult to kill the resolved structures.

4.4 Conclusion

This chapter was devoted to the development and first validation of the *active* approach within the framework of continuous hybrid approaches (here HTLES). Taking the configuration of the periodic hill flow as a reference, sensitivity studies were carried out in order to characterize the influence of the *active* approach with different data settings.

The conclusion of the comparison of the *active* approach against the Anisotropic Linear Forcing (ALF) method is decisive. The modifications to the system of equations of the ALF approach makes it possible to adapt the forcing method initially developed for zonal hybrid approaches with an overlapping zone to continuous hybrid approaches.

The sensitivity study with regard to the value of the coefficient has led to fix the coefficient $\mathcal{C} = 1$ in RANS-to-LES transition region. However, the same value of coefficient is unable to reduce the resolved energy when transitioning from LES-to-RANS. Hence, it is advisable to use a larger value of the coefficient ($1.5 < \mathcal{C} < 2$) in this region, which can be easily identified based on the sign of $\mathrm{d}r/\mathrm{d}t$.

In the configuration considered, the predictions of the quantities of interest are in good agreement with the references, significantly improving the results compared to those without forcing. These results are encouraging in particular because this *active* approach can be applied to any hybrid model.

In the last step of the chapter, analysis is focused on the ability of *active* HTLES to resolve turbulent fluctuations including the near-wall region treated in RANS mode. The

temporal power spectral density of the turbulent kinetic energy in *active* HTLES is compared with the reference periodic HTLES computation, which gives the measure of resolved turbulent energy in the domain. Globally, the behaviour is very well reproduced after the transition region, confirming the effectiveness of introducing the forcing at transition.

Finally, these results provide a proof of concept for generating the fluctuating resolved motion via the forcing proposed, which is independent of target statistics and which is not a synthetic generator. Active HTLES makes it possible to apply the forcing in RANS-to-LES transition or LES-to-RANS transition without the need of an overlapping region, which significantly simplifies the implementation and possibly reduces the computational cost.

CHAPTER 5

Backward facing step

This chapter is dedicated to the validation of the *active* approach proposed in chapter 3 by applying it to the Backward facing step. The first half of the chapter is dedicated to the application of the active method to the channel case and later in the chapter it is extended to the back-step flow.

Contents

5.1 Introduction

The backward-facing step is a classical test case in turbulence modeling. The sharp expansion of the flow creates a recirculation zone, which presents a challenge for turbulence models. It is fundamental to activate the forcing upstream of the step in order to have a reasonably developed resolved turbulence in the detached shear layer. Before the expansion (upstream), the backward-facing step is a channel. Hence, the first thing to do is to check if the forcing works in a channel case or not. This is a very challenging case, since there is no inflectional profile to generate resolved structures.

5.2 Channel case

The flow is characterized by the friction Reynolds number, $Re_\tau = u_\tau h/\nu = 590$, where u_τ is the friction velocity and h is the half-height of the channel. The overall size of the computational domain is $L_x \times L_y \times L_z = 64h \times 2h \times 3.2h$, discretized using the mesh given by $N_x \times N_y \times N_z = 640 \times 96 \times 64$, satisfying $\Delta y^+ \simeq 1$ at the wall, which is sufficiently fine for HTLES (Duffal et al., 2022).

The initial part of the channel ($x/h \in [0, 6.4]$) is treated in RANS mode by imposing the energy ratio $r = 1$ in the model. The gradual transition from RANS-to-LES occurs in $x/h \in [6.4, 12.8]$, by enforcing a modified energy ratio r_{mod}:

$$r_{\text{mod}} = f + (1 - f)\, r \quad \text{with} \quad f\left(\frac{x}{h}\right) = 2 - \frac{1}{6.4}\frac{x}{h} \quad \text{for} \quad x/h \in [6.4, 12.8] \tag{5.1}$$

and the rest of the channel is treated in LES mode. It is important to note that the periodic RANS computations are used as inlet boundary conditions. Since the Reynolds number is very low, the shielding function is deactivated for this test case in order to avoid having a large portion of the channel (up to $y^+ = 100$) in RANS mode. Since the objective is to test the efficiency of the forcing method, the fact that the absence of shielding function slightly degrades the results in comparison with DNS is not a significant issue. Also, the periodic computations are used as the reference here to compare the results of the active approach (for details refer to section 2.4.1).

5.2.1 Comparison using the coefficient $\mathcal{C} = 1$

The first step is to carry out a Periodic HTLES computation using a mesh whose computational domain is $L_x \times L_y \times L_z = 6.4h \times 2h \times 3.2h$ and discretized using $N_x \times N_y \times N_z = 64 \times 96 \times 64$, such that Δ_x, Δ_y and Δ_z is the same as for the mesh used for Active HTLES computations, in order to have access to validated reference data.

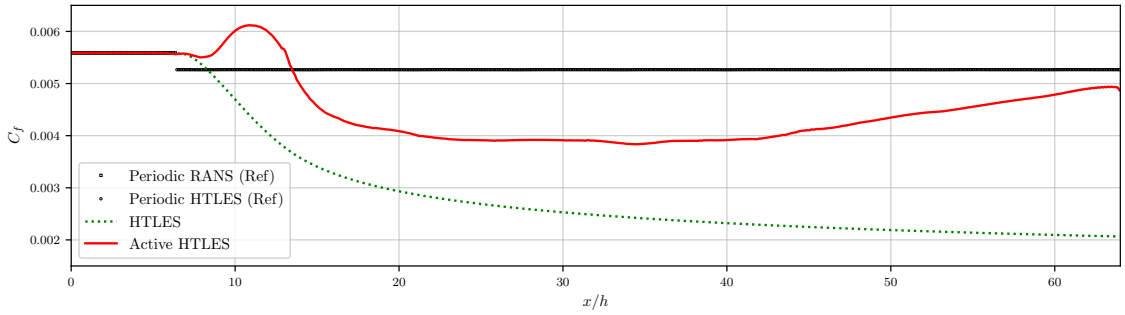

Figure 5.1 – Skin friction coefficient at the lower wall.

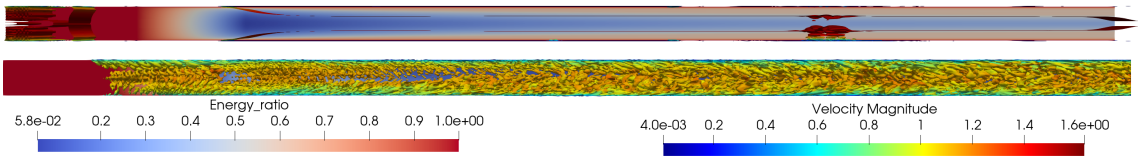

Figure 5.2 – Isocontours $Q = 0.05U_b^2/h^2$ colored with the velocity magnitude and, in the background, modeled-to-total turbulent energy ratio r, indicating the regions solved in RANS ($r = 1$) and in LES ($r < 1$). Top: HTLES without forcing, Bottom: Active HTLES.

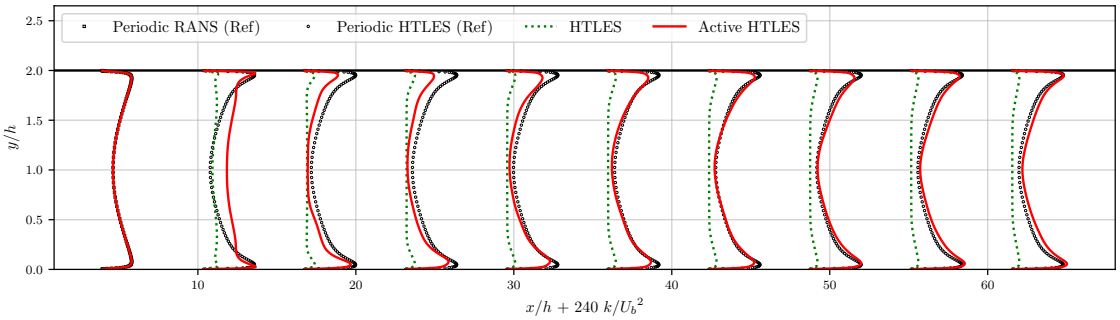

Figure 5.3 – Profiles of total turbulent kinetic energy (resolved+modeled).

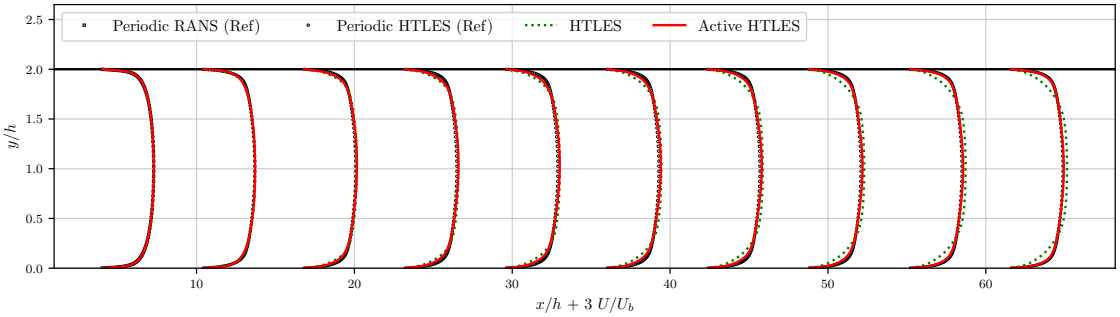

Figure 5.4 – Profiles of mean velocity.

Fig. 5.3 shows that without forcing, the total turbulent energy is severely underestimated, all along the channel, since, as can be seen in Fig. 5.2, virtually no resolved fluctuations are produced. This leads to completely wrong velocity profiles (refer to Figs. 5.4 and 5.5) and consequently, a much underestimated friction coefficient in Fig. 5.1.

On the other hand, when the forcing is applied, after a temporary overshoot of the turbulent energy, the flow rapidly converges towards the correct energy levels from $x/h = 15$, i.e., just after the end of the forcing region located at $x/h = 12.8$. In Fig. 5.5, an overestimation of U^+ is observed, which is due to the underestimation of friction velocity u_τ (or skin friction coefficient C_f). Although, the velocity profiles are significantly improved in case of applied forcing compared to the case without forcing due to the better prediction of friction velocity u_τ. It is seen in Fig. 5.2 that despite the lack of inflectional velocity profile, the active approach is able to rapidly generate resolved structures. Although not perfect, prediction of the friction coefficient is significantly improved (refer to Fig. 5.1).

Note that the coefficient $\mathcal{C} = 1$ is used here in this section; increasing further this coefficient can accelerate the recovery of the friction coefficient, at the cost of an increased initial

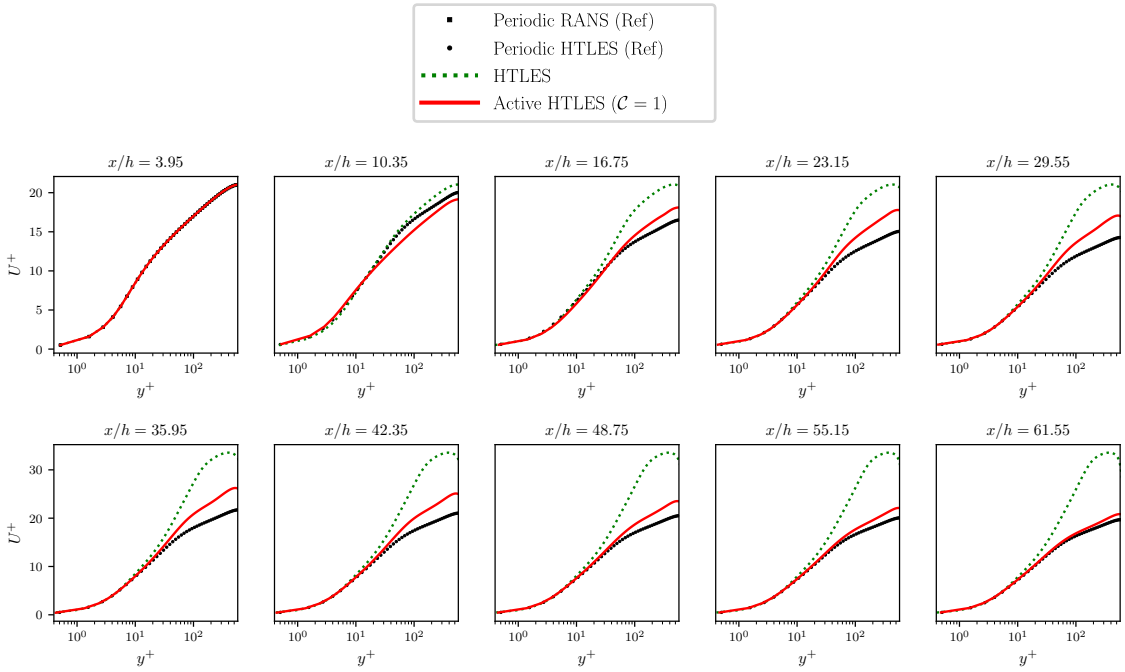

Figure 5.5 – Profiles of averaged velocity in semi-log scale.

overshoot of both C_f and total turbulent energy, which is discussed in the section 5.2.2.

5.2.2 Influence of different coefficient values

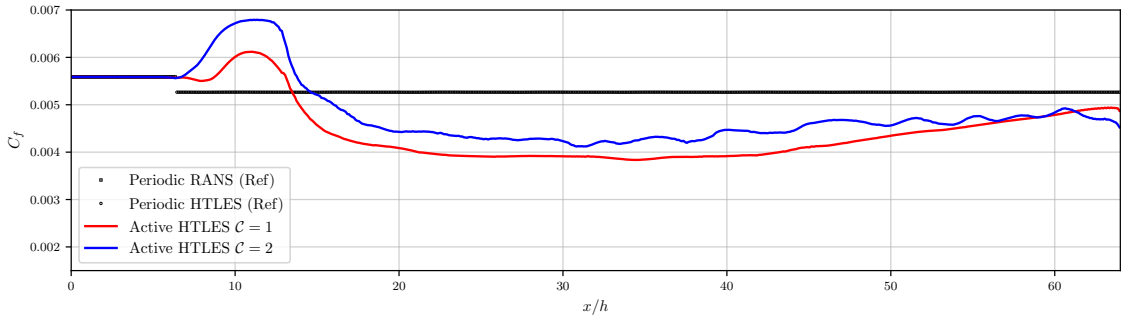

Figure 5.6 – Skin friction coefficient at the lower wall.

Increasing the value of the coefficient leads to better prediction of skin friction coefficient and velocity as can be seen in Figs. 5.6 and 5.7. Increasing the value of the coefficient to $\mathcal{C} = 2$, gives higher overshoots in the skin-friction coefficient and total turbulent kinetic energy at the RANS-to-LES transition (see Figs. 5.6 and 5.8, $6.4 < x/h < 12.8$). After $x/h = 15$, the underestimation of C_f is smaller, but the convergence towards the asymptotic value is not accelerated. Moreover, numerical instabilities appear. When the flow progresses further ahead in the spatial direction, after $x/h = 15$, the overshoot in the energy starts decreasing and around $x/h \simeq 30$, the energy predicted using $\mathcal{C} = 1$ and $\mathcal{C} = 2$ are of same order of magnitude. Moving further along in the streamwise direction, the total energy is underpredicted in the near-wall regions compared to periodic HTLES. Similarly, Fig. 5.7 indicates no significant improvement in the predictions of velocity profiles upon increasing the value of the coefficient. Hence, increasing the coefficient does not have a significant

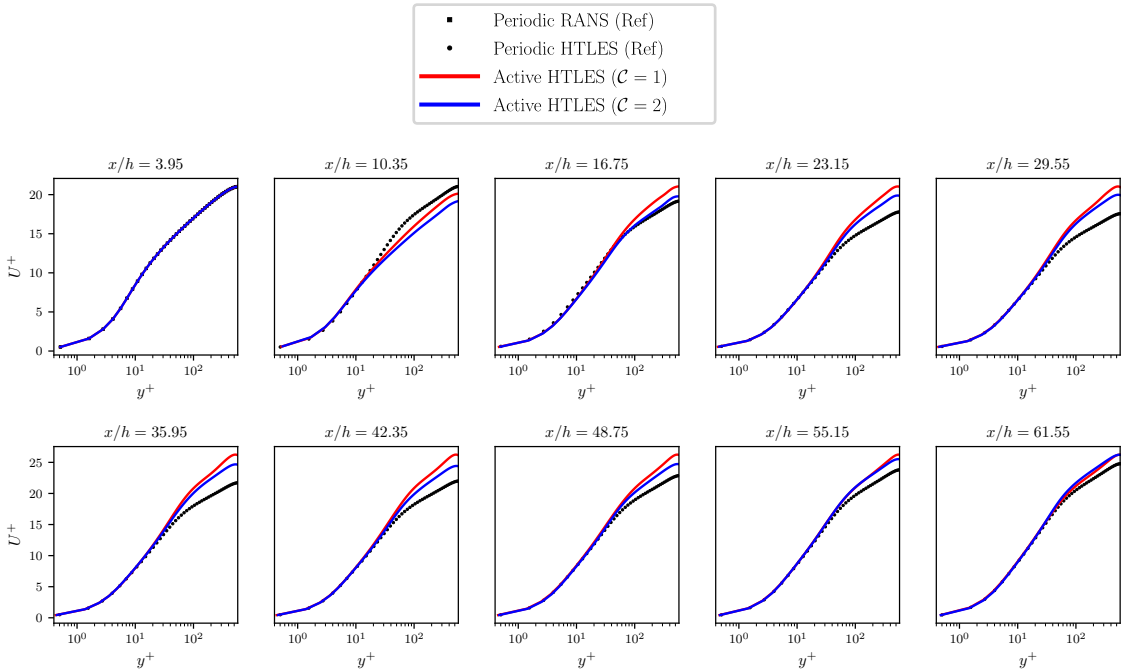

Figure 5.7 – Profiles of averaged velocity in semi-log scale.

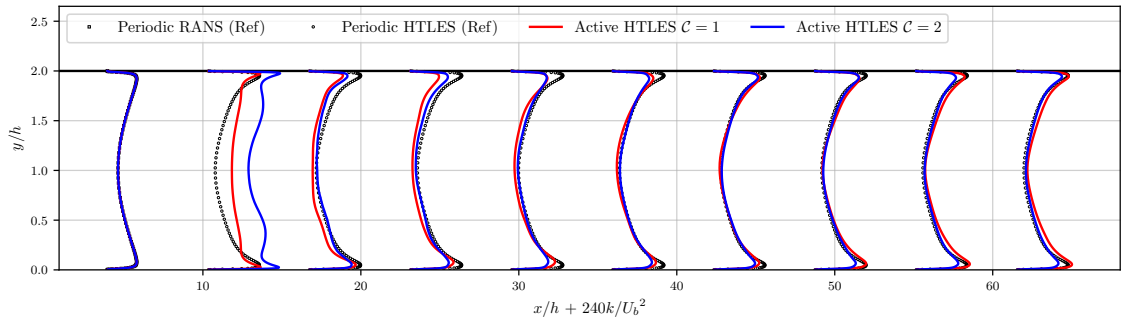

Figure 5.8 – Profiles of total turbulent kinetic energy (resolved+modeled).

impact on the prediction of the flow. Therefore, as for the case of the periodic hill, it is chosen to keep the coefficient at its theoretical value, $\mathcal{C} = 1$.

5.2.3 Spectral analysis

This section is dedicated to analyze the spectra of energy in the flow and to evaluate the unsteady information available. To do this, temporal spectra are produced, by recording the signals of the instantaneous variables at the positions explained in Table 5.1. It is important to note that all these probes are positioned at $y^+ = 50$ and $y^+ = 100$, from the wall.

Probes	P1	P2	P3	P4	P5	P6	P7	P8	P9	P10
x/h	3.2	9.6	16	22.4	28.8	35.2	41.6	48	54.4	60.8

Table 5.1 – Positions of the probes in streamwise direction used to record the signals to produce energy spectra.

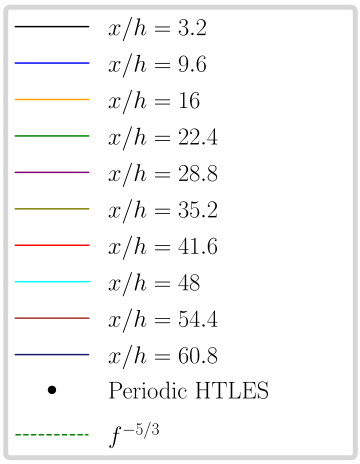

Figure 5.9 – Legends to read Energy spectrum presented in Fig. 5.10.

Periodic HTLES computation is used as a reference to compare the results of Active HTLES computation. Since, the shielding function is not used, the near-wall region ($y^+ = 50$) is also treated in LES mode.

Time signals for velocity are recorded at the positions mentioned in Table 5.1. The same method used in section 4.3.4 is used here to estimate the 1D power spectral density for the turbulent kinetic energy E_k. The main parameters are described below:

→ The signal is recorded over 2000000 time steps ($\simeq$ 31 flow through times), the time step $\mathrm{d}t = 0.001h/U_b$ is fixed in the study.

→ The signal is decomposed into 4 segments with 50% overlap, which leads to the reduction in the variance due to noise and smooth shape of the spectra.

→ The power spectral density using Welch's periodogram of the turbulent variables is calculated for each of the successive segments using Hann's window.

The cutoff frequency of the filter is defined by:

$$f_c = \frac{U_s}{2\Delta} \tag{5.2}$$

where $\mathrm{d}t$ is the time step, U_s sweeping velocity and Δ the characteristic size of the cells. Here, the dependence of cutoff frequency on time step is not considered because the time step is sufficiently small and fixed, $\mathrm{d}t = 0.001h/U_b$.

	Probes	P1	P2	P3	P4	P5	P6	P7	P8	P9	P10
f_s	$y^+ = 50$	11.85	11.85	11.77	10.23	10.32	10.39	11.26	11.79	12.15	12.45
	$y^+ = 100$	11.04	11.04	11.08	10.90	10.91	10.90	11.13	11.43	11.58	11.65

Table 5.2 – Cutoff frequency at different probes positions (in Hz).

Figs. 5.10 shows the energy spectra for probes at different locations. Energy spectra plotted for HTLES case without forcing show that the resolved energy is always under predicted irrespective of the position in streamwise or wall normal direction when compared to the periodic case (refer to Figs. 5.10a, and 5.10b). But when the forcing is activated in

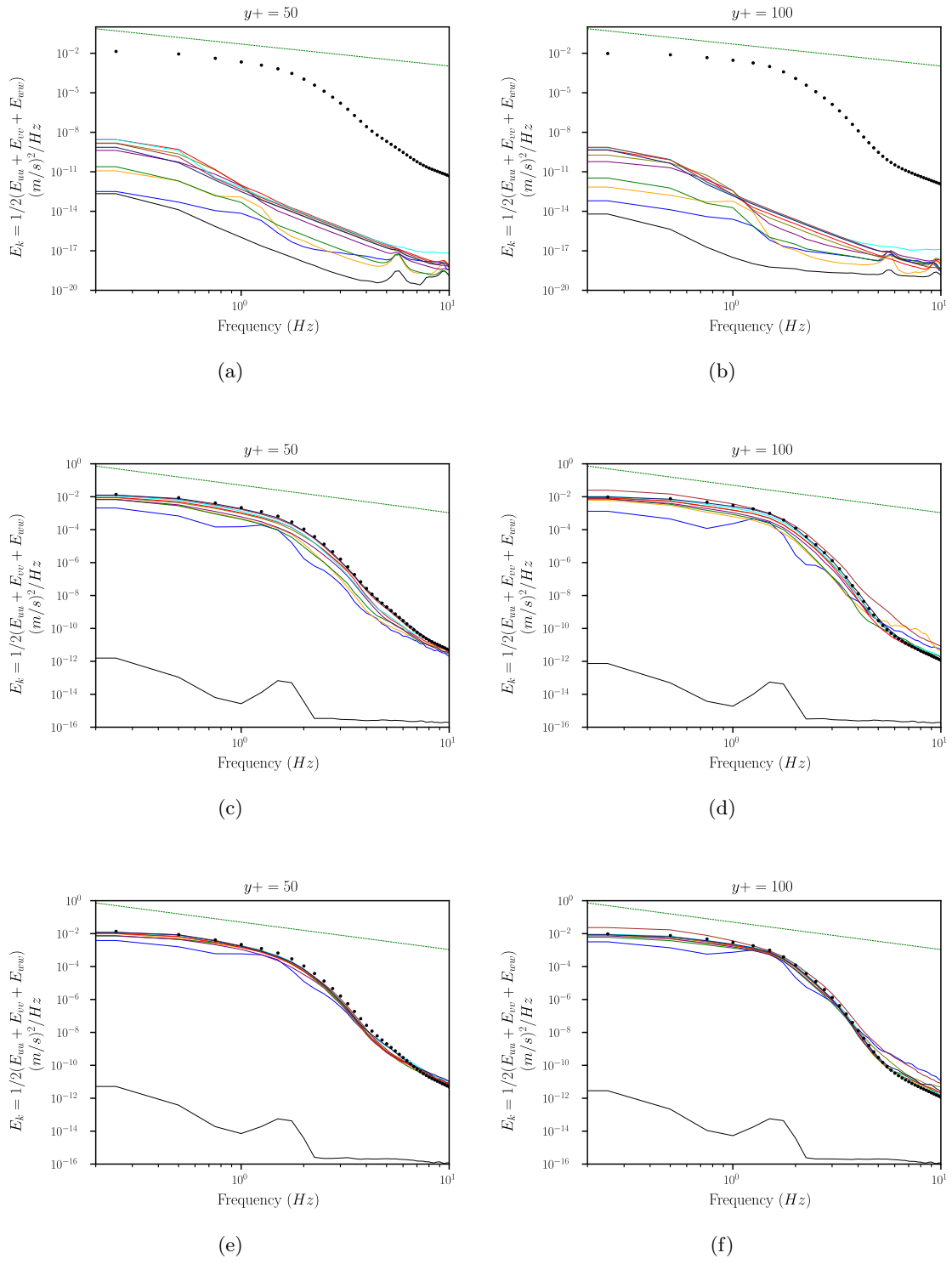

Figure 5.10 – PSD of the turbulent kinetic energy, for probes in Table 5.1 at different y^+ locations. (a) and (b) PSD for pure HTLES case; (c) and (d) for Active HTLES with $\mathcal{C} = 1$; (e) and (f) for Active HTLES with $\mathcal{C} = 2$. Comparing the Periodic HTLES with pure HTLES (without forcing), Active HTLES forcing RANS-to-LES transition with $\mathcal{C} = 1$ and Active HTLES forcing RANS-to-LES transition with $\mathcal{C} = 2$, respectively.

RANS-to-LES transition ($6.4 < x/h < 12.8$), irrespective of the value of the coefficient ($\mathcal{C}$) used, a sudden increase of the energy is observed compared to the energy in $x/h < 6.4$. It is interesting to note that upon activating the forcing in the transition region, all the frequencies are rapidly generated (refer to Fig. 5.10c to 5.10f, blue line). Also note that the high frequencies (between 10^0 and 2×10^0) are generated more rapidly compared to the low frequencies, which means that in the case with the forcing activated in the transition region, small scales are predicted more accurately than large scales in transition region.

5.3 Backward facing step

The case studied reproduces the geometry and the physical setup of the DNS without rotation of Lamballais (2014). In the backward facing step case the flow is subjected to a sudden increase of cross-sectional area, resulting in a separation at the point of sudden expansion. This is a representative model for separation flows, which are usually encountered in external aerodynamics, heat transfer systems, engine flows, flow around building, etc. To recall the geometry studied here, the streamwise direction is x. The half-height of the channel (y direction) upstream of the step is $h = 2H/3$, where H is the half-height downstream of the step. The lengths of the upstream part and the downstream part are $4H$ and $7.5H$, respectively. The length in spanwise direction (z) is $0.5H$, making the computational domain $L_x \times L_y \times L_z = 11.5H \times 1H \times 0.5H$. The spanwise direction is treated with a periodic condition and the upper wall at $y/H = 1$ is treated with a symmetric boundary condition. Profiles from periodic RANS channel flow computation is used as the inlet boundary condition. The flow is characterized by the bulk Reynolds number, $Re_b = U_H H/\nu = 5000$.

To evaluate the robustness of the active methodology against the length of the region where the forcing is activated, two different cases are studied here. In both the cases the forcing is applied before the sudden expansion of the channel (before the step). The main characteristics of the two cases are as follows:

→ **Case 1:** The forcing is applied in the transition region $x/H \in [-1, 0]$ by imposing a modified energy ratio r_{mod}:

$$r_{\text{mod}} = f + (1 - f)r \quad \text{with} \quad f\left(\frac{x}{H}\right) = -\frac{x}{H} \quad \text{for} \quad x/H \in [-1, 0] \tag{5.3}$$

At $x/H = -1$	At $x/H = 0$	At $x/H = 7.5$	At $y/H = 1$
$2\Delta y_1^+$	Δy_1^+	$5\Delta y_1^+$	$2\Delta y_1^+$

Table 5.3 – Characteristics of cell size (Δ_x and Δ_y) of the mesh used for case 1.

$N_{x_{\text{upstream}}}$	$N_{x_{\text{downstream}}}$	$N_{y_{\text{upstream}}}$	$N_{y_{\text{downstream}}}$	N_z	Total no. of cells
119	400	53	91	63	2.69M

Table 5.4 – Number of cells used for case 1.

The part up to $x/H = -1$ of the channel is treated in RANS mode by imposing the energy ratio $r = 1$ in the model and the rest is treated in LES mode. At $x/H = 0$, the

mesh is isotropic, with each cell size corresponding to the first cell size in wall normal direction (y). The first cell size at the wall is denoted as Δy_1^+, which corresponds to $\Delta y_1^+ \simeq 1$. The characteristics of this case are presented in Tables 5.3 and 5.4.

→ **Case 2:** The forcing is applied in the transition region $x/H \in [-2, 0]$ by imposing a modified energy ratio r_{mod}:

$$r_{\text{mod}} = f + (1 - f)r \quad \text{with} \quad f\left(\frac{x}{H}\right) = -\frac{x}{2H} \quad \text{for} \quad x/H \in [-2, 0] \tag{5.4}$$

The part up to $x/H = -2$ of the channel is treated in RANS mode by imposing the energy ratio $r = 1$ in the model and the rest is treated in LES mode. The mesh characteristics for this case are presented in Tables 5.5 and 5.6.

At $x/H = -2$	At $x/H = -1$	At $x/H = 0$	At $x/H = 7.5$	At $y/H = 1$
$5\Delta y_1^+$	$2\Delta y_1^+$	Δy_1^+	$5\Delta y_1^+$	$2\Delta y_1^+$

Table 5.5 – Characteristics of cell size (Δ_x and Δ_y) of the mesh used for case 2.

$N_{x_{\text{upstream}}}$	$N_{x_{\text{downstream}}}$	$N_{y_{\text{upstream}}}$	$N_{y_{\text{downstream}}}$	N_z	Total no. of cells
149	400	53	91	63	2.79M

Table 5.6 – Number of cells used for case 2.

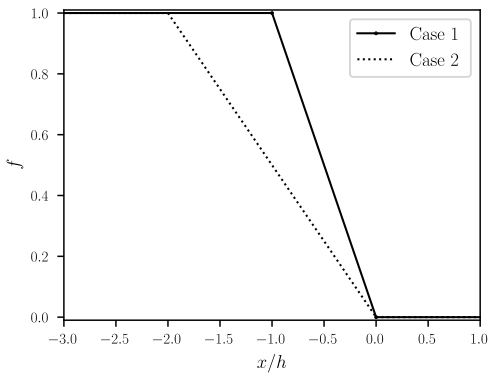

Figure 5.11 – Shape of the function f to impose a gradual transition.

It is important to note that the mesh satisfies $\Delta y_1^+ \simeq 1$.

For both cases, the mesh is created such a way that the cells are as isotropic as possible in the separation region. Also, a shielding function is applied up to $y^+ = 20$ by changing the coefficient $C1$ in Eq. (2.31) to 13.5 and keeping the same value for $p_1 = 8$ as before, to insure RANS mode in the near wall region. The coefficient $\mathcal{C} = 1$ is used for this test setup.

Figs. 5.12, 5.13, 5.14, 5.15 and 5.16 show the profiles of skin friction coefficient downstream of the step, total turbulent kinetic energy, observed energy ratio (i.e., computed during the simulation as $r_{\text{observed}} = k_m/(k_m + k_r)$), target energy ratio (i.e., used in the model), and streamwise velocity, respectively, at various streamwise locations. In RANS since all the scales are modeled, the target energy ratio and the observed energy ratio are 1.

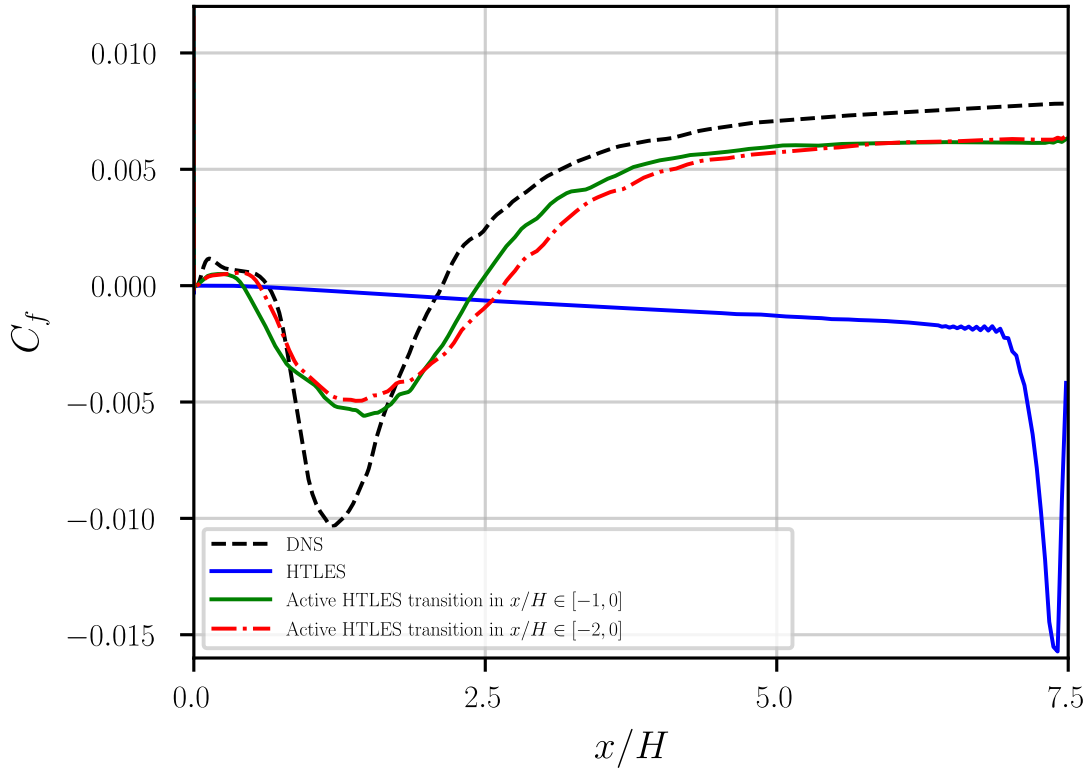

Figure 5.12 – Skin friction distribution at the lower wall downstream of the step.

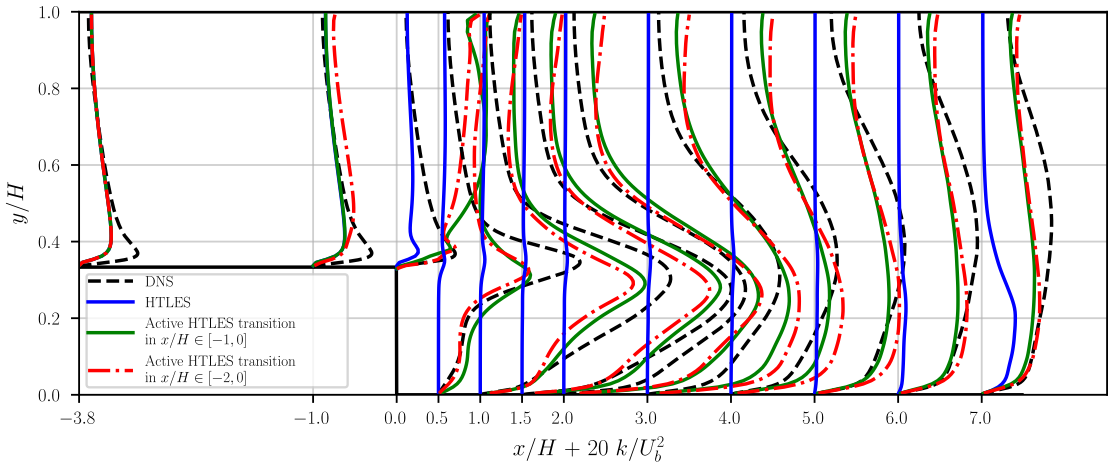

Figure 5.13 – Total turbulent kinetic energy (resolved+modeled). Comparing DNS results taken from Lamballais (2014) with HTLES without forcing, active HTLES with different regions of transition in streamwise direction.

The modified energy ratio in the transition zone makes it possible to visualize the interface between RANS and LES regions.

As mentioned earlier, periodic RANS profiles are imposed as inlet boundary condition. Hence, the profiles plotted at $x/H = -3.8$ corresponds to the RANS profiles for all the cases, for all turbulent quantities. Fig. 5.12 shows that when the forcing is not applied, the friction coefficient at the lower wall is overestimated in the recirculation region, and

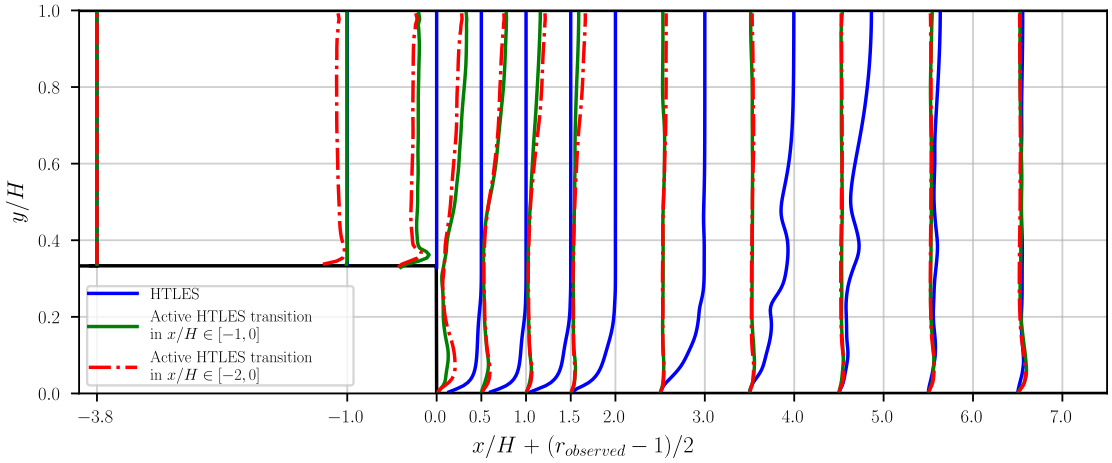

Figure 5.14 – Same figure as Fig. 5.13 for the observed energy ratio.

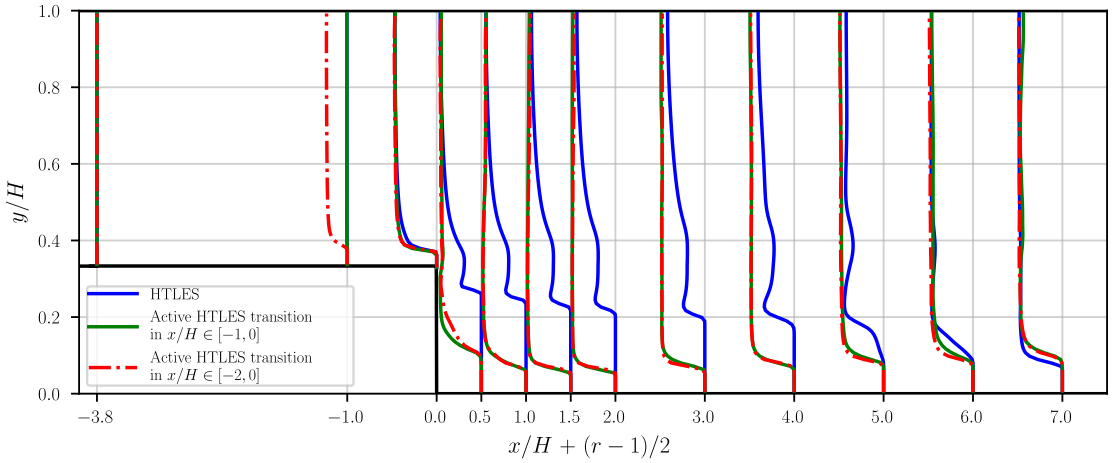

Figure 5.15 – Same figure as Fig. 5.13 for the target energy ratio.

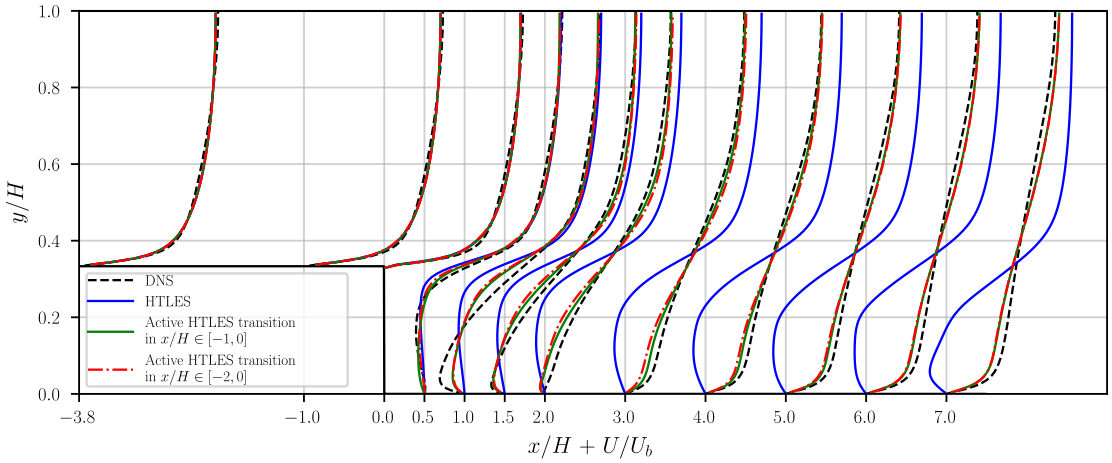

Figure 5.16 – Same figure as Fig. 5.13 for the streamwise velocity.

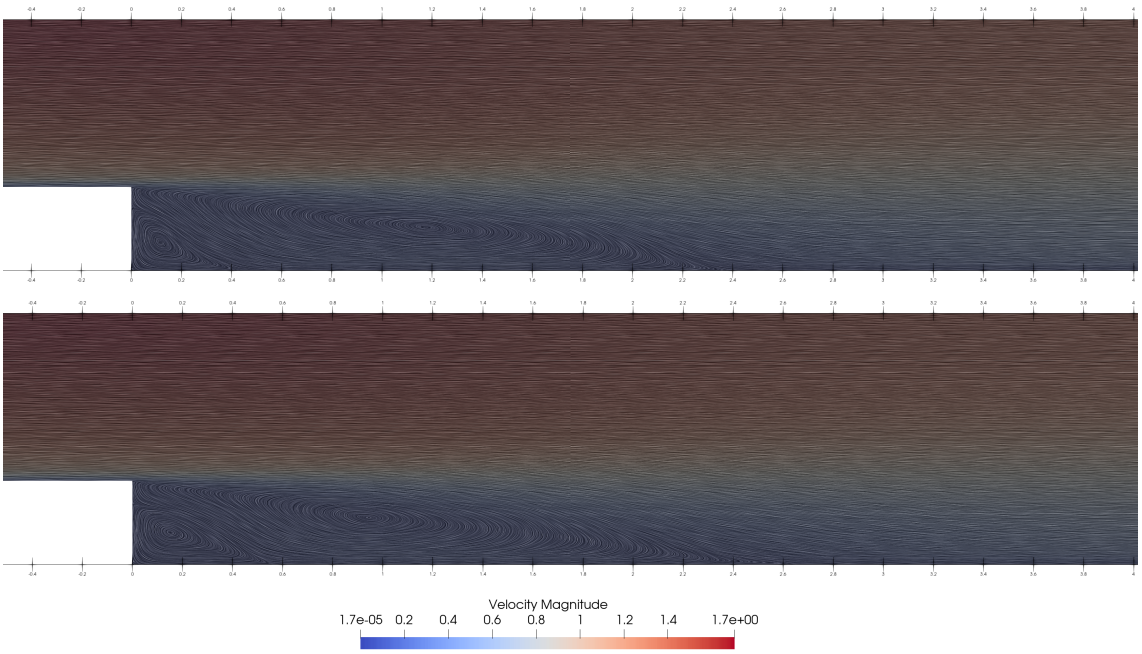

Figure 5.17 – Mean streamlines colored with velocity magnitude. Top: Transition region in $x/h \in [-1, 0]$, Bottom: Transition region in $x/h \in [-2, 0]$.

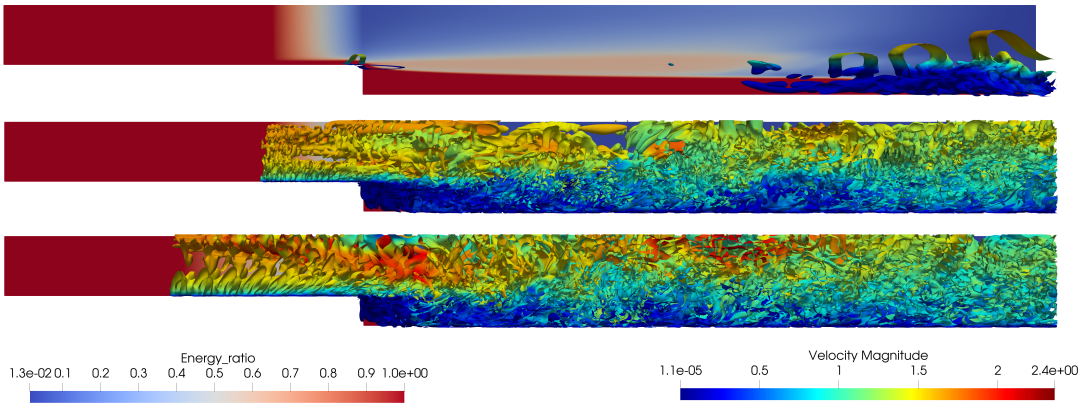

Figure 5.18 – Isocontours $Q = 0.05U_H^2/H^2$ colored with the velocity magnitude and in the background, modeled-to-total turbulent energy ratio r, indicating the regions solved in RANS ($r = 1$) and in LES ($r < 1$). Top: HTLES without forcing, Middle: Active HTLES for a transition in $x/h \in [-1, 0]$, Bottom: Active HTLES for a transition in $x/h \in [-2, 0]$.

globally the estimation is completely wrong. With the active HTLES for both the cases, it is drastically improved. Both the positive and the negative peak associated with the recirculation zones are underpredicted. Increasing the forcing region gives better predictions of the secondary recirculation zone, but does not improve C_f in the rest of the domain.

Regarding the total turbulent energy (refer to Fig. 5.13), for case 1, since the region where the forcing is applied is shorter compared to case 2, it experiences stronger gradient of energy ratio. Due to which case 1 exhibits stronger overestimation of total energy at $x/H = 0$. For both cases the correct levels of energy is observed from $x/H \simeq 1.5$ onwards, but overall the total energy is underestimated till $x/H = 3$. Comparing between the two cases of active HTLES, the case with larger forcing region estimates the profiles slightly better from $x/H = 3$ onwards. In contrast, for HTLES without forcing the total energy

remains close to zero, until the very end of the computational domain ($x/H > 6$).

Fig. 5.14 and 5.15 show the observed energy ratio profiles globally follow those of the target energy ratio even if some discrepancies appear, which shows that the partition of energy indeed reaches the expected level in case of active HTLES. In contrast, for HTLES without forcing the partition of energy reaches the expected levels at around $x/H = 7$, due to which in Fig. 5.13, the total energy is highly underestimated. Close to the wall, the meaning of the observed energy ratio is ambiguous since both k_m and k_r is zero.

Profiles of streamwise velocity are shown in Fig. 5.16, since the RANS mode is imposed in both the cases of active HTLES, the profiles which are imposed at the inlet are preserved. For HTLES without forcing, correct velocity profiles are never observed. For active HTLES, much better velocity profiles are obtained throughout the computational domain, except for the recirculation velocity which is underestimated at $x/H = 1$.

Fig. 5.17 shows mean streamlines computed using the line integral convolution (LIC) algorithm of Paraview. The two classically observed recirculation zones (Chen et al., 2018) are clearly visible: the main recirculation zone (clockwise) and the secondary recirculation zone (counterclockwise).

	Main recirculation zone up to x/H	Secondary recirculation zone up to x/H
DNS	2.13	0.63
HTLES	7.5	0.275
Active HTLES forcing $\in [-1, 0]$	2.35	0.4
Active HTLES forcing $\in [-2, 0]$	2.5	0.53

Table 5.7 – Observed recirculation zones. Comparing the DNS results with the two cases computed with Active HTLES.

Increasing the region of forcing gives more accurate prediction of secondary recirculation zone, whereas shorter region of forcing provides accuracy in predicting the primary recirculation zone, according to the C_f distributions shown in Fig. 5.12. The Q-Isosurfaces presented in Fig. 5.18 show that the active HTLES rapidly develops resolved scales, by means of volume forcing. Indeed, resolved structures are remarkably observed right from the beginning of the transition region, although they don't look like physical turbulent structures. However, for the HTLES without forcing, the resolved structures takes a very long time to appear, and are far from developed turbulent structures, even at the end of the domain.

5.4 Conclusion

This chapter was devoted to extend the validation of the *active* methodology to the backward facing step case. To do so, the first part of the chapter focused on studying the effects of this volume forcing in a channel flow. The study concludes the effectiveness of applying the forcing by looking at turbulent energy and velocity profiles, as well as by performing a spectral analysis. Profiles of turbulent quantities plotted for channel case proves that the coefficient to be used for these calculations is $\mathcal{C} = 1$.

Then this methodology is extended to the backward facing step case, where two different cases were tested, based on the length of the transition region. Irrespective of the length of the transition region, the active method yields similar results. Apart from the fact at the end of the transition region, the overshoot observed is larger for forcing applied to a shorter region, due to stronger gradient of energy ratio. These results show the effectiveness and the robustness of the active methodology.

CHAPTER 6

Conclusions and future prospects

Conclusions

In the context of turbulence modeling, the industrially mature RANS statistical formalism fails to capture the instantaneous coherent structures of the flow and sometimes the correct mean flow, but keeps the computational cost in line with the industrial standards. On the other hand, LES models are capable of capturing these information and are generally more accurate, but at a very high computational cost. Hence, during this thesis, a hybrid RANS/LES approach is used, which combines the advantages of RANS and LES formalisms in order to reach the compromise between increased capabilities of LES and reduced numerical cost of RANS.

It is well-known that the key objective of any hybrid model is to reduce the modeled turbulent kinetic energy in LES region, which in turn helps reducing the turbulent viscosity. For an ideal model this reduction in the modeled energy is compensated by the increase in the resolved energy. In reality, the growth of the resolved energy is not fast enough to compensate for the reduction in the modeled energy. This causes a stress decay in the model, which is known as "Modeled Stress Depletion" or "grey area" problem. The work done during this thesis is dedicated to solve this problem. The approach of this thesis is articulated according to the following stages, which globally correspond to the different chapters of the manuscript:

(i) review of the state of the art in turbulence modeling,

(ii) theoretical framework of Hybrid Temporal LES (HTLES) model,

(iii) theoretical development of a new methodology called *active* HTLES,

(iv) analysis, calibration and validation of the *active* HTLES methodology against pre-existing Anisotropic Linear Forcing (ALF) method using the periodic hills case,

(v) application and validation of the *active* HTLES using the backward facing step.

The main results are summarized below:

(i) The review of the state of the art in turbulence modeling made it possible to convey the prerequisite of the thesis, in particular identifying different approaches (DNS, RANS, LES, hybrid RANS/LES) based on the resolved portion of the turbulent energy spectrum. The exact transport equations of the statistically averaged quantities with a view to compare them with the hybrid models have been presented for the statistical approach of turbulence modeling.

This review has allowed to discuss the filtering approach within the framework of scale resolving modeling. It also gives an overview of the spatial and Eulerian temporal turbulent energy spectrum. Under the assumption that the spectral cutoff filter is in the inertial zone of a Kolmogorov spectrum, different LES models have been discussed. The comparison of the transport equations of the statistical modeling (statistical mean operator) and scale resolving modeling (filtering operator) show that they are formally identical and provide a solid basis for developing a hybrid RANS/LES model.

Within the framework of hybrid modeling, various models have been discussed, based on a modification of the transport equation for the eddy viscosity or turbulent kinetic energy (DES, DDES, IDDES), or based on the introduction of hybridization function in the transport equation of dissipation to control the transition (PANS, PITM, TPITM). It is important to note that the introduction of TPITM model acts as a guide for temporal hybrid approaches.

(ii) Following the state of the art in turbulence modeling, this chapter presents the uniform temporal filtering in the context of hybrid models. Theoretical framework of Hybrid Temporal LES (HTLES) is presented ensuring H-equivalence with the TPITM. Unlike other hybrid models which have hybridization function in the transport equation of the dissipation rate, HTLES model has the hybridization function in the transport equation of the turbulent energy, which directly controls the level of energy. This feature helps sustaining the resolved turbulence and avoids pseudo-relaminarization of the flow.

This model was then applied to a few different configurations to test the robustness of the model. The model produces very satisfactory predictions of the flow with periodic boundary conditions in streamwise as well as spanwise directions. The robustness of the formulation near the wall is ensured by implementing the near-wall shielding functions, which ensure that the near-wall region is treated in RANS mode.

In continuous hybrid RANS/LES modeling, the model incorporates a mechanism that helps reducing the modeled stresses when transitioning from RANS-to-LES, but lacks a mechanism to transfer this reduced energy to the resolved part. This creates an imbalance in the total stresses. Hence, when it comes to the more realistic cases with inlet and outlet boundary conditions, the results produced by the HTLES model for different flow configurations are not satisfactory due to the fact that we are lacking a mechanism that helps keeping the total turbulent energy constant. Instead, what happens is, upon transitioning from RANS-to-LES, the modeled energy k_m decreases drastically and the resolved energy k_r remains very low. This violates the fundamental law of conservation of energy. This gives a motivation to develop a new methodology for the missing mechanism to transfer energy from the modeled part to the resolved part.

(iii) When transitioning from RANS-to-LES, there is a shift from fully modeled to partially resolved quantities. Unfortunately, the growth of resolved fluctuations relies solely on natural instabilities of the flow and is not fast enough to counterbalance the stress decay imposed by the model. A simple analysis in spectral space shows that there is a missing element in the model which transfers energy from the modeled component to the resolved component, since the momentum equation remains unaffected by variations in grid resolution.

To address this issue, a new method is proposed based on the pre-existing Anisotropic Linear Forcing (ALF), to model the commutation terms resulting from grid step variations, which are responsible for energy transfer but are commonly disregarded.

This new approach, referred to as *active* hybrid RANS/LES, can be applied to any hybrid model as it is not dependent on any underlying formalism. More importantly, this method is highly versatile as it does not require information regarding the interface between RANS and LES regions. It relies solely on local quantities, in particular the material derivative of the resolution parameter. A coefficient $\mathcal{C}$ is introduced in the model to control the intensity of the forcing.

(iv) As the *active* approach developed within the framework of continuous hybrid approaches is based on Anisotropic Linear Forcing (ALF), this chapter first tests the methodology against HTLES to see if the *grey area* problem is solved and against ALF using periodic hills case, since it was tested successfully previously. The comparison against ALF method is decisive. The modifications to the system of equations of the ALF approach has made it possible to adapt the forcing method, initially developed for zonal approaches with an overlapping zone, to continuous hybrid approaches.

The introduction of this forcing (active approach) in the transition region shows that the predictions of the quantities of interest are in good agreement with the references, and a significant improvement compared to the results of HTLES is observed. A sensitivity study to the value of the coefficient was also carried out. The temporal power spectral density of the turbulent energy shows that globally the behaviour is very well produced due to the application of the forcing, confirming the effectiveness of introducing the forcing at transition.

(v) The backward facing step is a classical test case in turbulence modeling. It is fundamental to activate the forcing upstream of the step in order to have a reasonably developed resolved turbulence in the detached shear layer. As the upstream geometry represents a channel, first the testing in the channel flow was carried out. The study in channel case shows the effectiveness of applying the forcing in the transition region by looking at different profiles and by spectral analysis.

Within the backward-facing step configuration, a sensitivity study of the width of the forcing region in generating the resolved fluctuations was carried out. It shows that irrespective of the length of the forcing region, the active method yields similar results, apart from the fact that at the end of the transition region, a larger overshoot in energy is observed when the forcing is applied to a shorter transition region, due to stronger gradient of energy.

Finally, these results show the effectiveness and the robustness of the active methodology. These results provide a proof of concept for generating the fluctuating resolved motion via the proposed forcing, which is independent of target statistics and which is not a synthetic generator. Active HTLES makes it possible to apply the forcing in RANS-to-LES transition or LES-to-RANS transition without the need of an overlapping region, which significantly simplifies the implementation and possibly reduces the computational cost.

Future prospects

In the context of generating the resolved fluctuations, the results are very encouraging, also they are definitely not perfect. There is still need for some extra work to be done. Introduction of the forcing at the interface opens up a whole new prospect because we were missing a method of enrichment at the continuous interface.

During this thesis we have tested mainly incompressible flows and boundary layer flows with separation. It is necessary to test this new methodology with compressible flows, impinging jet flows, jets in cross flow, etc. The method looks like it is robust to a change of some parameters, but we are not at the end of testing the optimal values of these parameters. For example, further testing has to be carried out to find the optimal values for the length of the transition region, and position of this transition region.

The forcing method proposed here is independent of any underlying formalism. It just needs a parameter that drives the RANS-to-LES transition, making the method highly versatile. Taking the advantage of this quality, it is possible to extend this *active* approach to other hybrid RANS/LES models, which lacks resolved stresses at the RANS-to-LES interfaces.

It is important to note that here we have taken into account the commutation errors in the streamwise direction in convective terms only. Here we have considered Embedded LES (ELES) with the zones of LES occupying the entire channel, but we can also have within the same configuration of ELES very local zones of LES in the middle of RANS zone. In this case there is a question regarding whether the commutation error in the

diffusive terms while moving in the tangential direction should be taken into account or not. Further developments have to be done in this direction.

It would also be necessary to extend this model to heat transfer. Doing so, one fundamental question arises regarding the commutation error occurring in the transport equation of the resolved temperature, whether introduction of forcing is necessary or not. The response to that question remains unanswered.

As mentioned earlier the, *active* approach proposed in the thesis relies solely on the resolution of local quantities. In hybrid RANS/LES, the quality of the results is significantly user-dependent, as the description of the turbulent scales is dictated by the mesh designed by the user. Hence, in association with this *active* approach, a new methodology that automatically adapts (self-adaptive) the local scale of description of a turbulent flow based on the physical characteristics of the flow can act as an answer to the question of user influence on the final outcome.

Bibliography

Von Kármán, T (1937). "Turbulence. JR Aeronaut Soc 41: 1108–1141". In: *Twenty-fifth Wilbur Wright memorial lecture delivered to the Royal Aeronautical Society on May 27th*.

Kolmogorov, Andrej Nikolaevich (1941). "Equations of turbulent motion in an incompressible fluid". In: *Dokl. Akad. Nauk SSSR*. Vol. 30, pp. 299–303.

Shannon, C.E. (1949). "Communication in the Presence of Noise". In: *Proceedings of the IRE* 37.1, pp. 10–21. URL: https://doi.org/10.1109/jrproc.1949.232969.

Kampé, DE FERIET J (1951). "Theoretical and experimental averages of turbulent functions". In: *Proc. K. Ned. Akad. Wet.* Vol. 53, pp. 389–398.

Smagorinsky, Joseph (1963). "General circulation experiments with the primitive equations: I. The basic experiment". In: *Monthly weather review* 91.3, pp. 99–164.

Bradshaw, Peter et al. (1967). "Calculation of boundary-layer development using the turbulent energy equation". In: *Journal of Fluid Mechanics* 28.3, pp. 593–616.

Welch, Peter (1967). "The use of fast Fourier transform for the estimation of power spectra: a method based on time averaging over short, modified periodograms". In: *IEEE Transactions on audio and electroacoustics* 15.2, pp. 70–73.

Daly, Bart J et al. (1970). "Transport equations in turbulence". In: *The physics of fluids* 13.11, pp. 2634–2649.

Bradshaw, Peter (1972). "The understanding and prediction of turbulent flow". In: *The Aeronautical Journal* 76.739, pp. 403–418.

Jones, W Peter et al. (1972). "The prediction of laminarization with a two-equation model of turbulence". In: *International journal of heat and mass transfer* 15.2, pp. 301–314.

Tennekes, Hendrik et al. (1972). *A first course in turbulence*. MIT press.

Hinze, J (1975). "Turbulence". In: *New York*.

Launder, Brian Edward et al. (1975). "Progress in the development of a Reynolds-stress turbulence closure". In: *Journal of fluid mechanics* 68.3, pp. 537–566.

Leonard, Athony (1975). "Energy cascade in large-eddy simulations of turbulent fluid flows". In: *Advances in geophysics*. Vol. 18. Elsevier, pp. 237–248.

Tennekes, H (1975). "Eulerian and Lagrangian time microscales in isotropic turbulence". In: *Journal of Fluid Mechanics* 67.3, pp. 561–567.

Launder, Brian Edward et al. (1983). "The numerical computation of turbulent flows". In: *Numerical prediction of flow, heat transfer, turbulence and combustion*. Elsevier, pp. 96–116.

Kim, John et al. (1987). "Turbulence statistics in fully developed channel flow at low Reynolds number". In: *Journal of fluid mechanics* 177, pp. 133–166.

Schiestel, Roland (1987). "Multiple-time-scale modeling of turbulent flows in one-point closures". In: *The Physics of fluids* 30.3, pp. 722–731.

Speziale, CG (1987). "On the decomposition of turbulent flow fields for the analysis of coherent structures". In: *Acta Mechanica* 70.1, pp. 243–250.

Wilcox, David C (1988). "Reassessment of the scale-determining equation for advanced turbulence models". In: *AIAA journal* 26.11, pp. 1299–1310.

Germano, Massimo et al. (1991). "A dynamic subgrid-scale eddy viscosity model". In: *Physics of Fluids A: Fluid Dynamics* 3.7, pp. 1760–1765.

Kolmogorov, Andrei Nikolaevich (1991). "The local structure of turbulence in incompressible viscous fluid for very large Reynolds numbers". In: *Proceedings of the Royal Society of London. Series A: Mathematical and Physical Sciences* 434.1890, pp. 9–13.

Speziale, Charles G et al. (1991). "Modelling the pressure–strain correlation of turbulence: an invariant dynamical systems approach". In: *Journal of fluid mechanics* 227, pp. 245–272.

Germano, Massimo (1992). "Turbulence: the filtering approach". In: *Journal of Fluid Mechanics* 238, pp. 325–336.

Sandham, ND et al. (1992). "The late stages of transition to turbulence in channel flow". In: *Journal of Fluid Mechanics* 245, pp. 319–348.

Spalart, Philippe et al. (1992). "A one-equation turbulence model for aerodynamic flows". In: *30th aerospace sciences meeting and exhibit*, p. 439.

Kahlig, Peter (1993). "Some aspects of Julius von Hann's contribution to modern climatology". In: *Interactions Between Global Climate Subsystems: The Legacy of Hann* 75, pp. 1–7.

Menter, Florian R (1994). "Two-equation eddy-viscosity turbulence models for engineering applications". In: *AIAA journal* 32.8, pp. 1598–1605.

Ghosal, Sandip et al. (1995). "The basic equations for the large eddy simulation of turbulent flows in complex geometry". In: *Journal of Computational Physics* 118.1, pp. 24–37.

Le, Hung et al. (1997). "Direct numerical simulation of turbulent flow over a backward-facing step". In: *Journal of fluid mechanics* 330, pp. 349–374.

Spalart, Philippe R (1997). "Comments on the feasibility of LES for wings, and on a hybrid RANS/LES approach". In: *Proceedings of first AFOSR international conference on DNS/LES*. Greyden Press.

Hanjalić, K et al. (1998). "Contribution towards the second-moment closure modelling of separating turbulent flows". In: *Computers & fluids* 27.2, pp. 137–156.

Lund, Thomas S et al. (1998). "Generation of turbulent inflow data for spatially-developing boundary layer simulations". In: *Journal of computational physics* 140.2, pp. 233–258.

Wilcox, David C et al. (1998). *Turbulence modeling for CFD*. Vol. 2. DCW industries La Canada, CA.

Moser, Robert D et al. (1999). "Direct numerical simulation of turbulent channel flow up to Re τ= 590". In: *Physics of fluids* 11.4, pp. 943–945.

Chassaing, Patrick (2000). *Mécanique des fluides*.

Mellen, CP et al. (2000). "Large eddy simulation of the flow over periodic hills". In: *16th IMACS world congress*. Lausanne, Switzerland, pp. 21–25.

Nikitin, NV et al. (2000). "An approach to wall modeling in large-eddy simulations". In: *Physics of fluids* 12.7, pp. 1629–1632.

Pope, Stephen B et al. (2000). *Turbulent flows*. Cambridge university press.

Pruett, C David (2000). "Eulerian time-domain filtering for spatial large-eddy simulation". In: *AIAA journal* 38.9, pp. 1634–1642.

Spalart, Philippe R (2000). "Strategies for turbulence modelling and simulations". In: *International journal of heat and fluid flow* 21.3, pp. 252–263.

Travin, Andrei et al. (2000). "Detached-eddy simulations past a circular cylinder". In: *Flow, turbulence and combustion* 63.1-4, pp. 293–313.

Manceau, Remi et al. (2001). “Inhomogeneity and anisotropy effects on the redistribution term in Reynolds-averaged Navier–Stokes modelling”. In: *Journal of Fluid Mechanics* 438, pp. 307–338.

Spille-Kohoff, A et al. (2001). “Generation of turbulent inflow data with a prescribed shear-stress profile”. In: *TECHNISCHE UNIV BERLIN (GERMANY) HERMANN-FOTTINGER INST FUR STROMUNGSMECHANIK*.

Strelets, M (2001). “Detached eddy simulation of massively separated flows”. In: *39th Aerospace sciences meeting and exhibit*, p. 879.

Manceau, Rémi et al. (2002). “Elliptic blending model: A new near-wall Reynolds-stress turbulence closure”. In: *Physics of Fluids* 14.2, pp. 744–754.

Klein, Markus et al. (2003). “A digital filter based generation of inflow data for spatially developing direct numerical or large eddy simulations”. In: *Journal of computational Physics* 186.2, pp. 652–665.

Lundgren, Thomas S (2003). “Linearly forced isotropic turbulence”. In: *Center for Turbulence Research Annual Research Briefs 2003*.

Pruett, CD et al. (2003). “The temporally filtered Navier–Stokes equations: properties of the residual stress”. In: *Physics of Fluids* 15.8, pp. 2127–2140.

Temmerman, Lionel et al. (2003). “Investigation of wall-function approximations and subgrid-scale models in large eddy simulation of separated flow in a channel with streamwise periodic constrictions”. In: *International Journal of Heat and Fluid Flow* 24.2, pp. 157–180.

Archambeau, Frédéric et al. (Feb. 2004). “Code Saturne: A Finite Volume Code for the computation of turbulent incompressible flows - Industrial Applications”. In: *International Journal on Finite Volumes* 1.1.

Batten, Paul et al. (2004). “Interfacing statistical turbulence closures with large-eddy simulation”. In: *AIAA journal* 42.3, pp. 485–492.

Germano, Massimo (2004). “Properties of the hybrid RANS/LES filter”. In: *Theoretical and Computational Fluid Dynamics* 17, pp. 225–231.

Keating, Anthony et al. (2004a). “A priori and a posteriori tests of inflow conditions for large-eddy simulation”. In: *Physics of fluids* 16.12, pp. 4696–4712.

Keating, Anthony et al. (2004b). “Synthetic generation of inflow velocities for large-eddy simulation”. In: *34th AIAA Fluid Dynamics Conference and Exhibit*, p. 2547.

Schlüter, JU et al. (2004). “Large-eddy simulation inflow conditions for coupling with Reynolds-averaged flow solvers”. In: *AIAA journal* 42.3, pp. 478–484.

Breuer, M et al. (2005). “New reference data for the hill flow test case”. In: *ERCOFTAC QNET-CFD Knowledge Base Wiki: http://www. ercoftac. org/products_ and_ services/wiki*.

Chaouat, Bruno et al. (2005). “A new partially integrated transport model for subgrid-scale stresses and dissipation rate for turbulent developing flows”. In: *Physics of Fluids* 17.6, p. 065106.

Fröhlich, Jochen et al. (2005). “Highly resolved large-eddy simulation of separated flow in a channel with streamwise periodic constrictions”. In: *Journal of Fluid Mechanics* 526, pp. 19–66.

Girimaji, Sharath et al. (2005). “Partially-averaged Navier Stokes model for turbulence: Implementation and validation”. In: *43rd AIAA Aerospace Sciences Meeting and Exhibit*, p. 502.

Schiestel, Roland et al. (2005). “Towards a new partially integrated transport model for coarse grid and unsteady turbulent flow simulations”. In: *Theoretical and Computational Fluid Dynamics* 18.6, pp. 443–468.

Breuer, M et al. (2006). *A comparative study of the turbulent flow over a periodic arrangement of smoothly contoured hills. ERCOFTAC Series. Direct and Large-Eddy Simulation VI, vol. 10.*

Hoyas, Sergio et al. (2006). "Scaling of the velocity fluctuations in turbulent channels up to Re τ= 2003". In: *Physics of fluids* 18.1, p. 011702.

Jarrin, Nicolas et al. (2006). "A synthetic-eddy-method for generating inflow conditions for large-eddy simulations". In: *International Journal of Heat and Fluid Flow* 27.4, pp. 585–593.

Sagaut, Pierre (2006). *Large eddy simulation for incompressible flows: an introduction.* Springer Science & Business Media.

Spalart, Philippe R et al. (2006). "A new version of detached-eddy simulation, resistant to ambiguous grid densities". In: *Theoretical and computational fluid dynamics* 20, pp. 181–195.

Gatski, Thomas B et al. (2007). "Current trends in modelling research for turbulent aerodynamic flows". In: *Philosophical Transactions of the Royal Society A: Mathematical, Physical and Engineering Sciences* 365.1859, pp. 2389–2418.

Rapp, Christoph et al. (2007). "Experimental investigations on the turbulent flow over a periodic hill geometry". In: *Fifth international symposium on turbulence and shear flow phenomena*. Begel House Inc.

Shur, Mikhail L et al. (2008). "A hybrid RANS-LES approach with delayed-DES and wall-modelled LES capabilities". In: *International journal of heat and fluid flow* 29.6, pp. 1638–1649.

Breuer, Michael et al. (2009). "Flow over periodic hills–numerical and experimental study in a wide range of Reynolds numbers". In: *Computers & Fluids* 38.2, pp. 433–457.

Cokljat, Davor et al. (2009). "Embedded LES methodology for general-purpose CFD solvers". In: *Sixth International Symposium on Turbulence and Shear Flow Phenomena*. Begel House Inc.

Jarrin, N et al. (2009). "Reconstruction of turbulent fluctuations for hybrid RANS/LES simulations using a synthetic-eddy method". In: *International Journal of Heat and Fluid Flow* 30.3, pp. 435–442.

Spalart, Philippe R (2009). "Detached-eddy simulation". In: *Annual review of fluid mechanics* 41, pp. 181–202.

Barri, Mustafa et al. (2010a). "DNS of backward-facing step flow with fully turbulent inflow". In: *International Journal for Numerical Methods in Fluids* 64.7, pp. 777–792.

Barri, Mustafa et al. (2010b). "Turbulent flow over a backward-facing step. Part 1. Effects of anti-cyclonic system rotation". In: *Journal of fluid mechanics* 665, pp. 382–417.

Fadai-Ghotbi, Atabak et al. (2010). "Temporal filtering: A consistent formalism for seamless hybrid RANS–LES modeling in inhomogeneous turbulence". In: *International Journal of Heat and Fluid Flow* 31.3, pp. 378–389.

Hamba, Fujihiro (2011). "Analysis of filtered Navier–Stokes equation for hybrid RANS/LES simulation". In: *Physics of Fluids* 23.1, p. 015108.

Hanjalić, Kemal et al. (2011). *Modelling turbulence in engineering and the environment: second-moment routes to closure*. Cambridge university press.

Laraufie, Romain et al. (2011). "A dynamic forcing method for unsteady turbulent inflow conditions". In: *Journal of Computational Physics* 230.23, pp. 8647–8663.

Rapp, Ch et al. (2011). "Flow over periodic hills: an experimental study". In: *Experiments in fluids* 51.1, pp. 247–269.

Visscher, Jan et al. (2011). "Particle image velocimetry measurements of massively separated turbulent flows with rotation". In: *Physics of Fluids* 23.7, p. 075108.

Wallin, Stefan et al. (2011). "Commutation error mitigation in variable-resolution PANS closure: Proof of concept in decaying isotropic turbulence". In: *6th AIAA Theoretical Fluid Mechanics Conference*, p. 3105.

Choi, Haecheon et al. (2012). "Grid-point requirements for large eddy simulation: Chapman's estimates revisited". In: *Physics of fluids* 24.1, p. 011702.

Deck, Sébastien (2012). "Recent improvements in the zonal detached eddy simulation (ZDES) formulation". In: *Theoretical and Computational Fluid Dynamics* 26, pp. 523–550.

Poletto, R et al. (2012). "Embedded DDES of 2D hump flow". In: *Progress in Hybrid RANS-LES Modelling: Papers Contributed to the 4th Symposium on Hybrid RANS-LES Methods, Beijing, China, September 2011*. Springer, pp. 169–179.

Tran, Thanh Tinh et al. (2012). "A hybrid temporal LES approach. Application to flows around rectangular cylinders". In: *9th ERCOFTAC Int. Symp. on Eng. Turb. Modelling and Measurements*.

Chaouat, Bruno et al. (2013a). "Hybrid RANS/LES simulations of the turbulent flow over periodic hills at high Reynolds number using the PITM method". In: *Computers & Fluids* 84, pp. 279–300.

— (2013b). "Partially integrated transport modeling method for turbulence simulation with variable filters". In: *Physics of Fluids* 25.12.

Davidson, Lars et al. (2013). "Embedded large-eddy simulation using the partially averaged Navier–Stokes model". In: *AIAA journal* 51.5, pp. 1066–1079.

Sagaut, Pierre et al. (2013). *Multiscale and multiresolution approaches in turbulence-LES, DES and Hybrid RANS/LES Methods: Applications and Guidelines*. World Scientific.

Lamballais, Eric (2014). "Direct numerical simulation of a turbulent flow in a rotating channel with a sudden expansion". In: *Journal of fluid mechanics* 745, pp. 92–131.

Shur, Michael L et al. (2014). "Synthetic turbulence generators for RANS-LES interfaces in zonal simulations of aerodynamic and aeroacoustic problems". In: *Flow, turbulence and combustion* 93.1, pp. 63–92.

De Laage de Meux, B et al. (2015). "Anisotropic linear forcing for synthetic turbulence generation in large eddy simulation and hybrid RANS/LES modeling". In: *Physics of Fluids* 27.3, p. 035115.

Friess, Ch et al. (2015). "Toward an equivalence criterion for hybrid RANS/LES methods". In: *Computers & Fluids* 122, pp. 233–246.

Lee, Myoungkyu et al. (2015). "Direct numerical simulation of turbulent channel flow up to". In: *Journal of fluid mechanics* 774, pp. 395–415.

Schmidt, Stephan et al. (2015). "Extended synthetic turbulence inflow generator within a hybrid LES–URANS methodology for the prediction of non–equilibrium wall–bounded flows". In: *Flow, Turbulence and Combustion* 95, pp. 669–707.

Davidson, L. (2016). "Zonal PANS: evaluation of different treatments of the RANS–LES interface". In: *Journal of Turbulence* 17.3, pp. 274–307.

Larsson, Johan et al. (2016). "Large eddy simulation with modeled wall-stress: recent progress and future directions". In: *Mechanical Engineering Reviews* 3.1, pp. 15–00418.

Manceau, Rémi (2016). "Progress in hybrid temporal LES". In: *Symposium on Hybrid RANS-LES Methods*. Springer, pp. 9–25.

Nini, Michele (2016). "Analysis of a novel hybrid RANS/LES technique based on Reynolds stress tensor reconstruction". In:

Skillen, Alex et al. (2016). "Accuracy and efficiency improvements in synthetic eddy methods." In: *International Journal of Heat and Fluid Flow* 62, pp. 386–394.

Chaouat, Bruno (2017). "Commutation errors in PITM simulation". In: *International Journal of Heat and Fluid Flow* 67, pp. 138–154.

Schmidt, Stephan et al. (2017). “Source term based synthetic turbulence inflow generator for eddy-resolving predictions of an airfoil flow including a laminar separation bubble”. In: *Computers & Fluids* 146, pp. 1–22.

Chen, Lin et al. (June 2018). “A Review of Backward-Facing Step (BFS) Flow Mechanisms, Heat Transfer and Control”. In: *Thermal Science and Engineering Progress* 6, pp. 194–216. (Visited on 07/06/2023).

Erbig, Lars et al. (2018). “Experimental and numerical study of passive gap noise”. In: *2018 AIAA/CEAS Aeroacoustics Conference*, p. 3595.

Mockett, Charles et al. (2018). “Go4Hybrid: Grey Area Mitigation for Hybrid RANS-LES Methods”. In: *Notes on Numerical Fluid Mechanics and Multidisciplinary Design* 134.

Haywood, John S et al. (2019). “A control forced concurrent precursor method for LES inflow”. In: *Flow, Turbulence and Combustion* 102, pp. 849–864.

Holgate, Joshua et al. (2019). “A review of embedded large eddy simulation for internal flows”. In: *Archives of Computational Methods in Engineering* 26, pp. 865–882.

Duffal, Vladimir (Nov. 2020). “Développement d’un modèle hybride RANS-LES pour l’étude des efforts instationnaires en paroi”. PhD thesis.

Han, Yiyu et al. (2020). “Modification to improved delayed detached-eddy simulation regarding the log-layer mismatch”. In: *AIAA Journal* 58.2, pp. 712–721.

Manceau, Rémi (2020). *Turbulence modelling for CFD*.

Chaouat, Bruno et al. (2021). “Energy partitioning control in the PITM hybrid RANS/LES method for the simulation of turbulent flows”. In: *Flow, Turbulence and Combustion* 107.4, pp. 937–978.

Janin, Jérémie et al. (2021). “A new linear forcing method for isotropic turbulence with controlled integral length scale”. In: *Physics of Fluids* 33.4.

Kuhn, Thomas (2021). *Quantification of uncertainty in aeroacoustic cavity noise simulations with a discontinuous Galerkin solver*. Verlag Dr. Hut.

Piomelli, Ugo (2021). “Large-eddy simulations”. In: *Advanced Approaches in Turbulence*. Elsevier, pp. 83–131.

Duffal, Vladimir et al. (2022). “Development and Validation of a new formulation of Hybrid Temporal Large Eddy Simulation”. In: *Flow, Turbulence and Combustion* 108.1, pp. 1–42.

Heinz, Stefan (2022). “Remarks on energy partitioning control in the PITM hybrid RANS/LES method for the simulation of turbulent flows”. In: *Flow, Turbulence and Combustion* 108.4, pp. 927–933.

Kempf, Daniel et al. (2022). “Zonal Hybrid Computational Aeroacoustics Simulation of Trailing Edge Noise Using a High-Order Discontinuous Galerkin Method”. In: *28th AIAA/CEAS Aeroacoustics 2022 Conference*, p. 3021.

Schau, Kyle A et al. (2022). “An ensemble Synthetic Eddy Method for accurate treatment of inhomogeneous turbulence”. In: *Computers & Fluids* 248, p. 105671.

Appendices

APPENDIX A

$k-\omega$ SST HTLES model

The detailed formulation of the $k-\omega$ SST HTLES model (mentioned in section 2.3.3) is as follows:

$$\nu_{\text{sfs}} = \frac{a_1 k_{\text{sfs}}}{\max\left[a_1 \psi'(r)\,\omega^*_{\text{sfs}}, F_2 \widetilde{S}\right]} \tag{A.1}$$

$$\begin{aligned}
\frac{\partial k_{\text{sfs}}}{\partial t} + \widetilde{u_j}\frac{\partial k_{\text{sfs}}}{\partial x_j} &= P_k + \frac{\partial}{\partial x_j}\left[\left(\nu + \frac{\nu_{\text{sfs}}}{\sigma_k}\right)\frac{\partial k_{\text{sfs}}}{\partial x_j}\right] - \frac{k_{\text{sfs}}}{T_m}, \\
\frac{\partial \omega^*_{\text{sfs}}}{\partial t} + \widetilde{u_j}\frac{\partial \omega^*_{\text{sfs}}}{\partial x_j} &= \gamma_\omega \frac{1}{\psi'(r)}\widetilde{S}^2 + \frac{\partial}{\partial x_j}\left[\left(\nu + \frac{\nu_{\text{sfs}}}{\sigma_\omega}\right)\frac{\partial \omega^*_{\text{sfs}}}{\partial x_j}\right] - \beta_\omega {\omega^*_{\text{sfs}}}^2 \\
&\quad + (1-F_1)2\frac{1}{\sigma_{\omega 2}}\frac{1}{\psi'(r)\,\omega^*_{\text{sfs}}}\frac{\partial \omega^*_{\text{sfs}}}{\partial x_j}\frac{\partial k_{\text{sfs}}}{\partial x_j}
\end{aligned} \tag{A.2}$$

with the production limiter:

$$P_k = \min\left[\nu_{\text{sfs}}\widetilde{S}^2, a_2 C_\mu k_{\text{sfs}} \psi'(r)\,\omega^*_{\text{sfs}}\right] \tag{A.3}$$

In the context of hybridization the blending (weighting) functions are written as:

$$\begin{aligned}
&F_1 = \tanh\left[arg_1^4\right], \qquad F_2 = \tanh\left[arg_2^2\right], \\
&arg_1 = \min\left[\max\left[\frac{k_{\text{sfs}}^{1/2}}{C_\mu \omega^*_{\text{sfs}} d_w}, \frac{500\nu}{\omega^*_{\text{sfs}} d_w^2}\right], \frac{4\rho k_{\text{sfs}}}{\sigma_{\omega 2} CD_{k\omega} d_\omega^2}\right], \quad arg_2 = \max\left[\frac{2k_{\text{sfs}}^{1/2}}{C_\mu \omega^*_{\text{sfs}} d_w}, \frac{500\nu}{\omega^*_{\text{sfs}} d_w^2}\right], \\
&CD_{k\omega} = \max\left[2\rho\frac{1}{\sigma_{w2}\omega^*_{\text{sfs}}}\frac{\partial k_{\text{sfs}}}{\partial x_j}\frac{\partial \omega^*_{\text{sfs}}}{\partial x_j}, 10^{-20}\right].
\end{aligned} \tag{A.4}$$

The improved HTLES model, where the hybridization of the model is carried out by the energy ratio r, via the hybridization function $\psi'(r)$ and the modeled (modified) time scale T_m with the application of the shielding functions and Internal consistency constraint is written as follows:
Modeled time scale:

$$T_m = \frac{r}{\psi'(r)}\frac{k_m + c_r k_r}{C_\mu k_m \omega^*_m}, \qquad where \;\; c_r = \begin{cases} 0 \text{ if } r = 1, \\ f_s \text{ if } r < 1. \end{cases} \tag{A.5}$$

Energy ratio:

$$r = (1-f_s)\times 1 + f_s \times \min\left[1, r_K\right], \tag{A.6}$$

$$r_K = \frac{1}{\beta_0}\left(\frac{U_s}{\sqrt{k}}\right)^{2/3}\left(\omega_c \frac{k}{\varepsilon}\right)^{-2/3}, \tag{A.7}$$

$$\omega_c = \min\left[\frac{\pi}{\tau}, \frac{U_s \pi}{\Delta}\right], \quad U_s = U + \gamma\sqrt{k}, \quad \Delta = \Omega^{1/3}. \tag{A.8}$$

Shielding function:

$$f_s = 1 - \tanh\left[\max\left(\xi_K^{p_1}, \xi_D^{p_2}\right)\right], \tag{A.9}$$

$$\xi_K = C_1 \frac{\left(\nu^3/\varepsilon\right)^{1/4}}{d_w} \quad and \quad \xi_D = C_2 \frac{\Delta_{\max}}{d_w} \quad with \quad \Delta_{\max} = \max\left[\Delta_x, \Delta_y, \Delta_z\right]. \tag{A.10}$$

Hybridization function:

$$\psi'(r) = \frac{\beta_\omega}{C_\mu \gamma_\omega + r\left(\beta_\omega - C_\mu \gamma_\omega\right)}. \tag{A.11}$$

Constants of the model $k-\omega$ SST:

$$C = F_1 C_1 + (1 - F_1)\, C_2, \tag{A.12}$$

$$\gamma_{\omega 1} = \frac{\beta_{\omega 1}}{C_\mu} - \frac{C_\kappa^2}{\sigma_{\omega 1}\sqrt{C_\mu}}, \qquad \gamma_{\omega 2} = \frac{\beta_{\omega 2}}{C_\mu} - \frac{C_\kappa^2}{\sigma_{\omega 2}\sqrt{C_\mu}}. \tag{A.13}$$

C_μ	C_κ	a_1	a_2	σ_{k1}	σ_{k2}	$\sigma_{\omega 1}$	$\sigma_{\omega 2}$	$\beta_{\omega 1}$	$\beta_{\omega 2}$	$\gamma_{\omega 1}$	$\gamma_{\omega 2}$
0.09	0.41	0.31	10	$1/0.85$	1	2	$1/0.856$	0.075	0.0828	0.55	0.44

(A.14)

Constants of the HTLES method:

C_μ	γ	C_1	C_2	p_1	p_2
0.48	$2/3$	45	1.2	8	6

(A.15)

Estimation of statistically-averaged terms:

$$k = k_r + k_m, \quad k_r = \frac{1}{2}\left(\overline{\widetilde{u}_i \widetilde{u}_i} - \overline{\widetilde{u}_i}\;\overline{\widetilde{u}_i}\right), \quad k_m = \overline{k_{\text{sfs}}}, \tag{A.16}$$

$$\varepsilon \overset{\text{hyp}}{=} \varepsilon_m = C_\mu k_m \psi'(r)\, \omega_m^*, \quad \omega_m^* = \overline{\omega_{\text{sfs}}^*}, \tag{A.17}$$

$$U = \left(\sum_{i=1}^{3} \overline{\widetilde{u}_i}\right)^{1/2}. \tag{A.18}$$

The exponentially weighted average (Pruett et al., 2003) provides the estimate of the statistically averaged quantities, with a time filter width Δ_T being a few flow-through times, such that:

$$\frac{\partial \overline{f}(t, \Delta_T)}{\partial t} = \frac{\widetilde{f}(t) - \overline{f}(t, \Delta_T)}{\Delta_T}. \tag{A.19}$$

APPENDIX B

Paper A:
An active hybrid RANS-LES approach for grey area mitigation

An active hybrid RANS-LES approach for grey area mitigation

Mahitosh Mehta[1], Rémi Manceau[1], Vladimir Duffal[2] and Benôit de Laage de Meux[2]

[1]University of Pau & Pays Adour, E2S UPPA, CNRS, Inria, CAGIRE project-team, LMAP, Pau, France
[2]EDF R&D, MFEE Dept., 6 quai Watier, 78400 Chatou, France

Submitted to: Physics of Fluids

Abstract

Continuous hybrid RANS/LES approaches suffer from the well-known problem of excessively slow generation of resolved structures in the grey area, i.e., during the transition from the RANS mode to the LES mode. Indeed, when the mesh is refined in the direction of the flow, the model is designed to reduce the modeled energy, but there is no mechanism to transfer the equivalent amount of energy into the resolved motion. Hence, the total turbulent energy and turbulent stresses are underestimated, which strongly affects the prediction of the mean flow. This also constitutes a violation of the conservation of mechanical energy, which can only be corrected by an *active* approach, i.e., an approach that allows the injection of resolved energy. The aim of this work is to develop such an active approach based on the introduction of a fluctuating volume force into the resolved momentum equation, similar to the anisotropic linear forcing (ALF) method proposed previously. The major difference with ALF is that the new method does not require target statistics obtained by a RANS computation, but is based on a simple analysis of the rate of energy transfer related to variations in resolution, enabling the forcing to be extended to continuous hybrid RANS/LES. Application of the new method to the cases of a channel with or without periodic constriction shows a drastic improvement over the case without forcing. Although the method is applied herein to a particular hybrid RANS/LES approach (HTLES, hybrid temporal LES), it can easily be extended to any other approach, as long as a parameter identifies variations in resolution, and thus offers vast application prospects.

Keywords— Turbulence modeling, Hybrid RANS-LES, HTLES, Periodic hill flows, Volume forcing, Grey area mitigation

B.1 Introduction

Computational fluid dynamics (CFD) is a powerful tool for predicting complex turbulent flows. Although Reynolds-Averaged Navier–Stokes (RANS) computations are the industrial standard practice, they often do not provide accurate enough results in separated flow regions and also do not provide time-dependent information.

For instance, it is of great importance to describe the unsteady behavior of large-scale energetic structures of turbulence to predict aerodynamic loads and thermal fatigue in industrial applications. LES (Large-Eddy Simulation) can provide these quantities but at a

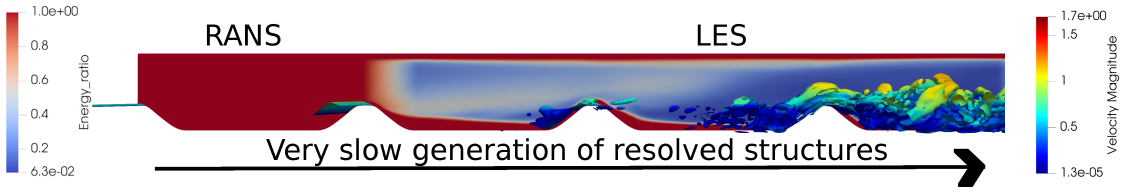

Figure B.1 – Isocontours $Q = 0.2U_b^2/h^2$ colored with the velocity magnitude and, in the background, modeled-to-total turbulent energy ratio r, indicating the regions solved in RANS ($r = 1$) and in LES ($r < 1$). Here the HTLES model of (Duffal et al., 2022) is used.

high computational cost, which motivates the use of hybrid RANS/LES models which offer the best potential to achieve the balance between LES and RANS advantages. Indeed, LES can capture large-scale structures in regions of interest, while RANS models are applied to regions where LES is not needed or too CPU-demanding. Over the last couple of decades many continuous hybrid RANS/LES approaches have been proposed, such as Detached Eddy Simulations (DES) and variants, (Spalart, 1997; Spalart et al., 2006; Shur et al., 2008) Partially Averaged Navier-Stokes (PANS) (Girimaji, 2005), Scale-Adaptive Simulations (SAS) (Menter et al., 2005), Partially Integrated Transport model (PITM) (Chaouat et al., 2005), Continuous Eddy Simulation (CES) (Heinz et al., 2020), to name a few (see, for instance Chaouat (2017a) or Heinz (2020), for recent reviews).

The main purpose of any continuous hybrid RANS/LES method is to reduce the modeled turbulent stresses in the LES region either by modifying the eddy-viscosity formulation, or by manipulating terms in the equations. While transitioning from RANS to LES, we go from fully modeled to partially resolved quantities and by doing so, the reduction in modeled energy should be compensated by the increase in resolved energy. However, the growth of the resolved fluctuations relies entirely on natural instabilities, and is generally not fast enough to compensate for the stress decay imposed in the model, a phenomenon known as Modeled Stress Depletion (Spalart, 2009). This is illustrated by Fig. B.1, which shows Q-isocontours for the periodic hill case, where upon transitioning from RANS to LES, it is seen that it takes a long time to generate the resolved structures. This lack of resolved energy in the transition zone from RANS to LES is also known as the *grey area* problem, and significantly degrades the mean flow predictions. This problem can be alleviated by decreasing to zero the subgrid viscosity in the initial region of a detached shear layer, in order to avoid this viscosity delaying the development of instabilities (Mockett et al., 2018). However, this solution relies essentially on the presence of inflectional velocity profiles and does not inject energy into the resolved motion, such that, as shown below, mechanical energy is still lost.

The problem of the absence of energy transfer between modeled and resolved parts can be clearly illustrated by a thought experiment, the simplified case of a RANS-to-LES transition in grid turbulence, as shown in Fig. B.2: this corresponds to famous grid turbulence experiments, as measured for instance by Comte-Bellot et al. (1966). In such a flow, turbulence is generated by the grid and convected downstream by a uniform flow. Due to the absence of a velocity gradient, there is no turbulence production, and the turbulent energy decreases as a power law of x. If an eddy-viscosity model is used for the subfilter stress, the molecular and turbulent diffusion terms in the resolved momentum equation write

$$\frac{\partial}{\partial x_j}\left[(\nu + \nu_{\text{sfs}})\frac{\partial \widetilde{u}_i}{\partial x_j}\right] \tag{B.1}$$

(the tilde stands for the filtering operator as defined in section B.2). In the RANS region, the resolved velocity is the mean velocity, i.e., the uniform velocity field. Consequently,

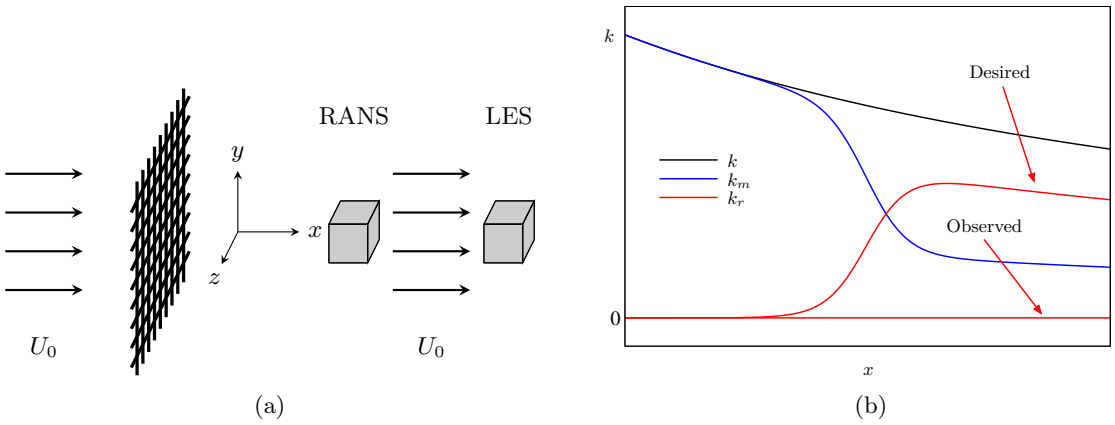

Figure B.2 – Illustration in grid turbulence of the problem of the absence of turbulent energy transfer between the modeled part and the resolved part. (a) Schematic view of a grid turbulence experiment. (b) Schematic evolution of the turbulent energy partition during a RANS-to-LES transition in hybrid RANS/LES.

in the momentum equation, the velocity gradient $\partial\widetilde{u}_i/\partial x_j$, the convection term $\widetilde{u}_j\partial\widetilde{u}_i/\partial x_j$ and the diffusion term (B.1) are zero. Therefore, the resolved momentum equation reduces to

$$\frac{1}{\rho}\frac{\partial\widetilde{p}}{\partial x_i} = 0 \tag{B.2}$$

whose solution is $0 = 0$. When at a given position the mesh is refined to switch to LES mode, the hybrid RANS/LES model strongly decreases the turbulent viscosity. However, since the turbulent viscosity does not appear in Eq. (B.2) as explained above, the RANS solution $0 = 0$ remains a solution of the equation. Resolved structures will appear only slowly, due to the natural instability of the flow. However, as the meshes used are much coarser than those required for DNS, this natural transition can be strongly delayed, or completely suppressed. Fig. B.2 shows the desired result: the modeled energy k_m is strongly reduced due to the refinement, which is compensated by an increase of the resolved energy k_r, so that the total energy $k = k_r + k_m$ remains insensitive to the refinement. We will in practice obtain $k_r \simeq 0$ and the energy k will decrease drastically, following k_m.

Two fundamental conclusions can be drawn from this thought experiment:

i) It is obvious that no modification of the model for the unresolved part can correct this problem, since the model is not involved in Eq. (B.2).

ii) There is actually here a fundamental problem of violation of the conservation of mechanical energy.

It will be seen below that the decrease of the modeled energy corresponds to a modification of the partition modeled/resolved energy, which generates terms in the momentum equation that are not taken into account. This loss of turbulent energy, and thus the decrease of the total turbulent stresses which drive the mean momentum, affects the mean velocity profiles in turbulent shear flows. Since the missing terms are actually forces, the goal of this paper is develop a volume forcing method to inject energy into the resolved motion.

It is legitimate to wonder whether it is necessary to correct this problem in all cases. Indeed, many applications of continuous hybrid RANS/LES models are available in the literature that do not introduce this type of forcing: if fluctuations appear naturally at the transition from RANS to LES, which is often the case in the presence of a detached shear layer, the solution is acceptable, and it is possible to promote the appearance of resolved structures, for example by radically decreasing the subgrid viscosity in this zone (Mockett

et al., 2018). However, it is important to note that in this case there is still a violation of the conservation of mechanical energy: there is no mechanism that transfers modeled energy to resolved energy. The growth of the resolved fluctuating energy is therefore necessarily obtained by taking from the mean flow this missing part of the mechanical energy, which consequently alters the mean flow. It is therefore preferable, in all cases, to correct this mechanical energy conservation issue.

To address this issue, a few methods have been developed that introduce, in one way or another, resolved fluctuations. A comparative study of several methods was performed by Keating et al. (2006). Synthetic turbulence methods are generally based on Fourier reconstruction techniques, where spatial and temporal correlations can be introduced (Shur et al., 2014; Janin et al., 2021). Other approaches introduce virtual vortices of simple shape, either by directly superimposing them to the velocity field or by introducing a restoring force in the momentum equation (Jarrin et al., 2006; Haering et al., 2022). Spille-Kohoff et al. (2001) proposed an approach based on a volume forcing of the wall-normal velocity in order to control the shear stress in a set of planes close to the LES inlet. Laraufie et al. (2011) modified this approach by controlling the diagonal Reynolds stress in the wall-normal direction rather than the shear stress. A common feature of all these approaches is that the interface between the RANS and LES zones must be geometrically simple (typically a plane normal to a shear layer) and the flow direction well identified. Indeed, when synthetic vortices are generated, a great deal of information is required to adapt their size, impose a possible periodicity in the transverse direction, and advect the vortices. Typically, the size and energy of the vortices must be obtained from existing information, such as upstream statistics from the RANS region or distance to the wall. Approaches based on volume forcing are also linked to a particular component of the Reynolds stress tensor and therefore to the relative orientations of the flow and the wall. For future application in complex industrial geometries, and for possible adaptation of the RANS and LES zones during the course of the computation, it is highly desirable to have a more flexible approach, requiring only quantities at the point under consideration and no limitation as to the orientation or geometry of the interface.One such approach is the ALF method (anisotropic linear forcing), which is a generalization of the above-mentioned volume forcing approaches, based on the imposition of a complete target Reynolds-stress tensor in a volume at the beginning of the LES region (De Laage de Meux et al., 2015; Kempf et al., 2022). This approach yields an appreciable reduction of the adaptation distance downstream of the inlet. However, it is still restricted to zonal RANS/LES approaches, and also requires target statistics.

In the present paper, a volume forcing method is proposed for continuous hybrid RANS-LES approaches. This method is a modification of the ALF to avoid the need for target statistics provided by a RANS calculation, which is at the origin of the restriction of the ALF to zonal hybrid RANS/LES with an overlap between the RANS and LES domains. Its essence is to evaluate the energy transfer between the modeled part of the turbulent spectrum and the resolved part, in order to inject the necessary energy into the resolved motion via a volume force. It is first evaluated in comparison with the ALF in the case of a series of hills with idealized inlet conditions (i.e., given by a preliminary periodic computation), for which the ALF has already been successfully tested (Duffal, 2020). Then it is further extended to a more realistic case consisting in a succession of inter-hill regions treated in RANS and LES, in order to investigate the influence of the new methodology and analyse the generation of the turbulent fluctuations. Finally, it is also validated for the case of a simple plane channel flow, which does not present a shear layer instability and thus is a more challenging case for the new method.

In the following section, the continuous hybrid RANS/LES method used herein (HTLES,

Hybrid Temporal LES) is briefly introduced and the results obtained in the periodic hill case are compared with the reference LES. These results in the periodic configuration will be used in the remainder of the article as reference results for the simulations in spatially developing cases. Section B.3 presents the theoretical arguments and analytical developments leading to the proposal of the new volume forcing method. Section B.4.1 is then devoted to the validation of this new approach in a case in LES mode with stationary inlet conditions, enabling comparison with the ALF method, and section B.4.2 to the case of a transition from RANS to LES followed by a transition from LES to RANS, which prefigures the use of this new active approach in practical applications. Section B.4.3 is dedicated to the extension of the validation to a plane channel flow and the investigation of the influence of the length of the RANS-to-LES transition region.

B.2 Hybrid RANS/LES framework

The active approach developed in this paper can potentially be applied to any hybrid RANS/LES method, as long as one can identify a parameter that drives the transition from RANS to LES, be it simply the mesh size or any other parameter that can be calculated during the computation. Here, the method used is the Hybrid Temporal LES (HTLES) (Manceau, 2016; Duffal et al., 2022; Hyde-Linaker et al., 2022; Mays et al., 2023), which is briefly presented below.

In filtered approaches, any flow variable f can be decomposed into two parts: a filtered part, $\widetilde{f}$, and a sub-filtered part, f'',

$$f = \widetilde{f} + f'' \ , \tag{B.3}$$

using a general spatio-temporal filtering operator denoted as $\widetilde{.}$,

$$\widetilde{f}(\mathbf{x},t) = \int_{\mathscr{D}} \int_{-\infty}^{t} \mathscr{G}(\mathbf{x},\mathbf{x}',t,t') f(\mathbf{x}',t') \mathrm{d}\mathbf{x}' \mathrm{d}t' \tag{B.4}$$

where $\mathscr{D}$ is the domain and $\mathscr{G}$ the filter kernel. This definition encompasses standard LES based on spatial filtering, and temporal LES on which the HTLES approach is built, hence the name Hybrid *Temporal* LES (Manceau, 2016) . Whatever the type of filter, the equation of the filtered momentum is :

$$\frac{\partial \widetilde{u}_i}{\partial t} + \widetilde{u}_j \frac{\partial \widetilde{u}_i}{\partial x_j} = -\frac{1}{\rho}\frac{\partial \widetilde{p}}{\partial x_i} + \nu \frac{\partial^2 \widetilde{u}_i}{\partial x_j \partial x_j} - \frac{\partial \tau_{ij_{\mathrm{sfs}}}}{\partial x_j} \tag{B.5}$$

where the subfilter scale (sfs) tensor is defined as the generalized second-order moment $\tau_{ij_{\mathrm{sfs}}} = \widetilde{u_i u_j} - \widetilde{u}_i \widetilde{u}_j$ (Germano, 1992). This equation is of the same form as the one obtained by using the Reynolds decomposition based on the statistical average $\overline{.}$, so that the cornerstone of all continuous hybrid RANS/LES methods is to use a model making it possible to transition the closure for this stress tensor from a RANS model to a LES model in some regions of the flow. It can be shown that this is equivalent to making the characteristic size of a spatial filter (resp. a temporal filter) in homogeneous turbulence (resp. statistically stationary turbulence) tend to infinity in Eq. (B.4) (Fadai-Ghotbi et al., 2010).

B.2.1 Hybrid model

In HTLES (Duffal et al., 2022), the underlying RANS model is sensitized to the filter width via the time scale $T_m(r)$, dependent on the resolution parameter r, which is the

modeled-to-total energy ratio

$$r = \frac{k_m}{k} \ , \tag{B.6}$$

where $k = k_m + k_r$ is the total turbulent energy, decomposed into a modeled part $k_m = \overline{k_{\text{sfs}}} = \overline{\tau_{ii_{\text{sfs}}}}/2$ and a resolved part $k_r = (\overline{\widetilde{u}_i \widetilde{u}_i} - \overline{\widetilde{u}_i}\ \overline{\widetilde{u}_i})/2$, were the overbar denotes statistical averaging, approximated by an exponentially-weighted average (Pruett et al., 2003) performed during the computation. Here, following Duffal et al. (2022) this approach is applied to the underlying k-ω SST RANS model, leading to the definition of a resolution-dependent turbulent time-scale

$$T_m(r) = \frac{r}{\psi\left(r\right)} \frac{k_m + c_r k_r}{C_\mu k_m \omega_m^*}, \tag{B.7}$$

where the hybridization function writes

$$\psi\left(r\right) = \frac{\beta_\omega}{C_\mu \gamma_\omega + r\left(\beta_\omega - C_\mu \gamma_\omega\right)} \tag{B.8}$$

and the subfilter-scale eddy-viscosity

$$\nu_{\text{sfs}} = \frac{a_1 k_{\text{sfs}}}{\max\left[a_1 \psi\left(r\right) \omega_{\text{sfs}}^*, F_2 \widetilde{S}\right]}. \tag{B.9}$$

The transport equations of the k-ω SST model then become

$$\begin{aligned}
\frac{\mathrm{d}k_{\text{sfs}}}{\mathrm{d}t} &= P_k + \frac{\partial}{\partial x_j}\left[\left(\nu + \frac{\nu_{\text{sfs}}}{\sigma_k}\right)\frac{\partial k_{\text{sfs}}}{\partial x_j}\right] - \frac{k_{\text{sfs}}}{T_m(r)}, \\
\frac{\mathrm{d}\omega_{\text{sfs}}^*}{\mathrm{d}t} &= \gamma_\omega \frac{1}{\psi\left(r\right)} \widetilde{S}^2 + \frac{\partial}{\partial x_j}\left[\left(\nu + \frac{\nu_{\text{sfs}}}{\sigma_\omega}\right)\frac{\partial \omega_{\text{sfs}}^*}{\partial x_j}\right] - \beta_\omega {\omega_{\text{sfs}}^*}^2 \\
&\quad + (1 - F_1) 2 \frac{1}{\sigma_{\omega 2}} \frac{1}{\psi\left(r\right) \omega_{\text{sfs}}^*} \frac{\partial \omega_{\text{sfs}}^*}{\partial x_j} \frac{\partial k_{\text{sfs}}}{\partial x_j},
\end{aligned} \tag{B.10}$$

where γ_ω, β_ω, a_1, a_2, σ_k, σ_ω, F_1 and F_2 are the usual coefficients and functions of the RANS model (Menter, 1994). The variable ω_{sfs}^*, solution of the second equation, is marked by a superscript star to emphasize that it is not the specific dissipation rate except at the RANS limit: in general, the specific dissipation rate is $\psi\left(r\right)\omega_{\text{sfs}}^*$, which appears in Eq. (B.9). When $r = 1$ (RANS mode), the equations of the RANS model are recovered. Note that the coefficient c_r in Eq. (B.7) is necessary to reach this limit properly (called the *internal consistency constraint*): if resolved structures penetrate from the LES region to the RANS region, their energy is not counted in order to avoid modifying the RANS model, since c_r is defined as

$$\begin{cases} c_r = 0 \text{ if } r = 1, \\ c_r = f_s \text{ if } r < 1, \end{cases} \tag{B.11}$$

where f_s is the shielding function defined below. When $r < 1$ (LES mode), T_m is reduced, which leads to an increase of the dissipation k_{sfs}/T_m in the k_{sfs} equation, which in turn decreases k_{sfs} and thus the turbulent viscosity ν_{sfs}, a mechanism similar to that operating in two-equation DES.

HTLES being based on temporal filtering, assuming an equilibrium Eulerian spectrum, the energy ratio r can be related to the highest frequency resolvable by the numerical scheme

$$\omega_c = \min\left(\frac{\pi}{\tau}, \frac{U_s \pi}{\Delta}\right) \tag{B.12}$$

through the relation

$$r_K = \frac{1}{\beta_0}\left(\frac{U_s}{\sqrt{k}}\right)^{2/3}\left(\omega_c \frac{k}{\varepsilon}\right)^{-2/3}, \tag{B.13}$$

where the index K indicates that this evaluation is based on the Kolmogorov assumptions (Manceau, 2016). In these relations, τ is the time step, Δ the grid step (estimated herein by the cubic root of the cell volume), $\beta_0 = 0.48$ and $U_s = U + \sqrt{2k/3}$ is the sweeping velocity (Tennekes, 1975). Note that if the time step τ is smaller than Δ/U_s (or the sweeping CFL number $\tau U_s/\Delta$ is less than unity) everywhere in the domain, which will be the case in practice in the present paper, the cut-off frequency ω_c is related to the grid step Δ and Eq. (B.13) reduces to the standard relations used, for instance, in PITM (Chaouat et al., 2005),

$$k_m = \int_{\kappa_c}^{\infty} E(\kappa)\, d\kappa = \frac{\Delta^{2/3}\varepsilon^{2/3}}{\beta_0 \pi^{2/3}}, \tag{B.14}$$

$$r_K = \frac{1}{\beta_0}\left(\frac{\pi}{\Delta}\frac{k^{3/2}}{\varepsilon}\right)^{-2/3}. \tag{B.15}$$

Following Duffal et al. (2022) a shielding function f_s is introduced in the model as

$$r = (1 - f_s) + f_s \min(1, r_K) \tag{B.16}$$

$$f_s = 1 - \tanh\left[\max\left(\xi_K^{p_1}, \xi_D^{p_2}\right)\right] \tag{B.17}$$

This function serves two objectives. The first is to avoid grid-induced separation when the mesh is ambiguous near the wall, by forcing the RANS mode independently of the mesh up to a certain distance from the wall, based on the dimensionless parameter

$$\xi_K = C_1 \frac{\left(\nu^3/\varepsilon\right)^{1/4}}{d_w}. \tag{B.18}$$

With the values used herein, $C_1 = 45$ and $p_1 = 8$, this parameter activates the shielding up to $y^+ \simeq 100$, as shown by Duffal et al. (2022). The second objective is to mitigate the log-layer mismatch (Nikitin et al., 2000), by accounting for the fact that near-wall cells are generally too elongated for LES in the near-wall region and postponing accordingly the RANS-to-LES transition based on the parameter

$$\xi_D = C_2 \frac{\Delta_{\max}}{d_w}, \tag{B.19}$$

with $C_2 = 1.2$ and $p_2 = 6$. $\Delta_{\max}$ is the longest edge of the local cell. For details about HTLES, its derivation and calibration, the reader is referred to Duffal et al. (2022).

B.2.2 Comparison with highly-resolved LES

In section B.4, the active hybrid RANS/LES approach will be tested in cases of the spatially developing flows. As illustrated in Fig. B.1, the main issue here is to ensure a fast transition from a RANS behavior to a developed LES behavior (with RANS regions along the walls). In the present section, we will therefore show a short validation of the fully developed behavior of the HTLES model described above, by performing periodic simulations that are compared with the reference refined LES (Breuer et al., 2009). A more detailed validation is available in Duffal et al. (2022). Once validated, this periodic HTLES solution will in turn serve as a reference for the simulations in spatial development presented in the following sections.

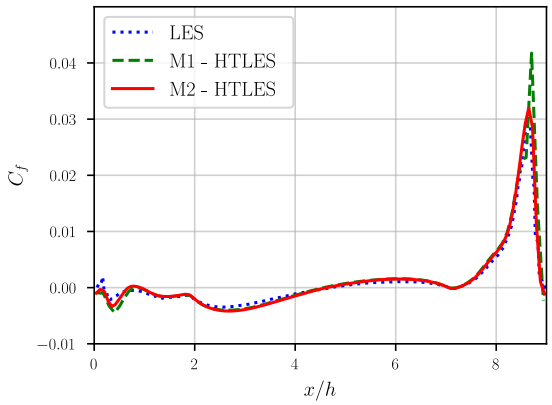

Figure B.3 – Comparison of HTLES and LES for the periodic hill. Skin friction along the lower wall.

For hybrid RANS/LES approaches, a periodic arrangement of 2D hills in a plane channel constitutes a standard benchmark case. Because low-frequency phenomena govern the characteristics of the mean flow, including moving separation and reattachment points, and large-scale structures generated by the detached shear layer have a strong influence on the recirculation region, reproducing the flow statistics is a real challenge for RANS models and hybrid RANS/LES generally bring a significant improvement.

The flow is characterized by the bulk Reynolds number, $Re_b = U_b h/\nu = 10595$, where U_b is the bulk velocity and h is the height of the hill. The computational domain is $L_x \times L_y \times L_z = 9h \times 3.035h \times 4.5h$, and periodicity is applied in the spanwise and streamwise directions. Using a source term in the streamwise momentum equation, a constant mass flow is imposed. The periodic hill flow is studied using a coarse mesh M1 ($N_x \times N_y \times N_z = 80 \times 80 \times 40$) and a fine mesh M2 ($N_x \times N_y \times N_z = 120 \times 120 \times 60$) containing more than three times more cells, which both satisfy $\Delta y^+ \simeq 1$ at the wall. As a reference, the highly resolved LES produced by Breuer et al. (2009) with 13.1 million cells is considered. Computations are performed using code_saturne (Archambeau et al., 2004), the open-source general purpose CFD software developed by EDF, based on a co-located finite-volume approach that accepts meshes with any type of cells and any type of grid structure. The velocity-pressure system is solved using a SIMPLEC algorithm. A hybrid second-order upwind (SOLU)/centered difference (CDS) scheme is utilized, similar to the one proposed by Travin et al. (2002), using c_r from Eq. (B.11) as a blending coefficient (Duffal et al., 2022).

The distribution of skin friction on the lower wall highlights the behavior of HTLES and LES. In Fig. B.3, it is seen that HTLES reproduces results similar to the reference data, using both grids, although M1 appears slightly too coarse at the top of the hill. Focusing on profiles extracted at different streamwise locations ($x/h = 0$, 2, 4, 6 and 8) for the mean velocity and total turbulent energy (resolved + modeled), the reference data are well reproduced for both grids as shown in Fig. B.4, although the turbulent energy is overestimated. The discrepancies between the two grids are minor considering the large difference in the grid resolution.

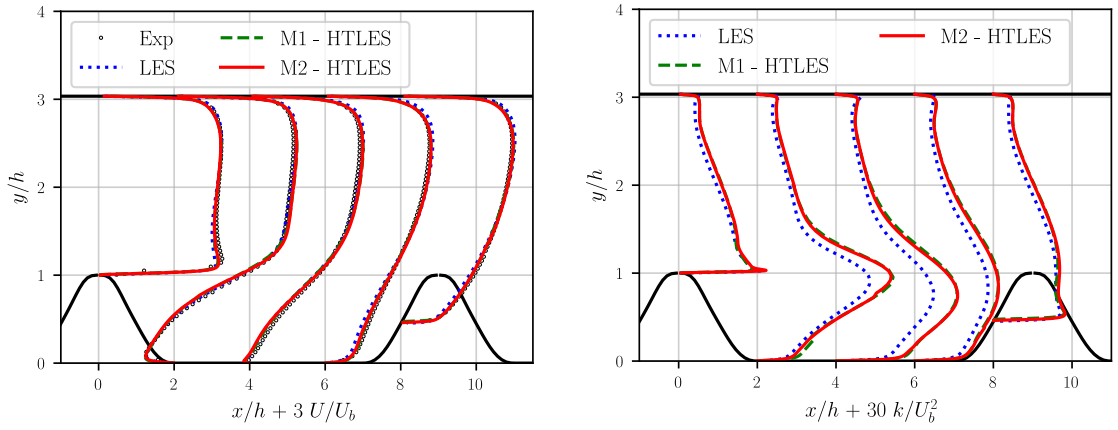

(a) (b)

Figure B.4 – Comparison of HTLES and LES for the periodic hill. (a) Streamwise velocity profiles and (b) total turbulent kinetic energy profiles.

B.3 Active hybrid RANS/LES approach

As mentioned in the introduction, the objective of this paper is to improve the transition between an upstream RANS zone and a downstream LES zone, i.e., to mitigate the grey area problem. Firstly, Fig. B.1 illustrates the baseline situation: we perform a channel simulation with periodic constriction, this time not in a periodic domain, but in a spatially developing domain, with inlet and outlet boundaries. The computational domain contains n inter-hill subdomains bounded by $n+1$ hills (the entrance and exit of the domain being located at the tops of the hills, the first and the last hills are in fact half-hills). There will be $n = 3$ subdomains in section B.4.1 and $n = 5$ subdomains in section B.4.2. Note that the term subdomain is used here for convenience to describe a region between two successive hills, but there is only one computational domain. In order to decouple the numerical issue from the modeling issue and also to avoid problems of connections between areas refined differently by unstructured or non-conforming meshes, all the simulations will be performed with the meshes used in section B.2.2, duplicated in each subdomain. The transition between upstream RANS mode and downstream LES mode will be imposed by prescribing a spatial evolution of the resolution parameter r in the model. On the other hand, in the LES area, r will still be given by Eq. (B.16). As illustrated by Fig. B.1, the resolved content in the LES region takes a long time to develop. In order to remedy this issue, we will now consider a new method to inject fluctuating energy in the resolved motion.

B.3.1 Theoretical framework

Although the active approach developed herein is applicable to any continuous hybrid RANS/LES model, it is convenient to illustrate its rationale from a filtering formalism. Indeed, the effect of a change of resolution on the energy partition between the resolved motion and the modeled motion is illustrated in Fig. B.5, here for a refinement, but the opposite is true for a coarsening. When going from a coarse mesh to a fine mesh, the cutoff wavenumber of the filter (or frequency for a temporal filter) is modified. As shown in Fig. B.5a, when the mesh is refined, the resolved energy increases and the modeled energy decreases. Consequently, the energy that appears shaded in Fig. B.5a corresponds to an energy transfer from the modeled part to the resolved part. It is this energy transfer

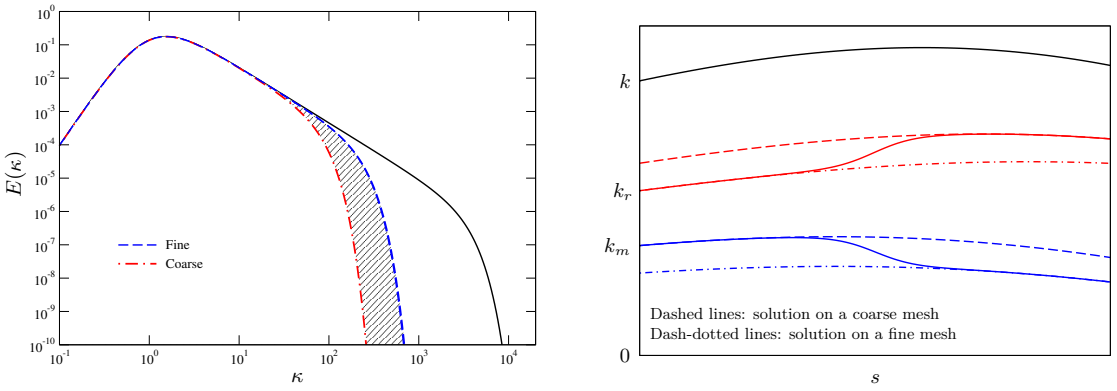

(a) (b)

Figure B.5 – Illustration of the transfer of energy from the modeled to the resolved part in hybrid RANS/LES due to a change in resolution. (a) In spectral space. (b) In physical space, with an arbitrary spatial evolution of k (s is the curvilinear coordinate along the streamline).

that we will try to represent in the *active* model. The interpretation in physical space is illustrated by Fig. B.5b, in which the typical evolution of the turbulent energy along a streamline is plotted. The solution on a coarse mesh, shown in dashed lines, exhibits some partitioning of the total turbulent energy between the modeled k_m and resolved k_r parts. On a finer mesh, the solution, represented in dash-dotted lines, exhibits a different energy partition, with more resolved energy and less modeled energy. In theory, however, this different distribution should not affect the total turbulent energy. If a fluid particle passes along a streamline through a zone of gradual mesh refinement, then the resolved and modeled energies should follow the evolution plotted in solid lines, and the total turbulent energy should remain constant.

This observation is related to the issue, shown by several authors (Ghosal et al., 1995; Germano, 2004; Fadai-Ghotbi et al., 2010; Wallin et al., 2011; Chaouat et al., 2013; Davidson, 2016), that when the equations for the filtered quantities are derived, terms arise due to the variation of the filter size in the equation due to the fact that the filter does not commute with the derivatives. These terms, also called commutation error, correspond to the transfer of energy which is missing in the model. For instance, following Chaouat et al. (2013) one can note that if the filter width of the kernel $\mathscr{G}$ defined by Eq. (B.4) is variable in space, the spatial derivative of a filtered quantity $\widetilde{f}$ generates the commutation error

$$\frac{\partial \widetilde{f}}{\partial x_i} - \widetilde{\frac{\partial f}{\partial x_i}} = \iiint_{\mathscr{D}} \int_{-\infty}^{t} \frac{\partial \mathscr{G}}{\partial x_i} f \, \mathrm{d}x' \mathrm{d}y' \mathrm{d}z' \mathrm{d}t'. \tag{B.20}$$

Here, a different and simpler way of viewing this problem is used, which has the additional advantage of not referring to a particular formalism and thus emphasizes the generality of the approach. It simply consists in considering, as illustrated by Fig. B.5b, that when the mesh is refined, the variables change (typically, the modeled turbulent energy is reduced): it is not a question here of a dependence on the numerical scheme, but of a dependence of the model on the grid step. Thus, it is proposed to express any filtered field ϕ as depending not only on the coordinates t and x_i, but also on the grid step Δ,

$$\phi\left(t, x_i, \Delta\right). \tag{B.21}$$

Thus, the variable is no longer a function of four parameters, three of space and one of time, but also of a fifth parameter representing the dependence of the variable on the grid step, illustrated in Fig. B.5b. In other terms, the variable is now part of a hyperspace of

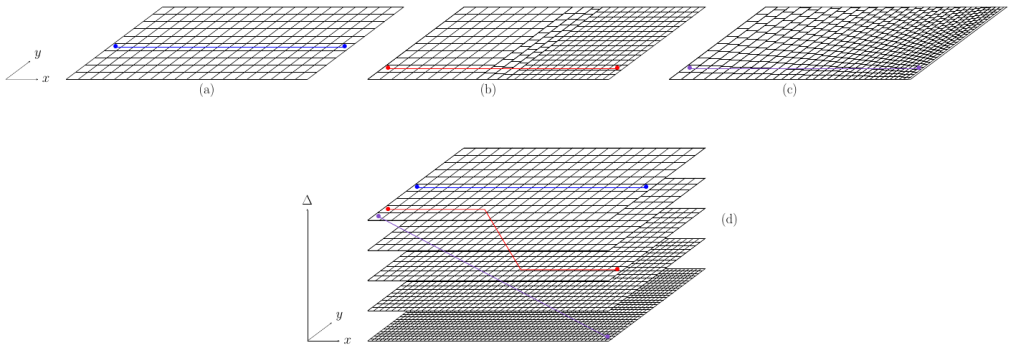

Figure B.6 – Fluid particle trajectories in: (a,b,c) physical space; (d) the hyperspace x_i-Δ (the z-direction is omitted). (a) Uniform mesh; (b) Mesh with a sudden refinement; (c) Mesh with a gradual refinement; (d) View in the (x-y-Δ) space of the three trajectories shown in figures (a), (b) and (c).

dimension five. Note that one could, in a completely equivalent way, express ϕ not as a function of Δ but as a function of the cut-off wavenumber κ_c or frequency ω_c, or of the energy ratio r as will be shown later on in the paper, but it is easier to visually represent a dependence on the grid step.

Fig. B.6d provides a representation of this hyperspace, in which here, for obvious reasons, the two dimensions z and t are not represented. If we follow a fluid particle (blue trajectory) crossing a domain meshed with a constant grid step Δ, Fig. B.6a, the fluid particle evolves at a constant Δ, i.e., remains in an horizontal plane in Fig. B.6d. On the other hand, if we follow the fluid particle (red trajectory) in Fig. B.6b, where the mesh is suddenly refined, the variables that are dependent on Δ are now modified by this refinement. Instead of remaining in the horizontal plane of constant Δ in Fig. B.6d, the solution goes from a coarse-mesh solution (horizontal plane at large Δ) to a fine-mesh solution (horizontal plane at a smaller Δ). In the region where the mesh is refined, the solution thus rapidly moves downward in the direction of small Δ's in the hyperspace. This is just a different way of representing the change in solution linked to a mesh refinement shown in Fig. B.5b. The purple trajectory of Figs. B.6c and d corresponds to the solution obtained on a gradually refined mesh.

This description in a five-dimensional hyperspace allows us to distinguish, in the evolution of the different physical quantities, what is due to the dynamics of the flow from what is due to the changes in grid step. Indeed, the total variation $\mathrm{d}\phi$ of the variable ϕ is expressed as

$$\mathrm{d}\phi = \frac{\partial \phi}{\partial t}\mathrm{d}t + \frac{\partial \phi}{\partial x_i}\mathrm{d}x_i + \frac{\partial \phi}{\partial \Delta}\mathrm{d}\Delta, \tag{B.22}$$

such that

$$\begin{aligned}\frac{\mathrm{d}\phi}{\mathrm{d}t} &= \frac{\partial \phi}{\partial t} + \frac{\partial \phi}{\partial x_i}\frac{\mathrm{d}x_i}{\mathrm{d}t} + \frac{\partial \phi}{\partial \Delta}\frac{\mathrm{d}\Delta}{\mathrm{d}t} \\ &= \underbrace{\frac{\partial \phi}{\partial t} + \nabla\phi \cdot U}_{\text{Material derivative}} + \underbrace{\frac{\partial \phi}{\partial \Delta}\frac{\mathrm{d}\Delta}{\mathrm{d}t}}_{\text{Extra term}}\end{aligned} \tag{B.23}$$

which is nothing but the summation of the classical material derivative and the extra term due to mesh variations. For the particular case of a constant grid step, this extra term disappears. Hence the material derivative of the filtered quantity can be decomposed in

two parts:

$$\frac{\mathrm{d}\phi}{\mathrm{d}t} = \left.\frac{\mathrm{d}\phi}{\mathrm{d}t}\right|_{\Delta} + \left.\frac{\mathrm{d}\phi}{\mathrm{d}t}\right|_{t,x_i} . \tag{B.24}$$

Following the standard notation used in thermodynamics,

$$\left.\frac{\mathrm{d}\phi}{\mathrm{d}t}\right|_{\Delta} = \frac{\partial\phi}{\partial t} + \nabla\phi \cdot U \tag{B.25}$$

denotes the derivative of the variable ϕ at constant Δ, i.e., the classical material derivative. It is the derivative taken in an horizontal plane in Fig. B.6d. Now,

$$\left.\frac{\mathrm{d}\phi}{\mathrm{d}t}\right|_{t,x_i} = \frac{\partial\phi}{\partial\Delta}\frac{\mathrm{d}\Delta}{\mathrm{d}t} \tag{B.26}$$

is the derivative at constant t and x_i, i.e., the part due only to variations of Δ, in others words, the derivative taken in the vertical direction in Fig. B.6d.

It is easy to interpret this term by looking at the quantities k, k_r and k_m. Indeed, as illustrated by Fig. B.5b, the total turbulent energy is independent of the grid step, and thus

$$\frac{\partial k}{\partial\Delta} = 0\,. \tag{B.27}$$

Since, $k = k_r + k_m$,

$$\frac{\partial k_r}{\partial\Delta} = -\frac{\partial k_m}{\partial\Delta}\,, \tag{B.28}$$

which reflects the fact that a variation of the grid step leaves the total energy unchanged but changes the energy partition.For example, if we follow a fluid particle as it passes through a mesh refinement zone, the case illustrated by Fig. B.5 and Fig. B.6b, applying Eq. (B.23) to k_m and k_r shows that their evolution along the streamline can be separated into two contributions: their mesh-independent dynamics

$$\left.\frac{\mathrm{d}k_m}{\mathrm{d}t}\right|_{\Delta} = \frac{\partial k_m}{\partial t} + U_k\frac{\partial k_m}{\partial x_k} \quad ; \quad \left.\frac{\mathrm{d}k_r}{\mathrm{d}t}\right|_{\Delta} = \frac{\partial k_r}{\partial t} + U_k\frac{\partial k_r}{\partial x_k} \tag{B.29}$$

and their variation due to the grid step refinement

$$\left.\frac{\mathrm{d}k_m}{\mathrm{d}t}\right|_{t,x_i} = \frac{\partial k_m}{\partial\Delta}\frac{\mathrm{d}\Delta}{\mathrm{d}t} \quad ; \quad \left.\frac{\mathrm{d}k_r}{\mathrm{d}t}\right|_{t,x_i} = \frac{\partial k_r}{\partial\Delta}\frac{\mathrm{d}\Delta}{\mathrm{d}t}. \tag{B.30}$$

As for the total turbulent energy k, it is independent of the grid step, so that

$$\left.\frac{\mathrm{d}k}{\mathrm{d}t}\right|_{t,x_i} = 0. \tag{B.31}$$

Since $k = k_r + k_m$, from Eqs. (B.30) and (B.31), we can conclude that the term

$$\frac{\partial k_r}{\partial\Delta}\frac{\mathrm{d}\Delta}{\mathrm{d}t} = -\frac{\partial k_m}{\partial\Delta}\frac{\mathrm{d}\Delta}{\mathrm{d}t} \tag{B.32}$$

represents the rate of energy transfer from the modeled part to the resolved part due the refinement of the grid, i.e., the shaded area in Fig. B.5a. It is therefore clear that this term must be accounted for in the evolution equations of these quantities. If numerous models take into account the variations of k_m, in order to reduce ν_t, there is no mechanism to add energy in the resolved part. Interestingly, by deriving the subfilter energy equations in the case of a variable filter, Chaouat (2017b) showed that different terms appear related to the

non-commutativity of the filter with the differential operators, and that the term (B.32), originating from the material derivative, is the dominant term. Our analysis shows that this additional term arises from the variations of the grid step, independent of any underlying formalism and is therefore valid for any scale-resolving approach in which the partition of energy is related to the grid step (or any other resolution parameter), such as the widely spread DDES or PANS approaches, and even pure LES.

In the framework of the HTLES model, the size of the filter can, possibly, be related to the time step τ, according to Eq. (B.12). Thus, there is also a sensitivity of the solution to the time step, and the extra term must be replaced by

$$\left.\frac{\mathrm{d}\phi}{\mathrm{d}t}\right|_{t,x_i} = \frac{\partial\phi}{\partial\Delta}\frac{\mathrm{d}\Delta}{\mathrm{d}t} + \frac{\partial\phi}{\partial\tau}\frac{\mathrm{d}\tau}{\mathrm{d}t} \tag{B.33}$$

Note that, in most of the usual simulations, the time step is constant and thus $\mathrm{d}\tau/\mathrm{d}t = 0$. However, since the material derivative inherently involves the time derivative, Eq. (B.33) encompasses cases where the time step or the grid step vary in time, such as with automatic mesh refinement methods.

The example of grid turbulence illustrated in Fig. B.2 shows that the hybrid model takes indeed into account the variations of the modeled energy as a function of the grid step. In other words, the transport equation of the modeled energy contains, as for all Δ dependent variables, the two contributions of Eq. (B.24), and the model is build in order to represent these two terms, i.e., both the natural evolution and the grid sensitivity of the modeled energy. For instance, in two-equation DES approaches, the variation of the modeled energy with the grid step is taken into account by replacing the turbulent length scale ℓ by $\min(\ell, C_{\mathrm{DES}}\Delta)$ in the dissipation rate. On the other hand, the momentum equation, and consequently the resolved turbulent energy, remains insensitive to variations of Δ: this is what we will try to model in the next section.

B.3.2 Modeling of the energy transfer due to variations of the resolution

In the situation described in Fig. B.5, where the mesh is refined, the HTLES turbulence model is sensitized to the variation of Δ because the transport equation of the subfilter energy

$$\frac{\mathrm{d}k_{\mathrm{sfs}}}{\mathrm{d}t} = P_{\mathrm{sfs}} + D_{\mathrm{sfs}} - \frac{k_{\mathrm{sfs}}}{T_m} \tag{B.34}$$

involves T_m which depends on the energy ratio r, which is linked to Δ by Eqs. (B.12) and (B.13). In other words, the model is intended to represent the total variation of k_{sfs}, i.e., both terms of Eq. (B.24),

$$\frac{\mathrm{d}k_{\mathrm{sfs}}}{\mathrm{d}t} = \left.\frac{\mathrm{d}k_{\mathrm{sfs}}}{\mathrm{d}t}\right|_{\Delta} + \left.\frac{\mathrm{d}k_{\mathrm{sfs}}}{\mathrm{d}t}\right|_{t,x_i}. \tag{B.35}$$

As mentioned in section B.3.1, the second term of Eq. (B.35) corresponds to the transfer of energy between the modeled part and the resolved part.

However, the resolved momentum equation does not contain a corresponding term. The only way to introduce a source of resolved energy is to add a force to the resolved momentum equation. Following De Laage de Meux et al. (2015), it is proposed to introduce a fluctuating force of the form

$$f_i = A_{ij}\widetilde{u}_i + B_i, \tag{B.36}$$

which linearly depends on the resolved velocity $\widetilde{u}_i$. Upon constructing the transport equation for the resolved stress $\overline{u_i'u_j'}$, where $u_i' = \widetilde{u}_i - \overline{\widetilde{u}_i}$ is the resolved fluctuating velocity, it

can be easily shown that the introduction of this force introduces the production term

$$T_{ij}^f = \overline{f_i' u_j'} + \overline{f_j' u_i'} = A_{ik}\overline{u_j' u_k'} + A_{jk}\overline{u_i' u_k'}, \tag{B.37}$$

where f_i' is the fluctuating part of the force. A mean force $\overline{f_i}$ also appears in the mean momentum equation, which must be equal to zero, because one does not want to influence the mean velocity. Hence,

$$\overline{f_i} = A_{ij}\overline{\widetilde{u}_j} + B_i = 0 \tag{B.38}$$

The production term of the resolved turbulent kinetic energy k_r being half the trace of that of the resolved stresses, it can be written as

$$T^f = A_{ik}\overline{u_i' u_k'}, \tag{B.39}$$

which is nothing else than the average work done by the force per unit time. If we want this power to be equal to the energy decrease in the modeled part due to the variations of Δ, the relation to satisfy is

$$A_{ik}\overline{u_i' u_k'} = -\frac{\partial k_m}{\partial \Delta}\frac{d\Delta}{dt}. \tag{B.40}$$

Individually, each component must satisfy

$$T_{ij}^f = A_{ik}\overline{u_j' u_k'} + A_{jk}\overline{u_i' u_k'} = -\frac{\partial \tau_{ij}^m}{\partial \Delta}\frac{d\Delta}{dt}\,, \tag{B.41}$$

where τ_{ij}^m is the modeled part of the Reynolds stress, i.e., the Reynolds average of the subfilter-stress tensor, $\tau_{ij}^m = \overline{\tau_{ij\mathrm{sfs}}}$. Anisotropy is simply accounted for by assuming

$$\frac{\partial \tau_{ij}^m}{\partial \Delta} \simeq \frac{\tau_{ij}^m}{k_m}\frac{\partial k_m}{\partial \Delta}. \tag{B.42}$$

Now, the modeled turbulent kinetic energy k_m is given by Eq. (B.14), such that

$$\frac{1}{k_m}\frac{\partial k_m}{\partial \Delta} = \frac{2}{3\Delta}. \tag{B.43}$$

The conclusion of this analysis is that, at each point of the domain, the following system of equations must be resolved to determine the values of A_{ij} and B_i, which define the fluctuating force f_i,

$$A_{ik}\overline{u_j' u_k'} + A_{jk}\overline{u_i' u_k'} = -\frac{2}{3}\mathcal{C}\,\tau_{ij}^m\frac{1}{\Delta}\frac{d\Delta}{dt}\,, \tag{B.44a}$$

$$B_i = -A_{ij}\overline{\widetilde{u}_j}\,. \tag{B.44b}$$

The statistical operator $\overline{\cdot}$ is approximated by exponentially-weighted averaging (Pruett et al., 2003) to evaluate the necessary quantities during the computation. Note that a coefficient $\mathcal{C}$ has been introduced in the right hand side of Eq. (B.44a). The analytical derivation above shows that $\mathcal{C} = 1$, but in practice, this coefficient introduces a degree of freedom to adjust the intensity of the forcing, as will be discussed later.

Finally, it should be pointed out that the implementation of the method is relatively straightforward. No additional transport equation compared to the standard HTLES method need to be considered. The resolved energy equation has only been introduced into the theoretical derivation to analyze energy transfers, and does not need to be solved. The only modification to the computational code is the introduction of the force f_i given by Eq. (B.36) as an explicit source term in the resolved momentum equation. This implies a very small increase of the computational cost, due to the solving of the system of Eqs. (B.44) by a direct method (LU decomposition) in each point of the domain. For the applications considered in the present article, the increase in CPU cost is less than 1%.

B.3.3 Accounting for the shielding functions

The forcing given by Eq. (B.44) is general and can be applied to any mesh-dependent hybrid RANS/LES approach, since Eq. (B.43) simply assumes a Kolmogorov spectrum. However, since many approaches introduce shielding functions, such as HTLES used herein, the dependence of the solution on the grid step Δ is disrupted near the walls. Therefore, it makes more sense in this case to consider the dependence of the solution on the energy ratio r directly,

$$\phi\left(t, x_i, r\right). \tag{B.45}$$

Upon following the same analytical procedure as in section B.3.2,

$$T^f = -\frac{\partial k_m}{\partial r}\frac{\mathrm{d}r}{\mathrm{d}t}. \tag{B.46}$$

Now, $k_m = rk$ and k is independent of the energy ratio r, such that

$$T^f = -k\frac{\mathrm{d}r}{\mathrm{d}t} \tag{B.47}$$

The system of equations to be solved becomes

$$A_{ik}\overline{u'_j u'_k} + A_{jk}\overline{u'_i u'_k} = -\mathcal{C}\tau_{ij}^m \frac{1}{r}\frac{\mathrm{d}r}{\mathrm{d}t} \tag{B.48a}$$

$$B_i = -A_{ij}\widetilde{u_j}\ , \tag{B.48b}$$

which is equivalent to Eq. (B.44) in the absence of shielding functions, since in this case Eq. (B.15) leads to

$$\frac{1}{r}\frac{\mathrm{d}r}{\mathrm{d}t} = \frac{2}{3}\frac{1}{\Delta}\frac{\mathrm{d}\Delta}{\mathrm{d}t}\ .$$

This expression thus makes it possible to take into account a more complex formulation than a simple dependence on the grid step Δ. It can be extended to any other resolution parameter.

B.4 Results and Discussion

The volume forcing given by Eq. (B.48) is a modification of the original ALF (Anisotropic Linear Forcing) proposed by De Laage de Meux et al. (2015) (see below). The ALF method was originally developed to generate fluctuations at the entrance of a LES domain in a zonal hybrid RANS/LES approach, with an overlap of the RANS and LES zones: in the overlap zone, the intensity of the forcing in LES is driven by the statistics given by the RANS. In order to validate that the modified ALF developed in the previous section, which does not use RANS statistics, works similarly to the original ALF, a configuration that makes it possible to compare the two approaches is first considered. In a second step, the validation of the new method, the continuous active hybrid RANS/LES approach based on this modified ALF, will be performed in a case that represents its real objective, namely a continuous RANS/LES hybrid simulation with transition from RANS to LES and from LES to RANS. Finally, the validation will be extended to the case of a plane channel, which is more challenging since it does not exhibit an inflectional velocity profile likely to easily generate structures.

B.4.1 Comparison with the original ALF

The configuration to compare the two approaches is the case $n = 3$ (3 inter-hill subdomains) described at the beginning of section B.3, in which the inlet conditions are independent of time. The aim of the forcing is to achieve rapid spatial development of the LES solution, i.e., to tend as quickly as possible towards the periodic HTLES solution presented in section B.2.2. If we were to use the periodic RANS solution as an inlet condition, the simulation would have to perform a double adaptation in order to tend towards the periodic HTLES solution: correcting the RANS velocity field and generating resolved structures. In order to decouple these two issues, we introduce here as inlet condition at $x/h = 0$ the mean profile resulting from the periodic HTLES solution, so as to focus solely on the issue of generating resolved structures, leaving the coupled problem for later (section B.4.2). The same mesh (M1) and numerical parameters as for the periodic HTLES are used, and a simulation without forcing is also performed.

In the original ALF, the forcing is designed in order to drive both the mean and fluctuating fields towards a target mean velocity $U_i^\dagger$ and Reynolds-stress tensor $\tau_{ij}^\dagger$ obtained from a RANS computation in an overlapping zone. By identifying the work done by the force as in section B.3.2, De Laage de Meux et al. (2015) showed that this can be achieved by using the system of equations

$$A_{ik}\overline{u_j'u_k'} + A_{jk}\overline{u_i'u_k'} = \frac{1}{\tau_r}\left(\tau_{ij}^\dagger - \overline{u_i'u_j'}\right) \ , \tag{B.49a}$$

$$A_{ij}\widetilde{\overline{u_j}} + B_i = \frac{1}{\tau_v}\left(U_i^\dagger - \widetilde{\overline{u_i}}\right) \ , \tag{B.49b}$$

where τ_v and τ_r are the relaxation times

$$\tau_r = \max\left(2\tau, 0.01\frac{k^\dagger}{\varepsilon^\dagger}\right) \qquad \text{and} \qquad \tau_v = \frac{5h}{U_b} \ , \tag{B.50}$$

with τ the time step and U_b the bulk velocity. The computation using this original ALF consists of two overlapping zones: the upstream zone, which only contains the flow statistics and provides the target mean velocity $U_i^\dagger$ and Reynolds-stress tensor $\tau_{ij}^\dagger$; and the downstream zone, treated with HTLES in LES mode (with shielding functions). In the overlap, which covers the region $x/h \in [0, 2]$, the ALF is activated. Again, to get rid of the detrimental influence of a RANS model, here the target solution is obtained from averaging in time the periodic HTLES, which can be viewed as an ideal RANS computation, since it indeed provides the targeted solution. Therefore, the computation in the upstream zone corresponds to the periodic HTLES computation described in section B.3 and is in practice performed in advance. The inlet conditions for the downstream computation is also the time-averaged periodic HTLES. Moreover, in order not to bias the comparison, it is ensured that, as for the modified ALF presented in previous section, the force does not influence the mean flow: the rhs of Eq. (B.49b) is replaced by 0.

Moreover, in order to make a fair comparison between the different approaches, the following procedure is used for the other spatially-developing HTLES computations, without forcing (standard HTLES) and with forcing (active HTLES). The same inlet conditions are used, with the average velocity profile obtained in periodic HTLES, and also k_{sfs} equal to the total turbulent energy. Just at the inlet, the RANS mode is activated, by imposing $r = 1$ in the model. A transition from RANS to LES is imposed gradually from $x/h = 0$ to $x/h = 2$, by enforcing a modified r

$$r_{\text{mod}} = (1 - f) + f\, r \quad \text{with} \quad f(\frac{x}{h}) = \frac{1}{2}\frac{x}{h} \quad \text{for} \quad \frac{x}{h} \in [0; 2], \tag{B.51}$$

such that $r = 1$ at the inlet and gradually reduces to the usual value in HTLES given by Eq. (B.16). Since the mesh is the same mesh as used for the periodic HTLES and for the HTLES with the ALF, after $x/h = 2$ the LES mode is activated.

From Fig. B.7, it can be seen that in the case of the standard HTLES, without forcing, the recovery of the total turbulent kinetic energy is very slow. Just after the inlet ($x/h \simeq 0$), the turbulent energy is virtually equal to the one of the periodic case, since it is entirely modeled ($r = 1$, RANS mode) and the periodic profile of the total turbulent energy is imposed as the boundary condition for the modeled energy k_{sfs}. In the RANS-to-LES transition region ($x/h \in [0, 2]$), k_{sfs} is gradually decreased due to Eq. (B.51), and the growth of resolved turbulent energy is supposed to compensate for this decrease. However, Fig. B.7 shows that this compensation mechanism does not work. Indeed, the total turbulent energy remains very small in the first subdomain ($x/h \in [0, 9]$); starts increasing, essentially in the detached shear layer, only in the second subdomain ($x/h \in [9, 18]$); and eventually recovers the expected level at the end of the third subdomain ($x/h > 24$) (it is recalled that there is only one computational domain and that the term subdomain is used to identify the regions between two successive hills). This underestimation is due to the very slow development of the turbulent structures and thus of the resolved energy. This has a great influence on the velocity profiles, visible in Fig. B.7: the lack of mixing of momentum by the turbulent structures is at the origin of a too weak entrainment and thus of an underestimation of the backward velocity and an overestimation of the size of the recirculation zone. Consequently, the friction coefficient C_f is very poorly reproduced, until the end of subdomain 2 (Fig. B.12a). When the turbulent energy returns to a correct level in the third subdomain, the velocity profiles are much better predicted and C_f tends towards the value obtained in the periodic simulation when approaching the last hill.

In contrast, it can be seen that the ALF is very efficient in generating resolved energy quickly and thus maintaining a total energy level very close to that obtained in the periodic simulation. This is achieved by forcing at each point in the region $x/h \in [0, 2]$ towards the target turbulent energy according to Eq. (B.49a). However, Fig. B.7a shows that at $x/h = 4$, after the end of the forcing region, a part of the generated fluctuations have been dissipated, and the turbulent energy is slightly underestimated. However, at the end of the first subdomain, the energy, the velocity profile (Fig. B.7d) and the friction coefficient (Fig B.12a) are very well reproduced. The results tend almost perfectly to the periodic results in the middle of the second subdomain (Figs. B.7b, B.7e and B.12a).

The challenge for the new forcing method, which has no target field but is simply based on the estimate Eq. (B.48a) of the energy rate to be injected into the resolved part, is to approach the very good results obtained with the ALF. It can be seen in Fig. B.7a that in the middle of the RANS-to-LES transition zone, at $x/h = 1$, the total turbulent energy is underestimated: the modeled energy has been reduced by the HTLES model, and the fluctuating energy generated by the forcing is not sufficiently developed yet. The activation of the forcing is related to the transition from RANS to LES driven by Eq. (B.51), which imposes a decrease of r along the streamlines. On the other hand, at the end of the transition zone ($x/h = 2$), we observe a slight overshoot of the turbulent energy in the detached shear layer and in the recirculation zone, and a stronger overshoot in the core of the flow. The velocity profiles (Fig. B.7d) are then slightly less accurate than those given by the ALF method. However, it can be seen that from the end of subdomain 1, the results given by the active HTLES are very close to those given by the ALF and the periodic HTLES, both for the turbulent energy, the velocity profiles and the friction coefficient.

It is to be noted here that the coefficient $\mathcal{C} = 1$ is used in Eq. (B.48a). A study of the influence of this coefficient has of course been performed (not shown here). An increase of $\mathcal{C}$ accelerates the production of resolved energy, at the cost of a stronger overshoot at the

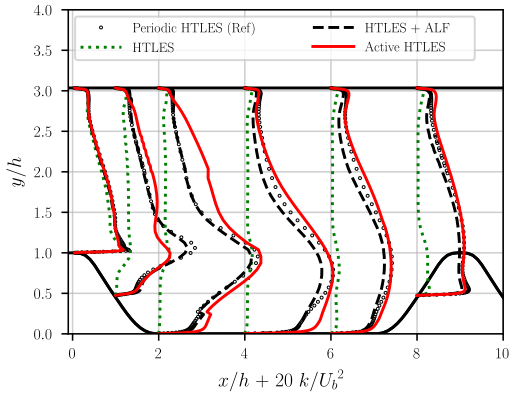

(a) Subdomain 1

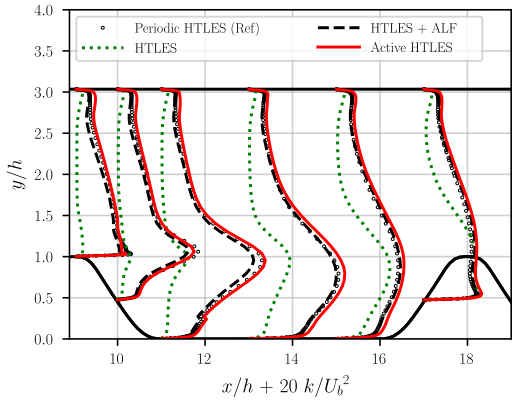

(b) Subdomain 2

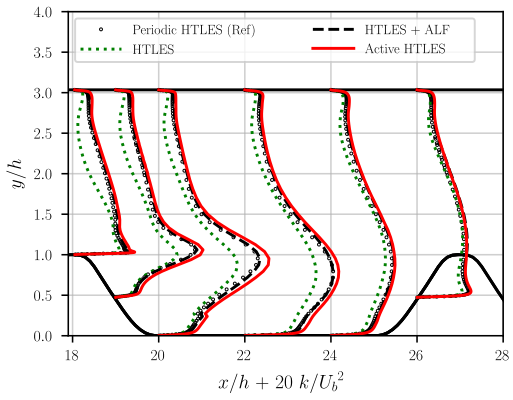

(c) Subdomain 3

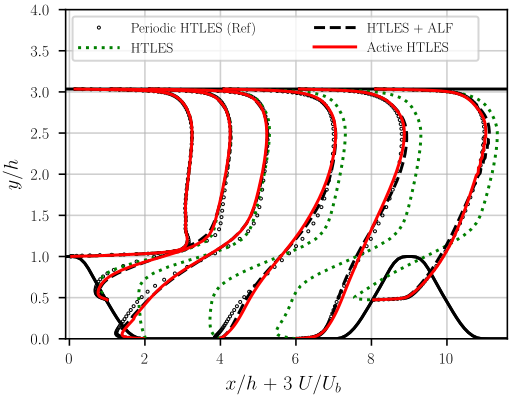

(d) Subdomain 1

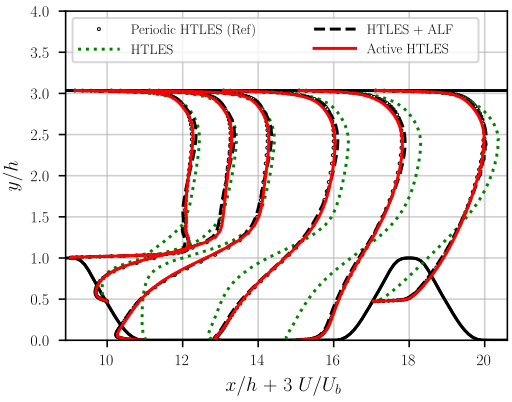

(e) Subdomain 2

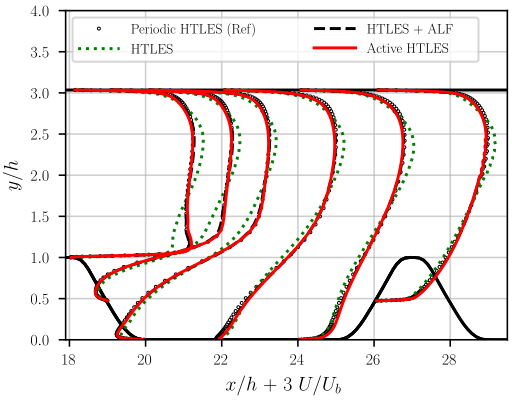

(f) Subdomain 3

Figure B.7 – Profiles of total turbulent kinetic energy (a,b,c) and mean velocity (d,e,f) in the different subdomains. Comparison of periodic HTLES, HTLES without forcing, HTLES with the ALF and Active HTLES, both with a forcing in the region $x/h \in [0, 2]$.

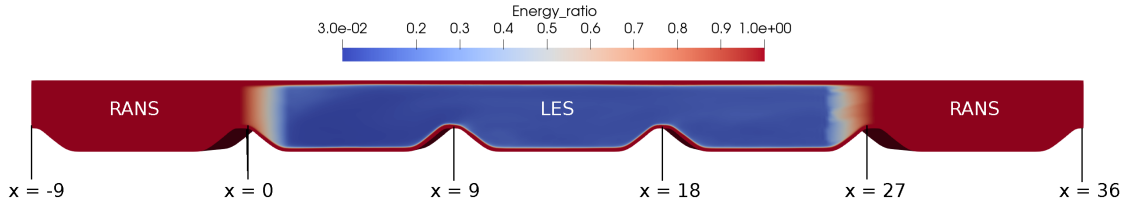

Figure B.8 – Geometrical representation of the case $n = 5$, showing the isocontours of the modeled-to-total energy ratio r, indicating the regions solved in RANS ($r = 1$) and in LES ($r < 1$).

end of the transition region; a decrease of $\mathcal{C}$ suppresses the overshoot but finally degrades the results at the exit of the transition region. Similar to what was observed for the ALF, a part of the resolved energy generated by the forcing is dissipated, and it can be considered that a small overshoot at the exit of the transition region for the active HTLES is favorable, such that the theoretical coefficient $\mathcal{C} = 1$ is kept for the following.

In conclusion, both the ALF associated with HTLES in zonal version and the new continuous approach called *active* HTLES achieve a fast transition from RANS to LES in this configuration. As the ALF was previously validated by De Laage de Meux et al. (2015) and Duffal (2020) this comparison was used to support the fact that it is possible to avoid the need for a target field in the forcing, by replacing the restoring term in Eq. (B.49a) with the estimate of the rate of energy to be transferred from the modeled part to the resolved part used in Eq. (B.48a).

This modification is decisive, since it makes it possible to adapt to continuous hybrid approaches the forcing method initially developed for zonal hybrid approaches with an overlapping zone. The following section is therefore devoted to the validation of the new approach in a configuration for which it was developed, with transition from RANS to LES and from LES to RANS.

B.4.2 Validation in a fully realistic configuration

The active approach is now tested in a more realistic scenario, where the simulation transitions from a fully developed RANS solution to LES, and back from LES to RANS at the end of the domain. The geometrical representation of this case $n = 5$ (5 inter-hill subdomains) is shown in Fig. B.8. Two subdomains are treated in RANS mode, one at the entrance and one at the exit; and the other three are treated in LES mode (once again, it is recalled that there is only one computational domain and that the term subdomain is used for convenience). The RANS-to-LES transition is imposed in the region $x/h \in [0, 2]$ using Eq. (B.51), and for the LES-to-RANS transition, the modified r is imposed in a similar way in the region $x/h \in [25, 27]$ using $f(x/h) = (27 - x/h)/2$.

Three cases are compared: (i) a standard HTLES without forcing; (ii) Active HTLES with forcing only activated in case of RANS-to-LES transition; (iii) Active HTLES with forcing both for RANS-to-LES and for LES-to-RANS transition. The results are compared with the periodic RANS solution in RANS regions and with the periodic HTLES transition in LES regions. The computations use the same mesh M1 as in sections B.2.2 and B.4.1 and the same numerical parameters.

Figs. B.12b, B.9, B.10 and B.11 show, for the three cases, the comparisons of the friction coefficient, Q-isocontours, turbulent energy profiles and mean velocity profiles, respectively. Note that in all these figures, the reference solution is the periodic RANS solution in subdomains 1 and 5, and the periodic HTLES solution in subdomains 2, 3 and 4. In the first subdomain, treated in RANS mode ($r = 1$), since the inlet conditions

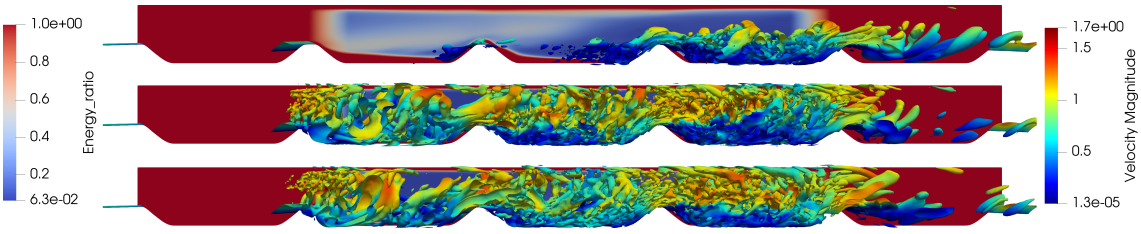

Figure B.9 – Isocontours $Q = 0.2U_b^2/h^2$ colored with the velocity magnitude and, in the background, modeled-to-total turbulent energy ratio r, indicating the regions solved in RANS ($r = 1$) and in LES ($r < 1$). Top: Without forcing, Middle: Forcing at the RANS-to-LES transition, Bottom: Forcing at both the RANS-to-LES and the LES-to-RANS transitions.

correspond to the periodic RANS solution, the three approaches preserve this solution almost perfectly. The small discrepancies are only due to the fact that at the end of the RANS region at $x/h = 0$, instead of having a periodicity condition, the transition zone from RANS to LES starts, which has a small influence on the upstream region.

From the isocontours $Q = 0.2U_b^2/h^2$ plotted in Fig. B.9, it is seen that when no force is applied, the resolved structures take a long time to develop after the RANS-to-LES transition located between $x/h = 0$ and $x/h = 2$. In contrast, when the forcing is applied, one can observe a rapid appearance of resolved structures.

This makes a major difference for the turbulent energy in the LES zone shown in Figs. B.10b, B.10c and B.10d. Without forcing, the turbulent energy is very strongly underestimated until the end of subdomain 4, in a manner very similar to the case studied in section B.4.1, in which the essential difference is that at $x/h = 0$, the periodic HTLES solution was used as a boundary condition, whereas here, the values at $x/h = 0$ are advected from the RANS zone. The velocity profiles in Fig. B.11 and especially the comparison of C_f in Figs. B.12a and B.12b show that this modification does not change much the results obtained in the LES zone, which are equally inaccurate.

When the forcing is introduced (regardless of whether it is activated or not in the downstream LES-to-RANS transition zone), the generation of resolved turbulent energy occurs rapidly (Fig. B.9). However, a larger overshoot is observed compared to the situation discussed in section B.4.1 (Fig. B.10b). This difference arises from the fact that the velocity profiles and turbulent variables at the location $x/h = 0$ are no longer the ideal periodic HTLES profiles, but rather those advected from the upstream RANS domain, which are quite different. Fig. B.12 illustrates that in this case, the reproduction of the friction coefficient is less accurate in the region $x/h \in [0, 9]$ compared to the case in section B.4.1, because the LES mode of HTLES, in addition to developing resolved structures, needs to correct the mean field originating from the RANS region. Fig. B.10f displays, at the end of the transition zone ($x/h = 2$), the breakdown of turbulent energy into modeled (k_m) and resolved (k_r) components. In the absence of forcing, the resolved energy is nearly zero throughout. As mentioned earlier, the reverse flow velocity is very low in the recirculation region (Fig. B.11b), causing complete flow relaminarization, with the modeled energy also going to zero. In contrast, with active HTLES, the resolved energy develops significantly, leading to the aforementioned overshoot. In this case, similar to the situation discussed in section B.4.1, the investigation of the influence of the coefficient $\mathcal{C}$ (not presented here) indicates that it is preferable to generate an overshoot at the end of the transition zone, thereby maintaining $\mathcal{C} = 1$. The recovery of the reference (periodic) HTLES solution is slower than in the idealized scenario discussed in the previous section, where periodic profiles were imposed at the inlet. The turbulent energy and velocity profiles still exhibit slight deviations from the periodic solution in the middle of subdomain 4 (Figs. B.10d

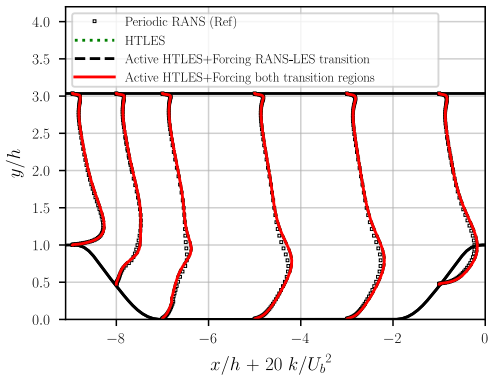

(a) Subdomain 1

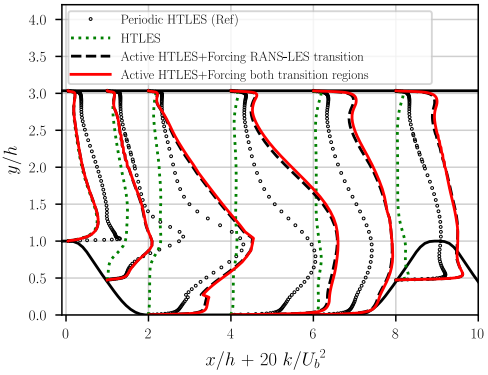

(b) Subdomain 2

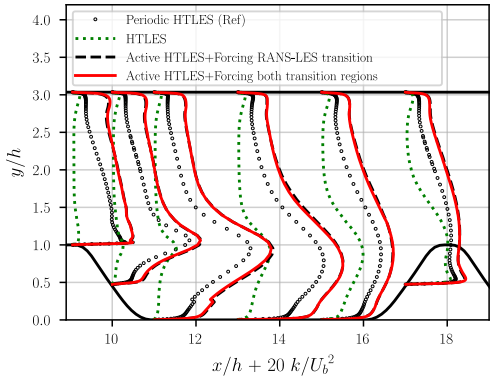

(c) Subdomain 3

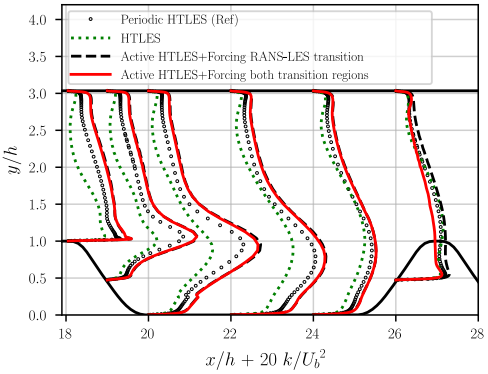

(d) Subdomain 4

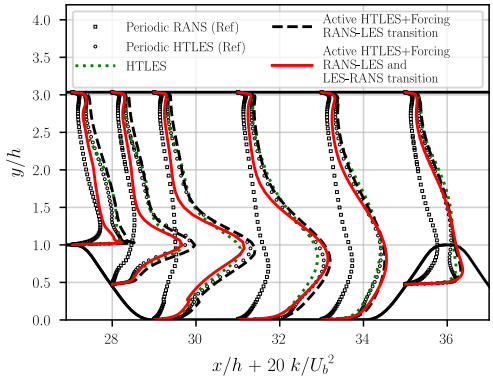

(e) Subdomain 5

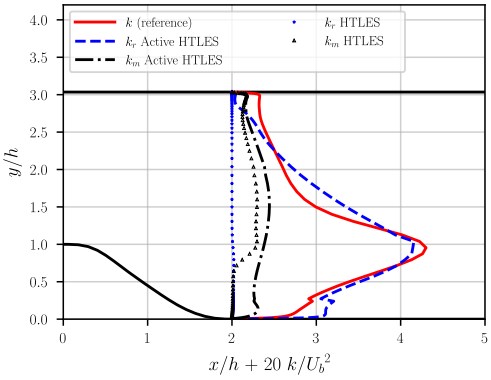

(f) Breakdown of total energy.

Figure B.10 – (a) to (e): Profiles of total turbulent kinetic energy in the different subdomains, (f): Breakdown of total turbulent kinetic energy into modeled turbulent kinetic energy and resolved turbulent kinetic energy at the end of the region of transition from RANS to LES in the case with forcing (active HTLES) in the first subdomain.

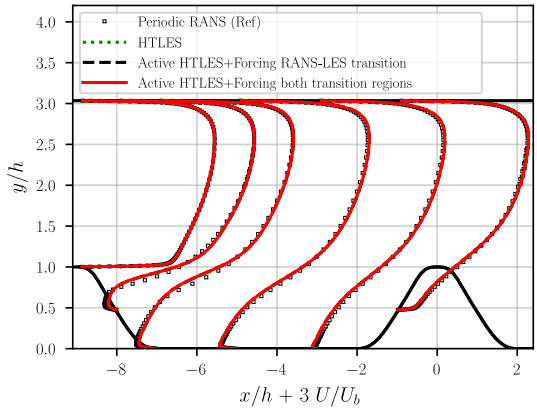

(a) Subdomain 1

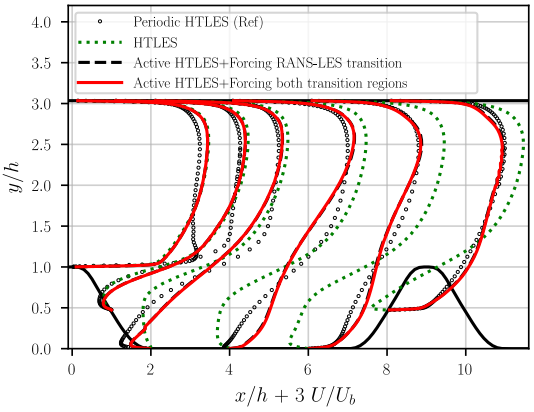

(b) Subdomain 2

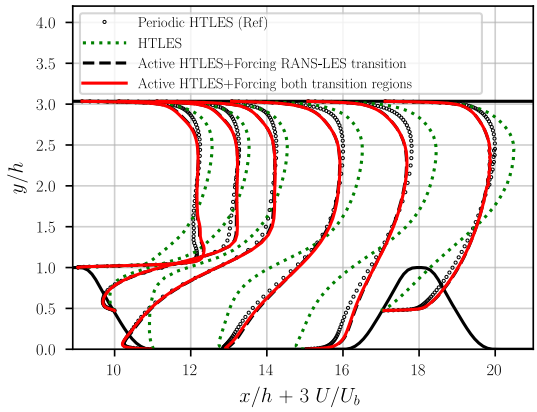

(c) Subdomain 3

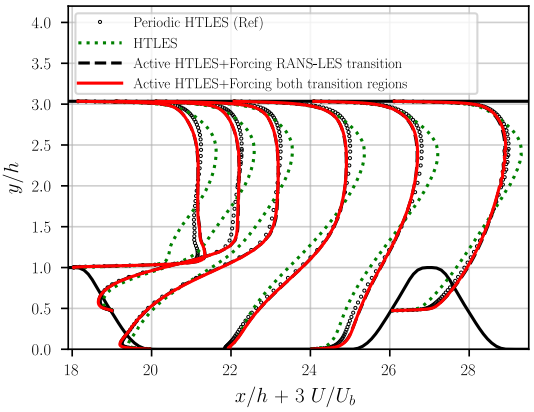

(d) Subdomain 4

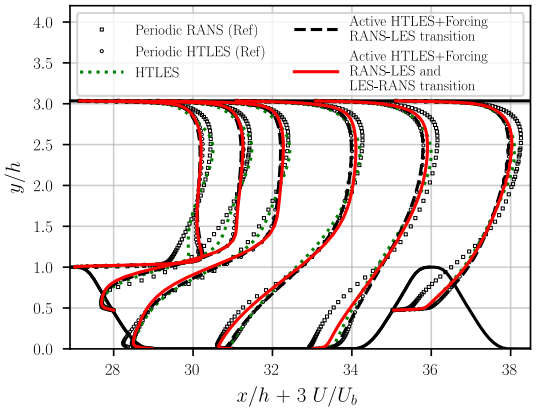

(e) Subdomain 5

Figure B.11 – Profiles of averaged velocity in different subdomains.

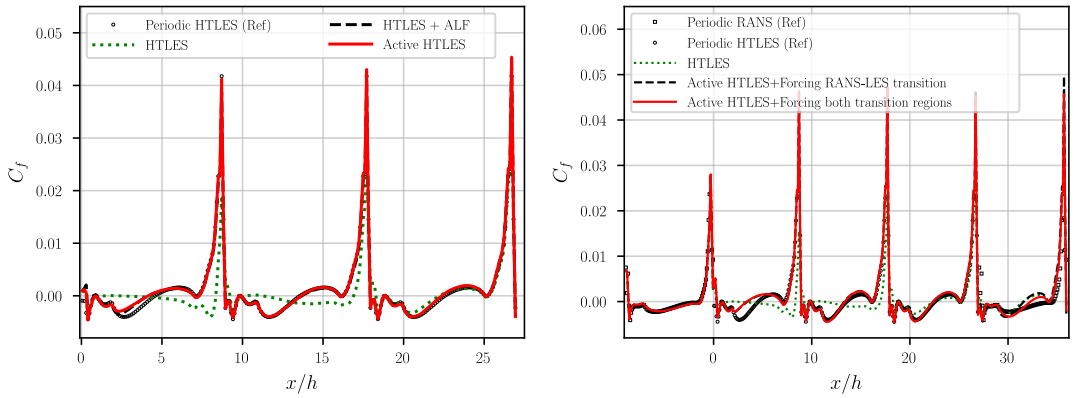

(a) Case $n = 3$ (b) Case $n = 5$

Figure B.12 – Skin friction coefficient along the lower wall

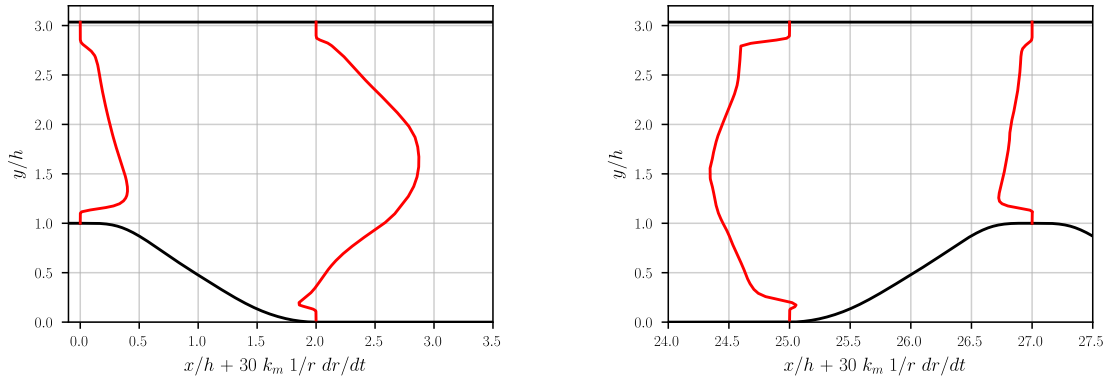

(a) RANS-to-LES transition (b) LES-to-RANS transition

Figure B.13 – Profiles of the half-trace of the rhs of the forcing (B.48) in the transition region (mean production of resolved energy). Case of active HTLES with forcing activated at both RANS-to-LES and LES-to-RANS transitions.

and B.11d). However, Fig. B.12b shows that the friction coefficient is very satisfactory starting from the end of subdomain 2, i.e., the first subdomain in LES mode.

An interesting observation in this context emerges when the forcing is applied also at the LES-to-RANS transition, i.e., at the end of subdomain 4 ($x/h \in [25, 27]$). Fig. B.13 illustrates the behavior of the half-trace of the rhs of Eq. (B.48a), which represents the average production of resolved energy due to the volume forcing. It reveals that the situations in the RANS-to-LES and LES-to-RANS transition zones are reversed. Specifically, in Fig. B.13a, the forcing contributes energy to the resolved motion, except near the lower wall at the location $x/h = 2$, where the flow reenters from the LES region into the near-wall RANS region imposed by the shielding function. Conversely, in Fig. B.13b, except for near the wall at the beginning of the hill, one predominantly observes a flow transitioning from the LES region ($r < 1$) to the RANS region ($r = 1$), resulting in a positive material derivative of r and consequently the destruction of resolved energy. However, Fig. B.9 reveals that resolved structures persist in all cases at the beginning of the RANS domain. Nonetheless, as shown in Fig. B.10e, turbulent energy is indeed reduced in the core of the flow due to the negative forcing, but not significantly in the separated shear layer and recirculation zone. Despite this modest effect, it is still visible that the velocity profiles within the recirculation zone are closer to the RANS profiles (Fig. B.11e). In Figs. B.10e

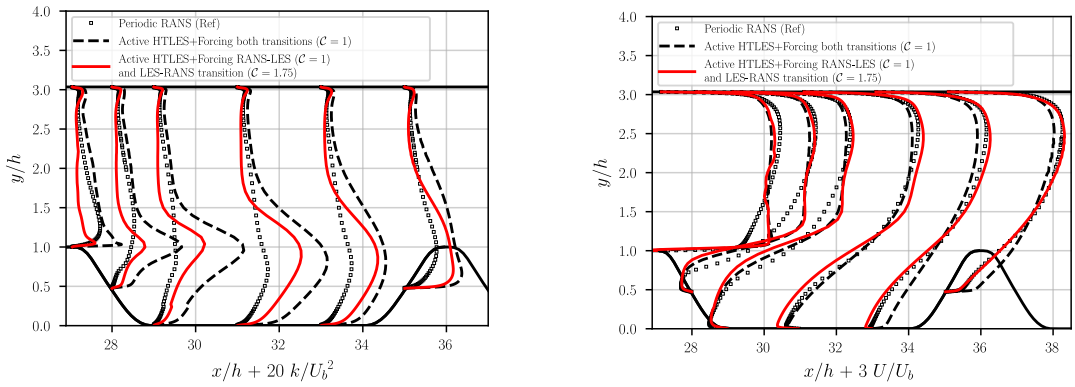

(a) Turbulent energy profiles

(b) Streamwise velocity profiles

Figure B.14 – Improvement of the LES-to-RANS transition (subdomain 5) by using different coefficients in the two transition regions.

and B.11e, the reference periodic HTLES solution is also shown, in order to emphasize that it is not a serious problem if resolved structures survive in the RANS zone after the RANS-to-LES transition, since the solution then remains close to the solution obtained in LES mode, which is better than the RANS solution. However, it may seem more consistent for the solution to return as rapidly as possible to the RANS solution. To this end, it is possible to increase the effect of the forcing by identifying the RANS-to-LES transition and the LES-to-RANS transition from the sign of $\mathrm{d}r/\mathrm{d}t$ in Eq. (B.48a), and using a larger coefficient $\mathcal{C} = 1.75$ in the second case instead of $\mathcal{C} = 1$. Fig. B.14 shows that this increase in coefficient indeed speeds up the transition to the RANS solution: in particular, even though there is still excessive resolved energy, the velocity profile of the RANS solution is recovered as the last hill is approached.

Finally, the robustness of the method to mesh refinement is verified using the two meshes M1 and M2 of section B.2.2. It can be seen from Fig. B.15, which compares streamwise velocities in subdomain 2 and friction coefficients at the lower wall, that mesh sensitivity is slightly more pronounced than for periodic HTLES, but does not significantly influence the results. In the transition zone at the beginning of subdomain 2, the velocity profiles are virtually identical, and only a moderate difference is observed in the second part of subdomain 2. However, the friction coefficients at the lower wall show no more difference between the M1 and M2 meshes than in the case of the periodic HTLES studied in section B.2.2. These results therefore show that the active method is relatively robust to mesh refinement.

B.4.3 Channel flow

The previous section successfully showed that the proposed active method can efficiently generate resolved structures at the RANS-to-LES transition in the case of the hill flow. This flow, representative of many detached flows, is a relatively favorable case. Indeed, resolved structures are generated, even if insufficiently, in the detached sheared layer, and the forcing has the role of amplifying them. Many other flows, in particular boundary layers, do not exhibit linear instability promoting the generation of resolved structures. It is also desirable in general to be able to generate these structures in a boundary layer upstream of an obstacle, for example, to be able to resolve the flow around the obstacle in LES mode. This is why the present section focuses on the question of the RANS-to-LES transition in a channel flow.

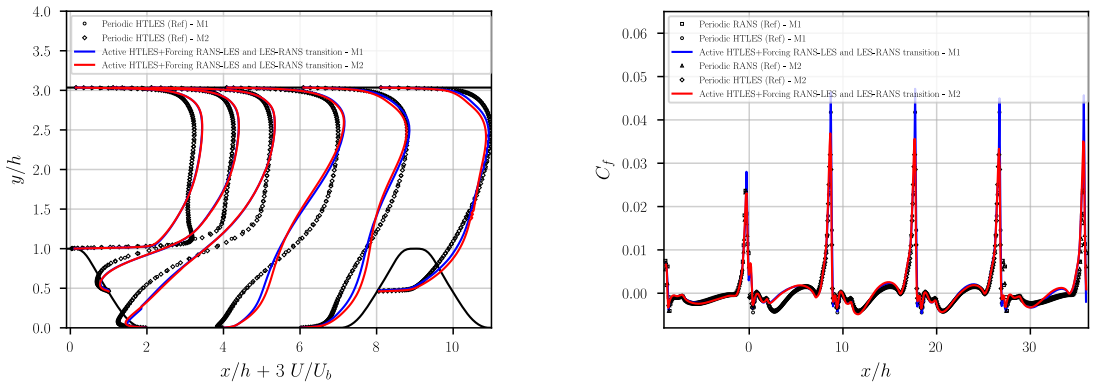

(a) Streamwise velocity profiles in subdomain 2

(b) Skin friction along the lower wall

Figure B.15 – Comparison of the solutions obtained with two different grids.

The flow is characterized by the friction Reynolds number, $Re_\tau = u_\tau h/\nu = 590$, where u_τ is the friction velocity and h is the half-height of the channel. The periodic solution, which will serve as a reference here, obtained in a domain of size $L_x \times L_y \times L_z = 6.4h \times 2h \times 3.2h$, was studied in detail by Duffal et al. (2022) and shown to be satisfactorily close to the DNS data (Moser et al., 1999). The mesh used here, $N_x \times N_y \times N_z = 64 \times 96 \times 64$, satisfying $\Delta y^+ \simeq 1$ at the wall, was shown to be sufficiently fine for HTLES (Duffal et al., 2022).

Here, simulations in spatial development are performed, with inlet and outlet conditions. The computational domain and the mesh used for the periodic calculation are simply duplicated ten times, so that the overall size is $L_x \times L_y \times L_z = 64h \times 2h \times 3.2h$, discretized using the mesh given by $N_x \times N_y \times N_z = 640 \times 96 \times 64$. The initial part of the channel, $(x/h \in [0, 6.4])$, is treated in RANS mode by imposing the energy ratio $r = 1$ in the model. The gradual transition from RANS-to-LES occurs in $x/h \in [6.4, 12.8]$, by enforcing a modified energy ratio r_{mod}, as done in previous section:

$$r_{\text{mod}} = f + (1 - f)\, r \quad \text{with} \quad f\left(\frac{x}{h}\right) = 2 - \frac{1}{6.4}\frac{x}{h} \quad \text{for} \quad x/h \in [6.4, 12.8] \tag{B.52}$$

and the rest of the channel is treated in LES mode ($f = 0$). Periodic RANS computations are used as inlet boundary conditions.

Fig. B.16c shows that without forcing, the total turbulent energy is severely underestimated, all along the channel, since, as can be seen in Fig. B.16b, virtually no resolved energy is produced. Note that in the computation without forcing, denoted simply as "HTLES" in the figures, the RANS-to-LES transition also occurs in the region $x/h \in [6.4, 12.8]$ and is imposed by Eq. (B.52). This leads to completely wrong velocity profiles (Fig. B.17) and consequently, a much underestimated friction coefficient in Fig. B.18. On the other hand, when the forcing is applied, the resolved turbulent energy shown in Fig. B.16b rapidly tends towards the correct level, at the end of the forcing region, located at $x/h = 12.8$. It is seen in Fig. B.19 that despite the absence of inflectional velocity profile, the active approach is able to rapidly generate resolved structures (note that only the first half of the computational domain $(x/h \in [0; 32])$ is shown in this figure). However, at the end of the forcing region $(x/h = 12.8)$, it is apparent that a part of the structures generated by the forcing rapidly disappear in the central region of the channel. In Fig. B.17, an improved velocity profile is observed compared to the case without forcing. Although far from perfect, the prediction of the friction coefficient is significantly improved (Fig. B.18), and tends to the periodic value at the end of the domain.

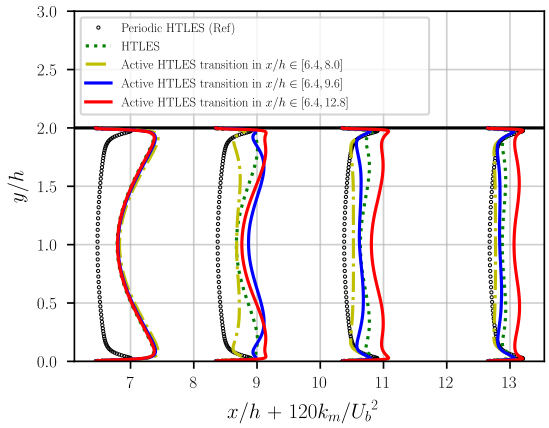

(a) Modeled contribution k_m

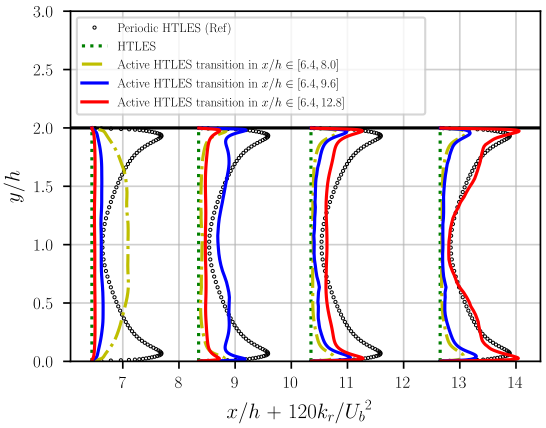

(b) Resolved contribution k_r

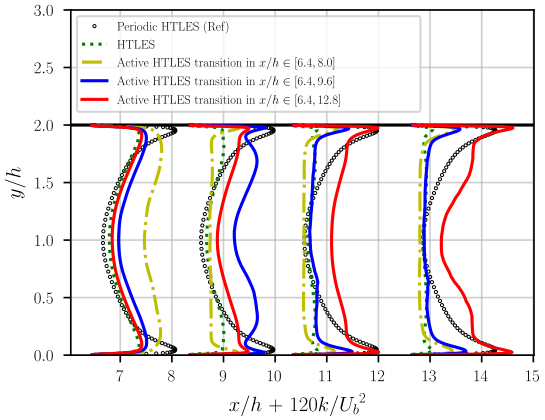

(c) Total turbulent energy $k = k_m + k_r$

Figure B.16 – Channel flow: Profiles of turbulent energy (modeled, resolved and total) in the region $x/h \in [6.4; 12.8]$ extracted at x/h =6.45; 8.35; 10.35 and 12.65.

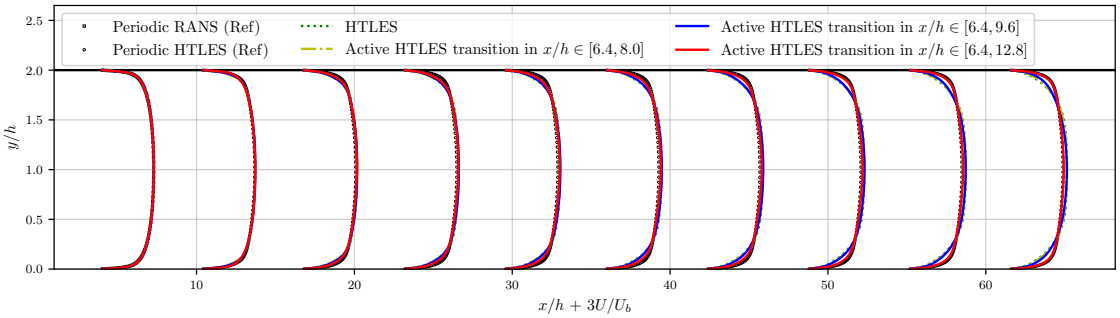

Figure B.17 – Channel flow: Profiles of the streamwise mean velocity extracted every $6.4h$ from $x = 3.5h$. In the RANS zone ($x/h \in [0; 6.4]$), the reference is the periodic RANS solution; in the LES zone ($x/h > 6.4$), it is the periodic HTLES solution.

It is interesting to look in more detail at Fig. B.16, which shows the modeled and resolved contributions to the total turbulent energy, in the transition zone ($x/h \in [6.4, 12.8]$). In the case without forcing, the gradual decrease of k_m is observed (Fig. B.16a), which tends towards the profile of the periodic solution at the exit of the transition zone. This decrease is not compensated by an increase in k_r, which remains virtually zero (Fig. B.16b), which

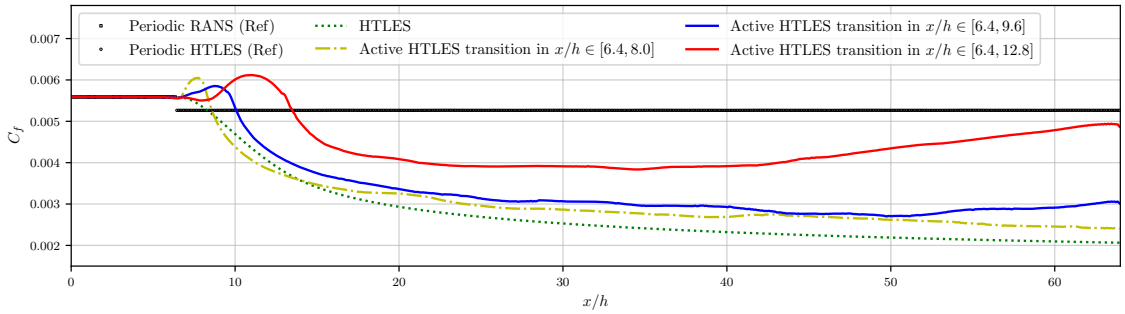

Figure B.18 – Channel flow: skin friction coefficient along the lower wall.

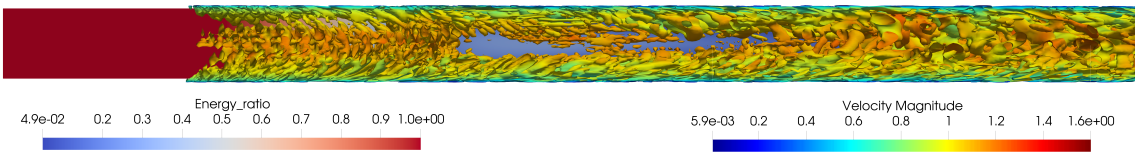

Figure B.19 – Channel flow: Q-isocontours obtained for a RANS-to-LES transition in the region $x/h \in [6.4; 12.8]$. Note that only the first half of the computational domain is shown ($x/h \in [0; 32]$).

causes the strong underestimate of $k = k_m + k_r$ (Fig. B.16). When the forcing is activated, k_r tends towards the periodic profile at the end of the transition zone. On the other hand, k_m no longer decreases as quickly as without forcing, which can be understood by looking at Eq. (B.7): the reduction of r tends to decrease the value of the time scale T_m, but this effect is partially compensated by the appearance of modeled energy k_r. Quite paradoxically, when the forcing is introduced, the overshoot observed in Fig. B.16c in the total energy is not due to the rapid increase in resolved energy but due to too slow a decrease in modeled energy.

So far in this section, the transition zone has been arbitrarily set to the interval $x/h \in [6.4, 12.8]$, which appears relatively long for practical applications. It is then legitimate to wonder if this length can be reduced: the intensity of the forcing (i.e., the work of the force) being controlled by the material derivative of r in the rhs of Eq. (B.48a), a shortening of the transition zone induces an intensification of the force, so that at the end of the transition zone, the right amount of energy has been transferred between the modeled part and the resolved part. Two additional simulations were therefore carried out, in which the transition zone starts at the same place but is shortened by a factor of two ($x/h \in [6.4, 9.6]$) and by a factor of four ($x/h \in [6.4, 8]$). Figs. B.17 and B.18 show that this actually has a very detrimental effect on the mean flow prediction. To understand this issue, the evolution of the modeled and resolved contributions in Fig. B.16 must be examined. Fig. B.16a shows that, as expected, when the RANS-to-LES transition is more abrupt, the modeled energy k_m decreases more quickly. Fig. B.16b indicates that indeed, the forcing being more intense, the resolved energy is produced more quickly, but unfortunately it does not survive at the end of the transition zone, when the forcing stops. For the case of a transition zone of length four times shorter, the first profile, located at $x/h = 6.45$, i.e., in the transition zone, shows that the resolved energy grows very quickly. However, the second profile, located at $x/h = 8.35$, just after the end of the transition zone, shows that this resolved energy is very quickly dissipated. The same phenomenon is observed for the case of a transition zone reduced only by a factor of two, simply shifted further downstream. Even in the case of the longest transition zone, some of the resolved structures are dissipated in the central region, as can be seen in Fig. B.19, but enough

remain for them to are regenerated quickly.

It can be concluded from this study that the forcing makes it possible to generate resolved structures efficiently, even in the absence of an inflectional velocity profile allowing structures to be generated naturally. Even in a channel, when the turbulent viscosity is reduced, very small fluctuations appear which the forcing manages to amplify during the iterations, until reaching the expected level. Indeed, the amplification of disturbances must not be considered only in the direction of the flow, but also over the iterations: at each point, the small initial fluctuations are amplified by the forcing at each iteration, until reaching the equilibrium solution. However, the study also shows that the RANS-to-LES transition should not be too rapid, otherwise the generated fluctuations are dissipated when leaving the forcing zone. We can compare this remark to the conclusions of the article by Druault et al. (2004) when the forcing is too intense, the fluctuations generated no longer resemble turbulent structures, and are then dissipated when the forcing stops. In other words, the introduction of the forcing modifies the equations of motion, and the structures generated are no longer solutions to the equations when the forcing stops. It is therefore appropriate to have a transition zone that is not too short so that the forcing term is not too strong compared to the other terms of the resolved momentum equation at the exit from the transition zone. In a general case, the question of the length of the minimum transition zone remains an open question.

B.5 Conclusions

In hybrid RANS/LES methods, when the flow transitions from a RANS zone to a LES zone, there is a shift from fully modeled to partially resolved quantities. This transition necessitates compensating for the reduction in modeled energy with an increase in resolved energy. Unfortunately, the growth of resolved fluctuations relies solely on natural instabilities and is not sufficiently rapid to counterbalance the stress decay imposed by the model. A simple analysis in spectral space reveals that the missing element is the transfer of energy from the modeled component to the resolved component, since the momentum equation remains unaffected by variations in grid resolution.

To address this issue, a method is proposed to model the terms resulting from grid step variations, which are responsible for this energy transfer but are commonly disregarded, through the use of a fluctuating volume forcing. Although the existence of these terms, due to commutation errors between the filter and the differential operators, has been noted by various authors using filter-based formalisms, the analytical approach used here is simpler and applies to any hybrid RANS/LES model, whether it explicitly refers to a particular formalism or not, as long as the turbulent energy partition between modeled and resolved scales depends on an identifiable parameter. It is demonstrated that the intensity of this force can be determined by equating the work done by the force per unit time to the decrease in modeled energy caused by grid step variations.

This novel approach, referred to as *active* hybrid RANS/LES, is validated in a channel flow configuration with periodic constriction. In this setup, the flow transitions from RANS to LES, and the purpose is to rapidly reach a fully developed periodic solution. The results indicate that in the absence of forcing, the development of resolved structures is slow, and it takes three times the inter-hill distance to approach the periodic solution. In contrast, when the forcing is introduced, the solution becomes immediately physically acceptable, with resolved structures developing rapidly. After just one inter-hill distance, the solution closely resembles the fully developed state. Furthermore, the forcing is capable of handling the LES-to-RANS transition by changing the energy transfer direction. This reduces the resolved energy when the flow reenters a RANS region.

The case of a plane channel finally shows that the forcing makes it possible to generate resolved structures even in a situation without a detached sheared layer which naturally creates fluctuations. The amplification during the iterations of fluctuations initially of very small amplitude makes it possible to reach a final equilibrium state with the desired level of resolved energy. However, the study of the influence of the spatial length of the transition zone shows that it is necessary not to introduce too brutal a forcing into the equations, otherwise it would generate structures that are not sufficiently realistic and which are dissipated at the exit from the forcing zone.

The active approach presented in this study has the potential to be applied to any hybrid RANS/LES method, provided a parameter driving the RANS-to-LES transition can be identified. It solves the problem of the appearance of resolved structures at the RANS-to-LES transition in the flow direction, but could also improve the normalwise transition and avoid the log-layer mismatch, in the spirit of the work of Hamba (2009) by considering, in addition to the material derivative (Eq. (B.23)), the diffusion terms. Importantly, this method is highly versatile as it does not require information about the interface between RANS and LES regions; it relies solely on local quantities, particularly the material derivative of the resolution parameter. This is a significant advantage over approaches that introduce synthetic vortices, which require scales evaluated from a RANS calculation or from the upstream RANS zone. Since it is based on a first principle, conservation of energy, it is to be assumed that the method is not fundamentally dependent on flow characteristics, and can be extended to other geometries and higher Reynolds numbers. The promising results obtained pave the way for a flexible utilization of continuous hybrid approaches in industrial configurations.

B.6 Compliance with ethical standards

Funding This study was funded by the E2S UPPA (ANR-16-IDEX-0002) and the ASTURIES project (grant E2S-20-ScientificChallenges-01).

Computing resources The computing resources were provided by MCIA (Mésocentre de Calcul Intensif Aquitain) and GENCI-IDRIS (Grants 2022-A0122A10980 and 2023-A0142A10980).

Conflict of interest The authors declare that they have no conflict of interest.

References

Comte-Bellot, G. et al. (1966). "The use of a contraction to improve the isotropy of grid-generated turbulence". In: *J. Fluid Mech.* 25, pp. 657–682.

Tennekes, H (1975). "Eulerian and Lagrangian time microscales in isotropic turbulence". In: *Journal of Fluid Mechanics* 67.3, pp. 561–567.

Germano, Massimo (1992). "Turbulence: the filtering approach". In: *Journal of Fluid Mechanics* 238, pp. 325–336.

Menter, Florian R (1994). "Two-equation eddy-viscosity turbulence models for engineering applications". In: *AIAA journal* 32.8, pp. 1598–1605.

Ghosal, S. et al. (1995). "The Basic Equations for the Large Eddy Simulation of Turbulent Flows in Complex Geometry". In: *J. Comput. Phys.* 118, pp. 24–37.

Spalart, Philippe R (1997). "Comments on the feasibility of LES for wings, and on a hybrid RANS/LES approach". In: *Proceedings of first AFOSR international conference on DNS/LES*. Greyden Press.

Moser, R. D. et al. (1999). "Direct numerical simulation of turbulent channel flow up to $Re_\tau = 590$". In: *Phys. Fluids* 11.4, pp. 943–945.

Nikitin, NV et al. (2000). "An approach to wall modeling in large-eddy simulations". In: *Physics of fluids* 12.7, pp. 1629–1632.

Spille-Kohoff, A et al. (2001). "Generation of turbulent inflow data with a prescribed shear-stress profile". In: *TECHNISCHE UNIV BERLIN (GERMANY) HERMANN-FOTTINGER INST FUR STROMUNGSMECHANIK*.

Travin, A. et al. (2002). "Advances in LES of Complex Flows". In: ed. by R. Friedrich et al. New York: Kluwer Acad. Chap. Physical and Numerical Upgrades in the Detached-Eddy Simulation of Complex Turbulent Flows, pp. 239–254.

Pruett, C. D. et al. (2003). "The temporally filtered Navier-Stokes equations: Properties of the residual stress". In: *Phys. Fluids* 15.8, pp. 2127–2140.

Archambeau, Frédéric et al. (Feb. 2004). "Code Saturne: A Finite Volume Code for the computation of turbulent incompressible flows - Industrial Applications". In: *International Journal on Finite Volumes* 1.1.

Druault, P. et al. (2004). "Generation of Three-Dimensional Turbulent Inlet Conditions for Large-Eddy Simulation". In: *AIAA J.* 42.3, pp. 447–456.

Germano, M. (2004). "Properties of the hybrid RANS/LES filter". In: *Theor. Comput. Fluid Dyn.* 17.4, pp. 225–231.

Chaouat, Bruno et al. (2005). "A new partially integrated transport model for subgrid-scale stresses and dissipation rate for turbulent developing flows". In: *Physics of Fluids* 17.6, p. 065106.

Girimaji, Sharath S. (Nov. 2005). "Partially-Averaged Navier-Stokes Model for Turbulence: A Reynolds-Averaged Navier-Stokes to Direct Numerical Simulation Bridging Method". In: *Journal of Applied Mechanics* 73.3, pp. 413–421.

Menter, Florian et al. (2005). "A scale adaptive simulation model using two-equation models". In: *43rd AIAA aerospace sciences meeting and exhibit*, p. 1095.

Jarrin, Nicolas et al. (2006). "A synthetic-eddy-method for generating inflow conditions for large-eddy simulations". In: *International Journal of Heat and Fluid Flow* 27.4, pp. 585–593.

Keating, A. et al. (2006). "Interface conditions for hybrid RANS/LES calculations". In: *International Journal of Heat and Fluid Flow* 27.5. Special issue of the 6th International Symposium on Engineering Turbulence Modelling and Measurements – ETMM6, pp. 777–788.

Spalart, Philippe R et al. (2006). "A new version of detached-eddy simulation, resistant to ambiguous grid densities". In: *Theoretical and computational fluid dynamics* 20, pp. 181–195.

Shur, Mikhail L et al. (2008). "A hybrid RANS-LES approach with delayed-DES and wall-modelled LES capabilities". In: *International journal of heat and fluid flow* 29.6, pp. 1638–1649.

Breuer, Michael et al. (2009). "Flow over periodic hills–numerical and experimental study in a wide range of Reynolds numbers". In: *Computers & Fluids* 38.2, pp. 433–457.

Hamba, F. (2009). "Log-layer mismatch and commutation error in hybrid RANS/LES simulation of channel flow". In: *Int. J. Heat Fluid Fl.* 30.1, pp. 20–31.

Spalart, P.R. (2009). "Detached-eddy simulation". In: *Annu. Rev. Fluid Mech.* 41, pp. 181–202.

Fadai-Ghotbi, Atabak et al. (2010). "Temporal filtering: A consistent formalism for seamless hybrid RANS–LES modeling in inhomogeneous turbulence". In: *International Journal of Heat and Fluid Flow* 31.3, pp. 378–389.

Laraufie, Romain et al. (2011). "A dynamic forcing method for unsteady turbulent inflow conditions". In: *Journal of Computational Physics* 230.23, pp. 8647–8663.

Wallin, Stefan et al. (2011). "Commutation error mitigation in variable-resolution PANS closure: Proof of concept in decaying isotropic turbulence". In: *6th AIAA Theoretical Fluid Mechanics Conference*, p. 3105.

Chaouat, B. et al. (2013). "Partially integrated transport modeling method for turbulence simulation with variable filters". In: *Phys. Fluids* 25.

Shur, Michael L et al. (2014). "Synthetic turbulence generators for RANS-LES interfaces in zonal simulations of aerodynamic and aeroacoustic problems". In: *Flow, turbulence and combustion* 93.1, pp. 63–92.

De Laage de Meux, B et al. (2015). "Anisotropic linear forcing for synthetic turbulence generation in large eddy simulation and hybrid RANS/LES modeling". In: *Physics of Fluids* 27.3, p. 035115.

Davidson, L. (2016). "Zonal PANS: evaluation of different treatments of the RANS–LES interface". In: *Journal of Turbulence* 17.3, pp. 274–307.

Manceau, Rémi (2016). "Progress in hybrid temporal LES". In: *Symposium on Hybrid RANS-LES Methods*. Springer, pp. 9–25.

Chaouat, B. (2017a). "The State of the Art of Hybrid RANS/LES Modeling for the Simulation of Turbulent Flows". In: *Flow Turbul. Combust.* 99.2, pp. 279–327.

Chaouat, Bruno (2017b). "Commutation errors in PITM simulation". In: *International Journal of Heat and Fluid Flow* 67, pp. 138–154.

Mockett, Charles et al. (2018). "Go4Hybrid: Grey Area Mitigation for Hybrid RANS-LES Methods". In: *Notes on Numerical Fluid Mechanics and Multidisciplinary Design* 134.

Duffal, Vladimir (Nov. 2020). "Développement d'un modèle hybride RANS-LES pour l'étude des efforts instationnaires en paroi". PhD thesis.

Heinz, S. (2020). “A review of hybrid RANS-LES methods for turbulent flows: Concepts and applications”. In: *Prog. Aerosp. Sci.* 114, p. 100597.

Heinz, S. et al. (2020). “Theory-based Reynolds-averaged Navier-Stokes equations with large eddy simulation capability for separated turbulent flow simulations”. In: *Physics of Fluids* 32.6.

Janin, J. et al. (2021). “A new linear forcing method for isotropic turbulence with controlled integral length scale”. In: *Phys. Fluids* 33, p. 045127.

Duffal, Vladimir et al. (2022). “Development and Validation of a new formulation of Hybrid Temporal Large Eddy Simulation”. In: *Flow, Turbulence and Combustion* 108.1, pp. 1–42.

Haering, Sigfried W. et al. (2022). “Active model split hybrid RANS/LES”. In: *Phys. Rev. Fluids* 7 (1), p. 014603.

Hyde-Linaker, G. et al. (2022). “Patient-specific computational haemodynamics associated with the surgical creation of an arteriovenous fistula”. In: *Med. Eng. Phys.*, p. 103814.

Kempf, Daniel et al. (2022). “Zonal direct-hybrid aeroacoustic simulation of trailing edge noise using a high-order discontinuous Galerkin spectral element method”. In: *Acta Acustica* 6.

Mays, M.D. et al. (2023). “Capturing the drag crisis in the flow around a smooth cylinder using a hybrid RANS-LES model on coarse meshes”. In: *Int. J. Heat Fluid Fl.* 103, p. 109203.

APPENDIX C

Paper B:
Grey area Mitigation in Hybrid RANS/LES by means of Volume forcing

Grey area Mitigation in Hybrid RANS/LES by means of Volume forcing

Mahitosh Mehta[1] and Rémi Manceau[1]

[1]University of Pau & Pays Adour, E2S UPPA, CNRS, Inria, CAGIRE project-team, LMAP, Pau, France, mahitosh-ajaykumar.mehta@univ-pau.fr

Proceedings of THMT 2023 - 10th International Symposium on Turbulence, Heat and Mass Transfer, Sep 2023, Rome, Italy.

Abstract

The *modelled-stress depletion* is observed when the fluid flows from a RANS to a LES zone in hybrid modelling due to the dramatic decrease of the modelled stresses and the too slow increase of the resolved stresses. With the aim of developing a general remedy, independent of the type of flow, the present work develops an *active* approach, which consists in injecting energy in the resolved part to compensate for the loss of energy in the modelled part. Very encouraging results are obtained for channel and periodic hill flows.

Keywords— Turbulence modeling, Hybrid RANS/LES, HTLES, Channel flow, Periodic hills flow, Volume forcing

C.1 Introduction

Although RANS is the industrial standard due to its reasonable cost, it fails to provide accurate predictions in many situations, in particular in separated regions. LES often gives more reliable results, and also provides unsteady quantities, but at a much higher computational cost. This has driven many researchers to propose an intermediate form of modeling called hybrid RANS/LES models to capture the large-scale unsteady structures in the areas of interest using LES mode and treating other regions in RANS where LES is very costly or not required.

Any hybrid RANS/LES method operates on a general purpose of reducing the turbulent viscosity ν_t in the LES region by various means. In continuous hybrid RANS/LES, during the transition from RANS mode to LES mode, the turbulent energy goes from a complete modeling to a partial resolution. But the reduced modeled energy due to the change in resolution is not transferred to the resolved energy as expected, and the slow growth of the resolved energy relies solely on the instabilities that naturally develop in the flow, which generally leads to the *grey area* problem. As a result, the accuracy of LES is significantly degraded.

Decreasing the subgrid viscosity to zero in the initial region of a shear detached layer can avoid the delayed development of the instabilities. But this only works in the flows with the inflectional velocity profiles (Mockett et al., 2018). To address this *grey area* problem, otherwise known as *Modeled Stress Depletion* (MSD), a few methods have been developed that inject energy into the resolved motion. They are mainly divided in two categories: i) Injection of synthetic turbulent fluctuations - this method superimposes some

artificially generated velocity fluctuations onto the RANS velocity field at the RANS/LES interface (Jarrin et al., 2006; Shur et al., 2014), and ii) Volume forcing of the momentum equation - this method introduces a volumic source term in the governing equations of the flow, which is activated in the transition zone (Spille-Kohoff et al., 2001; Laraufie et al., 2011; De Laage de Meux et al., 2015). Due to the possibility of a gradual increase in the intensity of this source term, this method does not introduce spurious noise due to the sudden appearance of turbulence. This method also yields appreciable reduction in the adaptation region compared to the injection of synthetic turbulent fluctuations (Shur et al., 2014).

In the present work, a volume forcing method is proposed for continuous hybrid RANS/LES approaches. This method evaluates the energy transfer between the modeled and the resolved part of the energy spectrum, in order to inject the necessary energy into the resolved motion.

C.2 Hybrid Temporal LES

Although the active approach presented in this paper is applicable to any hybrid approach, here a short description of the hybrid approach used is presented. Fadai-Ghotbi et al. (Fadai-Ghotbi et al., 2010) showed a consistent formalism for a seamless hybrid RANS/LES model using temporal filtering. In filtered approaches, any flow variable ϕ can be decomposed into a filtered part $\widetilde{\phi}$, and a sub-filtered part ϕ'' such that:

$$\phi = \widetilde{\phi} + \phi'' \tag{C.1}$$

Using a general spatio-temporal filtering operator, the filtered part can be written as

$$\widetilde{\phi}(\mathbf{x}, t) = \int_{\mathcal{D}} \int_{-\infty}^{t} \mathcal{G}\left(\mathbf{x}, \mathbf{x}', t, t'\right) \phi\left(\mathbf{x}', t'\right) \mathrm{d}\mathbf{x}' \mathrm{d}t' \tag{C.2}$$

where $\mathcal{D}$ is the domain and $\mathcal{G}$ the filter kernel. This definition encompasses both the standard LES which is based on spatial filtering and TLES (temporal LES) based on temporal filtering, on which the HTLES is approach is constructed (Manceau, 2016). It is important to note that the model does not imply any explicit filtering, but Eq. (C.2) represents the fact that the analytical developements are based on a temporal filtering formalism.

The HTLES model (Duffal et al., 2022) is sensitized to the filter width via the time scale $T_m(r)$, which is in turn dependent on the resolution parameter r, the modeled-to-total energy ratio. Under the framework of an equilibrium Eulerian temporal energy spectrum, the energy ratio can be evaluated as:

$$r = \frac{1}{\beta_0} \left(\frac{U_s}{\sqrt{k}}\right)^{2/3} \left(\omega_c \frac{k}{\varepsilon}\right)^{-2/3} \tag{C.3}$$

where $U_s = U + \sqrt{2k/3}$ is the sweeping velocity, ω_c the cut-off frequency depending on the grid step Δ. The HTLES model with underlying $k-\omega$ SST RANS model is written as:

$$T_m(r) = \frac{r}{\psi(r)} \frac{k_m + c_r k_r}{C_\mu k_m \omega_m^*}, \quad \text{where} \quad \psi(r) = \frac{\beta_\omega}{C_\mu \gamma_\omega + r\left(\beta_\omega - C_\mu \gamma_\omega\right)} \tag{C.4}$$

$$\nu_{\text{sfs}} = \frac{a_1 k_{\text{sfs}}}{\max\left[a_1 \psi(r)\, \omega_{\text{sfs}}^*, F_2 \widetilde{S}\right]} \tag{C.5}$$

$$\begin{aligned}\frac{\mathrm{d}k_{\mathrm{sfs}}}{\mathrm{d}t} &= P_k + \frac{\partial}{\partial x_j}\left[\left(\nu + \frac{\nu_{\mathrm{sfs}}}{\sigma_k}\right)\frac{\partial k_{\mathrm{sfs}}}{\partial x_j}\right] - \frac{k_{\mathrm{sfs}}}{T_m(r)},\\ \frac{\mathrm{d}\omega^*_{\mathrm{sfs}}}{\mathrm{d}t} &= \gamma_\omega \frac{1}{\psi\left(r\right)}\widetilde{S}^2 + \frac{\partial}{\partial x_j}\left[\left(\nu + \frac{\nu_{\mathrm{sfs}}}{\sigma_\omega}\right)\frac{\partial \omega^*_{\mathrm{sfs}}}{\partial x_j}\right] - \beta_\omega {\omega^*_{\mathrm{sfs}}}^2\\ &\quad + (1-F_1)2\frac{1}{\sigma_{\omega 2}}\frac{1}{\psi\left(r\right)\omega^*_{\mathrm{sfs}}}\frac{\partial \omega^*_{\mathrm{sfs}}}{\partial x_j}\frac{\partial k_{\mathrm{sfs}}}{\partial x_j}\end{aligned} \tag{C.6}$$

where $\psi(r)$ is the hybridization function. The coefficients and the blending functions have the same values as $k-\omega$ SST RANS model (Menter, 1994). The coefficient c_r acts as a limiting function to distinguish RANS region and LES region, such that the resolved energy penetrating from LES region does not modify the predictions of the RANS model in the RANS region (*internal consistency constraint*). c_r is defined as:

$$\begin{cases} c_r = 0 \text{ if } r = 1,\\ c_r = f_s \text{ if } r < 1. \end{cases} \tag{C.7}$$

To avoid grid-induced seperation when the mesh is ambiguous near the wall, and to reduce the log-layer mismatch, a shielding function f_s is introduced in the model.

$$r = (1-f_s)\times 1 + f_s \times \min\left[1, r_K\right], \quad \text{where} \quad r_K = \frac{1}{\beta_0}\left(\frac{\pi}{\Delta}\frac{k^{3/2}}{\varepsilon}\right)^{2/3} \tag{C.8}$$

$$f_s = 1 - \tanh\left[\max\left[\xi_K^{p_1}, \xi_D^{p_2}\right]\right], \quad \text{with} \quad \xi_K = C_1\frac{\left(\nu^3/\varepsilon\right)^{1/4}}{d_w} \quad \text{and} \quad \xi_D = C_2\frac{\Delta_{\max}}{d_w} \tag{C.9}$$

where the function ξ_K forces the model to stay in RANS mode up to a certain distance independent of the mesh resolution, typically up to $y^+ \simeq 100$ with $C_1 = 45$ and $p_1 = 8$. The function depending on the resolution of the mesh ξ_D, prevents early transition of the model to the LES mode where the cells are too elongated, with $C_2 = 1.2$ and $p_2 = 6$. For details about the calibration of the HTLES model, refer to Duffal et al. (Duffal et al., 2022).

C.3 Active hybrid RANS/LES approach

In filtered approaches, changing the filter size (refining the mesh) generates commutation terms in the equations which represent the energy transfer from the modelled to the resolved part (Fadai-Ghotbi et al., 2010). A simpler way to look at this issue consists in noting that, in theory, the resolved energy k_r and the modelled energy k_m are dependent on the grid step Δ, while the total turbulent kinetic energy $k = k_r + k_m$ is not. Now, considering any variable ϕ dependent on t, $\mathbf{x}$ and Δ, we have

$$\frac{d\phi}{dt} = \frac{\partial\phi}{\partial t} + \nabla\phi\cdot U + \frac{\partial\phi}{\partial\Delta}\frac{d\Delta}{dt}, \tag{C.10}$$

which is nothing but the summation of the classical material derivative and the extra term due to the variation of the grid step. Since we want to have k independent of Δ, we must satisfy the following relation because the energy partition changes with the change in grid step.

$$\frac{\partial k_r}{\partial\Delta}\frac{d\Delta}{dt} = -\frac{\partial k_m}{\partial\Delta}\frac{d\Delta}{dt}. \tag{C.11}$$

This term represents the rate of energy transfer from the modeled to the resolved part, due to the mesh variations. This mechanism does not exist in the models and must be introduced. Upon deriving the sub-filter energy equations, Chaouat showed that different terms

appear due to the non-commutivity of the differential operators with the filter (Chaouat, 2017), and the extra term originating from the material derivative is the dominant term. This extra term appears due to the variation of the grid, irrespective of the underlying formalism.

De Laage de Meux *et al.* (De Laage de Meux et al., 2015) proposed the ALF approach to generate fluctuations in the resolved motion by introducing a body force in the momentum equation of the form

$$f_i = A_{ij}\widetilde{u_j} + B_i \ , \tag{C.12}$$

where $\widetilde{u_i}$ is the resolved (filtered) velocity. The mean force $\overline{f_i}$ which appears in the mean momentum equation, which must be zero, as one does not want to influence the mean velocity:

$$\overline{f_i} = A_{ij}\overline{\widetilde{u_j}} + B_i = 0. \tag{C.13}$$

Forming the equation of the resolved stresses from the momentum equation, it can be shown that the force produces resolved stresses at the rate

$$T_{ij}^f = A_{ik}\overline{u_j' u_k'} + A_{jk}\overline{u_i' u_k'} = -\frac{\partial \tau_{ij}^m}{\partial \Delta}\frac{\mathrm{d}\Delta}{\mathrm{d}t}, \tag{C.14}$$

where u_i' stands for the fluctuating part of the resolved velocity, τ_{ij}^m the Reynolds averaged sub-filter stress tensor and $\overline{\cdot}$ for the Reynolds average. Anisotropy is simply accounted for by assuming

$$\frac{\partial \tau_{ij}^m}{\partial \Delta} \simeq \mathcal{C}\frac{\tau_{ij}^m}{k_m}\frac{\partial k_m}{\partial \Delta}, \quad \text{with} \quad k_m = \frac{1}{2}\tau_{ij}^m = \frac{\Delta^{2/3}\varepsilon^{2/3}}{\beta_0 \pi^{2/3}}. \tag{C.15}$$

In each point, the force must satisfy two constraints: i) Eq. (C.11), i.e., injecting energy in the resolved motion at the same rate it is removed from the modelled motion; ii) not acting on the mean flow. It can be shown that it is thus entirely determined by

$$A_{ik}\overline{u_j' u_k'} + A_{jk}\overline{u_i' u_k'} = -\mathcal{C}\frac{2}{3}\tau_{ij}^m \frac{1}{\Delta}\frac{\mathrm{d}\Delta}{\mathrm{d}t} \quad \text{and} \quad B_i = -A_{ij}\overline{\widetilde{u_j}} \ . \tag{C.16}$$

This system of equations can be applied to any mesh-dependent hybrid RANS/LES approach. In the case of the HTLES model, the dependence of the solution on the grid step is disrupted in the near wall region due to the introduction of the shielding function. Therefore, it is more logical to consider the dependence on the energy ratio r. Considering relation (C.8) between the energy ratio r and the grid step Δ, one can write

$$\frac{1}{r}\frac{\mathrm{d}r}{\mathrm{d}t} = \frac{2}{3}\frac{1}{\Delta}\frac{\mathrm{d}\Delta}{\mathrm{d}t}, \tag{C.17}$$

and the system of equations to be solved becomes

$$A_{ik}\overline{u_j' u_k'} + A_{jk}\overline{u_i' u_k'} = -\mathcal{C}\tau_{ij}^m \frac{1}{r}\frac{\mathrm{d}r}{\mathrm{d}t} \quad \text{and} \quad B_i = -A_{ij}\overline{\widetilde{u_j}} \ . \tag{C.18}$$

Similarly, this can be extended to any other resolution parameter.

C.4 Applications

This active approach is applied to the channel and periodic hill cases using the HTLES model (Duffal et al., 2022) based on the underlying $k-\omega$-SST RANS model, using Code_Saturne (Archambeau et al., 2004). Note that this approach can be applied to any hybrid RANS/LES method. Periodic RANS solutions are used as inlet boundary conditions.

C.4.1 Channel Case

The flow is characterized by the friction Reynolds number, $Re_\tau = u_\tau h/\nu = 590$, where u_τ is the friction velocity and h is the half-height of the channel. The overall size of the computational domain is $L_x \times L_y \times L_z = 64h \times 2h \times 3.2h$, discretized using the mesh given by $N_x \times N_y \times N_z = 640 \times 96 \times 64$, satisfying $\Delta y^+ \simeq 1$ at the wall, which is sufficiently fine for HTLES (Duffal et al., 2022).

The initial part of the channel ($x/h \in [0, 6.4]$) is treated in RANS mode by imposing the energy ratio $r = 1$ in the model. The gradual transition from RANS-to-LES occurs in $x/h \in [6.4, 12.8]$, by enforcing a modified energy ratio r_{mod}:

$$r_{\text{mod}} = f + (1 - f)\, r \quad \text{with} \quad f\left(\frac{x}{h}\right) = \max\left(0; 2 - \frac{x}{6.4}\right) \tag{C.19}$$

and the rest of the channel is treated in LES mode. Since the Reynolds number is very low, the shielding function is deactivated for this case. Also, the periodic computations are used as the reference here to compare the results of the active approach.

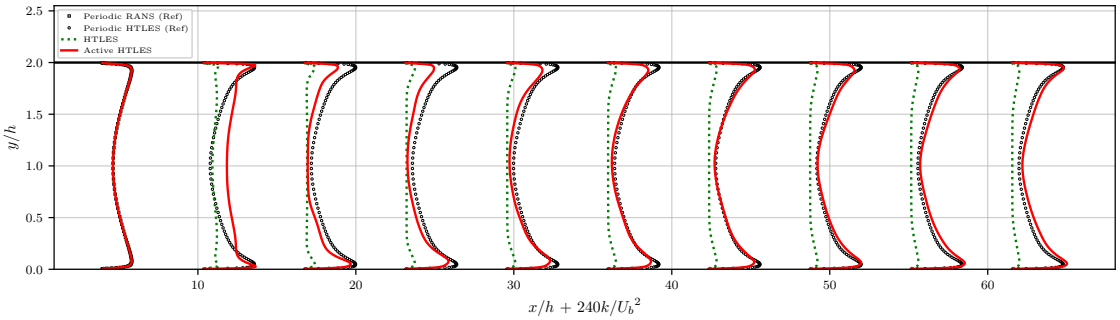

Figure C.1 – Profiles of total turbulent kinetic energy (resolved+modeled).

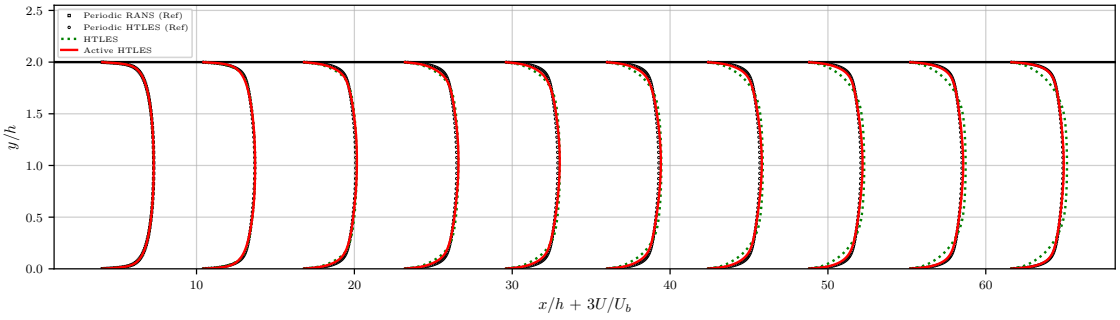

Figure C.2 – Profiles of averaged velocity.

Fig. C.1 shows that without forcing, the total turbulent energy is severely underestimated, all along the channel, since, as can be seen in Fig. C.4, virtually no resolved fluctuations are produced. This leads to a completely wrong velocity profile (Fig. C.2) and consequently, a much underestimated friction coefficient (Fig. C.3). On the other hand, when the forcing is applied, after a temporary overshoot of the turbulent energy, the flow exhibits rapid convergence towards the correct energy levels from $x/h = 15$. It is seen in Fig. C.4 that despite the lack of inflectional velocity profile, the active approach is able to rapidly generate resolved structures. Although not perfect, the friction coefficient is significantly improved. Note that the coefficient $\mathcal{C} = 1$ was used here. increasing this coefficient can accelerate the recovery to the correct value of C_f, at the price of an increased initial overshoot of both C_f and the total turbulent energy (not presented here).

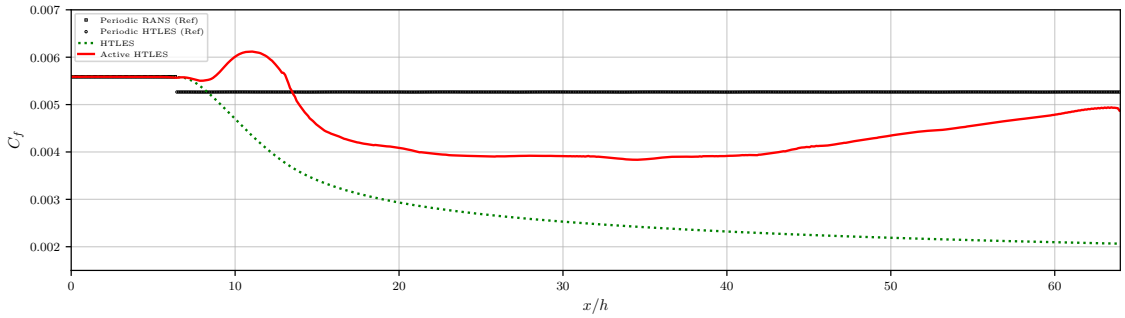

Figure C.3 – Friction coefficient.

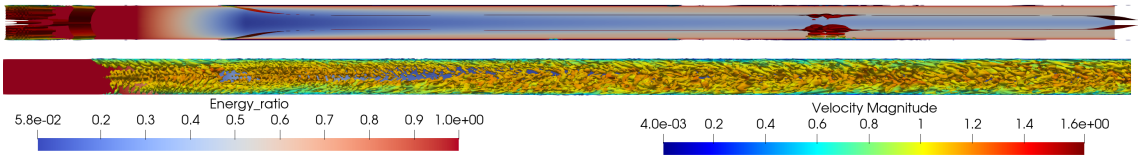

Figure C.4 – Isocontours $Q = 0.05U_b^2/h^2$ colored with the velocity magnitude, and, in the background, modelled-to-total turbulent energy ratio r, indicating the regions solved in RANS ($r = 1$) and in LES ($r < 1$). Top: HTLES without forcing. Bottom: Active HTLES.

C.4.2 Hill case

The active approach is now applied to a spatially developing channel with periodic constriction (so-called periodic hill case). As can be seen in Fig. C.7, the domain contains 6 hills. For convenience, this single computational domain is divided in 5 inter-hill subdomains for the post-processing. The size of each sub-domain is $9h \times 3.035h \times 4.5h$. The 5 sub-domains are treated as: 1-RANS; 2-RANS-to-LES transition; 3-LES; 4-LES-to-RANS transition and 5-RANS. First domain is kept in RANS mode by forcing the energy ratio $r = 1$, throughout the sub-domain. In sub-domain 2, the transitioning region starts at the top of the hill and is $2h$ long, as can be visualized in the background of Fig. C.7. In sub-domain 4, it ends at the top of the hill and is also $2h$ long. This transition is controlled through a modified energy ratio defined as:

$$r_{mod} = f + (1 - f)r \quad \text{with} \quad f\left(\frac{x}{h}\right) = \begin{cases} \max\left(0; 1 - \dfrac{x}{2}\right) \text{ if } \dfrac{x}{h} \in [0, 2] \\ \max\left(0; \dfrac{x - 25}{2}\right) \text{ if } \dfrac{x}{h} \in [25, 27] \end{cases} \tag{C.20}$$

Three different cases are studied: (i) Standard HTLES; (ii) Active HTLES with forcing activated only in the RANS-to-LES transition region ($x/h \in [0, 2]$); (iii) Active HTLES with forcing activated in both the RANS-to-LES ($x/h \in [0, 2]$) and the LES-to-RANS transition regions ($x/h \in [25, 27]$). The coefficient $\mathcal{C} = 1$ is applied. It is important to note that for all the cases the same mesh has been used, where each sub-domain is discretized such that $N_x \times N_y \times N_z = 80 \times 80 \times 40$, keeping $\Delta y^+ \simeq 1$. It is also important to mention that the shielding is activated in these cases, keeping the model in RANS mode up to $y^+ \simeq 100$.

Note that in sub-domains 1 and 5, profiles are compared with a periodic RANS solution, while in the other sub-domains the reference solution is the periodic HTLES. As the first sub-domain is forced to be in RANS mode ($r = 1$), all the different cases studied preserve the RANS solution almost perfectly, as the inlet boundary conditions correspond to the

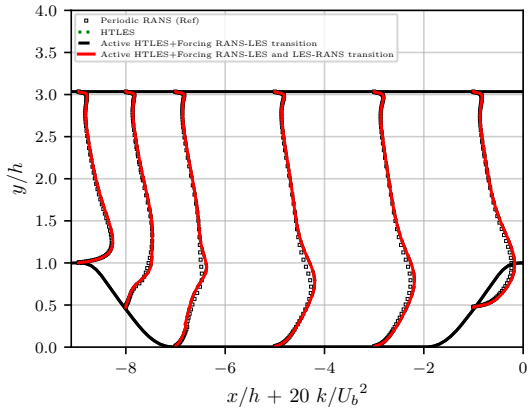

(a) sub-domain 1

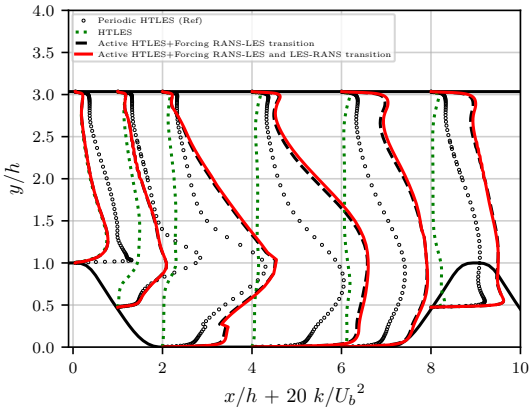

(b) sub-domain 2

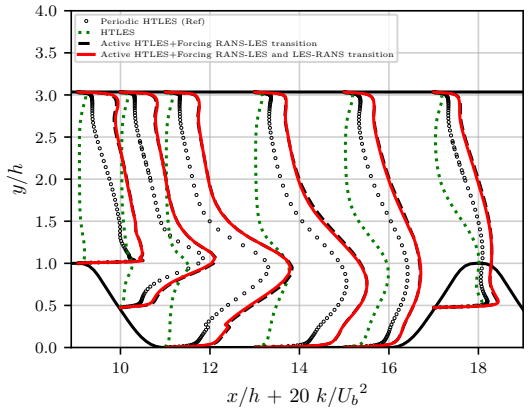

(c) sub-domain 3

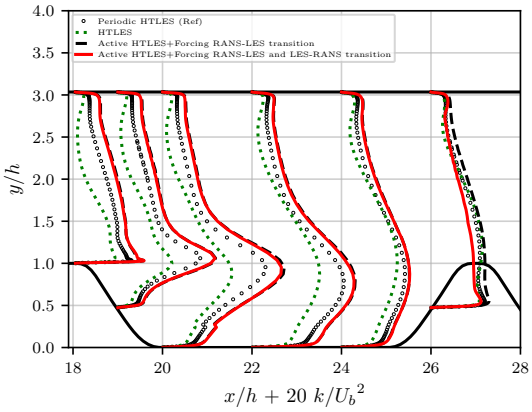

(d) sub-domain 4

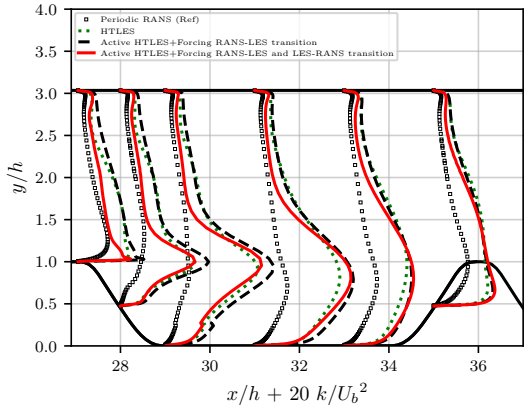

(e) sub-domain 5

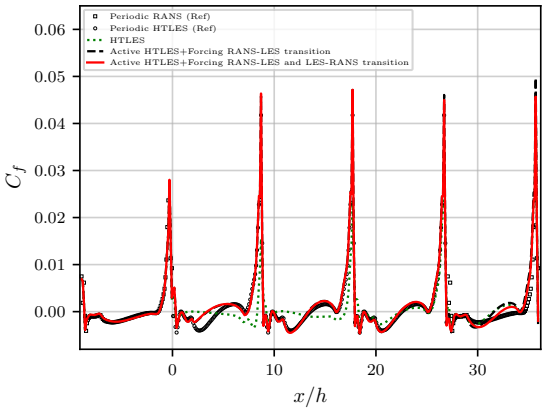

(f) Friction coefficient

Figure C.5 – (a) to (e): Profiles of turbulent kinetic energy (resolved+modeled) in the different subdomains; (f): Friction coefficient.

periodic RANS profiles. Fig. C.7 shows that the resolved structures take a long time to develop after the transition from RANS to LES, when the forcing is not applied, which is equally reflected in Figs. C.5(b), C.5(c), and C.5(d). It shows that the turbulent energy

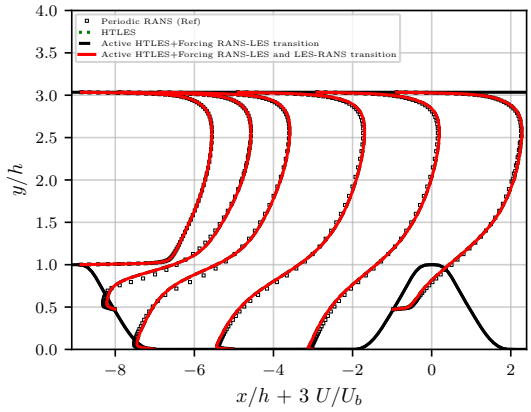

(a) sub-domain 1

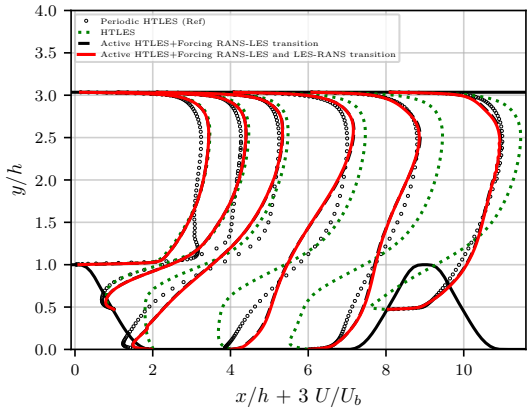

(b) sub-domain 2

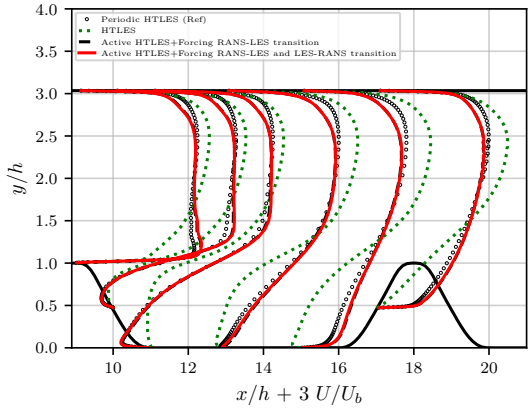

(c) sub-domain 3

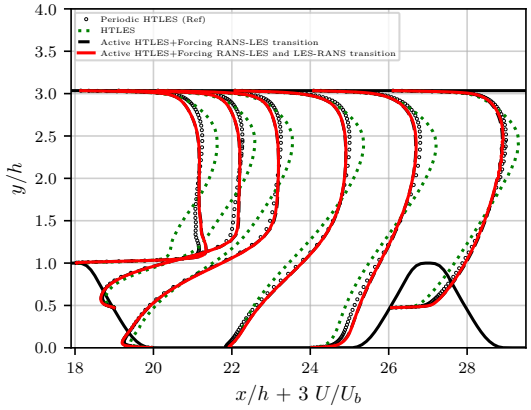

(d) sub-domain 4

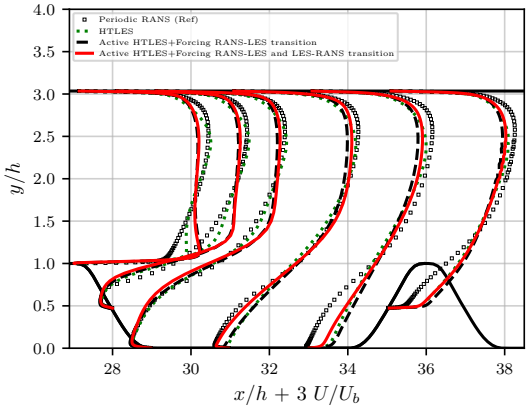

(e) sub-domain 5

Figure C.6 – Profiles of averaged velocity in the different subdomains.

remains too low until the fourth hill in the absence of forcing. Turbulent energy tends to the reference value at the end of the fourth sub-domain. In contrast, when the forcing is applied, the correct level of energy is obtained from the third hill onwards irrespective of the fact whether the forcing is activated in the LES to RANS transition or not. Fig. C.5

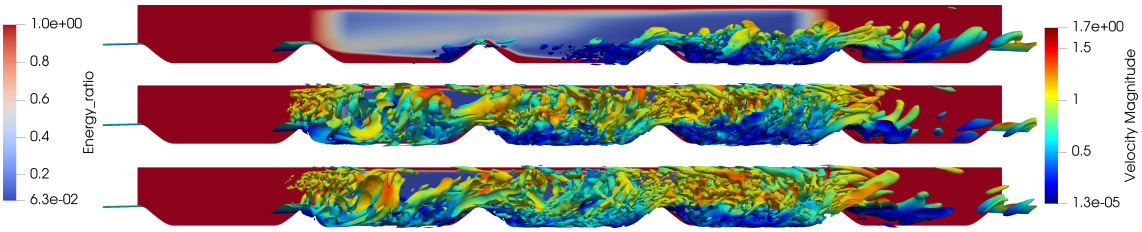

Figure C.7 – Isocontours $Q = 0.2U_b^2/h^2$. Top: No forcing. Middle: Forcing only in the RANS to LES transition region. Bottom: Forcing in both transition regions.

also suggests that introducing the forcing in the LES-to-RANS transition region helps in reducing the resolved energy (the rhs of Eq. (C.16) changes sign), but not sufficiently rapidly.

When the forcing is absent, the velocity magnitude in the recirculation region is under-estimated (Fig. C.6(b)), causing the flow to laminarize. The velocity is under-estimated in the lower half of the channel and over-estimated in the upper half of the channel. Profiles corresponding to the reference profiles are observed towards the end of the fourth sub-domain. In contrast to that, with the forcing applied, the profiles tend to the correct values as early as the second sub-domain.

Fig. C.5(f) shows the significant improvement of the friction coefficient induced by the rapid development of the resolved content. In the second-domain, the reproduction of the friction-coefficient is still not accurate because the LES mode has to generate the resolved structures in addition to correcting the mean field coming from the RANS region. However, from the end of the second sub-domain very satisfactory results are obtained. The influence of the value of coefficient $\mathcal{C}$ has been studied, but are not presented here. Increasing the value of the coefficient gives larger overshoot in the energy and velocity profiles initially, but not necessarily improve the overall results in the later part. Hence, it is preferable to maintain $\mathcal{C} = 1$.

C.5 Conclusion

In this work, an active hybrid RANS/LES method is presented, which injects energy into the resolved motion through a volume forcing when the solution transitions from RANS to LES. This method can be applied to any hybrid model. It only requires the introduction of a volume force into the resolved momentum equation, dependent on the material derivative of the grid step. This method promotes the rapid development of realistic resolved structures, mitigates the modelled-stress depletion issue and thus makes it possible to reach a fully developed LES solution more rapidly.

References

Menter, Florian R (1994). "Two-equation eddy-viscosity turbulence models for engineering applications". In: *AIAA journal* 32.8, pp. 1598–1605.

Spille-Kohoff, A et al. (2001). "Generation of turbulent inflow data with a prescribed shear-stress profile". In: *TECHNISCHE UNIV BERLIN (GERMANY) HERMANN-FOTTINGER INST FUR STROMUNGSMECHANIK*.

Archambeau, Frédéric et al. (Feb. 2004). "Code Saturne: A Finite Volume Code for the computation of turbulent incompressible flows - Industrial Applications". In: *International Journal on Finite Volumes* 1.1.

Jarrin, Nicolas et al. (2006). "A synthetic-eddy-method for generating inflow conditions for large-eddy simulations". In: *International Journal of Heat and Fluid Flow* 27.4, pp. 585–593.

Fadai-Ghotbi, Atabak et al. (2010). "Temporal filtering: A consistent formalism for seamless hybrid RANS–LES modeling in inhomogeneous turbulence". In: *International Journal of Heat and Fluid Flow* 31.3, pp. 378–389.

Laraufie, Romain et al. (2011). "A dynamic forcing method for unsteady turbulent inflow conditions". In: *Journal of Computational Physics* 230.23, pp. 8647–8663.

Shur, Michael L et al. (2014). "Synthetic turbulence generators for RANS-LES interfaces in zonal simulations of aerodynamic and aeroacoustic problems". In: *Flow, turbulence and combustion* 93.1, pp. 63–92.

De Laage de Meux, B et al. (2015). "Anisotropic linear forcing for synthetic turbulence generation in large eddy simulation and hybrid RANS/LES modeling". In: *Physics of Fluids* 27.3, p. 035115.

Manceau, Rémi (2016). "Progress in hybrid temporal LES". In: *Symposium on Hybrid RANS-LES Methods*. Springer, pp. 9–25.

Chaouat, Bruno (2017). "Commutation errors in PITM simulation". In: *International Journal of Heat and Fluid Flow* 67, pp. 138–154.

Mockett, Charles et al. (2018). "Go4Hybrid: Grey Area Mitigation for Hybrid RANS-LES Methods". In: *Notes on Numerical Fluid Mechanics and Multidisciplinary Design* 134.

Duffal, Vladimir et al. (2022). "Development and Validation of a new formulation of Hybrid Temporal Large Eddy Simulation". In: *Flow, Turbulence and Combustion* 108.1, pp. 1–42.

APPENDIX D

Paper C:
Towards self-adaptivity in hybrid RANS/LES based on physical criteria

Towards self-adaptivity in hybrid RANS/LES based on physical criteria

Martin David[1], Mahitosh Mehta[1] and Rémi Manceau[1]

[1]University of Pau & Pays Adour, E2S UPPA, CNRS, Inria, CAGIRE project-team, LMAP, Pau, France, martin.david@inria.fr

Proceedings of THMT 2023 - 10th International Symposium on Turbulence, Heat and Mass Transfer, Sep 2023, Rome, Italy.

Abstract

Hybrid RANS/LES methods can produce more reliable results than RANS with a reasonable computational cost. Thus, they have the potential to become the next workhorse in the industry. However, in continuous approaches, the location of the switching between the RANS and LES modes is based on the mesh and have a significant impact on the results. The present paper aims at developing a self-adaptive strategy based on physical criteria to mitigate the influence of the user's meshing choices on the results. The method is applied to the backward-facing step with the Hybrid Temporal LES (HTLES) model, but is applicable to any other hybrid approach. Starting from a RANS computation for initialization, successive HTLES are carried out and the mesh is refined according to the criteria. The results obtained show that the method converges and significantly improves the results when compared to RANS, with no intervention from the user. The comparison of the results with the DNS is very encouraging.

Keywords— Turbulence modeling, Hybrid RANS/LES, HTLES, Backward-facing step, self-adaptivity

D.1 Introduction

In industry, turbulent flows can be modeled either with RANS or LES. On the one hand, the RANS method makes it possible to investigate industrial cases thanks to its low computational cost, but it only produces steady results, which may not be sufficient for designing systems, and often lacks reliability. On the other hand, LES, by only modeling the smallest turbulence scales, provides more accurate results and gives access to unsteady information. However, its computational cost remains too high in most industrial simulations due to the complex geometry and the high Reynolds numbers encountered. Even if the computing means are expected to increase, LES should remain too expensive in many domains (Pope, 2004).

In many cases industry is wiling to resolve a larger range of the turbulence spectrum to get more information on the flow and handle strongly swirling flows, large-scale separation, acoustics issues, *etc.* For that reason, hybrid RANS/LES models are very promising because they reduce the computational cost of LES, give access to time-dependent information and provide more reliable results than RANS. In these approaches, modeled motions, associated with the RANS model and the LES model, and resolved motions, associated with the unsteady modes captured in the LES region, coexists. Hybrid RANS/LES

methods may be divided into two categories: zonal, or discontinuous, and non-zonal, or continuous, approaches. In the first case, two models are involved which are separated by an interface. The main challenge with these approaches is the connection between the two modes. In non-zonal, or continuous approaches, only one set of equations is used and the transition from RANS to LES relies on criteria updated during the computation. They are of growing interest because they are easier to use in industry than the zonal methods. Some of the most usual non-zonal hybrid RANS/LES models are the Detached Eddy Simulation (DES) (Spalart, 2000), the Partially integrated transport model (PITM) (Chaouat et al., 2005), the Partially averaged Navier-Stokes (PANS) method (Girimaji, 2005), and the scale adaptive simulation (SAS) (Menter et al., 2010). The reader is referred to Chaouat (Chaouat, 2017) or (Heinz et al., 2020) for recent reviews of hybrid RANS/LES methods.

In the continuous approaches, the critical point is the control of the switching between RANS and LES (Heinz et al., 2020). Indeed, it is determined by the grid size, which is controlled by the user, and has a major impact on the results. To ensure the reliability of CFD for the design, dimensioning and also certification of industrial systems, it is important to mitigate the influence of the user (Park et al., 2016). To this end, a self-adaptive strategy is proposed. The regions requiring LES mode are identified using a physical criteria: among the many non-dimensional quantities that can be evaluated from a RANS calculation, we have identified, in the case of the backward-facing step studied here, that the most relevant criterion is the production-to-dissipation ratio, which makes it possible to separate the zones close to equilibrium where a RANS model is sufficient, and the out-of-equilibrium zones where it is preferable to switch to LES mode to improve the quality of the results. Other criteria can be added without difficulty in the future to take into account the specific features of various configurations. The mesh is then refined in the zone identified by this criterion, so as to switch locally to LES, and the simulation is continued in hybrid RANS/LES. Based on the average solution of this calculation, the criterion is updated and the mesh is adapted accordingly. This iterative approach stops when the size of the LES zone reaches convergence. The strategy is applied to the backward-facing step case (Lamballais, 2014) with the HTLES (Duffal et al., 2022) method, in its active version (Mehta et al., 2023). In contrast to other self-adapting approaches of the literature, which aim at modifying the models based on physical criteria (Perot et al., 2009; Menter et al., 2010; Baglietto et al., 2017; Krumbein et al., 2020) the present approach only relies on remeshing to adapt the RANS and LES zones, an approach similar to the one proposed by (Limare et al., 2020).

The paper is organized as follows: after describing the self-adaptive strategy in section D.2, the hybrid RANS/LES model is presented in section D.3. In section D.4, the backward-facing step case study is depicted. The results are discussed in section D.5.

D.2 Self-adaptive strategy

The goal of the proposed strategy is to switch to LES mode in regions where it appears necessary, according to certain physical criteria. Although various criteria can be considered, in this paper, the criterion chosen is simply the equilibrium of turbulence evaluated by the production-to-dissipation ratio. In a computation, initially in full RANS mode, regions where to switch to LES are identified via a threshold

$$\frac{P}{\varepsilon} > \alpha. \tag{D.1}$$

Assuming a Kolmogorov spectrum, the energy partition between the modeled turbulent energy, k_m, and the resolved turbulent energy, k_r, is defined by

$$r = \frac{k_\mathrm{m}}{k} = \frac{1}{k}\int_{\kappa_c}^{\infty} E(\kappa)\mathrm{d}\kappa = \frac{3C_\kappa}{2}\left(\kappa_c \frac{k^{3/2}}{\varepsilon}\right)^{-2/3}, \tag{D.2}$$

with $\kappa_c = \pi/\Delta$ the cutoff wavenumber and $k = k_m + k_r$. The cell size to reach the desired energy ratio r is computed using Eq. (D.2):

$$\Delta = \left(\frac{2}{3}\frac{r\,k}{C_K}\right)^{3/2}\frac{\pi}{\varepsilon}. \tag{D.3}$$

A new mesh satisfying this constraint is generated and the simulation is continued in hybrid RANS/LES. The criteria (D.1) and (D.3) can then be updated from the hybrid RANS/LES results and a new mesh is generated, until convergence towards a final mesh. The process is summarized in Fig. D.1.

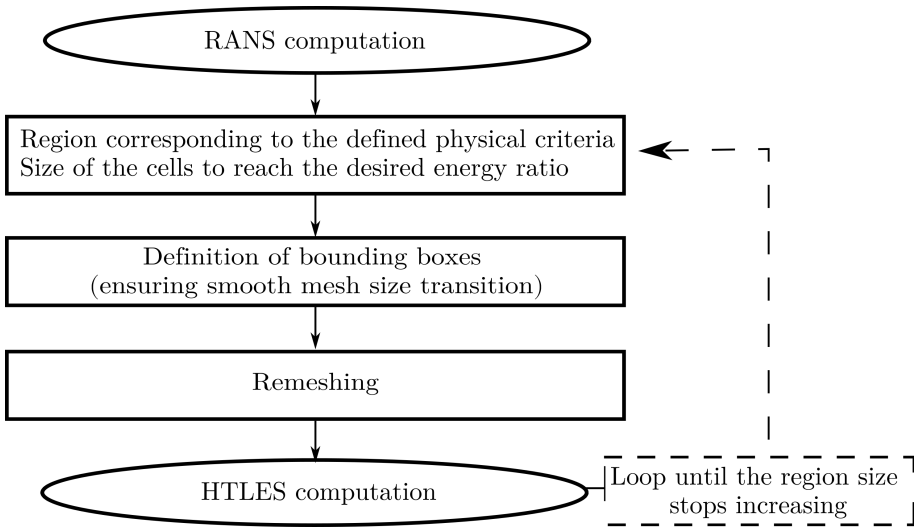

Figure D.1 – Algorithm used for the self-adaptive strategy.

D.3 Turbulence modeling

D.3.1 Hybrid Temporal LES

Although the self-adaptive methodology can be associated to any continuous hybrid RANS/LES approach, HTLES-$k-\omega$-SST (Duffal et al., 2022) is used in the present study. Derived from the PITM model (Chaouat et al., 2005; Fadai-Ghotbi et al., 2010), the HTLES is a continuous hybrid approach in which the hybridization term in the energy equation is based on a time scale driven by the partition of modeled energy. The solved equations are the following:

$$\begin{cases} \nu_\mathrm{sfs} = \dfrac{a_1 k_\mathrm{sfs}}{\max\left[a_1\psi(r)\omega^*_\mathrm{sfs}, F_2\widetilde{S}\right]}, \\ \dfrac{\partial k_\mathrm{sfs}}{\partial t} + \widetilde{U}_k\dfrac{\partial k_\mathrm{sfs}}{\partial x_k} = P_\mathrm{sfs} + D_{k\mathrm{sfs}} - \dfrac{k_\mathrm{sfs}}{T_\mathrm{m}}, \\ \dfrac{\partial \omega^*_\mathrm{sfs}}{\partial t} + \widetilde{U}_k\dfrac{\partial \omega^*_\mathrm{sfs}}{\partial x_k} = \gamma_\omega\dfrac{\omega^*_\mathrm{sfs}}{k_\mathrm{sfs}} + D^*_{\omega\mathrm{sfs}} - \beta_\omega {\omega^*_\mathrm{sfs}}^2 + C^*_{\omega\mathrm{sfs}}. \end{cases} \tag{D.4}$$

with F_2 the blending function and $a_1 = 0.31$ the usual coefficient of the k–ω SST model, P_{sfs} the production term, D_{ksfs} the dissipation term for k, $D_{\omega\text{sfs}}$ the dissipation term for ω, $C^*_{\omega\text{sfs}}$ the cross-diffusion term, $\beta_\omega = C_\mu(C_{\epsilon 2} - 1)$, $\gamma_\omega = C_{\epsilon 1} - 1$, $C_{\epsilon 1}$ and $C_{\epsilon 2}$ the usual coefficients of the RANS model. $\psi(r)$ is the hybridization function,

$$\psi(r) = \frac{\beta_\omega}{C_\mu \gamma_\omega + r(\beta_\omega - C_\mu \gamma_\omega)}, \tag{D.5}$$

with $r = (1 - f_s) + f_s \times \min[1, r_K]$, $f_s = 1 - \tanh\left[\max\left(\xi_K^{p1}, \xi_D^{p2}\right)\right]$, $\xi_K = C_1 \left(\nu^3/\varepsilon\right)^{1/4}/d_w$ and $\xi_D = C_2 \Delta_{\max}/d_w$ where d_w is the distance to the wall and $\Delta_{\max} = \max[\Delta_x, \Delta_y, \Delta_z]$. T_{m} is the turbulent time scale that drives the transition from the RANS mode to the LES mode

$$T_{\text{m}} = \frac{r}{\psi(r)} \frac{k_{\text{m}} + c_r k_r}{C_\mu k_{\text{m}} \omega^*_{\text{m}}}, \text{ where } c_r = \begin{cases} 0 \text{ if } r = 1, \\ f_s\left(\xi_K^{p1}, \xi_D^{p2}\right) \text{ if } r < 1. \end{cases} \tag{D.6}$$

This expression recovers the exact RANS formulation when $r = 1$. The energy ratio is computed as follows:

$$r = \frac{1}{\beta_0} \left(\frac{U_s}{\sqrt{k}}\right)^{2/3} \left(\omega_c \frac{k}{\psi(r)\varepsilon^*_{\text{sfs}}}\right)^{-2/3} \tag{D.7}$$

where $\omega_c = \min\left[\frac{\pi}{\mathrm{d}t}, \frac{U_s \pi}{\Delta}\right]$ is the cutoff frequency, $\Delta = \Omega^{1/3}$ with Ω the cell volume, and $U_s = U + \gamma\sqrt{k}$ is the sweeping velocity. The dissipation term is estimated as

$$\epsilon = \epsilon_m = C_\mu k_{\text{m}} \psi(r) \omega^*_{\text{m}} \tag{D.8}$$

The constants used are summarized in Tab. D.1 and more details can be found in (Duffal et al., 2022).

Table D.1 – Coefficients of the HTLES-$k-\omega$-SST model.

β_0	γ	C_1	C_2	p_1	p_2
0.48	2/3	13.5	1.2	8	6

D.3.2 Volume forcing

In continuous hybrid RANS/LES, during the transition from RANS mode to LES mode, the partition of the modeled turbulent energy decreases. However, the growth of the resolved energy is slow, leading to a strong local underestimation of the total turbulent energy. To mitigate this grey area issue, a volume forcing is added to enrich resolved turbulence at the RANS-to-LES transition (so-called *Active* HTLES) (Mehta et al., 2023). This is achieved by adding a body force $f_i = A_{ij}\widetilde{u}_i + B_i$, in the momentum equation where $\widetilde{u}_i$ is the resolved velocity. A_{ij} and B_i have to satisfy two constraints: (1) energy injection in the resolved scales is imposed by the rate of energy removal in the modeled scales; (2) the forcing should have no effect on the mean flow. They are computed for each point of the domain and it can be shown that they are determined by using the Reynolds average of the sub-filter stress tensor:

$$\begin{cases} A_{ik}\overline{u'_j u'_k} + A_{jk}\overline{u'_i u'_k} = -\tau^{\text{m}}_{ij} \frac{1}{r} \frac{\mathrm{d}r}{\mathrm{d}t}, \\ B_i = -A_{ij}\overline{\widetilde{u}_j}, \end{cases} \tag{D.9}$$

where u'_i is the fluctuating part of the resolved velocity and $\overline{\cdot}$ stands for the Reynolds average.

D.3.3 Numerical setup

The computations are carried out using code_saturne, a general CFD solver developed by EDF (Archambeau et al., 2004). It is based on a finite-volume method and uses a fully collocated arrangement for all the variables. A standard predictor-corrector scheme (SIMPLEC) computes the velocity-pressure system. The Crank-Nicholson time scheme and a spatial second-order (upwind in the RANS zone, centered in the LES zone) scheme are used for the discretization of velocity. For additional details on the numerical setup, the reader is referred to Duffal et al. (2022). In the next sections, the statistical quantities are evaluated using both a temporal averaging and a spatial averaging in the periodic direction (z).

D.4 Application to the backward-facing step

D.4.1 Geometry and physical configuration

The case studied reproduces the geometry and the physical setup of the DNS without rotation of Lamballais (2014). In the backward facing-step case the flow is subjected to a sudden increase of cross-sectional area, resulting in a separation at the point of expansion. This is a representative model for separation flows, which are usually encountered in external aerodynamics, engine flows, condensers, heat transfer systems, flow around buildings, *etc.* In the case studied, the streamwise direction is x. The half-height of the channel (y direction) is $h = 2H/3$ upstream of the step, where H is the half-height downstream. The length of the upstream part, respectively downstream part, is $4H$, respectively $16H$. The transverse direction (z) is H and is periodic. The upper boundary is treated with a symmetric boundary condition. A periodic RANS channel flow computation is used as the inlet boundary condition, after a grid convergence study. Regarding the physical setup, the bulk Reynolds number, $Re = U_H H/\nu$, is 5000.

D.4.2 Description of the algorithm

The algorithm shown in Fig. D.1 is initialized by a RANS computation performed on a fully structured grid composed of 95800 cells. The region where switching to LES mode is desirable and the cell size to reach the desired energy ratio r are respectively obtained from Eqs. (D.1) and (D.3), using here $\alpha = 1.4$ and $r = 0.15$, using the RANS results to evaluate P, ε and k. Then, successive HTLES are performed following the algorithm and the mesh and bounding boxes are adapted accordingly until convergence is reached. Note that the total production and dissipation are computed from $P = -\left(c_r \overline{u_i' u_j'} + \tau_{ij}^{\mathrm{m}}\right) S_{ij}$ where τ_{ij}^{m} is the Reynolds averaged sub-filter stress tensor, and S_{ij} is the strain rate tensor; and $\varepsilon = \varepsilon_{\mathrm{m}}/r_\varepsilon$ with $r_\varepsilon = 1 - \left(1 + 0.42 r_{\mathrm{eff}} R_t^{1/2}/\pi\right)^2$ the estimated modeled-to-total dissipation ratio, where R_t is the turbulent Reynolds number. In the RANS mode, fluctuations are null and $r_\varepsilon = 1$.

Bounding boxes are defined around the region satisfying the physical criterion given in Eq. (D.1) to adapt the mesh. Zones A, B, and C correspond to the RANS, transition, and LES zones, respectively. They are obtained using the following rules:

- Zone C (LES zone) is a rectangle which bounds are defined by the extrema of the $P/\varepsilon > \alpha$ region. The mesh is composed of unstructured cells in this zone according to Eq. (D.3).

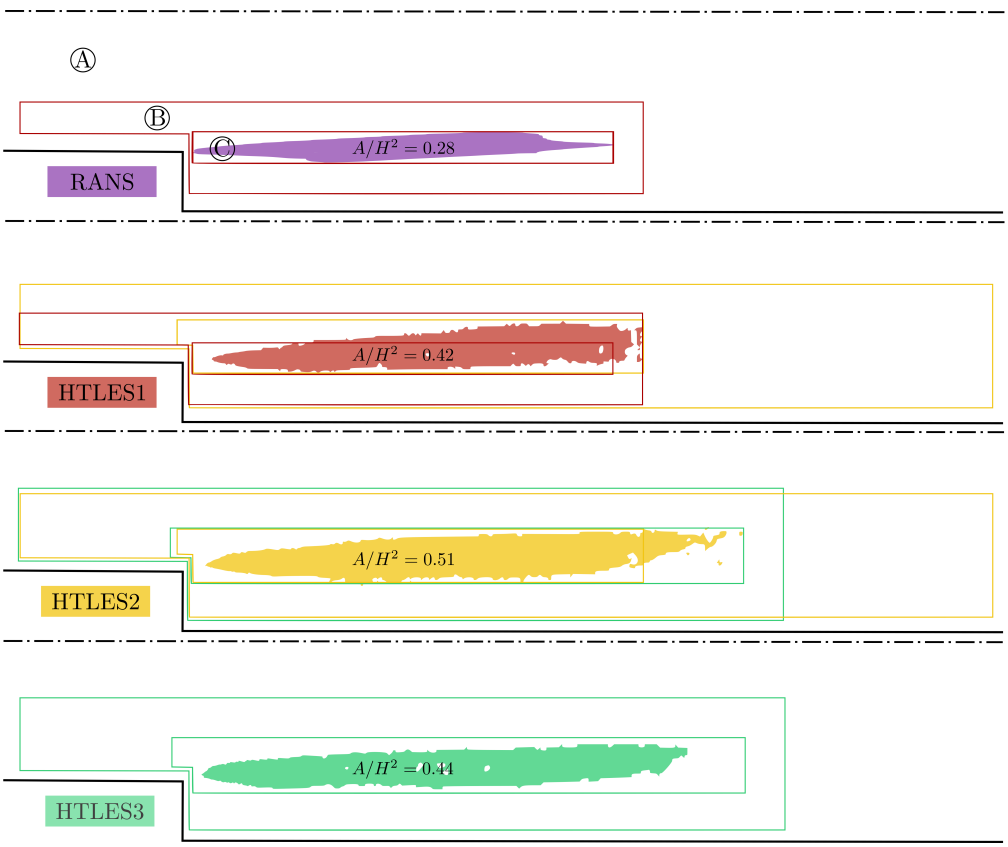

Figure D.2 – Visualization of the mesh zones and $P/\epsilon > \alpha$ regions for the successive computations. Zones A, B, and C correspond to the RANS, transition, and LES zones, respectively.

- Zone B (transition zone) is used to link zone A and zone C. It is characterized by a rectangular shape bounding zone C with a thickness that is equal to $\delta = 0.5 \langle l_I \rangle_{P/\varepsilon>\alpha}$ where $\langle l_I \rangle_{P/\varepsilon>\alpha}$ is the mean of the integral length scale in the zone satisfying Eq. (D.1). If at the end of a simulation $P/\varepsilon > \alpha$ zone extends until zone B bounds, the thickness of zone B is multiplied by ten in this direction for the mesh of the next iteration to mitigate the total number of iterations to reach the convergence of the method. Note that, upstream, the beginning of zone B is fixed with a length of $5\delta_{RANS}$ where δ_{RANS} is the thickness obtained with the RANS computation since the length necessary to develop turbulent structures is not supposed to change. The targeted cell size is equal to the maximum cell size obtained in zone C.
- Zone A (RANS zone) is defined by the rest of the domain. The energy ratio is imposed to unity and the mesh is kept unchanged.

Notice that the grids in zones B and C are also refined in the z-direction with the aim of obtaining cells in the refined region that are as isotropic as possible. A shielding function is applied until $y^+ = 20$ to insure RANS mode in the near wall region and the mesh remains structured. After the first HTLES, which is considered as a first basis since it is relying on the RANS computation,

- zone C is extended upstream with a length equal to δ,
- the targeted energy ratio is lowered from $r = 0.15$ to $r = 0.10$,
- a smoothing of the mesh is applied in zone B to increase the reliability of the results.

D.4.3 Grids obtained for the different simulations

The various bounding boxes and the $P/\varepsilon > \alpha$ regions obtained for the successive computations are displayed in Fig. D.2. The $P/\varepsilon > \alpha$ zone obtained for the ith computation is used to define the bounding boxes of the i+1th computation. In Fig. D.2, the mesh zones and $P/\varepsilon > \alpha$ regions are displayed. From HTLES1 to HTLES3, the bounding boxes used for the ith computation and the ones resulting from this computation are superimposed to highlight their evolution. Zone B of the HTLES2 is much larger than the others because the $P/\varepsilon > \alpha$ zone of HTLES1 is in contact with the right border of the transition zone obtained after the RANS computation (in red color), and in this case the algorithm decides to quickly expand the area. The algorithm is stopped when zone C does not extend anymore, which occurs between HTLES2 and HTLES3. A fourth and last HTLES is run, thus using the same zones but a cell sizes computed from HTLES3, to confirm the convergence of the results.

In this study, the GMSH software (Geuzaine et al., 2009) is used to generate the grids. The unstructured zones are meshed with the Packing of Parallelograms algorithm. The mesh obtained for the successive HTLES are displayed in Fig. D.3. The smallest cells are located around $x/H = 0.15$ and $y/H = 1/3$. The cell number and the averaged value of Δ, the cell size to reach the targeted energy ratio, in the region where criterion D.1 is satisfied and the area of zone C for the various computations are shown in Fig. D.4. After a monotonic increase, the value $\langle\Delta\rangle_{P/\varepsilon>\alpha}$ obtained with the HTLES3 is reduced when compared to HTLES2, and remains virtually constant between HTLES3 and HTLES4 computations. The same behavior is observed for the total number of cells between HTLES4 and HTLES5, which highlights the convergence of the algorithm.

D.5 Results and discussion

The results of the HTLES4 computation are not shown since they are virtually superimposed with those of the HTLES3. In Fig. D.5, the target energy ratio (i.e., used in the model), the effective energy ratio (i.e., computed during the simulation as $r_{\text{eff}} = k_{\text{m}}/(k_m + k_r)$), the streamwise velocity, and the turbulent kinetic energy profiles are displayed. In Fig. D.5a and D.5d, the DNS energy ratio and effective energy ratio are null since all scales are resolved. Similarly, in RANS $r = 1$ and $r_{\text{eff}} = 1$ since all scales are modeled. The HTLES energy ratio profiles makes it possible to visualize the interface between RANS and LES regions. The LES region is significantly increased from HTLES1 to HTLES2, then it stabilizes, which highlights the convergence of the self-adaptive method.

Regarding the streamwise velocity (Fig. D.5b), upstream $x/H = -1$, the RANS mode is imposed and the HTLES indeed preserves the RANS solution, as the inlet boundary conditions corresponds to the RANS solution in a periodic channel. The mesh refinement from $r = 0.15$ to $r = 0.1$ in the LES region and the definition of the zones has little influence on the streamwise velocity and turbulent kinetic energy (Fig. D.5c) profiles, which highlights the robustness of the method. The expansion of the LES zone in the recovery region (HTLES2 and HTLES3) improves the turbulent kinetic energy profiles at $x/H = 3$ and, for HTLES2, which presents the longest LES zone, until $x/H = 4$. The spikes of turbulent kinetic energy, principally observed at $x/H = 0$, are due the rapid RANS-to-LES transition in the vertical direction and to the forcing term that is function of the variation of the energy ratio. The overshoot of turbulent kinetic energy observed near the step in HTLES rapidly fades out. Comparing RANS with the HTLES3 computation, it appears that RANS significantly underestimates the amount of turbulent kinetic energy from $x/H = 0$ to $x/H = 2$, while the HTLES3 results show that the total turbulent energy

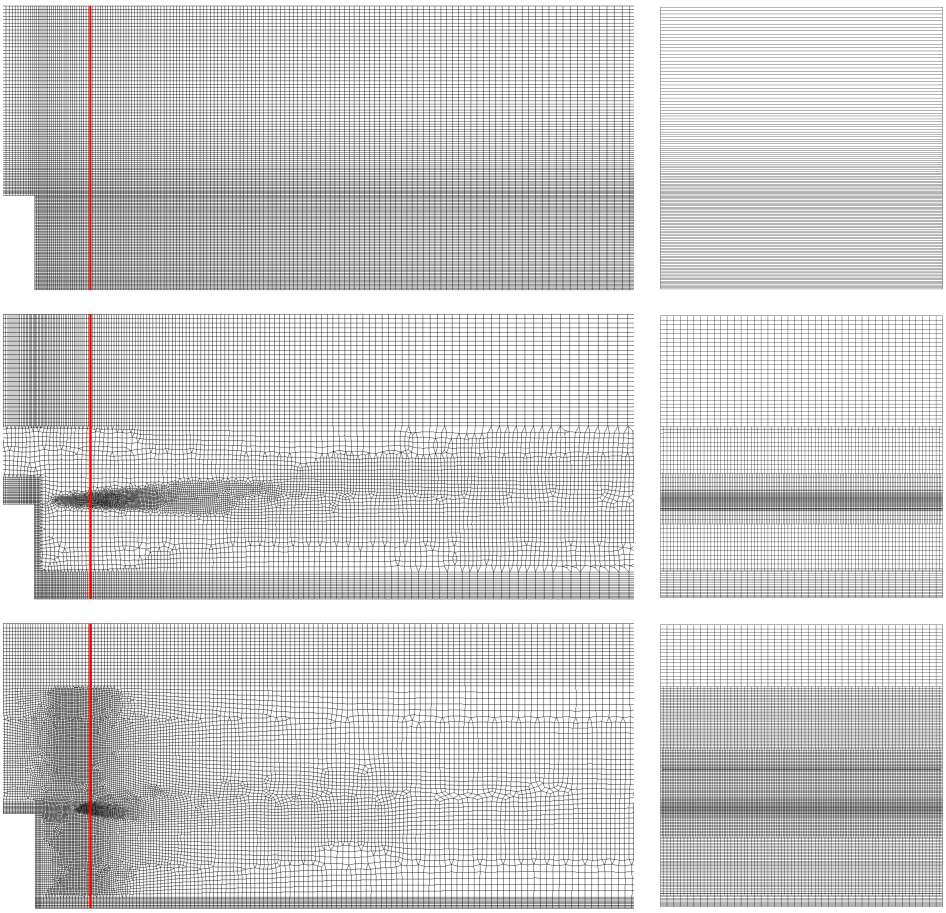

Figure D.3 – Views of the grids. From top to bottom: RANS, HTLES1, and HTLES3. On the left side, the XZ plane is presented. The red line corresponds to $x/H = 0.2$. On the right side, the YZ plane corresponding to this location is displayed.

is well estimated. A good agreement with DNS is found between $x/H = 1$ and $x/H = 3$, which explains the accuracy of the streamwise velocity profiles between $x/H = 2$ and $x/H = 4$. Downstream $x/H = 4$, the HTLES streamwise velocity profiles are slightly improved when compared to the RANS profiles.

The effective energy ratio profiles (Fig. D.5d) globally follow those of the energy ratio even if some discrepancies appear, which shows that the partition of energy indeed reaches the expected level. The results show that downstream the LES region, some resolved scales remain. Close to the wall, the meaning of the effective energy ratio is ambiguous since both k_m and k_r go to zero. The spikes in the profiles are due to the sharp variations of the total turbulent kinetic energy.

The skin friction distribution on the lower wall, shown in Fig. D.6, highlights the benefits associated with the self-adaptive method. Indeed, the HTLES3 profile leads to a relatively good prediction of the skin friction negative peak, and gives very good estimate of the reattachment location. HTLES gives remarkably better results than RANS in the recirculation zone and downstream of it. Moreover, the positive peak of C_f observed in DNS at $x/H \approx 0.1$, associated with the secondary counterclockwise recirculation zone, is well reproduced by the HTLES while it is not predicted by RANS. Far in the recovery region, HTLES3 tends toward RANS profiles since the RANS mode is reactivated.

Mean streamlines computed using the line integral convolution (LIC) are displayed in Fig. D.7. The two classically observed recirculation zones (Chen et al., 2018) are clearly

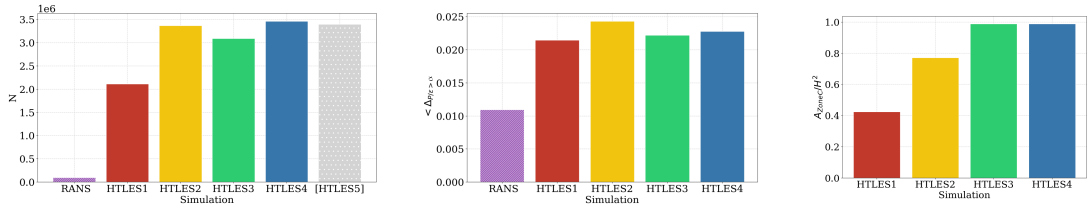

Figure D.4 – From left to right: number of cells, averaged value of Δ in the region where $P/\varepsilon > \alpha$, and area of Zone C. Note that HTLES5 has not been run but the mesh is displayed to highlight the convergence of the algorithm.

visible. The main recirculation zone (clockwise) extends up to $x/H = 2.1$ and the secondary recirculation zone (counterclockwise) to $x/H = 0.4$, to be compared to the DNS values, $x/H = 2.13$ and $x/H = 0.63$, respectively.

The Q-Isosurfaces presented in Fig. D.8 show that the active HTLES rapidly develops resolved scales, by means of the volume forcing. Indeed, turbulent structures are remarkably observed right from the beginning of the LES region. However, downstream of the LES region, the structures are advected into the RANS zone and are only gradually dissipated by the RANS eddy-viscosity. As can be seen on Fig. D.6, the solution transitions in this region from a LES to a RANS behavior.

D.6 Conclusions and perspectives

In this paper, a self-adaptive strategy is proposed to mitigate the influence of the user on the results of hybrid RANS/LES computations. In order to avoid the definition of the RANS and LES zones by the user choices at the time of the construction of the mesh, the zones where to switch to LES are determined by physical criteria (here, out-of-equilibrium regions identified by the ratio P/ε) and the mesh is refined in this zone.

The method is assessed on a backward-facing step with the HTLES-$k-\omega$-SST model. Starting from a RANS computation for initialization, successive HTLES are carried out using the results of the previous computation to generate the mesh of the next simulation. The outcomes of the study show that the self-adaptive strategy converges in four iterations. The results are physically consistent. They are significantly improved when compared to the RANS computation and in good agreement with the reference DNS results.

Future prospects concern the application of the self-adaptive method to other test cases, possibly with the application of other physical criteria, with the aim to develop a robust methodology useful for a wide range of applications.

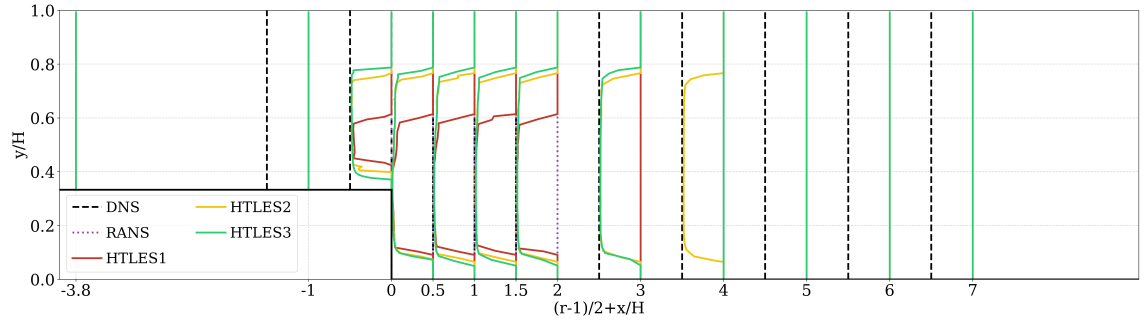

(a) Energy ratio

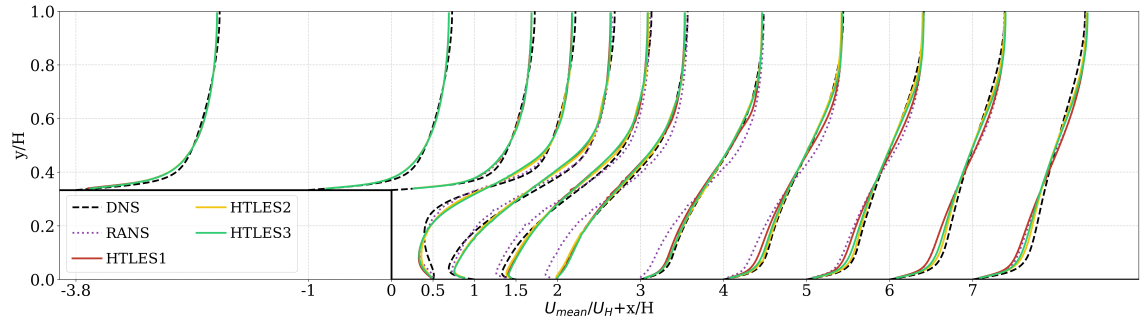

(b) Streamwise velocity

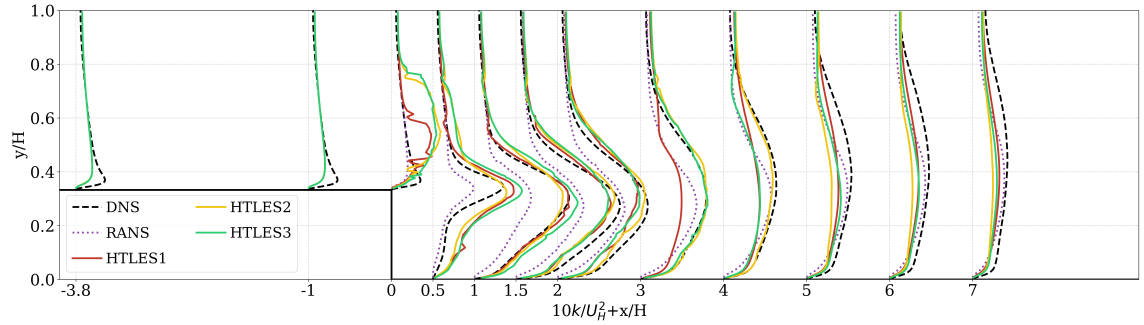

(c) Total turbulent kinetic energy

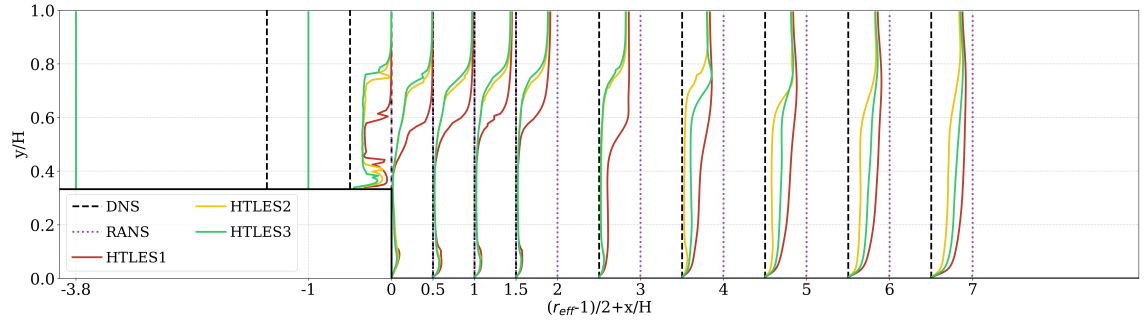

(d) Effective energy ratio

Figure D.5 – Profiles in the y direction for 12 streamwise locations. DNS results are from Lamballais (2014).

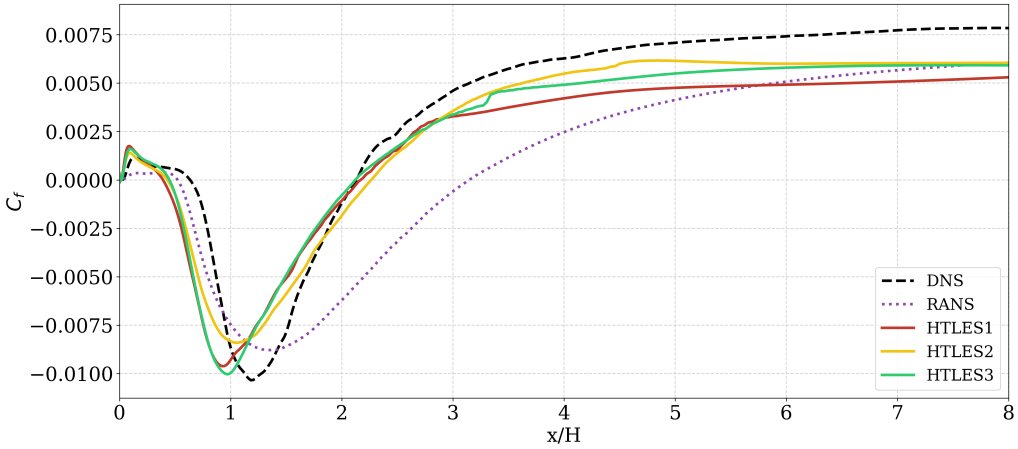

Figure D.6 – Distribution of skin friction on the wall downstream of the step. DNS results are from Lamballais (2014).

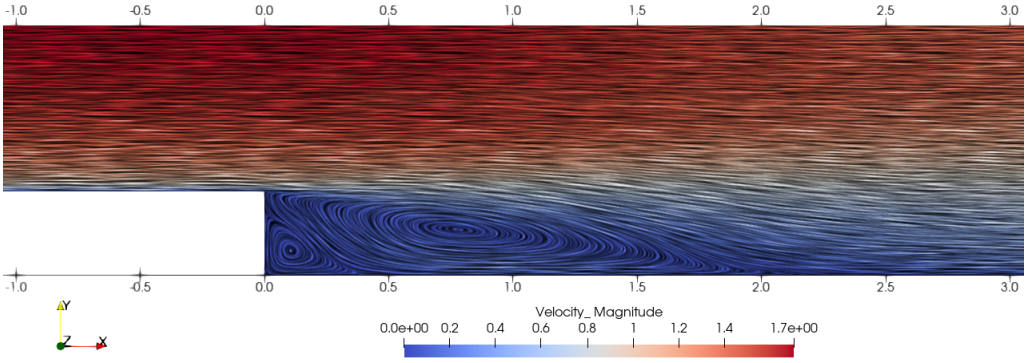

Figure D.7 – Mean streamlines of the HTLES3 colored with velocity magnitude.

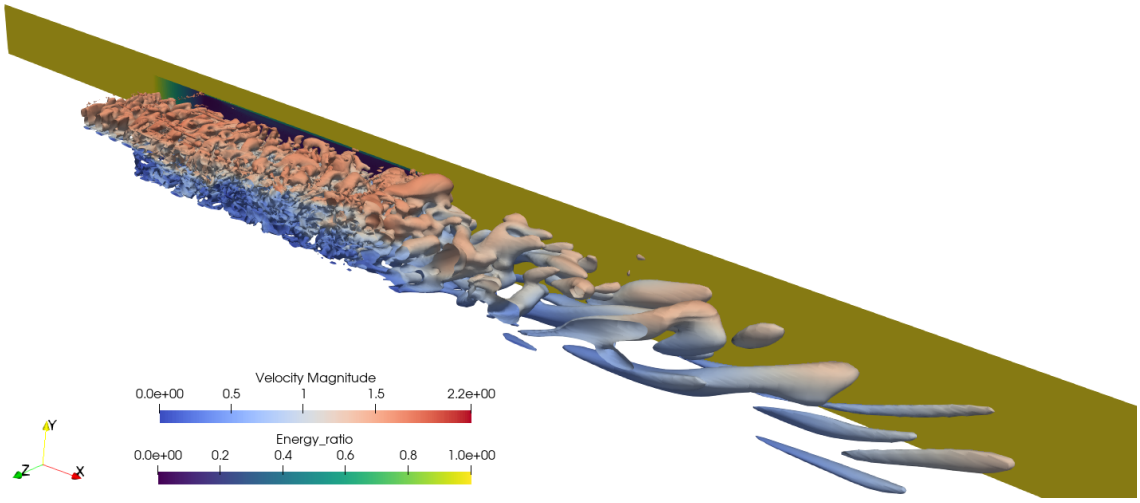

Figure D.8 – Q-Isosurfaces colored by the velocity magnitude ($Q = 0.3U_H^2/H^2$) and targeted turbulent energy ratio for the HTLES3.

References

Spalart, P. R (June 2000). "Strategies for Turbulence Modelling and Simulations". In: *International Journal of Heat and Fluid Flow* 21.3, pp. 252–263. (Visited on 06/26/2023).

Archambeau, Frédéric et al. (2004). "Code Saturne: A Finite Volume Code for the Computation of Turbulent Incompressible Flows - Industrial Applications". In: *International Journal on Finite Volumes* 1.1, http://www.latp.univ. (Visited on 04/18/2023).

Pope, Stephen B. (Mar. 2004). "Ten Questions Concerning the Large-Eddy Simulation of Turbulent Flows". In: *New Journal of Physics* 6.1, p. 35. (Visited on 06/26/2023).

Chaouat, B. et al. (2005). "A new partially integrated transport model for subgrid-scale stresses and dissipation rate for turbulent developing flows". In: *Phys. Fluids* 17.065106, pp. 1–19.

Girimaji, Sharath S. (Nov. 2005). "Partially-Averaged Navier-Stokes Model for Turbulence: A Reynolds-Averaged Navier-Stokes to Direct Numerical Simulation Bridging Method". In: *Journal of Applied Mechanics* 73.3, pp. 413–421. (Visited on 06/26/2023).

Geuzaine, Christophe et al. (2009). "Gmsh: A 3-D Finite Element Mesh Generator with Built-in Pre- and Post-Processing Facilities". In: *International Journal for Numerical Methods in Engineering* 79.11, pp. 1309–1331. (Visited on 06/30/2023).

Perot, J. Blair et al. (July 2009). "A Stress Transport Equation Model for Simulating Turbulence at Any Mesh Resolution". In: *Theoretical and Computational Fluid Dynamics* 23.4, pp. 271–286. (Visited on 07/11/2023).

Fadai-Ghotbi, Atabak et al. (June 2010). "Temporal Filtering: A Consistent Formalism for Seamless Hybrid RANS–LES Modeling in Inhomogeneous Turbulence". In: *International Journal of Heat and Fluid Flow*. Sixth International Symposium on Turbulence and Shear Flow Phenomena 31.3, pp. 378–389. (Visited on 07/04/2023).

Menter, Florian et al. (July 2010). "The Scale-Adaptive Simulation Method for Unsteady Turbulent Flow Predictions. Part 1: Theory and Model Description". In: *Flow Turbulence and Combustion* 85, pp. 113–138.

Lamballais, Eric (Apr. 2014). "Direct Numerical Simulation of a Turbulent Flow in a Rotating Channel with a Sudden Expansion". In: *Journal of Fluid Mechanics* 745, pp. 92–131. (Visited on 04/18/2023).

Park, Michael A. et al. (June 2016). "Unstructured Grid Adaptation: Status, Potential Impacts, and Recommended Investments Towards CFD 2030". In: *46th AIAA Fluid Dynamics Conference*. Washington, D.C.: American Institute of Aeronautics and Astronautics. (Visited on 07/11/2023).

Baglietto, Emilio et al. (Oct. 2017). "STRUCT: A Second-Generation URANS Approach for Effective Design of Advanced Systems". In: *ASME 2017 Fluids Engineering Division Summer Meeting*. American Society of Mechanical Engineers Digital Collection. (Visited on 07/11/2023).

Chaouat, Bruno (Sept. 2017). "The State of the Art of Hybrid RANS/LES Modeling for the Simulation of Turbulent Flows". In: *Flow, Turbulence and Combustion* 99.2, pp. 279–327. (Visited on 06/26/2023).

Chen, Lin et al. (June 2018). "A Review of Backward-Facing Step (BFS) Flow Mechanisms, Heat Transfer and Control". In: *Thermal Science and Engineering Progress* 6, pp. 194–216. (Visited on 07/06/2023).

Heinz, S. et al. (2020). "Hybrid RANS-LES Methods with Continuous Mode Variation". In: *Direct and Large Eddy Simulation XII*. Ed. by Manuel García-Villalba et al. ERCOFTAC Series. Cham: Springer International Publishing, pp. 441–447.

Krumbein, Benjamin et al. (2020). "A Scale-Resolving Elliptic-Relaxation-Based Eddy-Viscosity Model: Development and Validation". In: *New Results in Numerical and Experimental Fluid Mechanics XII*. Ed. by Andreas Dillmann et al. Notes on Numerical Fluid Mechanics and Multidisciplinary Design. Cham: Springer International Publishing, pp. 90–100.

Limare, Alexandre et al. (2020). "Adaptive Mesh Refinement with an Automatic Hybrid RANS/LES Strategy and Overset Grids". In: *Progress in Hybrid RANS-LES Modelling*. Ed. by Yannick Hoarau et al. Notes on Numerical Fluid Mechanics and Multidisciplinary Design. Cham: Springer International Publishing, pp. 159–168.

Duffal, Vladimir et al. (2022). "Development and Validation of a New Formulation of Hybrid Temporal Large Eddy Simulation". In: *Flow, Turbulence and Combustion* 108, p. 42. (Visited on 04/18/2023).

Mehta, M. et al. (2023). "Grey area mitigation in hybrid RANS/LES by means of volume forcing". In: *Proc. 10th Int. Symp. Turbulence, Heat and Mass Transfer, Rome, Italy.*